Triple Gauge Couplings and Polarization at the ILC and Leakage in a Highly Granular Calorimeter

Dissertation
zur Erlangung des Doktorgrades
des Department Physik
der Universität Hamburg

vorgelegt von
Ivan Marchesini
aus Verona

Hamburg
2011

Abstract

The work presented in this thesis was developed in the framework of detector R&D and physics studies for the International Linear Collider (ILC), a planned e^+e^- accelerator that will reach center of mass energies up to $500\,\mathrm{GeV}$ in its first stage.

In the first part of the thesis a simultaneous measurement of longitudinal beam polarization and Triple Gauge Couplings (TGCs) at the ILC is implemented, using fully simulated Monte Carlo events. In order to perform such a measurement, semileptonic decays of the W-pairs at $\sqrt{s} = 500\,\mathrm{GeV}$ are selected. Additionally, two techniques to measure the polarization alone are also compared.

Assuming 80% longitudinal polarization for the electron beam and 60% for the positron beam, a statistical relative precision of better than 0.2% on the average beam polarization of both beams is achieved at an integrated luminosity of $250\,\mathrm{fb}^{-1}$. In the option of a low positron polarization of 30%, with an integrated luminosity of $500\,\mathrm{fb}^{-1}$ the statistical relative precision on the average polarization is $\sim 0.1\%$ for the electron beam and $\sim 0.35\%$ for the positron beam. Three independent TGCs are fitted simultaneously with the polarization, without loosing sensitivity on the polarization. An absolute statistical uncertainty on the couplings is reached of the order of 10^{-3}.

The second part of the thesis presents the analysis of experimental data collected using the CALICE prototypes, during the 2007 test beam campaign at CERN. The complete setup of the experiment consisted of a silicon-tungsten electromagnetic calorimeter, an analog scintillator-steel hadron calorimeter and a scintillator-steel tail catcher. Events collected using pion beams in the energy range 8-100 GeV are selected and compared to the Monte Carlo simulations. While the leakage from the full setup is negligible, when removing the tail catcher information either partly or completely the energy loss becomes significant and affects the performance. The average measured energy decreases below the expected beam energy and the resolution deteriorates. A correction to the leakage was implemented for pions having the first hard interaction in the hadron calorimeter. The results obtained show that the correction is powerful in restoring the mean value of the measured energy distributions back to the expected beam energy, with an accuracy at the 1-2% level over the whole energy range. The relative improvement on the resolution is about 25% at $80\,\mathrm{GeV}$, decreasing at lower energies together with the impact of the leakage.

Zusammenfassung

Die hier vorgestellte Arbeit wurde im Rahmen der Forschung und Entwicklung von Detektoren, sowie Physikstudien für den Internationalen Linear Collider (ILC) entwickelt. Der ILC ist ein geplanter e^+e^- Beschleuniger mit einer Schwerpunktsenergie von bis zu $500\,\text{GeV}$.

Der erste Teil der Arbeit stellt eine gleichzeitige Messung der longitudinalen Strahlpolarisation, sowie der Triple Gauge Couplings (TGCs) am ILC vor auf der Basis von vollständig Monte Carlo-simulierten Ereignissen. Um eine solche Messung zu ermöglichen werden semileptonische W-Paarzerfälle selektiert. Darüber hinaus werden zwei weitere Techniken zur alleinigen Polarisationsmessung verglichen.

Bei einer angenommenen longitudinalen Polarisation von $80\,\%$ für den Elektron- und $60\,\%$ für den Positronstrahl und einer integrierten Luminosität von $250\,\text{fb}^{-1}$ wird eine relative statistische Präzision von besser als $0.2\,\%$ für beide Strahlen erreicht. Für eine niedrigere angenommene Positron-Polarisation von $30\,\%$ bei einer integrierten Luminosität von $500\,\text{fb}^{-1}$ wird eine relative Genauigkeit von $\sim 0.1\,\%$ für den Elektron- und $\sim 0.35\,\%$ für den Positronstrahl erreicht. Drei von einander unabhängige TGCs werden gleichzeitig zur Polarisationsmessung per Fit bestimmt ohne Sensitivität auf die Polarisationsmessung zu verlieren. Es wird eine absolute statistische Unsicherheit in der Größenordnung von 10^{-3} auf die Kopplungsstärken erreicht.

Im zweiten Teil der Arbeit wird eine Datenanalyse von experimentell mit Kalorimeter-Prototypen der CALICE Kollaboration aufgenommen Meßwerten vorgestellt. Die Daten wurden während der Testbeam Kampagne in 2007 am CERN aufgezeichnet. Der experimentelle Aufbau bestand aus einem elektromagnetischen Kalorimeter aus Silizium-Wolfram, einem analog ausgelesenen, hadronischen Kalorimeter aus Szintillatoren und Stahl und einem "Tail Catcher", der ebenfalls aus Szintillatoren und Stahlabsorbern bestand. Aufgezeichnete Pionstrahl-Ereignisse im Energiebereich zwischen $8\,\text{GeV}$ und $100\,\text{GeV}$ wurden selektiert und mit Monte Carlo Simulationen verglichen. Der Verlust von Teilchenenergie aus dem kompletten Aufbau ist vernachlässigbar, wird aber bei Nichtberücksichtigung der Information aus dem "Tail Catcher" signifikant und beeinflusst die Leistungsfähigkeit. Die mittlere gemessene Energie sinkt unterhalb die Strahlenergie und die Auflösung wird schlechter. Eine Korrektur dieses Energieverlustes wurde implementiert für Pionen, die die erste harte Wechselwirkung im hadronischen Kalorimeter haben. Die Resultate zeigen, daß die Korrektur die mittlere gemessene Energie wieder auf die erwartete Strahlenergie bringt mit einer Genauigkeit von ein bis zwei Prozent über den gesamten Energiebereich. Die relative Verbesserung der Auflösung ist ungefähr $25\,\%$ bei $80\,\text{GeV}$, mit abnehmender Tendenz für kleinere Werte zusammen mit dem abnehmenden Einfluss des Energieverlusts.

Contents

1 Introduction

During the last decades experimental evidences of the Standard Model (SM) have been accumulated at several experiments and the SM has come to be regarded as the best description of electromagnetic, weak and strong interactions up to the investigated energies. However, despite the many successes, some shortcomings have been identified and new theories have been formulated to rectify them.

A relevant feature of the SM is the presence of non-Abelian self-couplings between the gauge bosons, that carry the electromagnetic and the weak forces: the Ws, the Z and the γ. In particular, Triple Couplings between the Gauge bosons (TGCs) in the vertices $WW\gamma$ and WWZ occur, as largely experimentally established. A precise measurement of the TGCs not only represents a proof of the SM expectations, but is also a window to eventual new physics not predicted by the SM, contributing to the TGCs through the effect of new particles and couplings via radiative corrections. Should the new physics be not directly accessible at the available center-of-mass energies of ongoing or upcoming experiments, being sensitive to it via deviations from the SM values of the TGCs would be particularly relevant.

The measurement of the TGCs was performed at LEP (Large Electron-Positron collider) and Tevatron experiments. No deviations from the SM were observed, but the limits obtained at these experiments can be significantly improved at future colliders.

Today's most powerful high energy physics project is the proton-proton Large Hadron Collider (LHC) at CERN, where no major improvement on the experimental limits on anomalous couplings in the vertices $WW\gamma$ and WWZ is expected. Unprecedented precisions could be achieved at a future lepton collider, such as the International Linear Collider (ILC), a planned e^+e^- accelerator that will be able to reach center of mass energies up to $500\,\mathrm{GeV}$ in its first phase.

One of the unique features of the ILC is the possibility of both electron and positron beam polarization. A longitudinal electron polarization of at least 80% is part of the current ILC baseline design and the option of a longitudinal positron polarization is also considered. The positron beam produced by the baseline source has a polarization of 30% and beamline space has been reserved for an eventual upgrade up to a polarization of 60%.

The physics program of the ILC highly benefits from having polarized beams. The polarization provides a tool for strongly improving the sensitivity to new physics in SM precision tests, in searches for new particles and for the measurement of the interactions of new physics. For many of these applications, the benefit of the polarization is effective, provided that the systematics from the uncertainty on the beam polarization are brought to a negligible level.

While polarimeters are used to measure the polarization on a bunch-by-bunch basis, the absolute calibration of the average luminosity-weighted polarization at the interaction point (IP) with respect to the measurement of the polarimeters, can only be obtained

using a physics process. The W-pair production can be used to achieve this goal, due to its strong sensitivity to the beam polarization. The W-pair process is also a golden channel for the measurement of the TGCs, as the LEP experience teaches. Hence, it is possible to combine the two measurements in a global fit of polarization and TGCs. Such a measurement has been implemented using fully-simulated W-pairs in the International Large Detector (ILD) model for the ILC, at $\sqrt{s} = 500$ GeV. In order to measure the W charge with high purity, only semileptonic decays (q$\bar{\text{q}}l\nu$) of the W-pair are selected, where one W decays either into an electron or a muon, and the associated neutrino, while the other decays into a quark-antiquark pair.

Two techniques to measure the polarization alone have also been compared: i) the modified Blondel scheme, only relying on the different total cross sections of the W^+W^- production for different incoming beam polarizations; and ii) the angular fit method, which uses the distribution of the production angle $\cos\theta_W$ of the W^- with respect to the e^- beam axis. When fitting simultaneously the polarization and the TGCs, two angular observables describing the leptonic decay of the W are also exploited.

In order to exploit the physics potential of the ILC, a detector with excellent performances is indispensable. The particle flow approach has been identified as a possible way to achieve the precision goals.

The basic idea of particle flow is to limit the energy measurement with the hadron calorimeter to those neutral hadrons producing showers in it. The hadron calorimeter has by far the worst resolution among the sub-detectors of a high energy physics detector. The momentum of charged particles is measured more accurately by the tracking system and the photons by the electromagnetic calorimeter. If the calorimeters have a high granularity, it is possible to separate the clusters belonging to charged particles, neutral hadrons and photons. The energy of the charged particles and the photons can be measured by the tracking system and the electromagnetic calorimeter, respectively. The clusters assigned to these particles in the hadron calorimeter can, therefore, be subtracted and the remaining clusters should belong to showers initiated by neutral hadrons. Only for these objects the energy resolution of the hadron calorimeter plays actually a role.

The CALICE collaboration has constructed prototypes of highly granular calorimeters, in order to test the actual feasibility of the particle flow paradigm. The present study makes use of the data collected at CERN in 2007, when the configuration of the prototypes consisted of a silicon-tungsten electromagnetic sampling calorimeter (SiW-ECAL), a scintillator-steel hadron sampling calorimeter with analog readout (AHCAL) and a scintillator-steel tail catcher and muon tracker (TCMT).

Pion events have been selected and analyzed, focusing on the degradation of the response caused by the leakage of non-contained showers. The full experimental setup corresponds to a total depth of approximately 12 nuclear interaction lengths (λ_{I}) and leakage in the energy range considered (up to 100 GeV) is only a small effect. The impact on the average response for pions starting to shower in the AHCAL is less than 0.4%. However, in a future detector for a collider experiment, a coil is expected to be placed between the hadron calorimeter and the tail catcher. The presence of the coil will cause part of the hadronic showers to be lost, since the coil will not be instrumented for calorimetric measurements. For the work presented in the second part of the thesis, the presence of the coil has been simulated by removing the information of some TCMT layers and the consequent degradation of the energy resolution has been

measured.

In order to study the full potential of a highly granular hadron calorimeter, the energy resolution has also been studied after completely removing the TCMT information, which corresponds to reducing the total depth of the calorimetric system of about 5.8 λ_I. In such a configuration, the amount of leakage is significant and the energy resolution degrades. Exploiting the high granularity of the AHCAL and the possibility to reconstruct with high precision the shower development, a correction has been developed to recover from the leakage as much as possible, without relying on the TCMT presence.

This thesis is organized as follows:

- Chapter 2: the theory of the SM is described and its problems are underlined. The most popular extensions of the SM are introduced. Particular emphasis is given to the gauge principle, which has driven the formulation of the SM, and the related theory of TGCs.

- Chapter 3: the ILC accelerator and the ILD detector model are described. The software tools for massive simulations on the Grid of Monte Carlo events in the ILD detector are also illustrated.

- Chapter 4: the motivations for employing polarized beams at the ILC are reviewed, with general considerations and specific examples taken from the SM or its possible extensions. In the second part of the chapter the measurement of the polarization is discussed. The upstream and the downstream polarimeters are described as well as the sources of depolarization between the polarimeters and the IP, which motivate the study of data-driven polarization measurements.

- Chapter 5: the study of a combined measurement of the longitudinal beam polarization at the ILC and of the TGCs is presented. Two partial measurements of the polarization alone are also introduced. The study is completed with a realistic evaluation of the main sources of systematics expected at the ILC, in order to obtain reliable estimates of the precisions achievable.

- Chapter 6: the interactions of particles with matter are described and the principles of calorimetry are explained.

- Chapter 7: the prototypes of highly granular calorimeters built by the CALICE collaboration are illustrated. Special attention is paid to the AHCAL calorimeter, since it is of central importance for the leakage studies presented in Chap. 8.

- Chapter 8: the study of a correction to the leakage using pion events collected with the CALICE prototypes is presented.

  In the end of the thesis the conclusions of the two analysis performed are reported.

2 The Standard Model and Beyond

The Standard Model (SM) of particle physics was formulated between 1960 and 1970 by S. L. Glashow [1], A. Salam [2] and S. Weinberg [3], as a comprehensive theory of electroweak interactions. In 1971 G. 't Hooft proved its renormalizabilty [4, 5] and the model was immediately recognized as an extremely viable one. The success was affirmed experimentally in 1973 by the discovery of the neutral-current interactions in the Gargamelle experiment at CERN [6, 7], which the model had predicted. The discovery was confirmed the following year at Fermilab [8]. In 1973 the model was extended to the strong interactions and the hadronic sector by H. Fritsch, M. Gell-Mann and H. Leutwyler [9].

During the past 40 years experimental evidences of the SM have been accumulated at several experiments and the SM has come to be regarded as the correct description of electromagnetic, weak and strong interactions up to the investigated energies. One of the greatest successes was the detection at CERN in 1983 of the $W^{\pm}$ and the Z bosons [10, 11, 12], whose existence was predicted by the SM, together with the relative scheme of their masses and couplings. However, despite the many successes, some shortcomings have been identified and new theories have been formulated to rectify them.

In this chapter the theory of the SM is described and its problems are underlined. The most popular extensions of the SM are introduced. Special attention is paid to the gauge principle, which has driven the formulation of the SM (Sec. 2.2), and the related theory of TGCs.

2.1 The Particle Content of the Standard Model

A first classification of the known particles can be given according to their spin. Pauli formulated the necessity of such a quantum number in 1925, in order to explain the observed atomic energy levels [13]. The spin was afterward interpreted as an intrinsic angular momentum of the particles. This idea was first proposed by Kronig in 1925 and initially was not well received by the scientific community, in particular by the same Pauli (*"very clever but of course [it] has nothing to do with reality"* [14]), mainly due to the fact that it was classically untenable. The electron should have been rotating at a speed higher than the light speed, in order to produce the necessary angular momentum. The spin could be understood only in the context of the quantum theory.

Particles with half-integer spin are called fermions and are subject to the exclusion principle of Pauli, i.e. they cannot occupy the same quantum state at the same time. They are usually said to satisfy the Fermi-Dirac statistics. Particles with integer spin, called bosons, are described by the Bose-Einstein statistics and are not subject to the exclusion principle. In a gas of bosons brought to very low temperatures, the bosons will

Bosons	Scalars
$\gamma,\ W^+,\ W^-,\ Z,\ g_{1\ldots 8}$	ϕ (Higgs)
Fermions	
Quarks (3 color charges)	Leptons

charge				charge			
$2/3:$ $-1/3:$	$\begin{pmatrix} u \\ d \end{pmatrix}$	$\begin{pmatrix} c \\ s \end{pmatrix}$	$\begin{pmatrix} t \\ b \end{pmatrix}$	neutral : $-1:$	$\begin{pmatrix} \nu_e \\ e^- \end{pmatrix}$	$\begin{pmatrix} \nu_\mu \\ \mu^- \end{pmatrix}$	$\begin{pmatrix} \nu_\tau \\ \tau^- \end{pmatrix}$

Table 2.1: *Particle content of the Standard Model. From [16].*

tend to flood into the lowest energy level available, forming a so-called Bose-Einstein condensate, as proved in 1995 by Cornell and Wieman [15].

According to our present understanding, the elementary building blocks of matter are fermions with spin 1/2, while the interactions are carried by vector bosons, that have an integer spin 1 (Tab. 2.1). If some proposed extensions of the SM should turn out to be true, this distinction might not be so straightforward anymore (Sec. 2.8.1). The existence of an additional scalar (spin 0) particle called the Higgs boson, for which there is no direct experimental evidence, is also required by the SM in order to explain the mechanism that leads to the creation of masses (Sec. 2.6).

The known interactions are four: the electromagnetic, the weak, the strong and the gravitational. The electromagnetic interaction is carried by the photon, a massless and neutral particle. The mediators of the weak force are massive and can either be charged ($W^{\pm}$) or neutral (Z). The strong interaction is carried by the gluons (g), that are assigned a quantum number called color. Eight color states of the gluon exist. Gravity is not taken into account by the SM (Sec. 2.7). Since the gravitational attraction between elementary particles is negligible with respect to the other interactions that govern their behavior, this lacuna of the theory does not compromise the description of the electromagnetic, weak and strong interactions.

The fermions which undergo strong interactions are called quarks and are assigned a color charge. The fermions interacting only weakly and electromagnetically are called leptons. Leptons and quarks are grouped into three families. The first family consists of the electron (e^-) and its neutrino (ν_e) on the leptonic side and of the up (u) and down (d) quarks. The second family consists of the muon (μ^-) and its neutrino (ν_μ) and the charm (c) and strange (s) quarks. The third family consists of the tau (τ^-) and its neutrino (ν_τ) and the top (t) and bottom (b) quarks. All quarks and leptons are massive, though the mass of the neutrinos has never been directly measured, but indirectly proven from neutrino oscillations [17]. Each particle is associated to a corresponding antiparticle, which has the same mass but opposite quantum numbers. The neutrinos, that are the only neutral fermions, might be Majorana particles, i.e. they could be their own antiparticles. This property has not yet been proven experimentally and is being investigated by searching for neutrino-less β decays (e.g. [18]). The charges of all particles are multiples of the same reference charge, the charge e of the electron. All charged leptons have charge e, while the quarks have either charge $+\frac{2}{3}e$ or $-\frac{1}{3}e$ (as given in Tab. 2.1). This precise connection between the charges of leptons and quarks, for which there is no fundamental motivation in the SM, guarantees that the theory is anomaly free (Sec. 2.7.3).

The SM consists of a set of three quantum field theories, based on the principle of local gauge invariance (Sec. 2.2, 2.3 and 2.5). The electromagnetic and weak interactions

share the same gauge group $SU(2) \otimes U(1)$. The strong interaction is described by Quantum ChromoDynamics (QCD), a gauge theory based on the non-Abelian group $SU(3)$. In the following only the electroweak sector of the SM is described in detail.

2.2 The Gauge Principle and the QED

The gauge principle (or principle of gauge invariance) had a central role in the development of the twentieth century physics, driving the formulation of the theory of interactions (for a historical introduction see e.g. [19, 20]). The first mathematical germs of the gauge theory were developed by Weyl in 1918 [20, 21], in his failed attempt to extend Einstein's General Relativity, in order to describe gravitation and electromagnetism within a unified framework. The starting point of Weyl's work was the observation that the Riemannian geometry, used in General Relativity, contains an element of geometry at distance ("ferngeometrisches Element" [20]), that allows to compare the magnitude of two vectors at any arbitrarily separated points. He felt uneasy with this property, that seemed to him as an accidental inheritance from the Euclidean geometry, without a real physical motivation. In his work Weyl moved to a geometry where lengths of vectors can be compared only at the same spacetime point. He realized this by equipping the spacetime with a class of equivalent metrics, that differ only by a choice of the calibration (or gauge). A gauge transformation of the metric is justified in the presence of a potential (namely the electromagnetic field), changing accordingly to assure the invariance of the physical laws. Only classes of metrics and potentials connected by gauge transformations have a physical meaning, not the single choices inside the class.

Despite the fact that Weyl could re-derive successfully the property of conservation of the electric charge, as a direct implication of the invariance under gauge transformations, Einstein immediately recognized a weak point in the theory. The change in length of a field vector transported along a path depends in general on the path followed, in disagreement with any empirical evidence. For instance, two identical atomic clocks in adjacent spacetime points, which are moved and meet again after having followed different trajectories, would in general have different frequencies after the shift. This dependence of the behavior of clocks with their history is against any observation, in particular with the existence of stable atomic spectra.

In 1928-1929 Weyl reinterpreted his work within the new quantum mechanics, as suggested already in 1927 by London [22], achieving the modern formulation of the gauge principle [23, 20]. Following an independent approach in the framework of wave mechanics, also Fock [24] and Klein [25] had obtained similar results in 1926.

The fundamental change, with respect to the 1918 work, was that Weyl connected now electromagnetism with matter and not with gravitation. The arbitrary gauge transformation was not to be applied to the metric of the spacetime in the presence of an electromagnetic field, but to the wavefunction of the particles.

The details of the gauge principle in this final, correct, formulation are given in the following in its application to the theory of Quantum ElectroDynamics (QED), the first complete and successful theory based on the local gauge invariance. QED represents the relativistic and quantistic counterpart of classical electrodynamics, giving a precise description of the electromagnetic interactions.

The free Lagrangian of QED is given by the Dirac equation:

$$\mathcal{L}_\psi = \bar{\psi}(i\,\slashed{\partial} - m)\psi. \tag{2.1}$$

The four-component wavefunction ψ describes the electron (or any other spin-$\frac{1}{2}$ particle) of mass m and the corresponding antiparticle. The probability density associated to ψ is given by:

$$\rho \equiv \psi^\dagger \psi = \sum_{i=1}^{4} |\psi_i|^2. \tag{2.2}$$

The quantity ρ is not affected by local phase transformations, called *local gauge transformations*:

$$\psi \rightarrow \psi' = \exp\left[-i\alpha(x)\right]\psi. \tag{2.3}$$

In other words, all physical experiments would produce the same result when considering ψ or ψ'. This appears as a redundant and unphysical degree of freedom. On the other side, the Lagrangian is not invariant under the transformation in Eq. 2.3, since:

$$\mathcal{L}_\psi \rightarrow \mathcal{L}'_\psi = \mathcal{L}_\psi + \bar{\psi}\gamma_\mu\psi(\partial^\mu\alpha). \tag{2.4}$$

This is not surprising. Eq. 2.3 alters the wavefunction by arbitrarily changing its complex phase at each point of spacetime. With the given outset it is clear that a field, called *gauge field*, needs to be introduced, in order to explain the phase differences. The properties of this field, that will be indicated in the following with A_μ, are set by hand in order to obtain the invariance of the Lagrangian under the local gauge transformation. The field is required to transform like:

$$A_\mu \rightarrow A'_\mu = A_\mu + \frac{1}{e}\partial_\mu\alpha, \tag{2.5}$$

and enters the Lagrangian through the covariant derivative:

$$\partial_\mu \rightarrow D_\mu \equiv \partial_\mu + ieA_\mu. \tag{2.6}$$

With these two conditions one obtains:

$$\begin{aligned}
\mathcal{L}_\psi \rightarrow \mathcal{L}'_\psi &= \bar{\psi}'\left[(i\,\slashed{\partial} - e\,\slashed{A}') - m\right]\psi' \\
&= \bar{\psi}\exp(+i\alpha)\left[i\,\slashed{\partial} - e\left(\slashed{A} + \frac{1}{e}\,\slashed{\partial}\alpha\right) - m\right]\exp(-i\alpha)\psi \\
&= \mathcal{L}_\psi - e\bar{\psi}\gamma_\mu\psi A^\mu.
\end{aligned} \tag{2.7}$$

The new Lagrangian is invariant under the local phase transformation in Eq. 2.3. Identifying e with the electron charge and A_μ with the photon, the interaction term $-e\bar{\psi}\gamma_\mu\psi A^\mu$ arisen in the Lagrangian by requiring the gauge invariance represents the electromagnetic interaction.

This example clarifies the extent of the gauge principle. Imposing the invariance of the Lagrangian under certain local gauge transformations, one generates naturally the proper interaction terms and the interaction fields. The importance of the gauge principle as "*a guiding principle for writing fundamental interactions of fields*" [26] was clear to Salam and Ward, at the time the SM was under development [27, 26]:

> "*Our basic postulate is that it should be possible to generate strong, weak and electromagnetic interaction terms (with all their correct symmetry properties and also with clues regarding their relative strengths) by making local gauge transformations on the kinetic–energy terms in the free Lagrangian for all particles.*"

In order to regard A_μ as the physical photon field, it is necessary to add to the Lagrangian a term corresponding to its kinetic energy. Introducing the electromagnetic strength tensor:

$$F_{\mu\nu} \equiv \partial_\mu A_\nu - \partial_\nu A_\mu, \tag{2.8}$$

the kinetic term is given by:

$$\mathcal{L}_A = -\frac{1}{4} F_{\mu\nu} F^{\mu\nu}, \tag{2.9}$$

which is invariant under Eq. 2.3. The gauge field associated to the local phase transformation is expected to have an infinite range, since there is no spacetime limit to the phase transformation. Hence, the photon is massless. A hypothetical mass term for the gauge field:

$$\mathcal{L}_A^m = -\frac{1}{2} m_\gamma^2 A_\mu A^\mu, \tag{2.10}$$

would break the local gauge invariance. The description of massive vector bosons preserving the gauge invariance requires further expedients.

To conclude, it should be noticed that unphysical degrees of freedom are still present in the system after having applied the gauge principle, since A_μ is not fixed. Additional conditions, called *gauge fixing*, need to be applied. The problem of gauge fixing is rather complex, in particular for non-Abelian gauge transformations (Sec. 2.3), and lies outside the introductory purpose of this chapter. An overview of the topic can be found in [28].

2.3 Gauge Invariance for Non-Abelian Groups

The local transformation introduced in the previous section in Eq. 2.3 belongs to the unitary Abelian group known as the $U(1)$ group. In this section the extension of the gauge principle to non-Abelian groups is described.

In 1932 Heisenberg suggested that neutron and proton could be considered as two states of the same particle [29], observation at the time mainly driven by the fact that the masses of the two particles are nearly equal and that the light, stable, even nuclei

contain equal numbers of them [30]. In analogy to the spin, the isospin (at the time called isotopic spin) quantum number was introduced. The proton and neutron were then associated with different isospin projections $I_3 = +1/2$ and -1/2, respectively.

In 1937 Breit, Condon and Present showed the approximate equality of $p - p$ and $n - p$ interactions in the ^1S state [31], with the small residual differences attributable to magnetic interactions [32]. It seemed natural to generalize the equality, arriving at the concept of the total isospin conservation in nucleon-nucleon interactions, where the electromagnetic interaction can be neglected with respect to the strong interaction [30]. The isospin conservation was then extended to all strong interactions, supported by experimental observations of the energy levels of light nuclei and of pion-nucleon interactions [30, 33].

Considering the two-component wave function describing the field of isospin 1/2:

$$\psi \equiv \begin{pmatrix} \psi_p \\ \psi_n \end{pmatrix}, \tag{2.11}$$

the isospin conservation can be expressed as invariance under the global unitary transformation of the Lie $SU(2)$ group, the global isospin rotation:

$$\psi \rightarrow \psi' = U\psi, \quad U = \exp\left(-i\frac{\sigma^a}{2}\alpha^a\right) \simeq 1 - i\frac{\sigma^a}{2}\alpha^a, \tag{2.12}$$

where σ^a, $a = 1, 2, 3$ are the Pauli matrices.

In 1954 Yang and Mills observed that the invariance under global isospin rotation means that, when electromagnetic interaction can be neglected, the orientation of the isospin is of no physical significance [30]. They concluded that [27, 30]:

> *"The differentiation between a neutron and a proton is then a purely arbitrary process. As usually conceived, however, this arbitrariness is subject to the following limitation: once one chooses what to call a proton, what a neutron, at one spacetime point, one is then not free to make any choices at other spacetime points."*

Analogously to the local gauge phase-space transformation for the charged field, a local gauge transformation can be introduced for the isospin, as an arbitrary way of choosing the orientation of the isospin axis (i.e. "what to call a proton, what to call a neutron") at all space-time points. Such a transformation is obtained from Eq. 2.12, with the only difference that the gauge parameters depend on the spacetime points, i.e. $\alpha^a \rightarrow \alpha^a(x)$. Following the example of QED, Yang and Mills required the invariance under the local gauge isospin transformation, the main difference from QED being that it is a non-Abelian transformation.

The work of Yang and Mills can be generalized [34] for any non-Abelian group G with generators T_a satisfying the Lie algebra:

$$[T_a, T_b] = i\, C_{abc}\, T_c, \tag{2.13}$$

where C_{abc} are the structure constants of the group.

The general local gauge $SU(2)$ transformation is given by:

$$\Omega \equiv \exp\left[-i\,T^a\alpha^a(x)\right].$$

(2.14)

As in Sec. 2.2, a gauge boson field A_μ^a is introduced for each generator, entering the Lagrangian via the covariant derivative:

$$\partial_\mu \to D_\mu \equiv \partial_\mu - igT^a A_\mu^a,$$

(2.15)

and transforming like:

$$T^a A_\mu^a \to \Omega\left(T^a A_\mu^a + \frac{i}{g}\partial_\mu\right)\Omega^{-1},$$

(2.16)

or, with the substitution $\Omega \simeq 1 - i\,T^a\alpha^a(x)$:

$$A_\mu^{a\,\prime} = A_\mu^a - \frac{1}{g}\partial_\mu\alpha^a + C_{abc}\,\alpha^b A_\mu^c.$$

(2.17)

Using these relations the covariance of the Lagrangian is guaranteed. The strength tensor defined in Eq. 2.8 is generalized in the following way:

$$F_{\mu\nu}^a \equiv \partial_\mu A_\nu^a - \partial_\nu A_\mu^a + g\,C_{abc}\,A_\mu^b A_\nu^c.$$

(2.18)

The invariant kinetic term in the Lagrangian is then simply given by:

$$\mathcal{L}_A = -\frac{1}{4}F_{\mu\nu}^a F^{a\,\mu\nu}.$$

(2.19)

While also in the non-Abelian case an eventual mass term $A_\mu^a A^{a\,\mu}$ would be non-invariant under the local gauge transformation, there is a new feature with respect to the $U(1)$ case (writing the Lagrangian in a simplified way, with omission of the indices):

$$\mathcal{L}_A \propto (\partial A - \partial A)^2 + g(\partial A - \partial A)AA + g^2 AAAA,$$

(2.20)

i.e. the gauge fields have now triple and quartic *self couplings*. This property represents a notable success of the gauge theory. At the time, the necessity of self couplings was not driven by experimental observations or theoretical motivations. In fact, the gauge self couplings are not inserted by hand in the framework, but arise naturally when applying the gauge principle to a non-Abelian symmetry group. Only afterward it has been experimentally confirmed that this feature is actually realized in nature (cf. Fig. 2.1 and Sec. 2.5).

2.4 The Weak Interaction

In 1914 Chadwick first observed that the β spectrum is continuous [35], an observation that lead Pauli to propose in 1930 [36] the existence of a light, neutral and feebly interacting ("*it would have the same or perhaps 10 times bigger ability to get through [material] than a gamma-ray*" [36]) particle emitted during the β decay, that later on was given the name neutrino. The understanding of the phenomenon was improved by the discovery of the neutron by Chadwick in 1932 [37], that allowed Pauli to correctly describe the β decay in 1933 [38] as:

$$n \rightarrow p + e^- + \bar{\nu}_e. \tag{2.21}$$

The theory of weak interactions was officially born in 1934, when Fermi introduced the "contact interaction" Lagrangian to describe the β decay, based on the description of the phenomenon given by Pauli [39, 40]. The idea of Fermi was to mimic the interaction term of the well established QED Lagrangian (Eq. 2.7). The features of the interaction responsible for the β decay clearly differentiated it from the electromagnetic force, due to its lower intensity and the presence of charged currents, while the electromagnetism is always characterized by neutral currents. Hence, he replaced the coupling constant e in the QED interaction term with a new constant, nowadays known as the Fermi constant G_F. The Lagrangian he came up with was:

$$\mathcal{L}_{\text{weak}} = \frac{G_F}{\sqrt{2}} \left(\bar{\psi}_p \, \gamma_\mu \, \psi_n \right) \left(\bar{\psi}_e \, \gamma^\mu \, \psi_\nu \right), \tag{2.22}$$

known as "contact interaction" Lagrangian, since all the spinors are calculated at the same spacetime point. With I the 2×2 identity matrix and $\sigma_x, \sigma_y,$ and σ_z the Pauli matrices, one defines:

$$\gamma^0 = \begin{pmatrix} I & 0 \\ 0 & -I \end{pmatrix} \qquad \gamma^1 = \begin{pmatrix} 0 & \sigma_x \\ -\sigma_x & 0 \end{pmatrix} \tag{2.23}$$

$$\gamma^2 = \begin{pmatrix} 0 & \sigma_y \\ -\sigma_y & 0 \end{pmatrix} \qquad \gamma^3 = \begin{pmatrix} 0 & \sigma_z \\ -\sigma_z & 0 \end{pmatrix} \tag{2.24}$$

and, for later use:

$$\gamma^5 = i\gamma^0\gamma^1\gamma^2\gamma^3. \tag{2.25}$$

The forms γ_μ, that give pure vector interactions, were chosen by Fermi simply in analogy to the QED. The covariance of the Lagrangian would have been obtained, in principle, also by replacing the vector fields with one of the other 4 possible *Dirac bilinear covariant matrices*. In the most general case the Lagrangian is given by:

$$\mathcal{L}_{\text{weak}} = \frac{G_F}{\sqrt{2}} \sum_i C_i \left(\bar{\psi}_p \, \Gamma^i \, \psi_n \right) \left(\bar{\psi}_e \, \Gamma^i \, \psi_\nu \right), \tag{2.26}$$

with the scalar, pseudo–scalar, vector, axial and tensor structures:

$$\Gamma^S = 1, \quad \Gamma^P = \gamma_5, \quad \Gamma^V_\mu = \gamma_\mu, \quad \Gamma^A_\mu = \gamma_\mu\gamma_5, \quad \Gamma^T_{\mu\nu} = \sigma_{\mu\nu}, \tag{2.27}$$

where:

$$\sigma_{\mu\nu} \equiv \frac{i}{2} \left(\gamma_\mu \gamma_\nu - \gamma_\nu \gamma_\mu \right). \tag{2.28}$$

Already in 1936 [41] it became clear that some transitions needed to be described with a different bilinear form, with respect to the choice of Fermi. Nuclear transitions with $\Delta J = 0$ can be, in principle, described either with Γ^S or Γ^V currents, while $\Delta J = 0, \pm 1$ (but not $0 \to 0$) transitions can be taken into account either by Γ^A or Γ^T interactions. However, for the fundamental understanding of the physics behind the choice of the bilinear form, it would have been necessary to wait for another 20 years, with the discovery of the parity violation.

Meanwhile, the Fermi interaction was generalized to a broader class of phenomena. The fact that the β decay could be just one of the manifestations of a new interaction, the weak interaction, was first proposed by Pontecorvo in 1947 [42] and the idea was extended by Tiomno, Wheeler and John [43] and Lee, Rosenbluth, Yang and Chen-Ning [44] in 1949. It became clear that different processes like the β decay, the μ decay and the μ capture were all manifestations of the weak interaction, sharing the same coupling constant G_F.

A big step towards a clearer understanding of the weak interaction was represented by the discovery of the parity violation, which happened only in the nineteen-fifties. This delay is explained by the fact that the parity of a system, which defines its behavior under spacial reflection, was assumed to be a naturally conserved quantity.

In 1955, thanks to the work of Alvarez and Goldhaber [45] and Birge [46], emerged the so-called $\theta - \tau$ puzzle: "two" particles were discovered, called θ and τ, that seemed to be two states of the same particle, since they had the same width and the same mass. The only reason why they were given different names was that they had different decay modes, into states with opposite parity:

$$
\begin{aligned}
\theta^+ &\to \pi^+ + \pi^0 \,, & J^P &= 0^+ \,, \\
\tau^+ &\to \pi^+ + \pi^+ + \pi^- \,, & J^P &= 0^- .
\end{aligned}
$$

Assuming that the two particles were the same particle, would have been equivalent to assuming that the parity could be violated. In 1956 Lee and Yang [47] examined this possibility and proposed a possible way to test it.

A relevant observable with respect to the parity is the helicity, defined as the projection of the spin of a particle along the momentum direction:

$$h \equiv \vec{s} \cdot \hat{p}, \tag{2.29}$$

where $\vec{s}$ is the spin and $\hat{p}$ is the unit vector in the direction of the momentum. The helicity is a pseudoscalar and changes sign under spatial reflection. It is not a quantum number, since for massive particles its sign depends on the reference frame. The corresponding quantum number is called chirality, that merges with helicity only in the relativistic limit, when the speed is close to the speed of light c. Particles with negative helicity are called left-handed, while particles with positive helicity are called right-handed.

Lee and Yang realized that, if parity conservation is violated in weak interactions, then the average value of the helicity, or similarly defined pseudoscalar quantities, in the final state would not be zero. They proposed a test based on the β decay of polarized ^{60}Co. At the end of 1956 Madame Wu succeeded in realizing their proposed experiment [48], establishing not only that the weak force violates parity, but also leading to the conclusion that electrons are preferentially left-handed. Upon hearing the first results of the experiment, Lee and Yang started to develop the so-called two-component theory of the neutrino [49], which requires that the neutrino is either left-handed or right-handed. In 1958 an experiment carried out by Goldhaber [50] showed that the neutrino is always left-handed (when neglecting the mass of the neutrino, that in principle always allows to perform a Lorentz transformation which would flip the helicity).

The new discoveries lead to the formulation of the so-called V-A theory of weak interactions, that solves the problem of the choice of the bilinear covariant form in Eq. 2.26. The weak currents should be written using vector (V, γ^μ) and axial vector (A, γ_5) forms, like (example for the positively charged current):

$$J_{\text{lept}}^{+\,\mu} = \left[\bar{\psi}_e \, \gamma^\mu (1 - \gamma_5) \, \psi_\nu \right] , \qquad (2.30)$$

where the $(1-\gamma_5)$ terms introduces the parity violation. Actually the parity is not only violated, but maximally violated, as becomes clear when considering that the operator P_L:

$$P_L = \frac{1}{2}(1 - \gamma_5), \qquad (2.31)$$

is the left-handed projector, that replaces the full spinors ψ with their left-handed projections.

In parallel with the discovery of the V-A theory, in 1957 Schwinger [51] and Lee and Yang [52] developed also the idea that weak interactions are mediated by massive bosons, in order to solve a problem of unitarity violation in Eq. 2.22. In the Fermi Lagrangian all the interactions are taken at the same spacetime point. Even when considered only as an effective, or phenomenological, Lagrangian, it cannot be adequate at high energies. One can consider, for example, the reaction [53]:

$$\nu_\mu + e^- \rightarrow \nu_e + \mu^- , \qquad (2.32)$$

which, according to Eq. 2.22, would consist of an s-wave scattering. Its cross section is given by:

$$\sigma = \frac{4}{\pi}(G_F p_\nu)^2, \qquad (2.33)$$

where p_ν is the momentum of the neutrino in the center-of-mass system. From the unitarity bounds of the optical theorem one obtains the condition [53] that $p_\nu < 300\,\text{GeV}$. At high momentum transfer, i.e. at small distances, the contact Lagrangian approximation is not valid anymore, since it violates unitarity. In order to solve the problem the existence of intermediate vector bosons was formulated, in analogy to QED. Due to

the short range of the weak interactions, the weak vector bosons had to be very massive. At the time only processes occurring via charged current were known, therefore only the existence of two charged vector bosons was initially assumed (the $W^\pm$). The necessity of an additional, neutral, weak vector boson (the Z) was first introduced by Glashow in 1961 [1] and the first prove of a process occurring through neutral current was obtained experimentally in 1973 [6, 7].

The presence of massive mediators does not represent a full solution to the unitarity problem. For instance, the amplitude of the elastic scattering of the W bosons, $WW \rightarrow WW$, would grow indefinitely with energy for longitudinally-polarized particles [54, 55]. From unitarity conditions one derives the bound:

$$s \leq e\pi\sqrt{2}/G_F \sim (1.2\,\mathrm{TeV})^2, \tag{2.34}$$

on the center of mass energy, for the validity of a theory of weakly coupled massive gauge bosons.

The Higgs mechanism, which is explained in Sec. 2.6, cancels the divergence at high energies by destructive interference of the contributing graphs from an additional scalar particle, the Higgs boson.

2.5 The Electroweak Sector in the Standard Model

The electromagnetic and the weak interactions are treated together in the SM as a unified gauge theory. The gauge group of the electroweak sector of the SM is:

$$SU(2)_L \otimes U(1)_Y. \tag{2.35}$$

The $SU(2)$ gauge transformation acts on left-handed (L) weak isospin (I) doublets, while the $U(1)$ gauge theory acts on isospin singlets assigned the hypercharge Y. The weak hypercharges are chosen to reproduce the observed electric charges, through the connection $Q = I_3 + \frac{1}{2}Y$, known as the Gell-Mann-Nishijima formula.

The leptonic part of the electroweak sector is organized in the left-handed electroweak doublets:

$$\mathsf{L}_e = \begin{pmatrix} \nu_e \\ e^- \end{pmatrix}_L \quad \mathsf{L}_\mu = \begin{pmatrix} \nu_\mu \\ \mu^- \end{pmatrix}_L \quad \mathsf{L}_\tau = \begin{pmatrix} \nu_\tau \\ \tau^- \end{pmatrix}_L, \tag{2.36}$$

with weak isospin $I = \frac{1}{2}$ ($I_3 = +\frac{1}{2}$ for the neutrinos and $I_3 = -\frac{1}{2}$ for the corresponding leptons) and weak hypercharge $Y(\mathsf{L}_\ell) = -1$, and the right-handed charged leptons, constituting weak isospin singlets ($I = 0$) (here idealizing that the neutrinos are massless):

$$\mathsf{R}_{e,\mu,\tau} = e_R, \mu_R, \tau_R, \tag{2.37}$$

with weak hypercharge $Y(\mathsf{R}_\ell) = -2$.

The hadronic sector consists of the left-handed quark doublets:

$$\mathsf{L}_q^{(1)} = \begin{pmatrix} u \\ d' \end{pmatrix}_L, \quad \mathsf{L}_q^{(2)} = \begin{pmatrix} c \\ s' \end{pmatrix}_L, \quad \mathsf{L}_q^{(3)} = \begin{pmatrix} t \\ b' \end{pmatrix}_L, \tag{2.38}$$

with weak isospin $I = \dfrac{1}{2}$ and weak hypercharge $Y(\mathsf{L}_q) = \dfrac{1}{3}$, and the right-handed singlets:

$$\mathsf{R}_u^{(1,2,3)} = u_R, c_R, t_R \quad \text{and} \quad \mathsf{R}_d^{(1,2,3)} = d_R, s_R, b_R, \tag{2.39}$$

with isospin 0 and weak hypercharges $Y(\mathsf{R}_u) = \dfrac{4}{3}$ and $Y(\mathsf{R}_d) = -\dfrac{2}{3}$.

The primes on the lower components of the quark doublets in Eq. 2.38 signal that the weak eigenstates are mixtures of the mass eigenstates, according to the relations:

$$\begin{pmatrix} d' \\ s' \\ b' \end{pmatrix} = \begin{pmatrix} V_{ud} & V_{us} & V_{ub} \\ V_{cd} & V_{cs} & V_{cb} \\ V_{td} & V_{ts} & V_{tb} \end{pmatrix} \begin{pmatrix} d \\ s \\ b \end{pmatrix} \equiv \mathsf{V} \begin{pmatrix} d \\ s \\ b \end{pmatrix}, \tag{2.40}$$

where the 3×3 unitary CKM (Cabibbo [56]–Kobayashi–Maskawa [57]) matrix V expresses the quark mixing. The current best estimate of the V elements can be found in [58], and shows that the mixing between the quark families is rather limited. Complex phases are also present in the matrix, that account for CP violation in decays of quark-antiquark states, called mesons.

The fact that each left-handed lepton doublet is matched by a left-handed quark doublet guarantees that the theory is anomaly free, so that quantum corrections respect the gauge symmetry [59] (Sec. 2.7.3).

Under the local gauge transformations of the $SU(2)_L$ group, singlets and doublets transform like:

$$\mathsf{L} \rightarrow \mathsf{L}' = \exp\left(i\frac{g}{2}\sigma^a \alpha^a\right) \mathsf{L}, \quad \mathsf{R} \rightarrow \mathsf{R}' = \mathsf{R}, \tag{2.41}$$

where σ^a, $a = 1, 2, 3$ are the Pauli matrices. Analogously, under the local gauge transformation of the $U(1)_Y$ group they transform like:

$$\mathsf{L} \rightarrow \mathsf{L}' = \exp\left(i\frac{g'}{2}Y\beta\right) \mathsf{L}, \quad \mathsf{R} \rightarrow \mathsf{R}' = \exp\left(i\frac{g'}{2}Y\beta\right) \mathsf{R}. \tag{2.42}$$

α^a, $a = 1, 2, 3$, and β are functions of space and time, while g and g' are the coupling constants associated to the groups $SU(2)_L$ and $U(1)_Y$ respectively.

The gauge fields associated to the generators of the groups will be denominated in the following W and B:

$$\begin{aligned} SU(2)_L & \rightarrow & W_\mu^1, \ W_\mu^2, \ W_\mu^3, \\ U(1)_Y & \rightarrow & B_\mu. \end{aligned}$$

The strength tensors are defined analogously to Eq. 2.8 and Eq. 2.18:

$$
\begin{aligned}
W^i_{\mu\nu} &\equiv \partial_\mu W^i_\nu - \partial_\nu W^i_\mu + g\,\varepsilon^{ijk}\,W^j_\mu W^k_\nu\ , \\
B_{\mu\nu} &\equiv \partial_\mu B_\nu - \partial_\nu B_\mu,
\end{aligned}
$$

while the covariant derivatives are defined as in Eq. 2.15 and Eq. 2.66:

$$
\text{left}\quad:\quad \partial_\mu + i\,\frac{g}{2}\,\sigma^i\,W^i_\mu + i\,\frac{g'}{2}\,Y B_\mu, \tag{2.43}
$$

$$
\text{right}\quad:\quad \partial_\mu + i\,\frac{g'}{2}\,Y\,B_\mu. \tag{2.44}
$$

For the leptons the free Lagrangian is given by:

$$
\begin{aligned}
\mathcal{L}_{\text{leptons}} &= \ \bar{\mathsf{R}}\,i\,\slashed{\partial}\,\mathsf{R} + \bar{\mathsf{L}}\,i\,\slashed{\partial}\,\mathsf{L} \\
&= \ \bar{\ell}_R\,i\,\slashed{\partial}\,\ell_R + \bar{\ell}_L\,i\,\slashed{\partial}\,\ell_L + \bar{\nu}_L\,i\,\slashed{\partial}\,\nu_L \\
&= \ \bar{\ell}\,i\,\slashed{\partial}\,\ell + \bar{\nu}\,i\,\slashed{\partial}\,\nu,
\end{aligned} \tag{2.45}
$$

where no interactions are present, by definition, and all the particles are massless.

Applying the gauge principle with respect to the transformations in Eq. 2.41 and 2.42, one generates the interaction terms:

$$
\begin{aligned}
\mathcal{L}_{\text{leptons}} \quad\rightarrow\quad & \mathcal{L}_{\text{leptons}} + \ \bar{\mathsf{L}}\,i\gamma^\mu\left(i\frac{g}{2}\sigma^i W^i_\mu + i\frac{g'}{2}Y B_\mu\right)\mathsf{L} \\
& + \bar{\mathsf{R}}\,i\gamma^\mu\left(i\frac{g'}{2}Y B_\mu\right)\mathsf{R}.
\end{aligned} \tag{2.46}
$$

From this equation it is clear that the fields W^a_μ and B_μ do not represent the physical fields, since they would all interact with the neutrino, while a photon field not coupled to the neutrino is needed. The physical fields of the photon A_μ and the neutral weak field Z_μ are obtained performing a rotation with the Weinberg angle θ_W:

$$
\begin{pmatrix} A_\mu \\ Z_\mu \end{pmatrix} = \begin{pmatrix} \cos\theta_W & \sin\theta_W \\ -\sin\theta_W & \cos\theta_W \end{pmatrix} \begin{pmatrix} B_\mu \\ W^3_\mu \end{pmatrix}. \tag{2.47}
$$

The Weinberg angle is related to the coupling constants g and g':

$$
\cos\theta_W = \frac{g}{\sqrt{g^2 + g'^2}}. \tag{2.48}
$$

The charged weak fields are given by:

$$
W^\pm_\mu = \frac{1}{\sqrt{2}}(W^1_\mu \mp W^2_\mu), \tag{2.49}
$$

in such a way that the $V - A$ structure of the weak charged currents is reproduced:

$$\mathcal{L}^{\mathsf{L}(\pm)}_{\text{leptons}} = -\frac{g}{2\sqrt{2}} \left[\bar{\nu}\gamma^\mu(1 - \gamma_5)\ell \, W^+_\mu + \bar{\ell}\gamma^\mu(1 - \gamma_5)\nu \, W^-_\mu \right]. \tag{2.50}$$

The neutral part of the Lagrangian becomes:

$$\begin{aligned}
\mathcal{L}^{(\mathsf{L+R})(0)}_{\text{leptons}} &= -g \sin\theta_W \, (\bar{\ell}\gamma^\mu\ell) \, A_\mu \\
&\quad -\frac{g}{2\cos\theta_W} \sum_{\psi_i=\nu,\ell} \bar{\psi}_i\gamma^\mu(g^i_V - g^i_A\gamma_5)\psi_i Z_\mu,
\end{aligned} \tag{2.51}$$

where the first term gives the electromagnetic interaction and the second term the neutral weak current. The electromagnetic interaction term can be expressed in the familiar way, using the e coupling constant, according to the relations:

$$e = g \sin\theta_W = g' \cos\theta_W. \tag{2.52}$$

At this point the theory has already a great predictive power and can be easily applied to the quark sector, but it lacks a fundamental ingredient. As already mentioned above, the gauge principle alone does not allow to introduce mass terms for the gauge fields, without breaking the gauge invariance. Moreover, the $SU(2)_L \otimes U(1)_Y$ gauge symmetry forbids fermion mass terms $\bar{\psi}\psi = \bar{\psi}_R\psi_L + \bar{\psi}_L\psi_R$ in the Lagrangian, because the left-handed and the right-handed fields transform differently. To give masses to the gauge bosons and to the fermions, a mechanism needs to be found hiding the symmetry, as described in the next section.

To conclude the exposition of this part of the theory, it should be underlined that the non-Abelian nature of the $SU(2)_L$ group results in self-interactions between the gauge bosons (cf. Eq. 2.20). In particular, a TGC term is present in the Lagrangian, that can be expressed as [60]:

$$\begin{aligned}
\mathcal{L}_{TGC} &= -\tfrac{1}{2}g(\partial_\mu W^i_\nu - \partial_\nu W^i_\mu)\varepsilon_{ijk}W^{j\mu}W^{k\nu} \\
&= ig\sin\theta_W(\hat{W}^-_{\mu\nu}W^{+\mu} - \hat{W}^+_{\mu\nu}W^{-\mu})A^\mu + ig\sin\theta_W \hat{A}_{\mu\nu}W^{-\mu}W^{+\nu} \\
&\quad + ig\cos\theta_W(\hat{W}^-_{\mu\nu}W^{+\mu} - \hat{W}^+_{\mu\nu}W^{-\mu})Z^\nu + ig\cos\theta_W \hat{Z}_{\mu\nu}W^{-\mu}W^{+\nu},
\end{aligned} \tag{2.53}$$

where $i, j = 1, 2$, $\hat{V}_{\mu\nu} = \partial_\mu V_\nu - \partial_\nu V_\mu$ and $V_\mu = W_\mu, A_\mu, Z_\mu$. The first and the second terms describe the γWW vertex with coupling strengths $e = g\sin\theta_W$ while the third and the fourth terms describe the ZWW vertex with coupling strengths $g\cos\theta_W = e/\tan\theta_W$.

The TGC term, that arises naturally due the non-Abelian nature of the $SU(2)$ group, is experimentally well established. Fig. 2.1 shows the measured cross section of the W-pair production at LEP [61]. The prediction of the SM agrees perfectly with the data only when the TGC vertices are included. Under different assumptions it would follow a completely wrong trend.
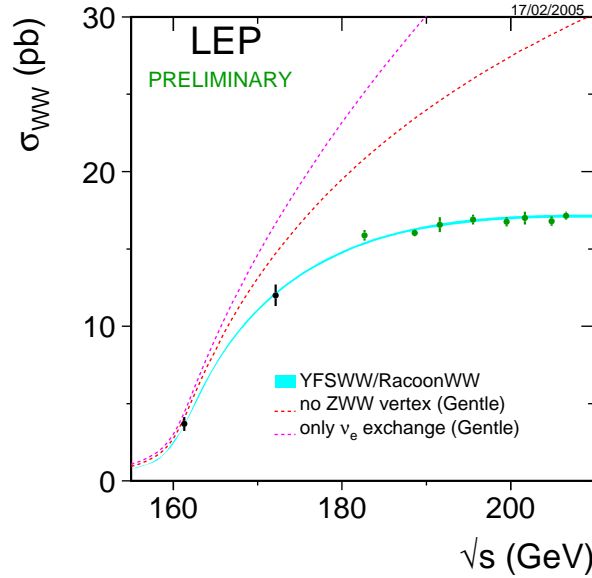
Figure 2.1: *The dependence of σ_{WW} on $\sqrt{s}$ as measured at LEP. The error bars include statistical and systematic contributions. The lower dashed curve shows the cross section that would be expected if the WWZ couplings were zero, while the upper dashed curve refers to the case where both the WWZ and the $WW\gamma$ vertices are excluded. The continuous curve shows the SM expectations with all the TGC vertices included. From [62].*

2.6 The Electroweak Symmetry Breaking

The masses in the SM are generated via the ElectroWeak Symmetry Breaking (EWSB), which is based on the Higgs mechanism [63, 64, 65].

The Higgs mechanism is related to the concept of spontaneous symmetry breaking, which can be introduced with the common example of a scalar self–interacting real field with Lagrangian:

$$\mathcal{L} = \frac{1}{2}\partial_\mu\phi\,\partial^\mu\phi - V(\phi), \tag{2.54}$$

where

$$V(\phi) = \frac{1}{2}\mu^2\phi^2 + \frac{1}{4}\lambda\phi^4, \tag{2.55}$$

is the potential and $\lambda > 0$.

The Lagrangian is invariant under the global discrete transformation:

$$\phi \to -\phi. \tag{2.56}$$

Depending on the sign of μ^2 two different situations occur for the vacuum, which are shown in Fig. 2.2.

For $\mu^2 > 0$ there is just one vacuum at $\phi_0 = 0$ (left plot), which obeys the reflection symmetry of Eq. 2.56. However, for $\mu^2 < 0$ there are two possible vacua states, for $\phi_0^\pm = \pm\sqrt{-\mu^2/\lambda}$ (right plot). This case corresponds to a wrong sign for the ϕ mass
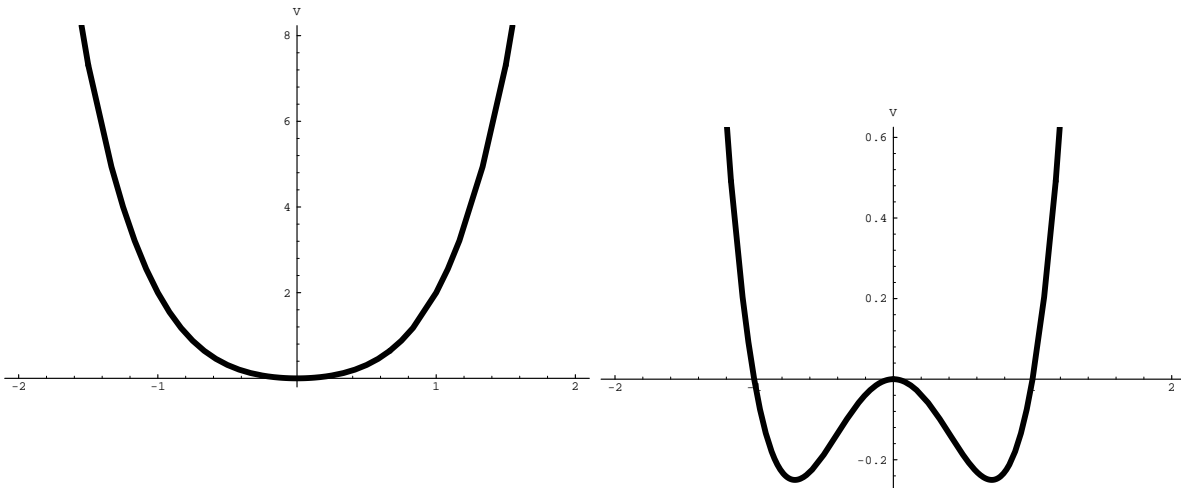
Figure 2.2: *Potential of a scalar, self-interacting field ϕ, $V(\phi) = \frac{1}{2}\mu^2\phi^2 + \frac{1}{4}\lambda\phi^4$, for $\mu^2 > 0$ (left) and for $\mu^2 < 0$ (right). From [27].*

term. $\phi_0 = 0$ in this case does not coincide with the energy minimum. Perturbative calculations should be done with expansions around ϕ_0^+ or ϕ_0^-. Since the Lagrangian is invariant under Eq. 2.56 the choice between ϕ_0^+ or ϕ_0^- is irrelevant. Nature will choose one of the two minima (e.g. $v = \phi_0^+$), resulting in the symmetry being *spontaneously broken*. In fact, after the choice of the minimum the Lagrangian is still invariant, while the vacuum is not.

Perturbative calculations around the chosen minimum can be written like:

$$\phi = v + \phi', \tag{2.57}$$

where ϕ' represents the quantum fluctuations around the minimum.

The vacuum of ϕ' is $\phi'_0 = 0$ and the perturbative Lagrangian is given by:

$$\mathcal{L}' = \frac{1}{2}\partial_\mu\phi'\partial^\mu\phi' - \frac{1}{2}\left(\sqrt{-2\mu^2}\right)^2\phi'^{\,2} - \lambda\,v\,\phi'^{\,3} - \frac{1}{4}\lambda\phi'^{\,4}. \tag{2.58}$$

This Lagrangian describes a scalar field ϕ' with real and positive mass, $M_{\phi'} = \sqrt{-2\mu^2}$. Due to the $\phi'^{\,3}$ term the new Lagrangian is not invariant under the reflection transformation. The mass term was "generated", when spontaneously breaking the original symmetry by a choice of the ground state.

In 1961 Goldstone [66] applied the concept of spontaneous symmetry breaking to global continuous transformations. His studies resulted in the so-called Goldstone theorem, which states that when an exact continuous global symmetry is spontaneously broken, a massless scalar particle is generated for each broken generator of the original symmetry group. This theorem seemed to move the concept of spontaneous symmetry breaking far from the description of reality, since there was no experimental evidence for such additional massless particles.

In 1964 Higgs and other authors [63, 64, 65] were able to find a way to bypass the Goldstone theorem. Higgs demonstrated that the Goldstone theorem is not applicable in those cases, when the Lagrangian of the system is invariant under local gauge transformations. The relevant side-effect is that some of the spin-one quanta, associated

with the gauge group, acquire mass in the process. The Higgs mechanism does not contradict the Golstone theorem, it rather represents an exception, where the Goldstone bosons get absorbed in the longitudinal degrees of freedom of the massive vector bosons (which would be absent if their masses were zero).

In the following, the details of the Higgs mechanism are given, showing its application to the electroweak sector of the SM.

A scalar field is introduced, given by the complex $SU(2)$ doublet:

$$\phi = \begin{pmatrix} \phi^+ \\ \phi^0 \end{pmatrix}, \tag{2.59}$$

where ϕ^+ and ϕ^0 are scalar fields. Analogously to Eq. 2.55, the Higgs potential is defined as:

$$V\left(\phi^\dagger \phi\right) = \mu^2 \left(\phi^\dagger \phi\right) + \lambda \left(\phi^\dagger \phi\right)^2, \tag{2.60}$$

with $\lambda > 0$. In order to apply the spontaneous breaking of the $SU(2)_L \otimes U(1)_Y$ symmetry, the vacuum for the scalar fields is chosen to be $\phi^+_{\text{vac}} = 0$ and $\phi^0_{\text{vac}} = \sqrt{-\mu^2/(2\lambda)}$, so that the v.e.v. (vacuum expectation value) of the $SU(2)$ doublet becomes:

$$\langle \phi \rangle_0 = \begin{pmatrix} 0 \\ v/\sqrt{2} \end{pmatrix}, \tag{2.61}$$

with $v \equiv \sqrt{-\mu^2/\lambda}$. The vacuum for the charged component has been set to zero, since the exact electromagnetic symmetry needs to be preserved. The spontaneous breaking of the $SU(2)_L \otimes U(1)_Y$ symmetry has to result in a $U(1)_{em}$ symmetry, of dimension one, which has to remain a symmetry of the vacuum.

The broken theory is expanded perturbatively around the chosen vacuum:

$$\Phi \equiv \exp\left(i\frac{\sigma^i \chi_i}{2v}\right) \begin{pmatrix} 0 \\ (v+H)/\sqrt{2} \end{pmatrix}. \tag{2.62}$$

Rewriting this expression like:

$$\simeq <\Phi>_0 + \frac{1}{2\sqrt{2}} \begin{pmatrix} \chi_2 + i\chi_1 \\ 2H - i\chi_3 \end{pmatrix} = \frac{1}{\sqrt{2}} \begin{pmatrix} i\sqrt{2}\omega^+ \\ v + H - iz^0 \end{pmatrix}, \tag{2.63}$$

the expected presence of the Goldstone bosons, $\omega^\pm$ and z^0, is made explicit. The Goldstone bosons are washed away by a $SU(2)_L$ gauge transformation:

$$\Phi \to \Phi' = \exp\left(-i\frac{\sigma^i \chi_i}{2v}\right) \Phi = \frac{(v+H)}{\sqrt{2}} \begin{pmatrix} 0 \\ 1 \end{pmatrix}, \tag{2.64}$$

where $\alpha_i = \chi_i/v$ (unitary gauge). The Lagrangian associated to the Higgs potential is given by:

$$\mathcal{L}_{\text{scalar}} = \partial_\mu \Phi^\dagger\, \partial^\mu \Phi - V(\Phi^\dagger \Phi). \tag{2.65}$$

With the usual expression of the covariant derivative:

$$\partial_\mu \to D_\mu = \partial_\mu + i\, g \frac{\sigma^i}{2} W^i_\mu + i\, \frac{g'}{2} Y B_\mu, \tag{2.66}$$

the Lagrangian can be written in terms of the new fields in Eq. 2.64:

$$\mathcal{L}_{\text{scalar}} = \left| \left(\partial_\mu + ig \frac{\sigma^i}{2} W^i_\mu + i \frac{g'}{2} Y B_\mu \right) \frac{(v+H)}{\sqrt{2}} \begin{pmatrix} 0 \\ 1 \end{pmatrix} \right|^2 \\ - \mu^2 \frac{(v+H)^2}{2} - \lambda \frac{(v+H)^4}{4}. \tag{2.67}$$

This Lagrangian contains the mass terms for the gauge fields, that can be expressed in terms of the physical fields $W^\pm$ and Z:

$$\frac{g^2 v^2}{4} W^+_\mu W^{-\,\mu} \tag{2.68}$$

and

$$\frac{g^2 v^2}{8 \cos^2 \theta_W} Z_\mu Z^\mu. \tag{2.69}$$

The predicted masses for the gauge bosons are, consequently:

$$M_W = \frac{gv}{2} \qquad M_Z = \frac{gv}{2 \cos \theta_W} = \frac{M_W}{\cos \theta_W}. \tag{2.70}$$

No quadratic term in A_μ appears, thus the photon remains massless, as required. Eq. 2.67 contains also terms involving exclusively the scalar field H, namely:

$$-\frac{1}{2}(-2\mu^2)H^2 + \frac{1}{4}\mu^2 v^2 \left(\frac{4}{v^3} H^3 + \frac{1}{v^4} H^4 - 1 \right), \tag{2.71}$$

from which it is possible to derive the Higgs mass:

$$M_H = \sqrt{-2\mu^2}. \tag{2.72}$$

Eq. 2.71 shows also the presence of self-interactions of the Higgs field.

The mass of the fermions is set via their Yukawa coupling to the Higgs field, that is:

$$\begin{aligned} \mathcal{L}^\ell_{\text{yuk}} &= -G_\ell \left[\bar{\mathsf{R}} \left(\Phi^\dagger \mathsf{L} \right) + \left(\bar{\mathsf{L}} \, \Phi \right) \mathsf{R} \right] \\ &= -G_\ell \frac{(v+H)}{\sqrt{2}} \left[\bar{\ell}_R \, (0 \;\; 1) \begin{pmatrix} \nu_L \\ \ell_L \end{pmatrix} + (\bar{\nu}_L \;\; \bar{\ell}_L) \begin{pmatrix} 0 \\ 1 \end{pmatrix} \ell_R \right] \\ &= -\frac{G_\ell \, v}{\sqrt{2}} \, \bar{\ell} \, \ell - \frac{G_\ell}{\sqrt{2}} \, \bar{\ell} \, \ell \, H, \end{aligned} \tag{2.73}$$

so that the masses of the charged leptons are given by:

$$M_\ell = \frac{G_\ell \, v}{\sqrt{2}}.$$

(2.74)

Once the mixing parameter $\sin^2 \theta_W$ is fixed by the study of neutral-current interactions, the theory predicts successfully the masses of the weak gauge bosons. An additional sign of elegance of the theory lies in the fact that the same angle accounts for the vanishing coupling between the photon and the neutrino and for the gauge bosons masses. The predictive power of the theory is more limited with respect to the Higgs sector. No a priori knowledge of the Higgs mass is given, nor a hint of the Yukawa couplings of the Higgs to the fermions, that remain free parameters. Indirect constraints on the Higgs mass are discussed in the following.

2.6.1 The Higgs Mass

The existence of one of the fundamental ingredients of the SM, namely the Higgs boson, has not yet been experimentally confirmed. From the electroweak theory it is not possible to derive a precise prediction for the mass of the Higgs, though in 1977 Lee, Quigg and Thacker could obtain a conditional upper bound through a unitarity argument [54, 67]. Considering the two-body collisions between the W-bosons, the Z-boson and the Higgs, four channels are particularly interesting:

$$W_L^+ W_L^- \quad \frac{Z_L Z_L}{\sqrt{2}} \quad \frac{HH}{\sqrt{2}} \quad HZ_L,$$

(2.75)

where L denotes the longitudinal polarization states, and the factors of $\sqrt{2}$ account for identical particle statistics. The s-wave amplitudes for these processes are asymptotically constant and proportional to $G_F M_H^2$. Imposing unitarity conditions one derives that $M_H \lesssim 1\,\text{TeV}$. If the mass of the Higgs boson does not satisfy this condition, the weak interactions among $W^\pm$, Z and the Higgs become strong at the TeV scale and could be spotted, for instance, by the presence of strong WW scattering (see also Sec. 3.3.3).

In order to set tighter constraints, one can demand that the electroweak sector of the SM is a consistent theory up to a certain cutoff energy scale Λ, where new physical phenomena would emerge. Two examples of cutoff are commonly considered in the literature: $\Lambda = 1\,\text{TeV}$ and $\Lambda \sim M_{\text{Planck}} \approx 10^{19}$ GeV. The former condition exemplifies the case of new physics beyond the SM contributing already at low energies, while the latter implies that the SM remains valid up to the Planck scale.

A lower bound can be achieved considering the $t\bar{t}H$ Yukawa coupling, that might destabilize the Higgs potential (Eq. 2.60) through loop corrections. In case of a too light Higgs, the broken-symmetry vacuum would no longer be the state of minimum energy [68, 69]. For a cutoff $\Lambda = 1\,\text{TeV}$, the requirement that the vacuum is the absolute minimum of the radiatively corrected Higgs potential leads to the condition [69, 70] (m_t is the top quark mass):

$$M_H|_{\Lambda=1\text{TeV}} \gtrsim 50.8 \text{ GeV} + 0.64(m_t - 173.1 \text{ GeV}),$$

(2.76)

already experimentally surpassed (see below), while for $\Lambda = M_{\text{Planck}}$ it rises to:

$$M_H|_{\Lambda = M_{\text{Planck}}} \gtrsim 134 \text{ GeV}. \tag{2.77}$$

An upper bound is obtained from the Higgs loop corrections to the quartic term in the Higgs potential (Eq. 2.60). To prevent them from diverging, the following requirements need to be fulfilled [71]:

$$\begin{aligned} M_H|_{\Lambda = M_{\text{Planck}}} &\lesssim 180 \text{ GeV}; \\ M_H|_{\Lambda = 1\text{TeV}} &\lesssim 700 \text{ GeV}. \end{aligned} \tag{2.78}$$

Additionally to these theoretical bounds on the Higgs mass, also experimental constraints exist. Combining the direct search results from all the LEP experiments, yields a 95% C.L. lower bound of 114.4 GeV for the mass of the SM Higgs boson [72]. The combined analysis from the Tevatron experiments exclude at 95% C.L. the existence of a SM Higgs boson with a mass between 160 and 170 GeV [73].

Indirect experimental bounds are also obtained from fits to precision measurements of electroweak observables. A global fit to the precision electroweak data accumulated during the last decades, mainly at LEP, SLC and Tevatron, gives $m_H = 87^{+35}_{-26}$ GeV, or $m_H < 157$ GeV at 95% C.L. [58]. If the direct LEP search limit of $m_H > 114.4$ GeV is also taken into account in the fit, the limit becomes $m_H < 186$ GeV at 95% C.L. [58].

2.7 Shortcomings of the Standard Model

The SM does not have the trademark of a really fundamental theory. On the one side, in order to apply the SM to the real world and make predictions for physical processes, too many free parameters need to be set (Sec. 2.7.5). For instance, the magnitudes of masses and mixings are not really calculated, but essentially accommodated according to experimental measurements. On the other side, there is no fundamental explanation in the SM for relevant properties, like the number of generations of quarks and leptons, or the quantization of the charge (Sec. 2.7.3). The same is true for the negative sign of the μ^2 coefficient in Eq. 2.60, which is a basic ingredient of the symmetry breaking.

Besides these general limitations, that at least do not affect the functionality of the theory, the SM has also more specific shortcomings. For instance, no dark matter (Sec. 2.7.1) candidate is provided and a hierarchy problem (Sec. 2.7.6) arises when considering the loop corrections to the Higgs mass.

Due to these imperfections, it is clear that the SM has to be considered as a low energy approximation of the real theory of interactions. However, it should be mentioned that it is an extremely good approximation, which has successfully described decades of high energy physics precision results.

In the following the most relevant motivations to go beyond the SM are summarized.

2.7.1 The Dark Matter

The problem of dark matter is probably the most tangible limit of the SM. Several independent observations agree that the known particles account for only a small fraction of the matter composing the universe. The contribution of ordinary matter to the total energy density of the universe is estimated to be 4.6% [74]. About one quarter of the universe, namely 22.7% [74], is assumed to consist of a new type of matter, called dark matter, which is likely to be composed of one or more species of sub-atomic particles, interacting very weakly with ordinary matter. The remaining 72.8% [74] is assumed to be given by dark energy, a hypothetical form of energy that permeates the universe, having a gravitationally repulsive effect. It explains both the flatness of the universe and the observed accelerated expansion (e.g. [75]).

The necessity of dark matter became largely accredited in the 1980's as a possible interpretation of the rotation curves of spiral galaxies. In 1970 Freeman noticed that the Keplerian decline, expected from the distribution of the visible mass, was not present in the galaxies NGC 300 and M 33 and considered an additional undetected mass as a possible justification [76]. The observation of flat rotation curves was later confirmed by successive studies (e.g. [77]).

The dark matter hypothesis is consistent also with measurements of the Cosmic Microwave Background [74] and with gravitational lensing observations, which allow to "see" the invisible dark matter through its relativistic bending effect on the light from distant sources (e.g. [78]).

Weakly interacting massive particles are present in the SM, namely the neutrinos, but they have been excluded as possible candidates of dark matter, due to constraints on the neutrino density in the universe ($\Omega_\nu h^2 < 0.0062$ at 95% CL [74]). Moreover, the SM neutrinos are not candidates for cold (non-relativistic at the time of the structure formation) dark matter, which is favoured by scenarios of the structure formation of the universe [79], due to the strong upper limits on the neutrino masses ($\sum m_\nu < 0.58$ eV at 95% CL [74]).

2.7.2 The Baryon Asymmetry

Experimental observations indicate that in the universe matter is largely dominating over antimatter. This asymmetry is usually expressed in terms of the baryon-to-photon ratio:

$$\eta \equiv \frac{n_b - \overline{n}_b}{n_\gamma}, \tag{2.79}$$

where n_b, $\overline{n}_b$, and n_γ are the number densities of baryons, antibaryons, and photons, respectively. Measurements based on the Big Bang nucleosynthesis and the abundances of light elements [58] and more accurate measurements of the Cosmic Microwave Background [74] give a value of η of $\approx 10^{-10}$. While in the early days of the Big Bang cosmology this asymmetry was considered to be an initial condition of the universe [80], it is currently believed that it was created dynamically. In particular, inflation would dilute an original asymmetry, due to the production of entropy during reheating [80]. The baryon asymmetry can be dynamically realized when three conditions are satisfied, first identified by Sakharov in 1967 [81]:

- the existence of processes that violate the baryon number.

- the loss of thermal equilibrium.

- C and CP violation.

The first condition is obvious. The second condition is required in order to avoid that those processes leading to a baryon excess are compensated by their inverse reactions. This requirement may occur naturally in an expanding universe. Finally, C and CP violation prevent the C- and CP-conjugate of the baryon-violating reactions to cancel on average any produced asymmetry.

In the SM the violation of the baryon number is possible through nonperturbative effects, as shown by 't Hooft in 1976 [82], and the CP violation is introduced by the CKM matrix. However, both effects are very small compared to the observed baryon asymmetry. There is no theorem proving that it is a priori impossible to create a baryogenesis scenario, which is able to obtain the measured value of η using only the ingredients provided by the SM. Attempts were made to construct such a mechanism, for instance the one by Farrar and Shaposhnikov in 1993 [83], but they have all been refuted (a confutation of the proposal in [83] is given in [84]).

2.7.3 Quantization of the Electric Charge

Two properties of the charge of elementary particles are missing a fundamental motivation in the SM: the quantization of the charge and the correlation of the charges in the leptonic and the hadronic sectors, which has been proven experimentally with an impressive precision [70]:

$$|Q_p + Q_e| < 10^{-21}|Q_e|, \tag{2.80}$$

where Q_p and Q_e are the charges of the proton and the electron, respectively.

Most notably the following equation is valid:

$$N_C(Q_u + Q_d) = -Q_e, \tag{2.81}$$

where N_C is the number of colors in QCD, while Q_u and Q_d are the electromagnetic charges respectively of the up- and down-type quarks. This relation, that holds just by chance in the SM, plays a major role in theory, since it assures that it is anomaly free [59].

In 1931 Dirac proved that the quantization of charge would be explained by the existence of a particle with a single magnetic pole, known as magnetic monopole [85, 86, 87]. Magnetic monopoles are foreseen by Gran Unified Theories (GUT, Sec. 2.8.2), as arisen in 1974 from the work of 't Hooft [88] and Polyakov [89]. The mass of the monopoles in some GUT scenarios can be very high, that would explain why no experimental evidence of monopoles has ever been found. For instance, in an $SU(5)$ model with a unification scale of 10^{16} GeV, the monopoles would have a mass of about $10^{17} - 10^{18}$ GeV [58, 90]. In GUTs also the connection between the charges in the hadronic and the leptonic sectors would emerge naturally, since QCD and the electroweak theory result from the breaking of a larger gauge symmetry (Sec. 2.8.2).

2.7.4 The Absence of Gravity and the Vacuum Catastrophe

Despite the negligible role that gravity plays in particle reactions, a really fundamental theory of interactions is expected to take it into account. This is not just a cosmetic issue. Strong motivations exist to have a full quantum theory of gravity, such as the vacuum energy problem, which is summarized in the following.

The value of the Higgs potential at the v.e.v. (Eq. 2.61) is:

$$V\left(\langle\phi^\dagger\phi\rangle\right) = \frac{\mu^2 v^2}{4} = -\frac{|\lambda|\, v^4}{4} < 0. \tag{2.82}$$

This potential is responsible for a uniform vacuum energy density in the universe (using the relation $M_H^2 = -2\mu^2$):

$$\varrho_H \equiv \frac{M_H^2 v^2}{8}. \tag{2.83}$$

Substituting into this expression $v = (G_F\sqrt{2})^{-\frac{1}{2}} \approx 246$ GeV and the current lower experimental bound on the Higgs mass $M_H \gtrsim 114.4$ GeV [58], one obtains:

$$\varrho_H \gtrsim 10^8 \text{ GeV}^4. \tag{2.84}$$

In order to take into account the effects of this vacuum energy in cosmology, it can be translated into a non-null cosmological constant $\Lambda = (8\pi G_N/c^4)\varrho_H$, to be added to Einstein's equation of General Relativity [70, 91].

In 1998 two independent measurements of very bright supernovae explosions, known as Type Ia [92, 93], led to the conclusion that the expansion of the universe is accelerating. This behavior can be attributed to a non-null cosmological constant, as one would also qualitatively expect from the Higgs potential. However, a huge quantitative discrepancy emerges when considering the bounds on the vacuum energy density in the universe, derived experimentally from measurements of the Cosmic Microwave Background [94], that set an upper limit about 50 orders of magnitude smaller than the SM lower bound in Eq. 2.84. This problem, known also as the *vacuum catastrophe*, clearly remarks that the relationship of the SM to gravitation cannot be simply ignored.

2.7.5 The Problem of Identity

In a fundamental theory scales, masses and couplings should emerge naturally, without the need of individual tunings. This is not the case for the SM, where a high number of free parameters need to be set. Unfortunately, also possible extensions of the SM are not really capable of improving this theoretical limitation and sometimes increase it even further.

Three factors are needed in the SM for the couplings of the gauge group $SU(3) \times SU(2) \times U(1)$. Two parameters are required to specify the Higgs potential. In the strong sector six parameters are needed for the quark masses and four for the CKM matrix, three for the mixing angles and one for the CP-violating phase. The same number of parameters are required in the leptonic sector as well (if the neutrino masses are not neglected). One parameter is needed for the QCD vacuum phase (topic here not

covered, see e.g. [95]) and two additional CP-violating phases enter in case the neutrinos are Majorana particles. Altogether, more than 20 free parameters are required.

The presence of free parameters is not simply an aesthetic problem of the theory, since it limits its predictive power. For example, the generation of the mass is explained by the Higgs mechanism, but not the actual value of the masses of quarks and leptons observed experimentally, which are determined by the apparently arbitrary couplings to the Higgs boson. The same is true for the CKM mixing mechanism. It represents a parametrization of the mismatch between flavor and mass eigenstates and of CP-violation, but does not provide any fundamental motivation.

2.7.6 The Hierarchy Problem

The mass of the Higgs boson receives quantum corrections via loop effects:

$$m_H^2 \left(p^2 \right) = m_{0,H}^2 + \mathcal{C} g^2 \int_{p^2}^{\Lambda^2} dk^2 + \dots \, , \qquad (2.85)$$

where g is the gauge coupling constant, $\mathcal{C}$ is a constant coefficient, and Λ is the reference scale up to which the SM is assumed to remain valid. The integral in Eq. 2.85 is quadratically divergent, giving corrections on the Higgs mass $\delta_{m_H^2} \propto \Lambda^2$. Assuming that the SM is the correct theory, describing the reality up to the Planck scale, $\Lambda \sim M_{\text{Planck}} \approx 10^{19}$ GeV. As seen above, unitarity conditions yield an upper limit on the Higgs mass of the order of $1\,\text{TeV}$. In order to satisfy this constraint, a fine tuning with a relative precision of the order of $m_H/\Lambda_P > 10^{16}$ is necessary. This might actually be the way of the world, but it seems a rather unnatural eventuality. A more natural option would be given by the presence of new physics, either intervening at the TeV scale to tame the divergent loop in Eq. 2.85 or realizing the symmetry breaking with an alternative mechanism to the Higgs.

2.7.7 Grand Unification

The three gauge groups of the SM $U(1)$, $SU(2)$ and $SU(3)$ are associated to three coupling constants. The polarization of the vacuum, due to the presence of virtual pairs of particles in it, implies that in Quantum Field Theory the couplings become the functions of a distance or an energy scale, i.e. they are running.

In the SM the strong and weak couplings associated with non-Abelian gauge groups decrease with energy, while the electromagnetic one associated with the Abelian group on the contrary increases. Extrapolating from the precision data, they approach each other at a scale of $\Lambda = 10^{16}$, without ever converging (cf. Fig. 2.3, left).

According to the GUT idea (Sec. 2.8.2), the interactions are contained in one force at very high energy scales. As a result of spontaneous symmetry breaking, the unifying group is broken and the unique interaction is split into three branches which we call strong, weak and electromagnetic interactions. Such a perspective requires the running constants to converge at high energies. The SM fails in this respect, but suggests the magnitude of the GUT scale $\Lambda = 10^{16}$. The unification is achieved by new theories, that introduce new physics beyond the SM (cf. Fig. 2.3, right).
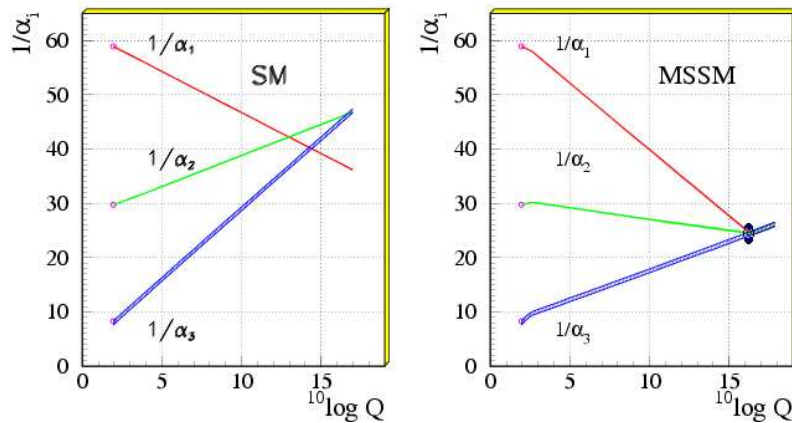
Figure 2.3: *Gauge coupling unification in the SM (left) and in a SUSY model (right). The plot is based on the extrapolation of the LEP data, as of 1991. The dark blob in the plot on the right represents model dependent corrections. From [58].*

2.8 Extensions of the Standard Model

The shortcomings of the SM reviewed in the previous section motivate the search for a new theory that must contain the SM as its low-energy limit. In particular, new particles or interactions, introduced by the new theory, should not spoil the successful predictions of precision observables through loop effects. In the following the most popular proposals for new physics beyond the SM are shortly introduced.

2.8.1 Supersymmetry

In the SM there is a fundamental dichotomy between fermions and bosons: fermions are the constituents of matter, while bosons are the mediators of the interactions. Supersymmetry (SUSY) (original papers [96, 97, 98]; general reviews [99, 100, 101]) relates the two categories under a new symmetry, that transforms a bosonic state $|B\rangle$ into a fermionic state $|F\rangle$, or vice versa. Denoting the Supersymmetry generator by Q, one can write:

$$Q|B\rangle \;=\; |F\rangle \tag{2.86}$$
$$Q|F\rangle \;=\; |B\rangle. \tag{2.87}$$

Q is a fermionic operator, therefore SUSY is said to introduce a new fermionic dimension. Every SM particle is associated by Q to a new supersymmetric particle. The naming convention for supersymmetric partners of SM fermions is to prepend an 's' to the name of their SM counterpart (e.g. the partner of a quark is called squark), while the partners of the SM bosons are identified by the suffix "-ino" (e.g. the supersymmetric partner of a gluon is called gluino). In the symbolic notation a tilde is put above the symbol used for the SM particles to represent their supersymmetric counterparts (e.g. to the τ corresponds the $\tilde{\tau}$). The supersymmetric partners differ from the corresponding SM particles only in their spin.

The fact that no supersymmetric partner has ever been discovered to date, clearly requires the SUSY symmetry to be broken, in order to push the masses of the super-symmetric particles beyond the energy regions already investigated.

SUSY addresses successfully many open issues of the SM:

- it gives the possibility to connect the gauge theories to gravity [102]. The SUSY algebra is a generalization of the Poincaré algebra:

$$
\begin{aligned}
\{Q_\alpha, Q_\beta\} &= \{\overline{Q}_{\dot\alpha}, \overline{Q}_{\dot\beta}\} = 0; \\
\{Q_\alpha, \overline{Q}_{\dot\beta}\} &= 2\sigma^m_{\alpha\dot\beta} P_m; \qquad [Q_\alpha, P_\mu] = 0.
\end{aligned}
\tag{2.88}
$$

  Therefore, an anticommutator of two SUSY transformations is a local coordinate translation. By making SUSY local it is possible to connect it with General Relativity.

- it solves the Hierarchy Problem, since the quadratic divergences in the loop corrections to the Higgs mass are stabilized by counter-diagrams with opposite spin statistics from the superpartners of SM particles [103].

- it achieves the unification of the interactions, with the convergence of the gauge couplings at a GUT scale of $\Lambda \approx 10^{16}$ GeV [104] (cf. Fig. 2.1).

- it addresses cosmological problems of the SM. Introducing new sources of CP-violation, some SUSY scenarios lead to consistent values of the baryon asymmetry [105]. Furthermore, SUSY can provide a promising candidate for the dark matter in our universe [106].

2.8.2 Grand Unified Theories

The success of the SM represents the success of the gauge theories as an extremely suitable framework for describing interactions in particle physics. In the SM there are three different gauge groups, $SU(3)_C$, $SU(2)_L$, and $U(1)_Y$, to which correspond three different couplings. It is natural to look for a single, non-Abelian grand unified gauge theory GUT with a single coupling, that would enable the unification of the three couplings [107, 108]. As seen in Sec. 2.7.7 the unification of forces is expected at a scale $\Lambda \approx 10^{16}$. Clearly, one must recover the SM at low energies, implying that the GUT gauge group G breaks into the SM gauge groups $G \rightarrow SU(3)_C \otimes SU(2)_L \otimes U(1)_Y$.

A strong motivation for a GUT comes from charge quantization and the correlation of fractional electrical charges with color charges (Sec. 2.7.3). Other successes of the theory are the possibility to predict the electroweak mixing angle $\sin^2 \theta_W$ [108] and the prediction of the b quark mass [109, 110], which remains remarkably successful if the effects of supersymmetric particles are included in the renormalization-group calculations [111]. A generic prediction of GUTs is also the proton decay, which is expected on general grounds, since there is no exact gauge symmetry to guarantee that the baryon number B is conserved. The prediction of the proton lifetime depends on the specific GUT model considered (e.g. [112]).

2.8.3 Warped Extra Dimensions

In Warped Extra Dimensions, or Randall-Sundrum (RS) models an extra spatial dimension with a strongly warped geometry (i.e. with an intrinsic curvature) is introduced [113, 114]. These models explain naturally the large hierarchy between the electroweak and Planck scales and the weakness of gravity. The weak scale is generated from a large scale of the order of the Planck scale through an exponential hierarchy. The exponential arises not from gauge interactions but from the metric itself.

RS models solve the Hierarchy Problem and can also provide an interpretation for the wide range of Yukawa coupling strengths. Such a hierarchy could come from different overlaps in the extra dimension of the wave functions of the particles with the Higgs field.

2.8.4 Technicolor

In the Technicolor theories [115, 116] a new non-Abelian gauge interaction is introduced together with additional massless fermions, called *technifermions*, and new force-carrying fields called *technigluons*. At the electroweak scale $\Lambda \approx 1\,\text{TeV}$ the technicolor coupling becomes strong, which leads to the formation of condensates of technifermions, responsible for the breaking of the global symmetry.

Massless Goldstone bosons, called *technipions*, appear during the symmetry breaking, three of which become the longitudinal components of the $W^{\pm}$ and Z^0 weak bosons, which acquire masses [117].

In order to produce the masses of the SM fermions, one needs to invoke Extended TechniColor models [118], where Technicolor and SM interactions are embedded into a larger group, which breaks at high energies. The massive gauge bosons involved in this breaking allow interactions between the SM fermions and the technifermions, giving rise to the couplings necessary to generate the fermion masses.

Technicolor address the Hierarchy Problem rather naturally and has a plausible mechanism for stabilizing the weak scale far below the Planck scale. In fact, the new interaction is asymptotically-free, i.e. it couples weakly at very high energies $\sim 10^{16}\,\text{GeV}$, while becoming strong at the electroweak scale [118].

Simple Technicolor models are not favored by electroweak precision data [119]. More complex Technicolor models need to be invoked to reconcile the theory with the electroweak data, such as Walking Technicolor theories [120], where the coupling strength evolves slowly with the energy scale, i.e. *walks*.

2.9 Triple Gauge Couplings

This section focuses on a model independent, phenomenological approach to physics beyond the SM, given by the effective Lagrangian [121]. In this approach, the SM is considered as an effective sub theory, providing a low energy approximation of a Grander Theory (GT). The GT would manifest itself at low energies through small deviations from the SM, which can be described by an effective Lagrangian, having a purely phenomenological meaning. The effective Lagrangian parametrizes in a model-independent way, i.e. in the most general way, the effects of the GT at low energies.

The effective Lagrangian for the TGCs in the vertices $WW\gamma$ and WWZ is given by [122]:

$$
\begin{aligned}
i\mathcal{L}_{eff}^{WWV} = \; & g_{WWV} \Big[g_1^V V^\mu \left(W_{\mu\nu}^- W^{+\nu} - W_{\mu\nu}^+ W^{-\nu} \right) + \kappa_V W_\mu^+ W_\nu^- V^{\mu\nu} + \qquad\qquad (2.89) \\
& \frac{\lambda_V}{m_W^2} V^{\mu\nu} W_\nu^{+\rho} W_{\rho\mu}^- + i g_5^V \varepsilon_{\mu\nu\rho\sigma} \left((\partial^\rho W^{-\mu}) W^{+\nu} - W^{-\mu} (\partial^\rho W^{+\nu}) \right) V^\sigma \\
& + i g_4^V W_\mu^- W_\nu^+ (\partial^\mu V^\nu + \partial^\nu V^\mu) - \frac{\tilde{\kappa}_V}{2} W_\mu^- W_\nu^+ \varepsilon^{\mu\nu\rho\sigma} V_{\rho\sigma} - \\
& \frac{\tilde{\lambda}_V}{2m_W^2} W_{\rho\mu}^- W^{+\mu}{}_\nu \varepsilon^{\nu\rho\alpha\beta} V_{\alpha\beta} \Big],
\end{aligned}
$$

where $V \equiv \gamma$ or Z, the overall couplings are defined as $g_{WW\gamma} = e$ and $g_{WWZ} = e \cot \theta_W$ and $\varepsilon^{0123} = 1$. Equation 2.89 gives the most general Lorentz invariant WWV vertex. It introduces fourteen complex parameters, i.e. 28 real couplings. In the SM, at tree level, the non-null couplings are $g_1^Z = g_1^\gamma = \kappa_Z = \kappa_\gamma = 1$, while all other couplings are vanishing. Electromagnetic gauge invariance fixes $g_1^\gamma = 1$ and $g_5^\gamma = 0$, when considering on-shell photons. g_1^V, κ_V and λ_V conserve C and P separately, while g_5^V violates C and P but conserves CP. Finally, g_4^V, $\tilde{\kappa}_V$ and $\tilde{\lambda}_V$ parameterize a possible CP-violation in the bosonic sector [122].

The couplings can be related to physical properties of the gauge bosons. The charge Q_W, the magnetic dipole moment μ_W and the electric quadrupole moment q_W of the W^+ can be related to the C- and P-conserving couplings [123]:

$$
Q_W = e g_1^\gamma, \quad \mu_W = \frac{e}{2m_W} \left(g_1^\gamma + \kappa_\gamma + \lambda_\gamma \right), \quad q_W = -\frac{e}{m_W^2} \left(\kappa_\gamma - \lambda_\gamma \right). \qquad (2.90)
$$

So far, the best limits on the TGCs have been obtained at LEP [124]. The couplings have been experimentally tested using the $e^+ e^- \to W^+ W^-$ process. The angular distributions of the W-pair are more sensitive to the TGCs than the inclusive measurement, based on the total cross section. The differential W-pair cross sections with respect to 5 angles are considered:

- the angle θ_W between the W^- and the e^- beam;

- the polar and azimuthal angles of the fermion in the decay $W^- \to f\bar{f}$ calculated in the rest frame of the W^-;

- the corresponding polar and azimuthal angles of the fermion in the decay of the W^+.

All the possible WW decays, summarized in Tab. 2.2 together with the branching ratios and the corresponding average selection efficiencies, are taken into account for the final combined results of the LEP experiments [124]. In addition, also the single-W [125, 126] $(e^+ e^- \to W^\mp e^\pm \nu(\bar{\nu}))$ and the single-γ [127, 128] $(e^+ e^- \to \gamma \bar{\nu}_e \nu_e)$ productions are exploited, being sensitive to the $WW\gamma$ vertex.

Some assumptions are made to reduce the number of free parameters in Eq. 2.89. Assuming C and P conservation the 14 complex couplings are reduced to 6 real couplings:

Decay Mode	BR	averaged ε
qqqq	45 %	85 %
$\mu\nu$ qq	15 %	80 %
e ν qq	15 %	80 %
$\tau\nu$ qq	15 %	60 %
$\ell\nu\ell\nu$	10 %	65 %

Table 2.2: *WW decay modes with the order of magnitude of the relative branching ratios BR and the approximate average selection efficiencies ε at the LEP experiments. From [62].*

g_1^γ, g_1^Z, k_γ, k_Z, λ_γ and λ_Z. g_1^γ is fixed by requiring electromagnetic gauge invariance. The requirement of local $SU(2)_L \times U(1)_Y$ gauge invariance introduces the further constraints [129]:

$$
\begin{aligned}
\Delta k_Z &= -\Delta k_\gamma \tan^2\theta_W + \Delta g_1^Z \\
\lambda_\gamma &= \lambda_Z,
\end{aligned}
\tag{2.91}
$$

with Δ indicating the deviation from the SM tree-level value and θ_W the electroweak mixing angle. One is then left with three independent real couplings: g_1^Z, k_γ and λ_γ.

Fits to these three TGCs are performed with methods where only one parameter is allowed to vary and the other two are fixed to their SM prediction. The constraints obtained combining the results from the LEP experiments are shown in Fig. 2.4. No significant deviations from the SM are found, within a few percent precision.

The ALEPH experiment at LEP also performed a fit to all 14 complex couplings, relaxing all the constraints on C and P conservation and on electromagnetic and $SU(2)_L \times U(1)_Y$ gauge invariance [130]. Out of all the 28 real parameters one at the time was allowed to vary, while the others were fixed to the SM predictions. The results of this test for the already considered couplings do not show significant deviations from the SM:

$$
\begin{aligned}
Re(g_1^Z) &= 1.066 \pm 0.076 \\
Re(k_\gamma) &= 1.071 \pm 0.061 \\
Re(\lambda_\gamma) &= 0.096 \pm 0.066.
\end{aligned}
\tag{2.92}
$$

The same is true for all the remaining couplings.

The Tevatron experiments have confirmed the results obtained at LEP, without improving the precision [131, 132]. While the LHC will excel in the measurement of the neutral ZZZ and $ZZ\gamma$ couplings, which are not discussed in this thesis, the foreseen experimental uncertainties on the TGCs is at the 10^{-2} level and is not expected to improve significantly the current limits [133]. A breakthrough can be made at the future ILC (Chap. 3), where it is possible to gain one order of magnitude in the uncertainty on the TGCs, reaching a sensitivity of the order of 10^{-3}. This topic is covered in Chap. 5.
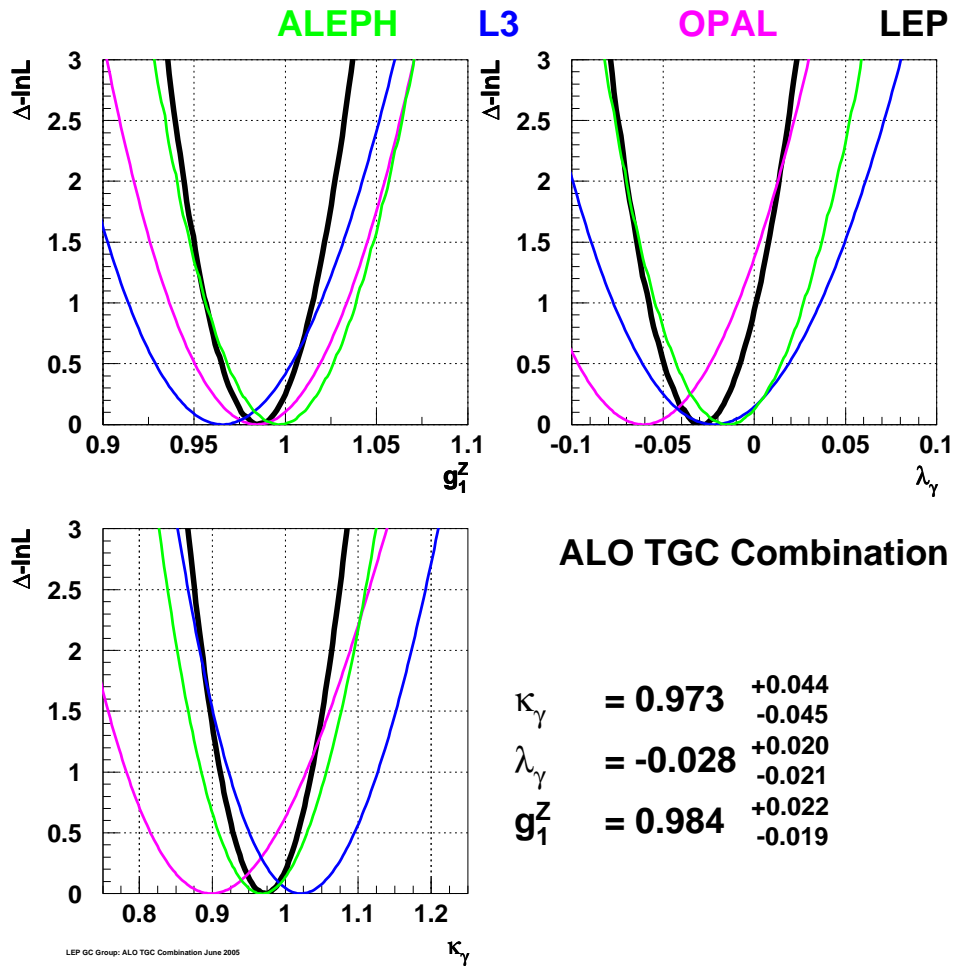
Figure 2.4: *Fit results on the TGCs at LEP. The likelihood fits for g_1^Z, k_γ and λ_γ from single-parameter fits are shown for the different experiments separately (thin colored curves) and for the combined results (thick black curve). The uncertainties indicate the 68% C.L. limits from the combined results. From [124].*

3 The International Linear Collider: Accelerator and Detectors

The most powerful particle accelerator nowadays collecting data is the LHC at CERN. It is designed to collide proton beams with a center of mass energy up to 14 TeV and is expected to reveal whatever lies beyond the energy frontiers of former experiments. However, since protons are composite particles, the type and the energy of the interaction between the colliding particles is unknown. The precision capabilities of any hadron collider are, for this reason, intrinsically limited and, in addition, the reconstruction of many physics processes suffers from large QCD backgrounds.

The ideal complement to the LHC on the precision side will be given by a high energy lepton collider. Leptons are elementary particles and can be collided with a well defined initial state. The environment at lepton colliders is clean and the momentum conservation eases the analysis of the decay products and the reconstruction of invisible particles through the missing momentum. The heavier leptons, the muon and the tau, are unstable particles and currently there is no realistic proposal on how to collide them in high energy accelerators. An electron-positron collider is the only promising choice in the not too far future.

For light particles like electrons, the synchrotron radiation limits the energy reach of ring accelerators. The power of the synchrotron radiation P_{sync} scales with the radius R of the accelerator, the particle mass m and the particle energy E like [134]:

$$P_{sync} \propto \frac{E^4}{R \cdot m^4}.$$ (3.1)

The Large Electron-Positron Collider (LEP) was most probably the highest energy ring accelerator for electron-positron collisions ever built, due to this limitation, reaching center of mass energies of about 200 GeV [135]. Higher energies can be obtained with a linear collider.

The most advanced project for a linear electron-positron collider is the ILC, which will be able to reach center of mass energies up to 500 GeV in its first phase. The possibility of having polarized beams, together with a tunable beam energy, will play an important role in the precision reach of the experiment.

In order to exploit the physics potential of the machine, a detector with excellent performances is indispensable. The International Large Detector (ILD) is a multi-purpose detector concept, based on the paradigm of particle flow (Sec. 3.4.1), designed to achieve the desired precision goals.

Both projects, the ILC and the ILD, are still in the design phase. A short overview of their current status is given in this chapter.

3.1 The Accelerator

The machine design parameters for the ILC have been set in 2007 in the Reference Design Report (RDR) [136], to which refers the description given in this section. However, since the project is still under development, changes are expected before the Technical Design Report (TDR), which is anticipated for 2012. In particular, modifications to the RDR design driven by cost saving issues have been considered. To exemplify the main items currently under discussion a proposal that has been discussed in detail in the ILC community, the SB2009 [137], is shortly reviewed.

The ILC has a tunable center of mass energy ranging from 200 GeV to 500 GeV, with an option of a 1 TeV upgrade. A possibility to run at the Z-pole is also considered (the so-called Giga-Z option), which would allow very precise measurements of SM physics. The accelerator is based on superconducting radio frequency (RF) niobium cavities, operated at 1.3 GHz to reach an average accelerating gradient of 31.5 MeV/m. The luminosity is $2 \cdot 10^{34}\,\mathrm{cm}^{-2}\mathrm{s}^{-1}$, which will give an integrated luminosity of 500 fb^{-1} within approximately the first four years of operation.

While an electron polarization of at least 80% is part of the ILC baseline design, the positron polarization is considered only as an option. However, the positron beam produced by the baseline source has a polarization of 30% and beamline space has been reserved for an eventual upgrade up to 60%. In Chap. 4 it is shown that the physics programme would highly benefit from having both beams polarized.

3.1.1 Machine Layout

The ILC layout in the RDR design is sketched in Fig. 3.1. The main components of the machine are:

- a source for polarized electrons;

- an undulator-based positron source, driven by the partially accelerated main electron beam;

- 5 GeV electron and positron damping rings with a circumference of 6.7 km, housed in a common tunnel at the center of the ILC;

- beam transport from the damping rings to the main LINear ACcelerator (linac), followed by a two-stage bunch compressor system;

- two 11 km long main linacs, accelerating the beams with a pulse length of 1.6 ms and a repetition rate of 5 Hz;

- a 4.5 km (2.25 km for each beam) long beam delivery system, which brings the beams into collision with a 14 mrad crossing angle.

The current preference is to have only one interaction region, where two detectors alternate in the so-called *push-pull* scheme. While one detector collects interactions, the other detector can be maintained or upgraded in the meantime.

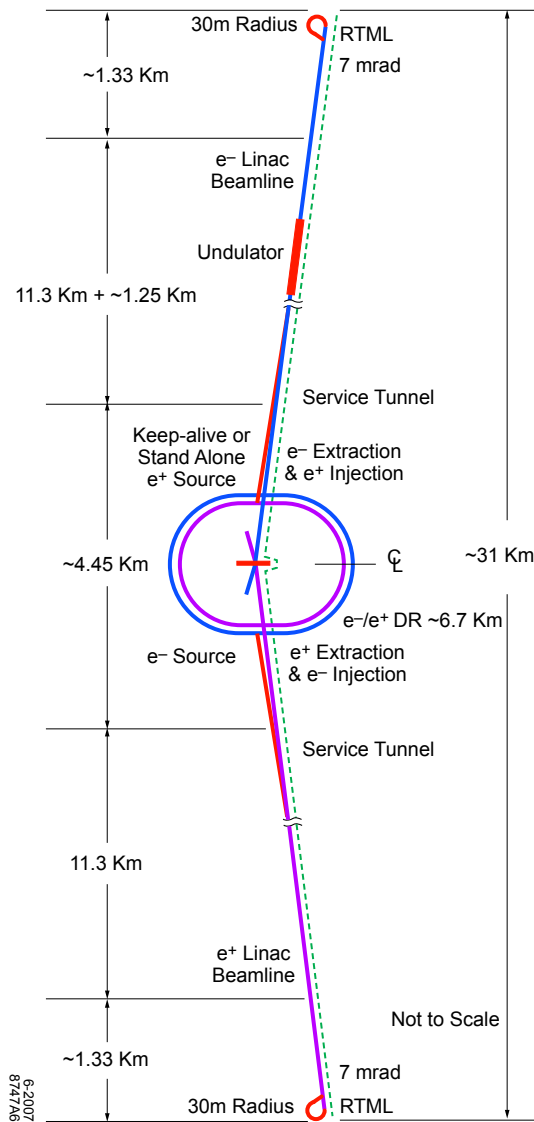The nominal beam parameters are summarized in Tab. 3.1.

Figure 3.1: *Schematic layout of the International Linear Collider as defined in the Reference Design Report. From [136].*

Beam Parameter	Value at the IP
Bunch population	2×10^{10}
Bunches per train	2625
Repetition rate	5 Hz
Bunch interval	369 ns
RMS bunch length	300 μm
Normalized horizontal emittance	10 mm $\cdot$ mrad
Normalized vertical emittance	0.04 mm $\cdot$ mrad
RMS horizontal beam size	640 nm
RMS vertical beam size	5.7 nm

Table 3.1: *Nominal ILC beam parameters at the interaction point [136].*
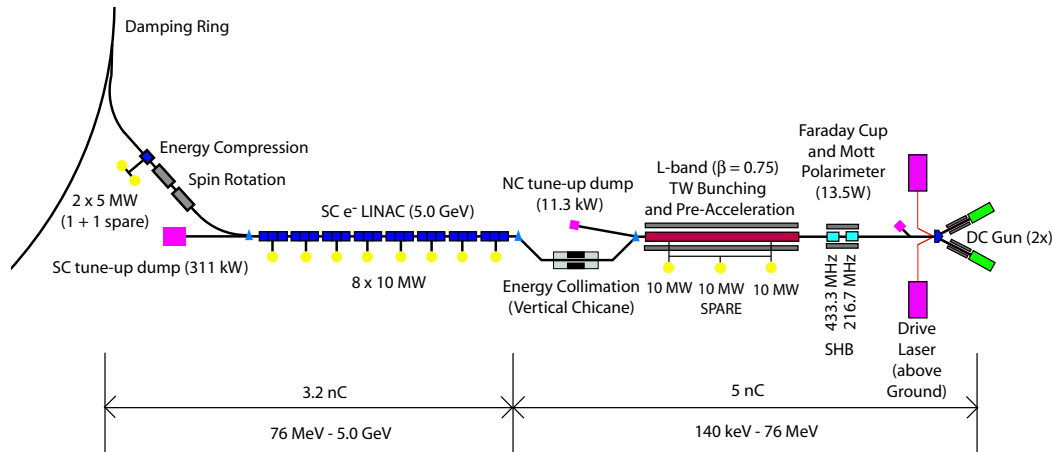
Figure 3.2: *Electron particle source. From [136].*

With respect to a hadron collider the event rates are comparatively low. A low-level trigger system is believed to be non-necessary and it is planned to record the data from every single bunch crossing. The events are selected and discriminated only with software triggers, allowing a high efficiency and preventing to discard any unexpected signature from new physics.

3.1.2 The Polarized Particle Sources

The electron source is shown in Fig. 3.2. It comprises a direct current (DC) gun, with a polarized laser shining on photo-cathodes, yielding electrons with a high polarization of at least 80%. The circular polarization of the laser beam can be reversed train-to-train, thereby allowing fast reversal of the electron spin. The emitted electrons are collected and pre-accelerated in normal conducting structures. Afterwards, the beam is accelerated to 5 GeV in a superconducting linac. The spin vectors of the beam particles need to be parallel to the field of the bending magnets in the damping ring, in order to preserve the polarization. The spin is rotated vertically before the injection into the damping ring, using superconducting solenoids. The rotation back to the longitudinal direction is performed before the injection into the main linac. After the spin rotation a separate superconducting structure compresses the beam energy to match the acceptance of the damping ring.

The partially accelerated (150 GeV) electron beam is passed through a helical undula-tor, to produce photons with a high intensity, a high polarization and a high energy (the energy spectrum peaks at about 10 MeV). The helical undulator is a structure of superconducting dipole magnets, which forces the traveling electrons to emit syn-chrotron radiation, producing circularly polarized photons. The photons are addressed against a thin titanium target, in which there is a good polarization transfer to the positrons and the electrons that are produced in pairs [138]. To avoid damage to the target, it is designed as a rotating wheel. The reason why the high energy of the electron beam is required is to keep the positron yield high. At lower energies the positron bunches would not be filled to full capacity and the overall luminosity would be reduced. Due to the undulator the electron beam obtains an additional energy dispersion, though not compromising the final performance. This scheme for produc-ing polarized positrons was proven by the experiment E166 at the Stanford Linear
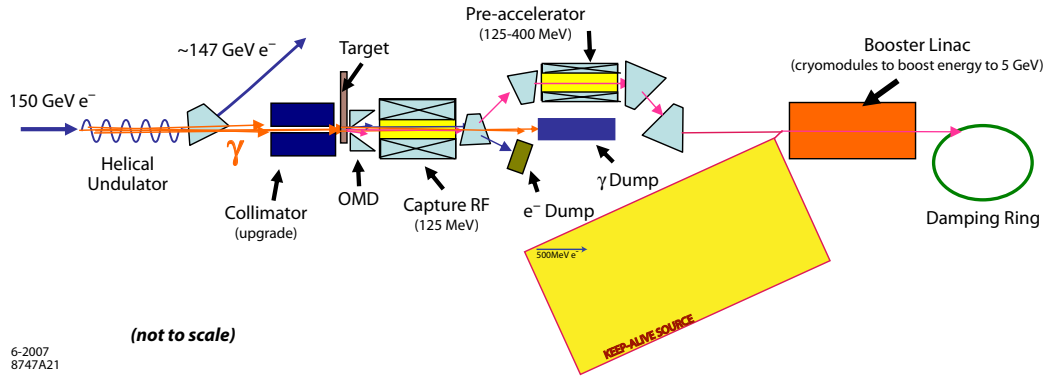
Figure 3.3: *Positron particle source. From [136].*

Accelerator Center (SLAC) [139].

Although the baseline design of the ILC only requires unpolarized positrons, the positron beam produced using a helical undulator has a polarization of at least 30%. The inital distribution of the positrons after the production is correlated in energy and polarization. The low energy positrons are less polarized, while high-energy positrons are strongly polarized. An inevitable compromise has to be made between the number of accepted positrons and the beam polarization. Removing the low-energy positrons via bunch energy compression would result in a higher degree of polarization [140, 141]. An increase of the polarization can be achieved also by a collimation of the photon beam, which cuts lower energetic photons with lower polarization, and the intensity loss could be compensated, e.g. with a longer undulator [142]. Beamline space has been reserved for instrumentations necessary for an upgrade up to a polarization of 60%.

The produced positrons are captured and accelerated to the damping ring, as shown in Fig. 3.3. Positrons are captured using an optical matching device (OMD) and a normal conducting RF band structure with solenoidal focusing and accelerated to 125 MeV. The baseline OMD is a normal conducting pulsed flux concentrator, generating a solenoidal magnetic field which peaks in strength at 5 T, close to the target, and falls off to 0.5 T to match the solenoidal field at the entrance of the RF capture section. The electrons and remaining photons are separated from the positrons and dumped. The positrons are accelerated to 400 MeV in a normal conducting linac with solenoidal focusing, accelerated to 5 GeV using a superconducting linac with quadrupole focusing and finally injected into the damping ring, after spin rotation and energy compression.

The polarization of the positrons needs to be preserved and transported to the IP. In the current baseline the positron helicity can only be reversed by changing the polarity of the superconducting spin rotator magnets, which is a slow process. The polarized positrons would collide with polarized electrons, whose helicity is flipped quickly. This scheme has several drawbacks, which are summarized in [142]. Half of the running time would be necessarily spent on the inefficient positron electron helicity combinations with equal sign, '+ +' and '− −', which are less interesting for the physics. Moreover, for several relevant measurements, like the left-right asymmetry measurement (see Chap. 4) or data-driven polarization measurements (see Chap. 5), samples with different helicity sets are required, having the same luminosity each. The same measurements require, as well, that the absolute value of the average polarization is equal for the + and − helicty states, for both beams. Without fast helicity reversal, the

different samples would be obtained from different runs, taken at different moments, and corrections accounting for long term variations of the luminosity, the polarization or detector efficiencies would be necessary, introducing additional systematic uncertainties.

Hence, proposals have been made to modify the baseline configuration to provide random selection of the positron helicity train-by-train [143]. Parallel spin rotator beamlines and kicker magnets should be introduced before the damping ring. Two rotation lines using solenoids with opposite fields would be needed, for the two orientations of the spin, and the fast kicker magnets would distribute the positron trains to the different lines. Positron spin rotation and flipping could be done at 5 GeV [144] using superconducting solenoids or at 400 MeV, directly after the positron pre-accelerator, using normal magnets [145]. This last choice would eliminate expensive superconducting magnets, simplify the engineering and reduce costs. The spin rotator system for the electron beam could be moved to lower energies, as well.

The positron source system also includes an auxiliary source to generate a low intensity positron beam (Keep Alive source). This is used for commissioning and also allows various beam feedbacks to operate if the main electron beam is not active. This source uses a 500 MeV electron beam colliding on a tungsten-rhenium target to produce positrons. The positrons are then captured and accelerated to 400 MeV. The Keep Alive and the main source both use the same linac to accelerate from 400 MeV to 5 GeV. In the RDR the Keep Alive source is designed to account for the 10% bunch intensity in each train, though this specification is under review.

3.1.3 The Damping System

The emittance expresses to which extent the particles of the beam occupy the space and the momentum phase space. A particle beam with low emittance is a beam where the particles are confined to a small volume and have nearly the same momentum vector. Keeping the emittance low results in a higher luminosity, as the sizes of the colliding particle bunches depend on it, and affects the luminosity (cf. Eq. 3.4).

The purpose of the damping rings is to reduce the emittance of the beams before they enter the main accelerator. The particles pass through bending magnets and additional wigglers, which make them cool off by emitting synchrotron radiation. The lost energy is restored by accelerating cavities. Since the radiation can have a transverse component, while the energy is recovered only in the longitudinal direction, the process results in the desired reduction of the emittance.

The damping rings have also the task to assemble the bunch train. In the RDR design one train contains 2625 bunches. Since the process of damping requires 25 ms, the rings have to accommodate the whole train. The kickers need several nanoseconds to insert and extract the bunches, limiting the packing density. Therefore, the damping rings need a considerable circumference of 6.7 km to accommodate a whole train. In order to save costs, the two damping rings are designed to occupy the same tunnel at the center of the ILC site.

3.1.4 The Main Linac

After the extraction from the damping rings both beams are transferred to the Ring To Main Linac (RTML) section, which transports the particles to the main linacs. The beams reach the linac with an energy of 15 GeV and need to be accelerated up to 250 GeV.

The acceleration is achieved with superconducting niobium cavities, each containing 9 accelerating cells. They are operated at a temperature of 2 K and a frequency of 1.3 GHz. The average accelerating gradient is 31.5 MeV/m. In the RDR design the accelerator tunnel is accompanied by a service tunnel, housing the RF sources and the power supplies. The total length of the linacs, about 11 km, is defined by the accelerating gradient, which is close to the foreseeable limit for the employed technology. Ongoing prototype studies have shown that the accelerating gradient may eventually be increased up to 40-50 MeV/m [146]. Since niobium loses its superconductivity at a certain critical electric and magnetic field strength [147], it will not possible to reach much higher values.

When the machine is working at center of mass energies below 300 GeV, the electron beam is accelerated to 150 GeV before reaching the positron source and afterward decelerated in the remaining part of the linac, hence optimizing the positron production yield.

3.1.5 The Beam Delivery System and the Final Focus

The last 2 km of the accelerator accommodate the Beam Delivery System (BDS). This part of the machine has several purposes. It cleans the beam from halo particles using collimators and spoilers that scrape off the beam halo and halo muons. It also contains the instrumentation for the beam diagnostics, such as polarimeters (see Chap. 4).

The very last 20 m before reaching the detectors constitute the final focus system, that focuses the beam to few 100 nm horizontally and few nm vertically. The beams cross with an angle of 14 mrad. The crossing angle easies the extraction of the beams after the collision and is small enough, such that beam-induced backgrounds mainly escape along the beam tube, without reaching the detectors. In order to increase the overlaps between the two beams during the collision, the bunches are rotated on the horizontal plane shortly before the interaction, using crab cavities.

The Beamstrahlung

The repetition rate of bunch trains at the ILC is relatively low (5 Hz), due to limitations in the available RF power. To keep the number of interactions high, this effect is compensated by a strong focusing of the beams. The resulting small bunch sizes imply that the bunches have a very high space charge and are thus accompanied by a strong electric field. Since the colliding fields have opposite charge, this results in a strong attraction of one bunch to the other, so that the beam particles are accelerated towards the center of the oncoming bunch.

On the one hand this has a positive effect, since the bunches result even more compressed, increasing the effective amount of interactions. On the other hand, the beam particles deflected by the electromagnetic field of the opposite beam emit a large

amount of synchrotron radiation, which is known as beamstrahlung [148, 149]. The average energy loss δ_{BS} of a particle in the colliding bunches is given by:

$$\delta_{BS} \propto \frac{E}{\sigma_z} \times \frac{n^2}{(\sigma_x + \sigma_y)^2}, \tag{3.2}$$

where $\sigma_{x,y,z}$ are the sizes of the beam in the x,y or z direction. The z axis lays along the direction of the beams, while x and y are the coordinates in the transverse direction. E is the beam energy and n is the number of particles in each bunch. The primary energy distribution gets wider, as a consequence of the beamstrahlung, with tails towards lower energies.

The beamstrahlung itself is not a relevant source of detector background, because it is strongly focused in the forward direction, such that it exits the detector through the beam tube. However, the synchrotron photons can interact with photons coming from the other beam (synchrotron photons or virtual ones, emitted by the beam particles), yielding $e^{\pm}$ pairs. One of the particles in the pair has necessarily a charge opposite to the charge of its parent beam and gets defocused by the opposite beam. Such particles can reach the detector causing the so-called pair background [150, 151]. During the bunch crossing depolarization effects occur as well (see Sec. 4.3).

The Luminosity

The luminosity ($\mathcal{L}$) is defined as the density of particles that pass each other per time unit t:

$$\mathcal{L} = \frac{N^2}{t \times A}, \tag{3.3}$$

where A is the transverse area of the beam at the interaction point and N the number of particles. The number of interactions per time unit is, therefore, given by the luminosity multiplied by the cross section of the considered process.

The luminosity is given by [151]:

$$\mathcal{L} = \frac{n_b N^2 f_{rep}}{4\pi \sigma_x \sigma_y} H_D, \tag{3.4}$$

where n_b is the number of colliding bunches, N is the number of particles per bunch, f_{rep} is the repetition rate, x and y are the transverse bunch sizes (in the case of Gaussian beam profiles), and H_D is an enhancement factor that takes the mutual beam-beam interaction into account.

As already mentioned, reducing the beam sizes increases the number of interactions (luminosity) but also increases the beamstrahlung. The luminosity varies with the product $\sigma_x \sigma_y$, while the beamstrahlung varies with the sum $\sigma_x + \sigma_y$. The way to achieve small $\sigma_x \sigma_y$ and large $\sigma_x + \sigma_y$ at the same time, increasing the luminosity while keeping the beamstrahlung under control, is to make σ_x and σ_y as different as possible, i.e. to have a flat beam.

Since the beamstrahlung widens the energy spectrum of the beams, with tails at lower energies, when quoting the luminosity it is important also to quote the percentage of

interactions taking place at energies close to the nominal energy. For the nominal ILC beam parameters at 500 GeV, the luminosity spent within 1% of the nominal center of mass is 83% [152].

3.2 The SB2009 Proposal

Studies are ongoing in the ILC community aiming at a major cost reduction of the machine, with a redefinition of the baseline, that should not affect the physics potential of the experiment. As an example of the discussed changes to the RDR design the SB2009 proposal is here illustrated [137].

The main change (and major cost reduction) is to house the main linac and its support system in a single tunnel, implying a redesign of the RF system. Another major cost reduction comes from the beam power, which is reduced by a factor 2, meaning half as many bunches in a train and automatically the need of smaller damping rings and a reduced need of cooling. The total luminosity is kept the same as in the RDR by using a stronger final focusing. This, however, increases the beamstrahlung and reduces the luminosity spent within 1% of the nominal center of mass from 83% to 72% at 500 GeV. The key factor in order to recover the same luminosity as in the RDR is the travelling focus scheme [153], where the focus at the IP is adjusted along the bunch. If such a scheme should not turn out to be feasible, the total luminosity would be 25% less.

The number of beamstrahlung pairs per bunch crossing is increased by a factor 2. Preliminary studies show that this might be a problem for the BeamCal (Sec. 3.4.2), which has a readout fast enough to read single bunch crossings. In this way the increased amount of pairs is not compensated by the reduced number of bunches [152].

The source of the positron is moved to the end of the electron linac, instead of occupying the intermediate position where the electron beam reaches an energy of 150 GeV. Although this choice would not imply significant financial savings, however, from the operational point of view, the new location is preferable. The main linac tunnel is kept free from a potentially delicate subsystem and rather concentrate it with other subsystems (the electron source, the damping rings, the BDS, etc.) to the central part of the ILC site, where the access and the maintenance would be eased. The move of the positron source causes a reduction of the luminosity for center of mass energies below 300 GeV, i.e. when the electron beam is below 150 GeV. For such energies the positron bunches are not fully filled. Solutions are being investigated, in particular using the fact that at lower beam energies there is enough spare RF power to increase the repetition rate to 10 Hz. One would then accelerate every other electron train to 150 GeV to produce positrons and every other, at the lower energy desired, would be sent to the detector. How the damping rings could accommodate the higher repetition rate is also under study.

Another consequence of the move of the positron source is that the electron beam energy spread increases. While the electron polarization is not changed in the SB2009, the positron polarization achievable at $\sqrt{s} = 500$ GeV is only about 22%. This is due to the fact that increasing the drive beam energy beyond 150 GeV gives a higher positron yield, but reduces the achievable polarization at the same time [154]. As already mentioned, with the RDR configuration a higher positron polarization can be achieved. In Chap. 4 and 5 the motivations for a high positron polarization are given.

In [152] the physics performances of the SB2009 proposal and the RDR design have been compared on a few targeted examples: the analysis of the $\tilde{\tau}$ in the SUSY benchmark point SPS1a' [155], which is sensitive to background and polarization, and the measurement of the mass of a light SM Higgs with the recoil mass method [156], which is sensitive to the luminosity at lower E_{CMS}.

For the $\tilde{\tau}$ analysis a degradation of the performance by 15-20% is found when changing from the RDR to the SB2009 parameters. This is true for both the cross section measurements and for the end-point analysis, to measure the $\tilde{\tau}$ mass from the spectrum of the decay products. The degradation would increase up to 20-40%, if the travelling focus concept should turn out to be unfeasible.

For the SM Higgs recoil mass study, which considers a light Higgs of 120 GeV, the performance depends on the energy. For a center of mass energy of 350 GeV the SB2009 parameters degrade the quality of the mass measurement by 110% and the cross section measurement by 10%, with respect to the RDR. At 250 GeV the worsening would be respectively of 70% and 65%. Without travelling focus the corresponding numbers would be 160% and 30% at 350 GeV or 80% and 85% at 250 GeV.

These studies show a major degradation of the performances when changing from the RDR to the SB2009 parameters, the biggest impact coming from the move of the positron source. A series of workshops to solve this and other issues have been organized for 2011, in view of changing the baseline design in time for the TDR in 2012.

3.3 The Physics Program and the Implications on the Detector Design

In [136] the physics program of the ILC has been described in detail. It ranges from precise measurements of the SM physics and the investigation of the Higgs sector up to the study of the properties of new physics beyond the SM. In this section a short overview of some of the physics goals is given, focusing on the main requirements on the detector design that they imply. Further examples of physics studies at ILC are given in the Chap. 4, concentrating on the role of the beam polarization.

3.3.1 Vertex Finding Performance

Important analysis will be demanding in terms of flavor tagging, such as top quark and Higgs studies.

The top quark is not simply another quark. Being the heaviest particle known in the SM, it has a large coupling to the Higgs and is expected to play a special role in the electroweak symmetry breaking. The current experimental uncertainty on the top mass induces the largest parametric uncertainty in the prediction of electroweak precision observables [157, 158]. Therefore, a precise measurement of the top quark mass is important for consistency tests of the SM and to increase the sensitivity to new physics from indirect constraints. As of today, it is known with a large uncertainty of $\Delta m_t = 1.1$ GeV [159]. Though at the LHC the statistical uncertainty on the top mass measurement will be very small, the systematics are expected to limit the performance
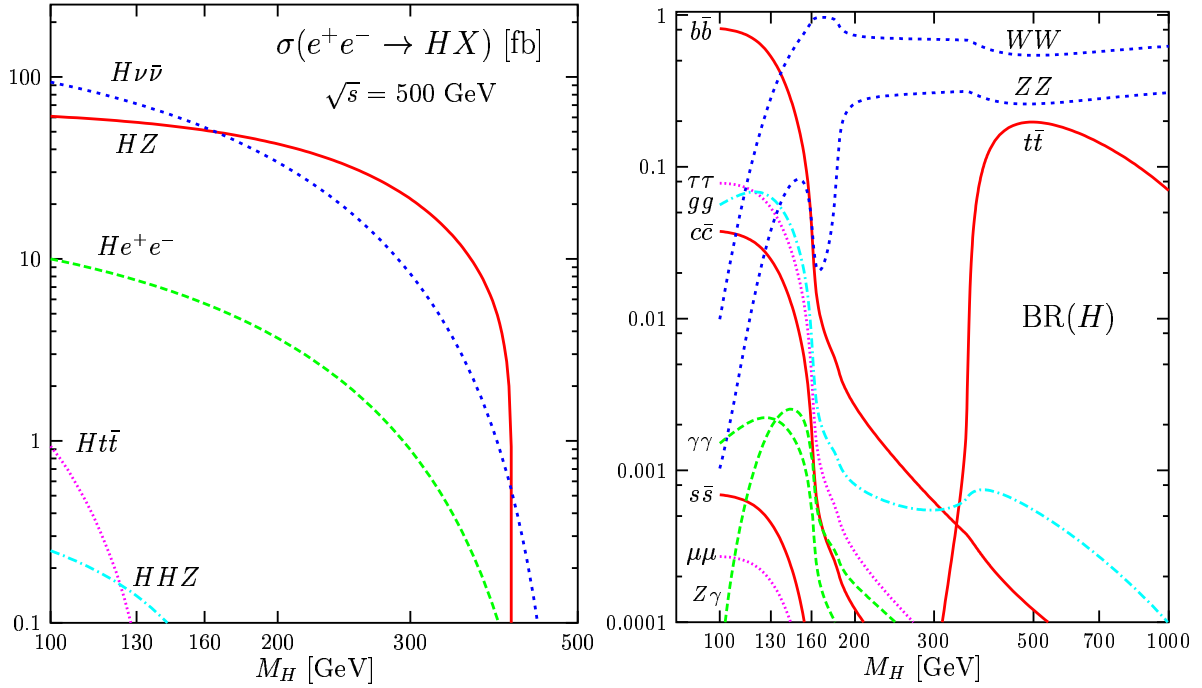
Figure 3.4: Production cross sections of the SM Higgs boson at the ILC (left) and its branching ratios (right) as a function of M_H for $\sqrt{s} = 500\,\mathrm{GeV}$. From [164].

with a final precision of the order of $1\,\mathrm{GeV}$ [160, 161]. At the ILC the precision could be one order of magnitude better, below $100\,\mathrm{MeV}$, including both experimental and theoretical uncertainties on the definition of the top mass [157]. The top quarks will be pair-produced in the process $e^+e^- \to t\bar{t}$ with two main subsequent decays: the fully hadronic, $t\bar{t} \to (bq\bar{q})(\bar{b}q\bar{q})$, and the semi-leptonic, $t\bar{t} \to (bq\bar{q})(\bar{b}l\nu)$. A good flavor tagging information, allowing the identification of the b-jets in the final state, plays an important role in the reconstruction of the decay products.

If the Higgs boson exists, it will be most likely discovered by the LHC experiments (see e.g. [133, 162]). The ILC will have the major goal of performing precise measurements of its properties. The determination of the Higgs boson branching fractions is central in the context of the SM, since it represents a test of the hypothesis that the strength of the Higgs coupling depends linearly on the particle masses. The Higgs production cross sections at the ILC are shown in the left plot of Fig. 3.4 for $\sqrt{s} = 500\,\mathrm{GeV}$. The dominant channels are the Higgsstrahlung, $e^+e^- \to HZ$, and the WW-fusion, $e^+e^- \to H\nu\bar{\nu}$. The plot on the right in the same figure shows that a light Higgs, with a mass approximately below $140\,\mathrm{GeV}$, decays predominantly to $b\bar{b}$, $\tau\bar{\tau}$, gg and $c\bar{c}$ pairs. In [163] the performance in the measurement of the branching ratios of a light Higgs $H \to b\bar{b}$, $H \to c\bar{c}$ and $H \to gg$ at the ILC has been studied, using the Higgs-strahlung process. All the three possible decay topologies of the Z boson can be exploited: $Z \to q\bar{q}$, $Z \to \nu\bar{\nu}$, $Z \to l^+l^-$. The flavor tagging has clearly a key role in this analysis, to distinct the different hadronic decays of the Higgs.

The heavy flavor tagging capability of a detector demands an accurate determination of the impact parameter $IP_{r\Phi,z}$. The goal for its resolution at the ILC has been set to:

$$\delta(IP_{r\Phi,z}) \leq 5\mu \oplus \frac{10\mu\mathrm{mGeV}/c}{p\sin^{3/2}\theta}, \tag{3.5}$$
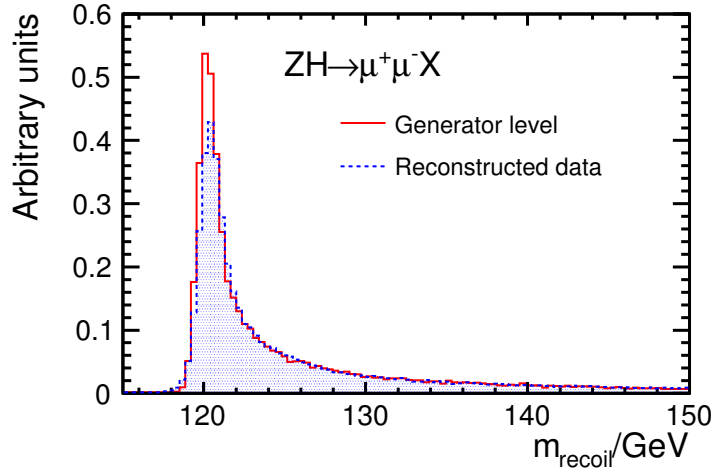
Figure 3.5: The Higgs recoil mass distribution in the $\mu^+\mu^-X$ channel, at the generator level and from the reconstructed muon pair momenta. From [163].

where p is the momentum of the particle and θ is the polar angle of the track. This precision is 2-3 times better than that of the SLD (SLC Large Detector, at the SLAC Linear Collider) pixel detector [165], the best obtained so far. To achieve it the vertex detector has to be placed as close as possible to the beam pipe, compromising with the increasing beam background.

3.3.2 The Tracking

A relevant study at the ILC, which exemplifies the need of an excellent tracking, is the measurement of the Higgs mass from the already mentioned Higgsstrahlung production, $e^+e^- \rightarrow HZ$. Since the center of mass at the ILC is well known, the mass of the Higgs boson can be measured with precision from the recoil mass of the Z, the highest precision being achieved in the decay channel of the Z boson $Z \rightarrow \mu^+\mu^-$ [163]. This measurement is completely model-independent and does not need any assumption on the decay mode of the Higgs. The width of the peak of the recoil mass distribution is a convolution of the finite resolution of the detector and the luminosity spectrum of the center of mass energy from the intrinsic beam energy spread and beamstrahlung. Therefore, the final precision depends on the precision with which the beam energy can be measured (a 10^{-4} precision is aimed for at the ILC [166]), the beam energy spread, which is at the permill level, and the precision with which the momenta of the decay products of the Z can be measured. When using the $Z \rightarrow \mu^+\mu^-$ decay channel, the momentum resolution has a non-negligible contribution. This is shown in Fig. 3.5, which compares the Higgs recoil mass obtained at the generator level and from the reconstructed muon pair momenta in the ILD detector model (cf. Sec. 3.4.2). Though the ILD detector simulation assumes an excellent tracking (cf. Sec. 3.4.2), the detector response leads to a broadening of the recoil mass peak from 560 MeV to 650 MeV. Hence, though the main contribution comes from the beam energy spectrum, the contribution of the momentum resolution is non-negligible, being of the order of 300 MeV.

Another example is given by the measurement of the center of mass energy from the radiative returns to the Z, with subsequent decay to muons, $e^+e^- \rightarrow \mu^+\mu^-\gamma$. This

channel provides on the long time scale a valuable cross check of the measurements of the beam energy performed by the spectrometers [166, 167]. The energy spectrometers are placed upstream and downstream of the interaction point. It is important to be able to compare their measurements with a direct detector measurement of the center of mass energy based on physics events.

Further examples of studies, where the performance highly depends on the tracker's momentum resolution, can be taken also from physics beyond the SM. For instance, the mass measurement of the sleptons in some SUSY scenarios. Part of the SUSY spectrum might be kinematically accessible at the ILC energies, for example gauginos and sleptons with masses below $250\,\mathrm{GeV}$ would be produced at $\sqrt{s} = 500\,\mathrm{GeV}$. In this scenario sleptons are pair produced and lead to a final state with two leptons and missing momentum. The slepton masses are determined by looking at the endpoints of the momentum spectrum of the decay leptons (see e.g. [163]).

The design goal for the momentum resolution has been set to:

$$\delta(\frac{1}{p_t}) \sim 5 \cdot 10^{-5} (\mathrm{GeV}/c)^{-1}, \tag{3.6}$$

which is about 10 times better than what was reached at LEP [168].

3.3.3 The Energy Resolution

Many interesting processes at the ILC appear in multi-jet final states. The reconstruction of the invariant mass of two or more jets is essential to distinguish between W, Z and Higgs bosons and provides an essential tool for discovering new states or decay modes. Ideally, the di-jet mass resolution should be comparable to the natural decay width of the parent particle, from which it was originated, which is usually around a few GeV.

An example, where the separation between W and Z is necessary, is the WW-scattering process, studied at $\sqrt{s} = 1\,\mathrm{TeV}$ in [163]. This process is a test of the electroweak symmetry breaking. If the symmetry breaking is obtained via a light Higgs, the WW-scattering is suppressed. Observing it, in the absence of any discovery of a light Higgs, would hint at an electroweak symmetry breaking accomplished by strongly coupled quanta above $1\,\mathrm{TeV}$ [169, 170]. At the ILC the WW-scattering can be probed via the process $e^+e^- \to \nu_e\bar{\nu}_e q\bar{q}q\bar{q}$, which has contributions also from the $W^+W^- \to ZZ$ vertex. The reconstruction of the di-jet masses, with an excellent jet energy resolution, allows the separation of the two processes, as shown in Fig. 3.6 for simulated events in the ILD detector model (cf. Sec. 3.4.2).

The separation between the two gauge bosons might be useful also to some SUSY studies. For instance, in [171] a SUSY scenario is considered where the chargino $\tilde{\chi}_1^{\pm}$ and the neutralino $\tilde{\chi}_2^0$ are nearly mass degenerate and decay predominantly into $W^{\pm}\tilde{\chi}_1^0$ and $Z\tilde{\chi}_1^0$, respectively. The production at the ILC would occur in the processes $e^+e^- \to \tilde{\chi}_1^+\tilde{\chi}_1^- \to W^+\tilde{\chi}_1^0 W^-\tilde{\chi}_1^0$ and $e^+e^- \to \tilde{\chi}_2^0\tilde{\chi}_2^0 \to Z\tilde{\chi}_1^0 Z\tilde{\chi}_1^0$. The fully-hadronic final states, where the gauge bosons decay into $q\bar{q}$ pairs, can only be separated relying on the jet-energy resolution.
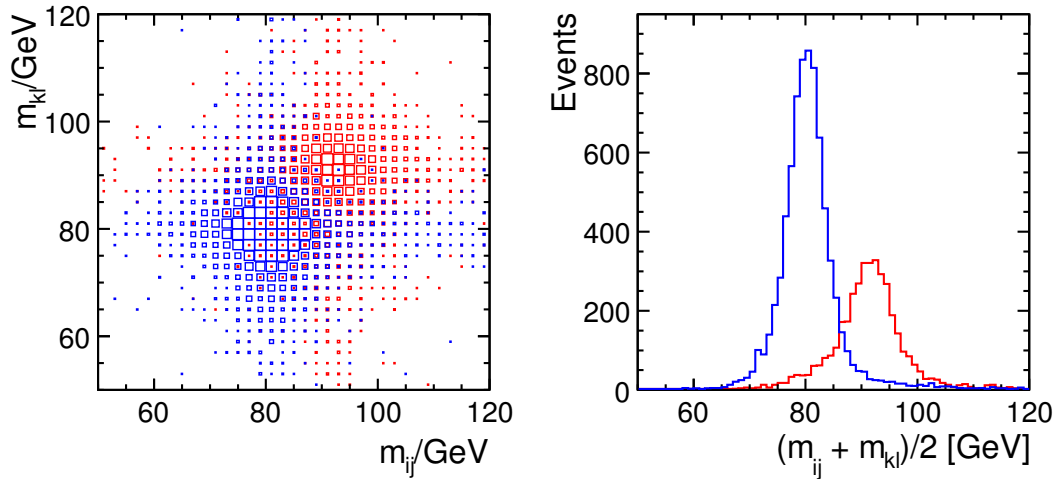
Figure 3.6: The reconstructed di-jet mass distributions for the best jet-pairing in se-
lected $\nu_e \bar{\nu}_e WW$ (blue) and $\nu_e \bar{\nu}_e ZZ$ (red) events at $\sqrt{s} = 1\,\mathrm{TeV}$ (left). Dis-
tributions of the average reconstructed di-jet mass for the best jet-pairing
for $\nu_e \bar{\nu}_e WW$ (blue) and $\nu_e \bar{\nu}_e ZZ$ (red) events (right). From [163].

The goal for the jet-energy resolution has been set to:

$$\left(\frac{\Delta E}{E} \right)_{jet} \leq 3 - 4\%, \tag{3.7}$$

which, for jet energies approximately below 100 GeV, translates into:

$$\left(\frac{\Delta E}{E} \right)_{jet} = \frac{30\%}{\sqrt{E[\mathrm{GeV}]}}. \tag{3.8}$$

To conclude this section, it should be added that the performance of a detector is
not expressed only by the momentum and energy resolution. Other relevant requisites
are hermeticity, to reveal particles boosted in the forward direction and to allow the
reconstruction of invisible decay products from the momentum conservation, a good
pattern recognition, to suppress backgrounds, and particle identification capabilities.

3.4 A Detector for the ILC

At the time this thesis is written two detector concepts for the ILC are being developed:
the Silicon Detector (SiD) [172], based on a silicon tracking technology, and the ILD,
which is described in detail in the following. They are both based on the concept of
particle flow, which combines the information of tracking and calorimeters, in order to
get the best overall reconstruction.

3.4.1 The Particle Flow Concept

The LEP experiments provide detailed information about the particle composition of
jets [173]. On average, after the decay of short-lived particles, roughly 62% of the

jet energy is carried by charged particles (mainly hadrons), around 27% by photons, about 10% by long-lived neutral hadrons (e.g. n, $\bar{n}$ and K_L), and around 1.5% by neutrinos. From these numbers emerges that only 10% of particles are exclusively measured by the hadronic calorimeter, which has by far the worst resolution amongst all sub-detectors. At the ILD the energy resolution of the hadron calorimeter (HCAL) is expected to scale like $\sigma_E/\sqrt{E} \sim 49\%$, the electromagnetic calorimeter (ECAL) will have a resolution of the order of $\sigma E/\sqrt{E} \sim 17\%$ and the tracking system should provide an overall momentum resolution $\delta_p/p \sim 2 \cdot 10^{-5}$ [163]. At energies approximately below 100 GeV, the accuracy obtained using the tracking system in the reconstruction of charged particles is better than anything that could be achieved using the calorimeters. The particle flow approach consists in the reconstruction of the energy of each particle with the best suited sub-detector system.

Using highly granular calorimeters it is possible to separate the energy deposits belonging to charged particles, neutral hadrons and photons. Charged particle tracks are extrapolated to the calorimeters and clusters of calorimetric hits are assigned to the tracks using topological information. The total energy of the clusters that are assigned to a track, therefore belonging to charged particles like charged pions, electrons and muons, is replaced by the momentum sum as given by the tracking system. Clusters coming from photons are identified using a dedicated reconstruction and their energy is measured using the ECAL. The HCAL plays a role only for the remaining neutral hadrons, detected in the combination of ECAL and HCAL. A visual example of the clustering is shown in the left plot of Fig. 3.7. Different colors correspond to different particles identified within a jet. Due to the high granularity, even close-by showers produced by different particles can be distinguished.

In the ideal case the jet energy resolution σ_{jet} obtained with the particle flow approach is given by:

$$\sigma_{jet} = f_{ch} \cdot \sigma_{ch} \oplus f_\gamma \cdot \sigma_\gamma \oplus f_{h^0} \cdot \sigma_{h^0}, \tag{3.9}$$

where f is the energy fraction of the particles, ch indicates the charged particles, h^0 the neutral hadrons and γ the photons. σ_{ch} is the resolution achieved using the tracker, σ_γ is obtained from the ECAL and σ_{h^0} is the HCAL resolution.

In the real world some limitations are unavoidable. Hits deposited in the calorimeter by the passage of neutral particles will be sometimes accidentally associated to a close-by shower induced by a charged particle. Only the energy of the charged particle, given by the tracking system, will be accounted for and the energy of the additional hits from the neutral particle will be lost. Similarly, if part of a charged hadron shower is identified as a separate neutral cluster, the energy is effectively double-counted as it is already accounted for by the track momentum. A second particle that does not really exist would be reconstructed together with the charged particle and the energy overestimated. The two effects are accounted for in a so-called 'confusion' term, that worsens the jet energy resolution:

$$\sigma_{jet} = f_{ch} \cdot \sigma_{ch} \oplus f_\gamma \cdot \sigma_\gamma \oplus f_{h^0} \cdot \sigma_{h^0} \oplus \sigma_{conf}. \tag{3.10}$$

The 'confusion' rather than the calorimetric resolution is the limiting factor in the particle flow performance. The truly crucial aspect is the ability to correctly assign calorimetric energy deposits to the correct reconstructed particle. This places stringent
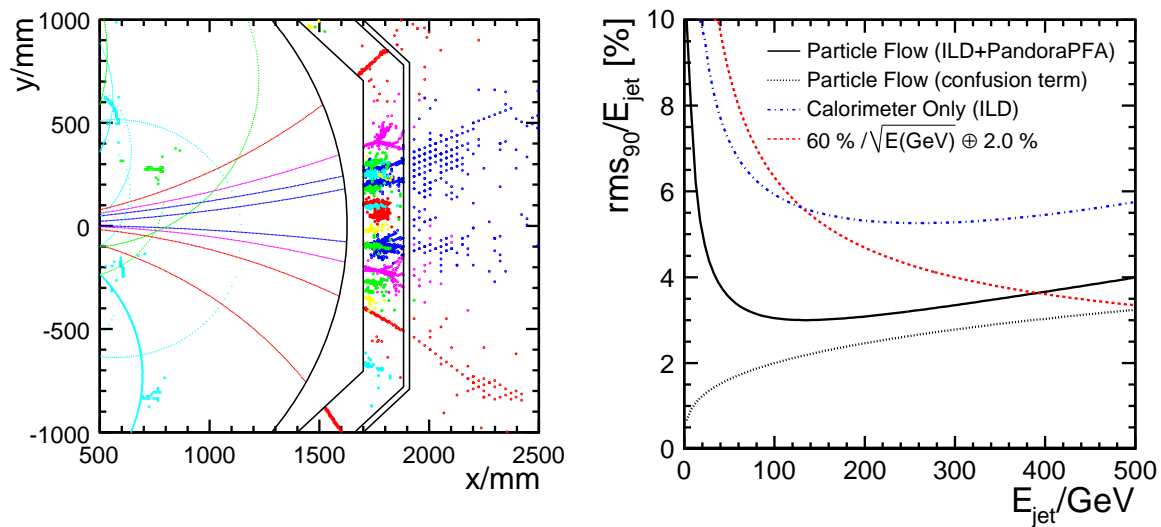
Figure 3.7: *The left plot shows an event display of a 100 GeV jet reconstructed with a particle flow algorithm. The different clusters, assigned to different particles, are distinguished with the color code (gray scale). The plot on the right shows the empirical functional form of the jet energy resolution obtained from particle flow calorimetry (PandoraPFA [174] and the ILD concept). The estimated contribution from the confusion term only is shown (dotted). The dot-dashed curve shows a parametrization of the jet energy resolution obtained from the total calorimetric energy deposition in the ILD detector. In addition, the dashed curve, $60\%/\sqrt{E} \oplus 2\%$, is shown to give an indication of the resolution achievable using a traditional calorimetric approach. From [174].*
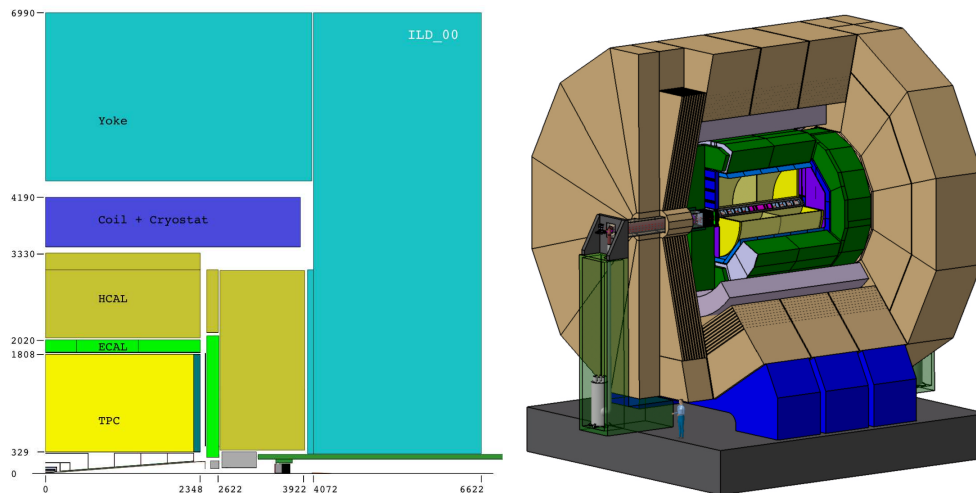
Figure 3.8: *The ILD detector model: schematic view of one quadrant of the ILD (left) and 3-dimensional view of the full detector (right). From [163].*

requirements on the granularity of the ECAL and the HCAL. Additionally, the material budget in front of the calorimeter has to be minimized as much as possible, since it degrades the track association to the energy deposits in the calorimeter. A high magnetic field, helping in the separation of adjacent tracks, plays also a key role in particle flow.

Fig. 3.7 (right) shows the empirical functional form of the jet energy resolution obtained from particle flow calorimetry in the ILD detector, using the PandoraPFA algorithm [174], and compares it with what is achievable using a traditional calorimetry. In the jet energy range of interest for the ILC (below 250 GeV at a center of mass of 500 GeV), the jet energy resolution obtained using the particle flow performs much better.

3.4.2 The International Large Detector Concept

The ILD detector design and performances are described in detail in the Letter of Intent document [163]. A 3D and a schematic view of the ILD are shown in Fig. 3.8.

The detector has the common onion-like structure, which is typical of many high energy physics multi-purpose detectors. The vertex detector close to the beam pipe is surrounded by the tracking system, which in turn is surrounded by the calorimeters. The superconducting coil is placed outside the calorimeters, in order to minimize the material budget between the calorimeters and the tracking, as required by the particle flow. The detector is enclosed by a return yoke, which is instrumented for tail catching and muon identification purposes.

The movable platform, visible in the 3D view, will be needed to move safely the detector in the push-pull scenario.

In the following the components of the detector are described with more details.

The Vertex Detector

The VerTeX detector (VTX) is dedicated to the measurement of the impact parameter of charged tracks. It provides also track segments for track reconstruction, fundamental

in particular for low momentum particles that do not reach the main tracking devices, due to the high bending magnetic field. The VTX plays also a key role in the time-stamping for bunch separation.

The design is still evolving, but some fundamental aspects are already well defined, though the VTX is not yet associated to a specific sensor technology. Two alternative geometries are under consideration. In the first option 6 cylindrical layers are grouped 2 by 2 in 3 super-layers, while the second option features 5 layers equidistant to one another. The layers are equipped with very thin ($\lesssim 50~\mu$m) pixel sensors, providing a single point resolution of $< 3~\mu$m all over the sensitive area. The innermost layer has a radius of 15-16 mm, a value at which the beam-related background is expected to be still acceptable. The 3 super-layers design is assumed for the present study.

A high occupancy will affect the detector, in particular in the innermost layers, posing demanding requirements on the readout technology and on the radiation hardness. A continuous and a train-by-train readout, in which the signal is stored during the whole train and read out in between two trains, are both being investigated. The radiation hardness has to be achieved without adding up more than a few permill of a radiation length X_0 (Sec. 6.1.1).

The Main Tracker

The main tracker is a large volume Time Projection Chamber (TPC). It is a gaseous detector, based on the ionization of the gas by the charged particles, when they traverse the chamber. Though with a moderate single point and double-hit resolutions with respect to a silicon tracker, it provides the unique feature of a quasi-continuous three-dimensional tracking. This is particularly relevant in the reconstruction of non-pointing tracks. The TPC gives good particle identification via the specific energy loss dE/dx, with a $\sim 5\%$ resolution. This is valuable for many physics analysis and in particular for electron identification.

The material budget goals for the inner and outer field cages are about $1\%\,X_0$ and $3\%\,X_0$, respectively, while the chamber gas adds another $1\%\,X_0$. The readout end-caps will be more demanding, with a $15\%\,X_0$ thickness. They need to be designed with the finest granularity possible, to minimize the occupancy arizing from the TPC drifttime, when integrating over about 100 bunch-crossings.

The TPC alone provides a momentum resolution of $\delta(\frac{1}{p_t}) \sim 9 \cdot 10^{-5}\,(\text{GeV}/c)^{-1}$ and more than 97% efficiency for tracks with $p_t > 1\,\text{GeV}/c$. It is supported by additional silicon trackers.

The Silicon Tracking

The silicon tracking system is designed to support the VTX and the TPC. The combination of gaseous and silicon based tracking offers some unique advantages. The silicon tracking is relatively easy to calibrate and will help to monitor possible field distortions in the TPC, as well as improving alignment and bunch tagging. The silicon tracker is made of two sets of detectors:

- The Silicon Internal Tracker (SIT) and the Silicon External Tracker (SET), are located in the barrel region, respectively between the VTX and the TPC and

outside the TPC. The two detectors consist of double-sided silicon strips. The SIT improves the momentum resolution and the reconstruction both of low p_t and long-lived charged particles. The SET provides an additional entry point to the ECAL after the TPC end wall, helping particle flow in connecting the tracks to the calorimetric hits. SIT and SET together provide three precision space points, improving the overall momentum resolution, alignment and bunch separation.

- The Forward Tracking Detector (FTD) and the End-cap Tracking Detector (ETD), located respectively in the forward region, on each side on the VTX, and on the very forward region, between the TPC and the ECAL end-caps. The FTD consists of seven disks on each side of the VTX. The first three disks are equipped with silicon pixels, while the latter four with silicon micro-strips. The ETD is instrumented with micro-strips on one side only. It helps to minimize the effect of the material at the TPC end plates, improving the matching efficiency between the tracks in the TPC and the shower clusters in the ECAL. The two detectors contribute to extend the overall tracking angular coverage to the very forward region.

The overall momentum resolution obtained combining silicon and gaseous detectors is of $\delta \left(\frac{1}{p_t} \right) \sim 2 \cdot 10^{-5} \, (\text{GeV}/c)^{-1}$, with a 99% efficiency for tracks with $p_t > 1 \, \text{GeV}/c$.

The Electromagnetic Calorimeter

The ECAL is a sampling calorimeter with tungsten ($X_0 = 3.5 \, \text{mm}$, $R_M = 9 \, \text{mm}$ and $\lambda_I = 99 \, \text{mm}$) as absorber material. The tungsten allows a compact design with a depth of 24 X_0 within only 20 cm and a good separation of showers generated by nearby particles. Two choices for the active material are considered, either silicon or scintillator. The here presented study assumes a silicon-tungsten ECAL.

In the barrel region the ECAL has a cylindrical shape, approximated by eight large octants, each subdivided into five modules. A design with large modules is preferred to minimize the cracks, with the inter-modules boundaries inclined such as they do not point back to the interaction point. The ECAL end-caps are placed right in front of the ETD and are divided into four modules each.

The ECAL is longitudinally segmented into 30 layers, with varying tungsten thicknesses. The active material has a high transverse segmentation, of $5 \times 5 \, \text{mm}^2$ for the silicon technology. In the scintillator proposal planes of $1 \times 4.5 \, \text{cm}^2$ strips are arranged orthogonally in adjacent layers.

The calorimeter contains 10^8 readout channels in total in the silicon option, while they get significantly reduced ($\sim 10^7$) with the silicon strips structure. The feasibility of a silicon-tungsten ECAL has been tested by the CALICE collaboration (see Chap. 7). From test beam measurements, using $1 \times 1 \, \text{cm}^2$ pixels, with 10 layers of $0.4 \, X_0$, 10 layers of $0.8 \, X_0$ and 10 layers of $1.2 \, X_0$ tungsten, an energy resolution was achieved of:

$$\frac{\sigma_E}{E} = \frac{(16.6 \pm 0.1)\%}{\sqrt{E[\text{GeV}]}} \oplus (1.1 \pm 0/1)\%. \tag{3.11}$$

The signal-over-noise ratio achieved was ~ 7.5 [175].

The Hadron Calorimeter

Two main options for the HCAL are studied. An analogue HCAL, with steel as absorber and scintillator as active material, and a digital HCAL, which uses gaseous devices as active medium. At the time the present study was developed, results from prototypes of the digital calorimeter were not yet at the level where its performance could be demonstrated. Therefore, the analogue design was simulated, using a $3 \times 3 \,\mathrm{cm}^2$ segmentation of the scintillator and 2 cm thick absorber plates. The barrel part of the detector has an octagonal shape, as the ECAL, with 48 layers, corresponding to $5.5 \,\lambda_I$.

As the HCAL must be placed within the coil, the absorber has to be non-magnetic. Stainless steel ($X_0 = 1.76 \,\mathrm{cm}$, $R_M = 1.7 \,\mathrm{cm}$ and $\lambda_I = 16.8 \,\mathrm{cm}$) satisfies this requirement, as well as giving further advantages: it is self-supporting and has a moderate λ_I/X_0 ratio. This allows a fine longitudinal sampling in terms of X_0, with a reasonable total number of layers necessary to reach a sufficient depth in terms of λ_I. The fine granularity is useful in the resolution of shower sub-structures, needed for particle separation in the particle flow perspective. Moreover, it is beneficial for the measurement of the electromagnetic fraction in the hadronic showers. The knowledge of the electromagnetic fraction allows to develop weighting techniques for a software-wise compensation, accounting for the difference between electromagnetic and hadronic response. This results in improved energy resolution and the linearity.

Forward Detectors

Additional detectors are placed in the forward region, with different tasks:

- **The LumiCal**. The LumiCal is a cylindrical electromagnetic calorimeter for the precise measurement of the luminosity. It is placed within the ECAL end-cap, covering the region around the beam pipe, between 32 and 74 mrad. In the current design it has 30 layers of tungsten alternated with silicon sensor planes. The luminosity is measured using Bhabha scattering, aiming to reach a precision of at least 10^{-3}.

- **The BeamCal**. The BeamCal is a solid state sensor-tungsten calorimeter, providing fast monitoring of the luminosity using beamstrahlung pairs. It is located in front of the final focusing quadrupoles, together with a 5 cm thick graphite block that absorbs low energetic back-scattered particles. It covers the polar angle range between 5 and 40 mrad.

  The BeamCal helps the suppression of the background from two-photon processes in delicate analysis. The deposition of high energetic electrons on top the beamstrahlung background can be identified with high efficiency, though with modest energy resolution, which is not relevant for suppression purposes.

- **The Pair Monitor**. A single layer of single pixel sensors is placed in front of the BeamCal, to measure the distribution of the beamstrahlung pairs. This information is useful for beam tuning. In fact, integrating over several bunch crossings, the pair monitor can reconstruct the beam sizes at the interaction point with a precision of a few percent.

- **The GamCal**. To measure the beamstrahlung spectrum a small fraction of the beamstrahlung photons are converted into electrons or positrons using a thin diamond foil or a gas-target, placed about 100 m downstream of the detector. An electromagnetic calorimeter, called GamCal, can measure the produced particles to assist the beam tuning, in particular in conditions of low luminosity.

- **The LHCal**. The LHCal is located inside the HCAL end-cap. It is a hadronic calorimeter, with 40 layers of tungsten of 1 cm thickness, alternated with the sensitive material (e.g. silicon sensors) planes, adding up to $\sim 4\,\lambda_I$. The purpose of the LHCal is to support the HCAL at small polar angles.

The Coil and the Muon System

The HCAL is surrounded by a superconducting coil, providing a solenoidal central field of nominal 3.5 T and maximum 4 T, in a volume of 6.9 m in diameter and 7.35 m in length. The TPC poses stringent requirements on the integral field homogeneity:

$$\left| \int_0^{2.25\text{m}} \frac{B_r}{B_z} dz \right| \leq 10\,\text{mm}. \tag{3.12}$$

An additional field has been proposed, to guide the low energetic pair background towards the beam pipe, the so-called anti-DID (Detector Integrated Dipole) field, induced by windings on the coil.

The coil is surrounded by an iron yoke. The barrel yoke has a dodecagonal shape and is longitudinally divided into three parts. The inner part is made of 10 iron plates, each 100 mm thick, with a gap of 40 mm between them to house sensitive material for tail catching and muon detection. The outer part of the barrel yoke has a coarser segmentation, with three iron plates of 560 mm each, also spaced with 40 mm gaps for muon detectors.

The end-cap yokes have also a dodecagonal shape and a similar structure, though with only two thick 560 mm layers in the outer part. A 100 mm thick field shaping plate is added inside each end-cap to improve field homogeneity.

The total weight of the yoke is 13400 t: around 7000 t for the barrel yoke and 3250 t for each end-cap yoke.

3.5 Detector Simulation on the Grid

The need of computing resources in high-energy physics is always growing in time, due to the increasing amount of experimental data and to the growing complexity of the experiments and of the related physics analysis. For projects still in the design phase, as the ILC, detailed Monte Carlo simulations are necessary, taking into account realistic detector effects (commonly indicated as *full simulations*). Not only the relevant signal processes need to be simulated, but also their complete backgrounds. Only in this way Monte Carlo studies can provide reliable predictions on the expected performances of the experiment and trigger the optimization of the detector design.

In view of the ILD Letter of Intent document [163] two massive Monte Carlo productions have been performed. One for the ILD detector model and, previously, one for a

former detector model from which the ILD design has evolved, the LDC (Large Detector Concept) [176]. During these massive productions all the SM processes and some dedicated processes for SUSY and Higgs studies have been fully simulated. In the first production for the LDC detector model about 20 million events were processed and twice more events were simulated for the ILD. The extent of these efforts is comparable to the Monte Carlo productions of running experiments.

In order to achieve these results a production system was implemented, relying on the Grid infrastructure [177]. The system was based an a set of scripts written in Bash [178], which were used in conjunction with a MySQL database [179]. The database served as a catalog for the Monte Carlo data produced and helped the bookkeeping of the running simulations. The database tables dedicated to the persistent data were provided with a web interface, to allow an easy access from the non-expert users.

In this section an overview of the Grid and of the Monte Carlo production system is given.

3.5.1 The Grid

The term Grid in computing was chosen as a metaphor for making computer power as distributed and as easy to access as an electric power grid [177]. The Grid concept in high-energy physics got boosted by the LHC community, in view of the enormous need of resources by the LHC experiments, once running. In the few years preceding the launch of the experiment, the LHC Computing Grid (LCG) [180] was developed, with contributions also from other projects, such as HERA and the ILC. The Grid resources, which are both computational and storage, are dislocated at several institutes around the world. The contributing sites are organized in a pyramidal structure of so-called Tiers, with on top the Tier-0, which is the CERN Computer Centre. The second level comprises large national facilities, the Tier-1s, that are currently eleven, followed by the regional Tier-2s, like universities or other scientific institutes, that are currently about 140[1]. Tier-3s are the local computing resources from which the individual scientists access the main facilities and are not formally engaged to the LCG system. The Tiers have different sizes and are also differentiated by their involvement in the several tasks of the Grid, such as data storage, general-purpose computing support and specialized analysis.

Individuals working at the same project, or experiment, belong to the same Virtual Organization (VO). VOs comprise a certain amount of computational and storage resources, that the members are allowed to use. Currently, only a limited number of Tiers support the ILC VO.

Several Tiers offer Storage Elements (SEs), where data is saved. The location of the files is stored in the LCG File Catalog (LFC), that provides a central registration of the data distributed amongst the various SEs. The file name in the LFC is called *logical file name* (LFN), while the real location on the SE is called *Storage URL* (SURL). Files can be replicated to several SEs, in order to speed up the access from different geographical locations and to reduce the burden of requests of the files from the single SEs. In this case, to the replicated files corresponds generally one single LFN, associated to more SURLs.

---

[1]Information obtained from the official LCG website, https://lcg.web.cern.ch/LCG/public/tiers.htm, consulted on the 2011-04-05.

The jobs are sent to the so-called Computing Elements (CEs), where they are scheduled on local batch queues for execution on the site's Worker Nodes (WNs). The jobs are allowed to run up to a specific time and memory limit.

The jobs are distributed to the CEs by Resource Brokers (RBs) using the Workload Management System (WMS).

Job Submission

In order to work on the Grid, the user describes the job to be performed in a Job Description Language (JDL) file. The JDL file includes all the necessary arguments and the name of the executable script. The user can either choose a certain CE and a determined queue, where to run the job, or specify settings such as the CPU time and memory needed by the job, that is then addressed by the RB to a CE offering a compatible queue. Small files needed during the execution of the job, such as configuration macros, can be sent together with the job in the input sandbox, while bigger files need to be previously saved on one or more SEs and accessed directly through their LFC during the execution of the job. Analogously, small output files, as the standard output and error streams, are retrieved directly together with the user-defined output sandbox, while bigger files are saved to a SE location during the execution of the job.

The JDL file is submitted through the User Interface (UI) software and received by the RB, together with the input sandbox. The RB delivers the job to a CE, that schedules it on a local queue. Before the job actually starts, the WN downloads the input sandbox from the RB. Once the job has finished, the output sandbox is transferred to the RB, from which the user can retrieve it through the UI. The user is informed of the status of the job (e.g. "scheduled", "running", "aborted" or "done") by quering the Logging and Bookkeeping (LB) system at any time.

3.5.2 Overview of ILCSoft

The detector simulation is performed within the framework of ILCSoft (Software for the ILC) [181]. The backbone of ILCSoft is the LCIO (Linear Collider Input/Output) package [182], that furnishes a model to store and access the data. In order to allow the integration with previous software frameworks LCIO is compatible with JAVA, C++ and Fortran. The data format currently associated to the LCIO data model is the SIO (Simple Input/Output).

The simulated Monte Carlo data include all the relevant information, such as hits registered in the calorimeters and in the trackers and the Monte Carlo truth. The information is enriched during the reconstruction phase, when the response of the detector is simulated and reconstruction algorithms (such as particle flow or jet finders) are applied. Jets, vertexing information, tracks, particle flow objects are added to the data files. In order to keep LCIO independent from specific applications, it allows to access only the low-level information of the objects stored, without any additional elaborated functionality. For instance, it is possible to extract the energy and the position of clusters, hits and jets or to obtain parents and daughters of the Monte Carlo true particles.

The detector simulation within ILCSoft is performed using Mokka [183], a Geant4 [184] based application. Geant4 is a toolkit written in C++, used to simulate the interactions of Monte Carlo particles with matter, e.g. with the detector components. Particle decays and interactions can be handled and the sensitive components of the detector and the magnetic fields inside it can be defined.

Several models exist, which give different approximations of the behavior of particles when traversing matter, in particular for hadronic particles, that cannot be described exactly 8.2.1. Several "physics lists" are available in GEANT4, which combine different models in different energy ranges, with random choice between the different models at those energies where they overlay. For the LDC and the ILD massive Monte Carlo productions the physics list LCPhys [185] was used.

The detector geometry is described using Mokka, specifying the shape of the detector components and their position, the sensitive regions and the composition of the materials employed. Mokka offers also the possibility to generate directly the Monte Carlo particles, using the so-called particle gun, but for the purpose of the massive productions an elaborated Monte Carlo generator has been used, which is not part of the ILCSoft framework. The Monte Carlo events were generated at SLAC [186] using Whizard [187, 188] and the O'Mega matrix element generator [189, 188]. The beamstrahlung spectrum was taken into account in the event generation and simulated using Guinea Pig [190]. Initial state radiation and final state radiation were included, as well.

After the simulation the events are reconstructed using Marlin [191] (Modular Analysis and Reconstruction for the Linear Collider). Marlin is a C++ framework structured in processors, which are code modules dedicated to specific tasks. The processors act subsequently on the data stream, performing analysis and adding new objects to the stream. Typical tasks of Marlin processors are the digitization of the detector, the reconstruction of tracks and clusters, the vertexing and the flavor tagging. The particle flow algorithm PandoraPFA [174] is also included in Marlin, as well as jet finder algorithms, such as the Durham jet finder algorithm [192] that was applied during the massive Monte Carlo productions.

3.5.3 The Production System

The production system was based on a MySQL database, whose structure is sketched in Fig. 3.9. Three tables contained the permanent data and were provided with a web interface[2]: "Input_Files", "MC_Data" and "RECO_Data". The "Input_Files" table contained the SE locations of the Whizard files, which are required as input to the Mokka simulations, and all the relevant information, such as the process, the cross section, the polarization of the beams and the number of events contained in the files. Before the massive Monte Carlo productions, the Whizard files produced at SLAC have been copied to the Desy SE and cataloged in this table. The "MC_Data" table stores similar information for the Mokka simulations, including the link to the corresponding event file in the "Input_Files" table, that was simulated. The "RECO_Data" table collects the records of the final outputs of the Marlin reconstruction. The two additional tables "Grid_jobs" and "Grid_Reco_jobs" are used for booking of the grid jobs, respectively for Mokka and Marlin jobs. The relevant information of the jobs scheduled

---

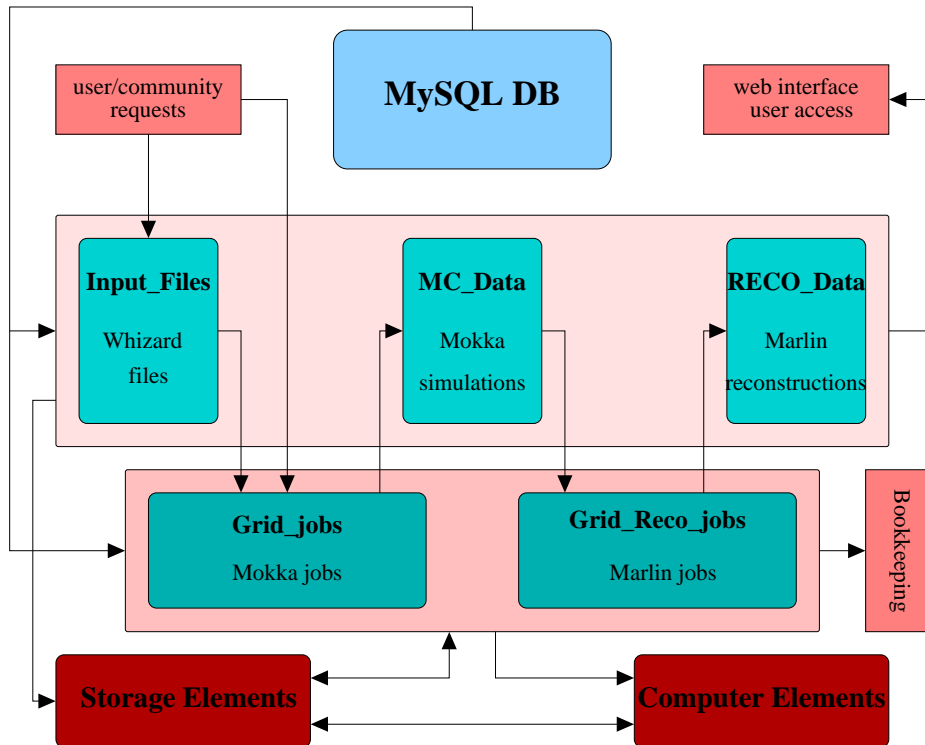[2]Web location: `http://www-flc.desy.de/simulation/database/` .

Figure 3.9: *Structure of the MySQL database for the massive Monte Carlo productions.*

for submission are stored, until the jobs are successfully completed and checked. Afterward they get deleted from these intermediate tables and their outcome registered to the permanent ones.

A system of Bash scripts schedules the Mokka jobs for submission, in order to simulate the desired number of events for the different processes. During the jobs the Whizard files, containing the events to be simulated, are copied from their SE location to the local WN, where the job runs, together with an archive file containing all the needed software, including Mokka. Mokka is then locally installed and the simulation executed. On completion of Mokka, the files with the simulated events are checked to contain the expected number of events. In case of success an archive file is created, containing the Mokka log file and macros, as well as the standard output and error streams of the job. The archive files and the files with the simulated events are saved in the Desy SE at the end of the job.

A system of Bash scripts checks the completed Mokka jobs, including their exit status and the existence of the expected output (simulations and archives) at the expected locations, with a consistent file size. The successfully completed jobs are written to the "MC_Data" table.

Similar procedure is followed for the Marlin jobs, with just two relevant differences. The Marlin jobs do not install locally the needed software, but use a pre-installed version of ILCSoft available on the Grid CEs. This difference is due essentially to historical reasons, since Mokka has become available with the pre-installed version of ILCSoft later than Marlin, when the production system was already completed. The second difference is that the Marlin jobs do not download locally to the WN the needed input files (i.e. the Mokka simulations), but they read them directly from the SE during the execution of the Marlin reconstruction.

Similar check routines as for the Mokka jobs are applied also to the reconstruction jobs, whose successful outcome is stored in the "RECO_Data" table. For convene of the users, the Marlin reconstructed files are saved also in a light format, containing only the essential information, that are usually enough for most of the physics analysis. Such a file format is known as DST and it was defined at Zeuthen (DESY) for storage of the fundamental particle collision (i.e. event) information: tracks, clusters, particle flow objects, jets, true Monte Carlo and flavor tagging objects.

4 Beam Polarization at the ILC

In this chapter the motivations for employing polarized beams at the ILC are reviewed, with general considerations and specific examples taken from the SM and SUSY (Sec. 2.8.1).

In the second part of the chapter the measurement of the polarization is discussed. The upstream and the downstream polarimeters are described as well as the sources of depolarization between the polarimeters and the IP, which motivate the study of data-driven polarization measurements.

4.1 Importance of the Beam Polarization

Indicating with N_R (N_L) the number of beam particles with definite right-handed (left-handed) helicity $\lambda = +\frac{1}{2}$ ($\lambda = -\frac{1}{2}$), the longitudinal polarization of the beam is defined as:

$$\frac{N_R - N_L}{N_R + N_L}. \tag{4.1}$$

Since the beam particles can be regarded as being massless, the helicity corresponds to their chirality (Sec. 2.4).

The beam polarization will maximize the physics potential of the ILC, both in the performance of precision tests and measurements of the SM and in revealing the properties of new physics beyond the SM, such as SUSY. In the following the benefits given by the longitudinal beam polarization are shortly introduced with a few examples. In particular, the importance of having both the beams polarized is emphazised, since a high e^- polarization alone cannot replace the essential contribution of having a polarized e^+-beam in addition. Some considerations about the transverse beam polarization are also made, though the present work is concerned with longitudinal polarization only.

For a complete overview of the topic the interested reader is refered to [193], from which most of the following examples are taken.

4.1.1 Separation of the Production Diagrams

With longitudinally-polarized beams one can distinguish between two different cases, depending on the production diagrams:

- in annihilation diagrams, as shown in Fig. 4.1, the helicities of the incoming beams are coupled to each other. In the SM they need to be opposite from one another in order to recombine into the vector boson mediator, the Z or the γ,
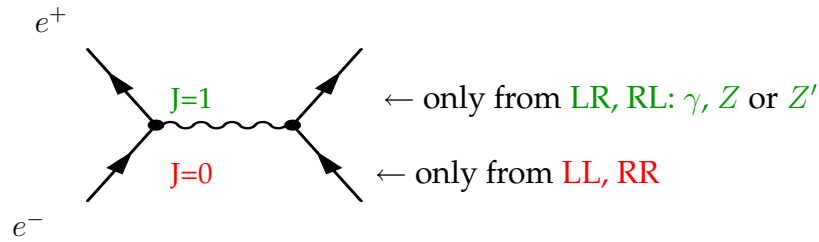
Figure 4.1: *Possible configurations in s-channel diagrams: the helicities of the incoming e^+e^- beams are directly coupled. Within the SM only the recombination into a vector particle with $J = 1$ is possible, which is given by the LR (Left-handed electron, Right-handed positron) and RL configurations. New physics models might contribute to $J = 1$ but also to $J = 0$, hence the LL or RR configurations. From [193].*
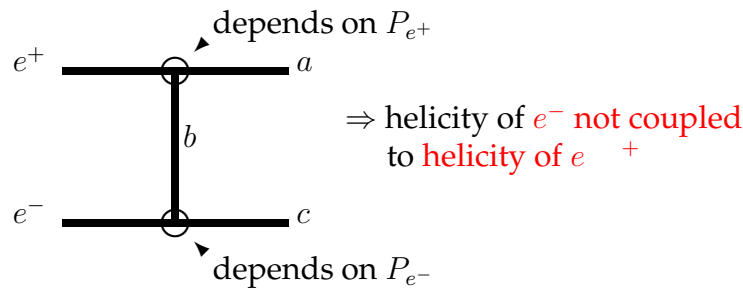

Figure 4.2: *Possible configurations in t- and u-channel diagrams: the helicity of the incoming beam is directly coupled to the helicity of the final particle and is completely independent from the helicity of the second incoming particle. From [193].*

since only in this way they can add up to give $J = 1$. This might not be true in case of new physics. Some models allow *s*-channel diagrams to be mediated by a scalar particle. An example is given in Sec. 4.1.5.

- in exchange diagrams, as shown in Fig. 4.2, the helicities of the incoming beams are directly coupled to the helicities of the final particles. In this case all helicity configurations for the beams are in principle possible, although some constraints might be given by the allowed couplings between the beam particles and the produced ones. This is the case, for example, for the W-pair production, which is of interest to the work presented in Chap. 5, since the W has a pure left-handed (right-handed) coupling to electrons (positrons).

The differences of the *s*-channel and *t*-channel dependence on the polarization can have several benefits. For instance, suitable combinations of the beam polarizations can be used to enhance signal rates and suppress backgrounds. Moreover, in *t*-channel processes the helicities/chiralities of the beam particles can be related directly to the properties of the produced (new) particles and their interactions, allowing the investigation of the underlying theory with a minimal number of assumptions. These concepts are clarified in the following with some specific examples.
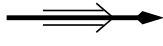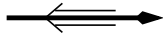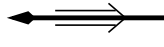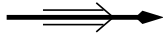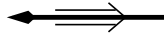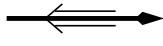
Figure 4.3: *Possible longitudinal spin configurations in e^+e^- collisions, with longitudinally-polarized beams. The thick arrow represents the direction of motion of the particle and the double arrow its spin direction. The first column indicates the corresponding total cross section for each configuration and 100%-polarized beams. The fourth column reports the fraction of each configuration contributing to the total cross section, where P_{e^-} is the electron polarization and P_{e^+} the positron polarization. The last column indicates the total spin projection onto the e^+e^- direction. From [193].*

4.1.2 Statistical Advantages

With longitudinally-polarized beams cross sections at an e^+e^- collider can be expressed as [194] (cf. Fig. 4.3):

$$
\begin{aligned}
\sigma_{P_{e^-}P_{e^+}} &= \frac{1}{4}\Big\{(1 + P_{e^-})(1 + P_{e^+})\sigma_{\mathrm{RR}} + (1 - P_{e^-})(1 - P_{e^+})\sigma_{\mathrm{LL}} \\
&\quad + (1 + P_{e^-})(1 - P_{e^+})\sigma_{\mathrm{RL}} + (1 - P_{e^-})(1 + P_{e^+})\sigma_{\mathrm{LR}}\Big\},
\end{aligned}
\tag{4.2}
$$

where σ_{RL} is the cross section obtained with a completely right-handed polarized e^--beam ($P_{e^-} = +1$) and a completely left-handed polarized e^+-beam ($P_{e^+} = -1$). The cross sections σ_{LR}, σ_{RR} and σ_{LL} are defined analogously.

As already mentioned, in the case of e^+e^- annihilation into a vector particle, such as in the SM s-channel production, only the two $J = 1$ configurations σ_{RL} and σ_{LR} contribute. The cross section for arbitrary beam polarizations (P_{e^-}, P_{e^+}) is then given by:

$$
\begin{aligned}
\sigma_{P_{e^-}P_{e^+}} &= \frac{1 + P_{e^-}}{2}\frac{1 - P_{e^+}}{2}\sigma_{\mathrm{RL}} + \frac{1 - P_{e^-}}{2}\frac{1 + P_{e^+}}{2}\sigma_{\mathrm{LR}} \\
&= (1 - P_{e^-}P_{e^+})\frac{\sigma_{\mathrm{RL}} + \sigma_{\mathrm{LR}}}{4}\left[1 - \frac{P_{e^-} - P_{e^+}}{1 - P_{e^+}P_{e^-}}\frac{\sigma_{\mathrm{LR}} - \sigma_{\mathrm{RL}}}{\sigma_{\mathrm{LR}} + \sigma_{\mathrm{RL}}}\right] \\
&= (1 - P_{e^+}P_{e^-})\,\sigma_0\,[1 - P_{\mathrm{eff}}\,A_{\mathrm{LR}}],
\end{aligned}
\tag{4.3}
$$

with:

$$\text{the unpolarized cross section:} \quad \sigma_0 = \frac{\sigma_{\mathrm{RL}} + \sigma_{\mathrm{LR}}}{4},$$

$$\text{the left-right asymmetry:} \quad A_{\mathrm{LR}} = \frac{\sigma_{\mathrm{LR}} - \sigma_{\mathrm{RL}}}{\sigma_{\mathrm{LR}} + \sigma_{\mathrm{RL}}},$$

$$\text{and the effective polarization:} \quad P_{\mathrm{eff}} = \frac{P_{e^-} - P_{e^+}}{1 - P_{e^+} P_{e^-}}. \tag{4.4}$$

Together with the effective polarization P_{eff} (Eq. 4.4) it is possible to introduce an effective luminosity $\mathcal{L}_{\mathrm{eff}}$ as well, where the ratio $\mathcal{L}_{\mathrm{eff}}/\mathcal{L}$ reflects the fraction of interacting particles:

$$\mathcal{L}_{\mathrm{eff}} = \frac{1}{2}(1 - P_{e^-} P_{e^+})\mathcal{L}. \tag{4.5}$$

In case only the e^--beam is polarized, P_{eff} is simply equal to the e^- polarization. No statistical benefit is obtained in this case, since the fraction of interacting particles is 0.5, as for an unpolarized e^--beam. Adding an e^+ polarization, P_{eff} increases and gets closer to 100% than either of the two beam polarizations alone. The fraction of interacting particles also increases. Some numerical examples are given in Tab. 4.1.

e^--beam	e^+-beam	P_{eff}	$\mathcal{L}_{\mathrm{eff}}/\mathcal{L}$
$P_{e^-} = 0$,	$P_{e^+} = 0$	0%	0.50
$P_{e^-} = -100\%$,	$P_{e^+} = 0$	-100%	0.50
$P_{e^-} = -80\%$,	$P_{e^+} = 0$	-80%	0.50
$P_{e^-} = -80\%$,	$P_{e^+} = +30\%$	-89%	0.62
$P_{e^-} = -80\%$,	$P_{e^+} = +60\%$	-95%	0.74

Table 4.1: *Effective polarization and effective luminosity for unpolarized beams and some combinations of the beam polarizations. Note: without additional positron polarization there is no gain in the effective luminosity regardless of the electron polarization.*

If both beams are polarized the relative statistical precision on P_{eff} is better than the statistical error on the individual polarizations of the beams, independently from the fact that the errors are correlated or uncorrelated. If one assumes an equal relative precision $x \equiv \Delta P_{e^-}/P_{e^-} = \Delta P_{e^+}/P_{e^+}$ of the two beam polarizations, the gain obtained on $\Delta P_{\mathrm{eff}}/P_{\mathrm{eff}}$ is shown in Fig. 4.4 (right), in the example of uncorrelated errors.

The improvement on $\Delta P_{\mathrm{eff}}/P_{\mathrm{eff}}$ is proportional to the improvement on the left-right asymmetry, that one measures by running the experiment with two different polarization configurations. One would choose one configuration with the electron beam predominantly left-handed and the positron beam right-handed and the second one with both spins reversed. The asymmetry A_{LR} is obtained by the cross sections measured for both cases, according to Eq. 4.4. For a positron polarization of $P_{e^+} = 60\%$ the error on A_{LR} is reduced by a factor of about 3, with respect to the case with only electron polarization, while for $P_{e^+} = 30\%$ the improvement is about a factor of 2 [195].
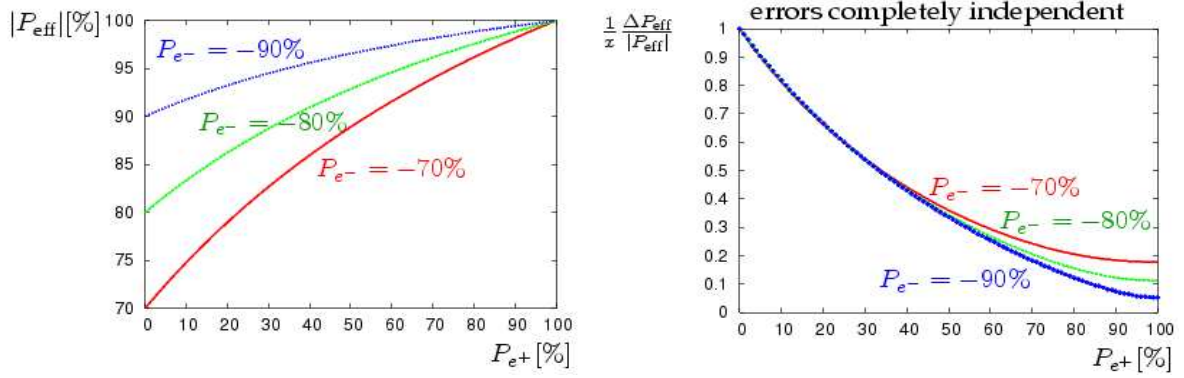
Figure 4.4: *Left: effective polarization, P_{eff}, vs. positron beam polarization, P_{e^+}, and for different polarizations of the electron beam, P_{e^-}. Right: relative uncertainty on the effective polarization, $\Delta P_{\text{eff}}/|P_{\text{eff}}| \sim \Delta A_{\text{LR}}/A_{\text{LR}}$, normalized to the relative polarimeter precision $x = \Delta P_{e^-}/P_{e^-} = \Delta P_{e^+}/P_{e^+}$ for independent errors on P_{e^-} and P_{e^+}. From [195].*

4.1.3 Background Suppression

The use of longitudinally polarized beams plays a major role in reducing the background contribution as much as possible, while enhancing the signal rates. This is particularly important for searches for new physics, where the signal contribution is often expected to be extremely small compared to the SM background.

In those cases where the signal and the background exhibit a different polarization dependence, the gain in polarizing both beams is obvious: using the proper polarization combination it is possible to enhance the signal and suppress the background simultaneously.

A benefit is also obtained in those cases where the signal and the background show a similar dependence on the beam polarization. Even if the ratio S/B cannot be improved (S and B indicate the number of signal and background events, respectively), one can still improve the significance of the signal over the fluctuations of the background. This could be useful, since new physics beyond the SM is expected to have generally very small cross sections and a peak due to its contribution could in some cases be compatible with a fluctuation of the background.

Assuming a Gaussian distribution for the background, which is suitable thanks to the high luminosity foreseen at the ILC, the fluctuations of the background are of the order of $\sqrt{B}$. In order to get a significance of $\mathcal{N}_\sigma$ standard deviations for the signal, it is required that:

$$S > \mathcal{N}_\sigma \times \sqrt{B}. \tag{4.6}$$

Choosing the polarization set in which the cross sections of background and signal are maximally enhanced, for example by a factor 2, the significance is increased by a factor of $\sqrt{2}$:

$$\frac{2 \cdot S}{\sqrt{2 \cdot B}} = \sqrt{2}. \tag{4.7}$$

4.1.4 Polarized Beams in Standard Model Tests

High-precision tests of the SM will be a relevant part of the physics program at the ILC. In particular, if the new physics should lie beyond the direct energy reach of the collider these tests will be the only tool to reveal it by means of indirect constraints.

Top Studies

At hadron colliders top quarks are pair-produced via gluon exchange, therefore the neutral electroweak couplings of the top quark are accessible only at lepton colliders, where the main SM production process occurs via γ, Z exchange.

Polarization effects in the determination of the top vector coupling $v_t = (1 - \frac{8}{3}\sin^2\theta_W)$ at a linear collider have been studied at the top threshold in [196]. A precise determination of the vector coupling requires a precise measurement of the left-right asymmetry $A_{\rm LR}$, since $A_{\rm LR}$ can be written in terms of the effective electroweak mixing angle $\sin^2\theta_{\rm eff}$ [193]:

$$A_{\rm LR} = \frac{2(1 - 4\sin^2\theta_{\rm eff})}{1 + (1 - 4\sin^2\theta_{\rm eff})^2}. \tag{4.8}$$

As already mentioned, the relative uncertainty $\Delta A_{\rm LR}/A_{\rm LR}$ is proportional to $\Delta P_{\rm eff}/P_{\rm eff}$ and the statistical precision on $A_{\rm LR}$ improves by a factor 3 if $(P_{e^-}, P_{e^+}) = (\mp 80\%, \pm 60\%)$, with respect to the case $(P_{e^-}, P_{e^+}) = (\mp 80\%, 0)$ (see Sec. 4.1.2). Similar improvements have been estimated also for the continuum at $500\,{\rm GeV}$ [193].

Top physics represents also an interesting field for new-physics searches. For instance, Flavor-Changing Neutral (FCN) couplings are relevant to numerous extensions of the SM. The single-top production $e^+e^- \to t\bar{q} \to W^+b\bar{q}$ is sensitive to FCN anomalous couplings via the tVq vertex ($V = \gamma, Z$ and $q = u, c$). Beam polarization comes into play in the background suppression. The background is dominated by the $W^+ + 2{\rm jets}$ final state, with W^+ decaying into $l\nu$ and one jet misidentified as a b-jet.

With a polarization $(P_{e^-}, P_{e^+}) = (80\%, 0)$ the background decreases by a factor of $1/(1 - P_{e^-}) \approx 5$, while 90% of the signal is kept, with respect to the case without beam polarization. An additional e^+ polarization of 45% reduces the background by a factor 8.1 and increases the signal by 17% with respect to the values obtained without polarization [197]. These numbers refer to a center of mass energy of $500\,{\rm GeV}$.

Higgs Studies

Although the discovery of the Higgs boson, if it exists, is expected at the LHC (e.g. [133]), the ILC will have the major task of studying its properties with a higher precision. The benefit of polarization in this context is mainly a statistical one, since it helps separating the Higgs production processes, suppressing the background and improving the precision on the measurement of its general couplings.

The main production processes of the Higgs boson at the ILC are the Higgs-strahlung ($e^+e^- \to HZ$) and the WW-fusion ($e^+e^- \to H\nu\bar{\nu}$), shown in Fig. 4.5. Assuming a light Higgs boson with $m_H \le 130$ GeV, the two processes might have similar cross sections at $\sqrt{s} = 500\,{\rm GeV}$. In such a case the polarization would be very helpful in separating
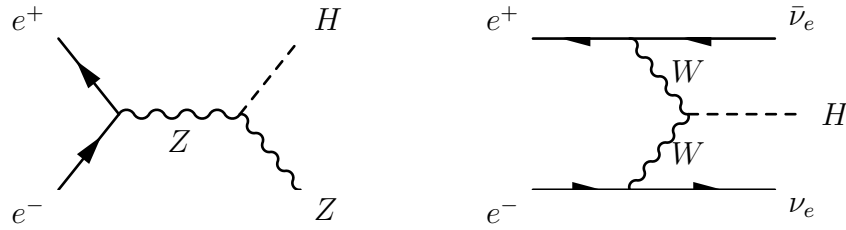
Figure 4.5: *Main production processes of the SM Higgs boson at the ILC: the Higgs-strahlung (left) and the WW fusion (right). From [198].*

the two production processes. The $H\nu_e\bar{\nu}_e$ final state contains important contributions from both the HZ-production and the WW-fusion, although with different shapes of the missing mass distributions. With $(P_{e^-}, P_{e^+}) = (+80\%, -60\%)$ the Higgs-strahlung is the favoured process and the WW-fusion is suppressed. The ratio between the two production cross sections increases by a factor 4, compared to the case without positron polarization. The relative contribution of the two processes can be extracted from the missing mass distributions without strong model assumptions. At the same time, the polarization is helpful in suppressing the backgrounds. The suppression of the W-pair background can be enhanced by a factor 2, if $(P_{e^-}, P_{e^+}) = (+80\%, -60\%)$ is used instead of $(P_{e^-}, P_{e^+}) = (+80\%, 0\%)$. Comparing the same two polarization configurations, the ZZ-background is not so strongly reduced, but the statistical significance $S/\sqrt{B}$ of the Higgs-strahlung signal is improved by more than 20% [193, 199].

The beam polarization can have an impact also on the measurement of the Higgs boson couplings. The determination of the general Higgs couplings ZZH and $Z\gamma H$ was studied in the $e^+e^- \to HZ \to Hf\bar{f}$ channel using an optimal-observable method [200]. For $\sqrt{s} = 500\,\mathrm{GeV}$, $\mathcal{L}_{\mathrm{int}} = 300\,\mathrm{fb}^{-1}$ and $(P_{e^-}, P_{e^+}) = (\pm80\%, 60\%)$, the sensitivity on the couplings is improved by about 30% with respect to $(P_{e^-}, P_{e^+}) = (\pm80\%, 0)$.

Due to its large mass, the top quark is expected to play a key role in the mechanism of electroweak symmetry breaking and mass generation. Therefore, an accurate measurement of the top-Higgs Yukawa coupling is particularly important. A recent study of the $e^+e^- \to t\bar{t}H$ channel showed that, for an integrated luminosity of $1\,\mathrm{ab}^{-1}$ and at $\sqrt{s} = 500\,\mathrm{GeV}$, this process is observable with a significance of 4.1 σ without any beam polarization. With $(P_{e^-}, P_{e^+}) = (-80\%, +30\%)$ a significance of 5.4 σ is obtained [201].

Precision Measurements at the GigaZ

In the GigaZ option the ILC would spend part of the running time at the Z-boson resonance, with high luminosity, collecting about 10^9 Z events. This dedicated Z-factory is meant to deliver measurements of electroweak precision observables with unprecedented accuracy [157]. The experimental accuracies on the mass of the weak gauge bosons, on their decay widths and on the weak mixing angle $\sin^2\theta_{eff}$ will provide a high sensitivity to quantum effects of New Physics. Measuring the left-right asymmetry at the Z-pole with high precision is particularly important for the determination of $\sin^2\theta_{eff}$. As already seen, the beam polarization strongly improves the performance of such a measurement.

The two single most precise measurements today available, A_{FB}^b by LEP and A_{LR}^e by SLD, lead to a large discrepancy in $\sin^2\theta_{eff}$:
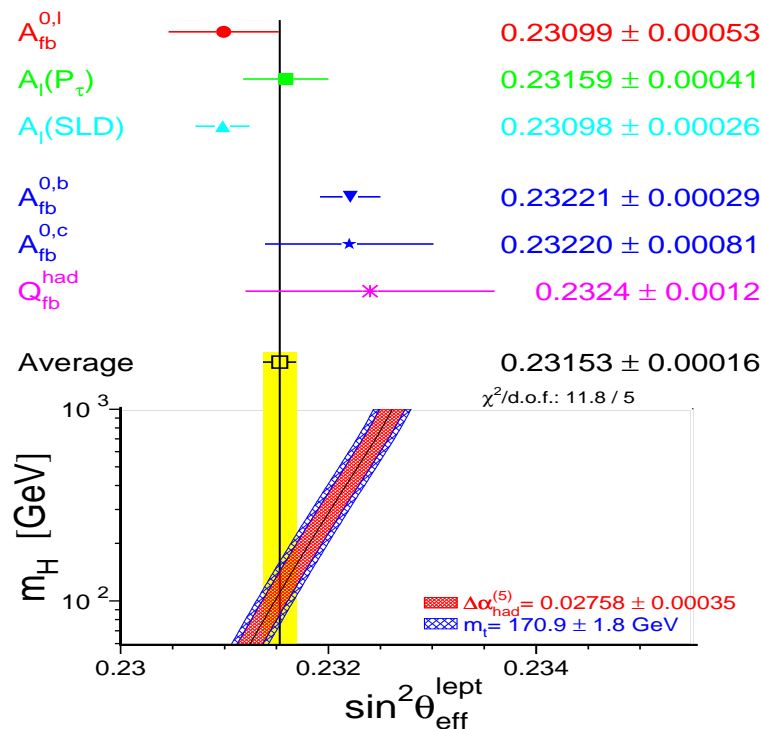
Figure 4.6: *Individual measurements and world-average of $\sin^2\theta_{\text{eff}}$. The experimental results are compared with the prediction within the SM as a function of $M_{H^{\text{SM}}}$ for $m_t = 170.9 \pm 1.8\,GeV$ and $\Delta\alpha_{\text{had}}^5 = 0.02758 \pm 0.00035$ [202].*

$$A_{\text{FB}}^b(\text{LEP}) : \sin^2\theta_{\text{eff}}^{\text{exp,LEP}} = 0.23221 \pm 0.00029 \ , \tag{4.9}$$

$$A_{\text{LR}}^e(\text{SLD}) : \sin^2\theta_{\text{eff}}^{\text{exp,SLD}} = 0.23098 \pm 0.00026 \ . \tag{4.10}$$

The two measurements differ by more than $3\,\sigma$ and lead to a large discrepancy in several predictions. For instance, the former (latter) one prefers a value of the mass of the SM Higgs $M_{H^{\text{SM}}} \sim 32(437)$ GeV [157]. The averaged value of $\sin^2\theta_{\text{eff}}$, as shown in Fig. 4.6, prefers $M_{H^{\text{SM}}} \sim 110$ GeV [157].

The uncertainty on $\sin^2\theta_{eff}$ also affects the allowed range of some SUSY parameters and the possibility to disentangle different physics scenarios. Fig. 4.7 shows one example of how a precise measurement of $\sin^2\theta_{\text{eff}}$ yields constraints on the SUSY mass parameter $m_{1/2}$ in a specific model, the CMSSM (Constrained Minimal Supersymmetric Standard Model) [203].

4.1.5 Polarized Beams in Searches for Supersymmetry

SUSY is one of the most promising candidates for physics beyond the SM (Sec. 2.8.1). If nature has realized SUSY, the discovery of SUSY is expected at the LHC (e.g. [205]). Once SUSY is discovered, one of the main goals of the ILC is to precisely determine the fundamental parameters of the theory to help unravel the underlying specific SUSY model. This is a challenging task. For instance, in a minimal model, the MSSM (Minimal Supersymmetric Standard Model), there are 105 parameters [206]. At least some
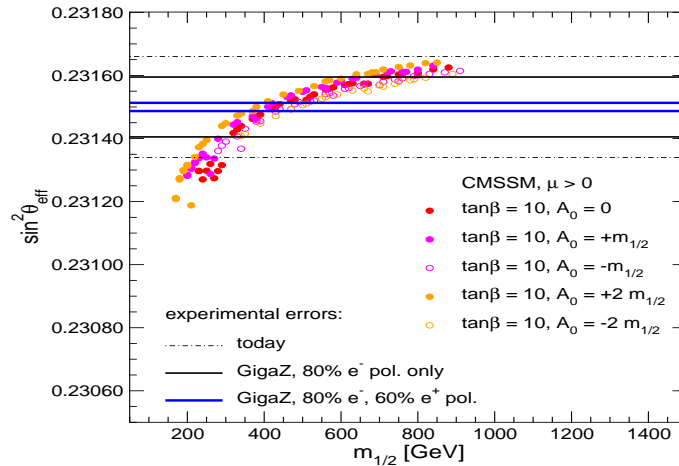
Figure 4.7: *The precision measurement of $\sin^2\theta_{\text{eff}}$ yields constraints on the allowed range for the SUSY mass parameter $m_{1/2}$ in a specific model, the CMSSM. The allowed range of $m_{1/2}$ is reduced by a factor of about 5 when using $(|P_{e^-}|, |P_{e^+}|) = (80\%, 60\%)$ instead of $(|P_{e^-}|, |P_{e^+}|) = (80\%, 0\%)$. Experimental constraints from LEP searches and cold-dark-matter searches have been taken into account. Figure taken from [204].*

of the new SUSY particles are predicted to be accessible at the ILC [207]. However, constraints on the SUSY parameters can be obtained also from precise measurements of the SM, which is particularly important if part of the SUSY spectrum should not be accessible. Polarization plays an important role in enhancing the small cross sections expected from some SUSY signals while reducing the background processes, but also in providing new observables. Some examples are given in the following.

Chiral Quantum Numbers and Yukawa Couplings

If nature is supersymmetric, all new SUSY particles carry the same quantum numbers of the SM particles, with the exception of the spin, which differs by half a unit. Corresponding to the two chirality states of the known leptons and quarks, right- and left-handed, one has the right and left scalar partners. One important test of SUSY at the ILC will be to probe that the SUSY partners of e^- and e^+, respectively the selectron $\tilde{e}^-$ and the spositron $\tilde{e}^+$, are associated according to the following relations:

$$e^-_{\text{L,R}} \leftrightarrow \tilde{e}^-_{\text{L,R}} \quad \text{and} \quad e^+_{\text{L,R}} \leftrightarrow \tilde{e}^+_{\text{R,L}}. \tag{4.11}$$

The selectron production, $e^+e^- \rightarrow \tilde{e}^+_{L,R}\tilde{e}^-_{L,R}$, with polarized beams can be used in order to perform such a measurement [208]. The process occurs via γ, Z exchange in the s-channel and via neutralino exchanges, $\tilde{\chi}^0_{1,2,3,4}$, in the t-channel. In the t-channel both pair productions, $\tilde{e}^+_L\tilde{e}^-_L$ and $\tilde{e}^+_R\tilde{e}^-_R$, as well as associated production, $\tilde{e}^+_L\tilde{e}^-_R$ and $\tilde{e}^+_R\tilde{e}^-_L$, are possible, whereas in the s-channel only pairs, $\tilde{e}^+_L\tilde{e}^-_L$ and $\tilde{e}^+_R\tilde{e}^-_R$, can be produced. In case the selectron masses are close together, namely $m_{\tilde{e}_L} = 200$ GeV and $m_{\tilde{e}_R} = 195$ GeV, both $\tilde{e}_L$, $\tilde{e}_R$ decay via the same channels, $\tilde{e}_{L,R} \rightarrow \tilde{\chi}^0_1 e$. Fig. 4.8 (left) shows that the separation of the pairs $\tilde{e}^-_L\tilde{e}^+_R$ from $\tilde{e}^-_R\tilde{e}^+_R$ in $e^+e^- \rightarrow \tilde{e}^+_{L,R}\tilde{e}^-_{L,R}$ may not be possible with electron polarization only, since both cross sections are numerically very close. However, if both beams are polarized the RR configuration of the incoming
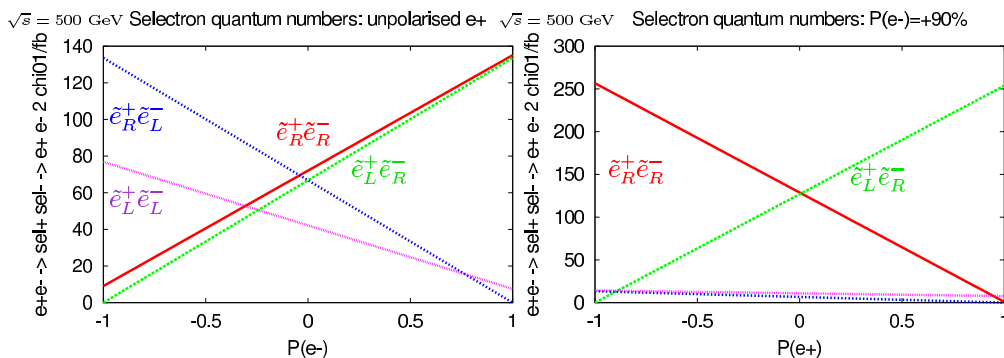
Figure 4.8: *Cross section of the selectron pair production in case of unpolarized positron beam (left) and both beams polarized (right, $P(e^-) = 90\%$). From [208].*

beams separates the pairs and the association of the selectrons to the chiral quantum numbers can be experimentally tested, as shown in Fig. 4.8(right) [208]. In addition, the configuration where both beams are right-polarized, in particular, strongly suppresses the SM background, e.g. the W^+W^- production.

Another important property of SUSY is that the SU(2) and U(1) Yukawa couplings have to be identical to the corresponding SM gauge couplings. The Yukawa couplings could be determined from the production cross sections of $\tilde{e}_\mathrm{R}^+\tilde{e}_\mathrm{R}^-$ and $\tilde{e}_\mathrm{L}^+\tilde{e}_\mathrm{R}^-$, assuming that the masses and mixing parameters of the neutralinos have already been determined in the gaugino/higgsino sector [193, 209]. Analogously to the previous example, if the two pairs have almost identical cross sections and decay modes, the different combinations of $\tilde{e}_\mathrm{R}$ and $\tilde{e}_\mathrm{L}$ can only be distinguished by having both beams polarized.

Polarization at the Resonance of New Particles

The polarization of both beams allows to probe the spin of particles produced as resonances, distinguishing between theoretical models without the need of challenging final-state analysis. An example is given by an R-parity-violating SUSY model [210], where R-parity is a new quantum number introduced by SUSY, defined as:

$$P_R = (-1)^{3(B-L)+2S}, \tag{4.12}$$

where S is the spin, B the baryon number and L the lepton number. In such a scenario scalar neutral particles, the sneutrinos, can be produced in the s-channel, giving $\mu^+\mu^-$ pairs in the final state:

$$e^+e^- \rightarrow \tilde{\nu}_\tau \rightarrow \mu^+\mu^-. \tag{4.13}$$

Such decays can be observed at the ILC, controlling the di-lepton SM background thanks to the beam polarization. Since the sneutrinos couple only to left-handed $e^\pm$, this process is enhanced in the LL polarization combination. For such a configuration the SM background is strongly suppressed and the signal over background ratio becomes $S/B \sim 12$ for $(P_{e^-}, P_{e^+}) = (-80\%, -60\%)$ at the resonance. In case only the electron beam is polarized $(P_{e^-}, P_{e^+}) = (-80\%, 0)$ the ratio would only be $S/B \sim 5$. These values were obtained in a study performed at $\sqrt{s} = 650$ GeV for $m_{\tilde{\nu}} = 650$ GeV,

$\Gamma_{\tilde{\nu}} = 1$ GeV, an angular constraint of $45° \leq \theta \leq 135°$ and the R-parity violating couplings $\lambda_{131} = 0.05$ and $\lambda_{232} = 0.05$, respectively [211, 193].

Some extensions of the SM gauge group predict a new neutral gauge boson, called Z' [212]. Considering the same $\mu^+\mu^-$ final state of the previous example, the s-channel Z' exchange with $m_{Z'} \sim m_{\tilde{\nu}}$ would manifest itself by a peak in the cross section at the resonance [213], corresponding to a spin-1 resonance. The polarization would allow to distinguish this peak from the spin-0 one of the R-parity-violating SUSY model. In fact, in this case, the signal would be enhanced for the LR and RL configurations of the longitudinal polarization, which suppress the sneutrino exchange.

4.1.6 Transverse Polarization

The present study is only concerned with longitudinal polarization. For completeness, it should be mentioned that the physics program at the ILC would benefit also from transversely-polarized beams [193].

Since the measured baryon asymmetry of the Universe cannot be explained by the small amount of CP violation present in the SM, novel sources of CP violation are searched for (Sec. 2.7.2). Having both beams transversely polarized would open the possibility to detect even small CP-violating phases [214].

Transversely-polarized beams would provide new observables, such as azimuthal asymmetries, which are sensitive to non-standard interactions. One example is given by interactions mediated by spin-2 gravitons in specific extra-dimensional models [215, 216].

Although longitudinally-polarized beams are sufficient to measure most TGCs, however, in the most general case, where a non-null imaginary part is also allowed (see Sec. 2.9), an exception would be given by the $\tilde{h}_+$ coupling. As shown in [217] this coupling is only accessible with transversely-polarized beams.

4.2 Measurement of the Polarization

At the ILC both upstream and downstream polarimeters are provided. The foreseen locations of the polarimeters and energy spectrometers in the Beam Delivery System (BDS) according to the RDR are shown in Fig. 4.9. The upstream polarimeter is placed around 1800 m before the interaction point (IP), while the downstream polarimeter is around 180 m downstream of the IP.

4.2.1 Compton Polarimetry

Compton polarimetry has been chosen both for the upstream and downstream polarimetry [136]. A Compton polarimeter is based on the Compton scattering of polarized beam electrons and positrons off polarized laser light. The longitudinal beam polarization is obtained by measuring the asymmetry in the energy spectra of the
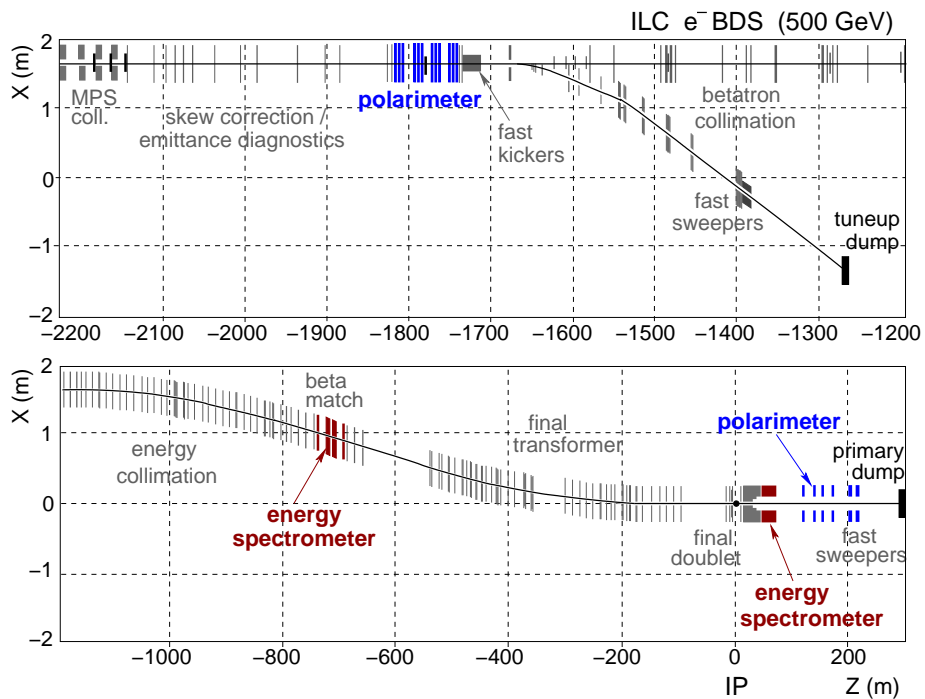
Figure 4.9: *Beam Delivery System as described in the RDR. The upper part shows the region from 2200 m to 1200 m upstream of the e^+e^- IP, including the polarimeter chicane at 1800 m. The lower part shows the region from 1200 m upstream to about 300 m downstream of the IP, including the upstream energy spectrometer at 700 m as well as the extraction line energy spectrometer and the polarimeter around 180 m downstream of the IP ($z = 0$ m). From [166].*
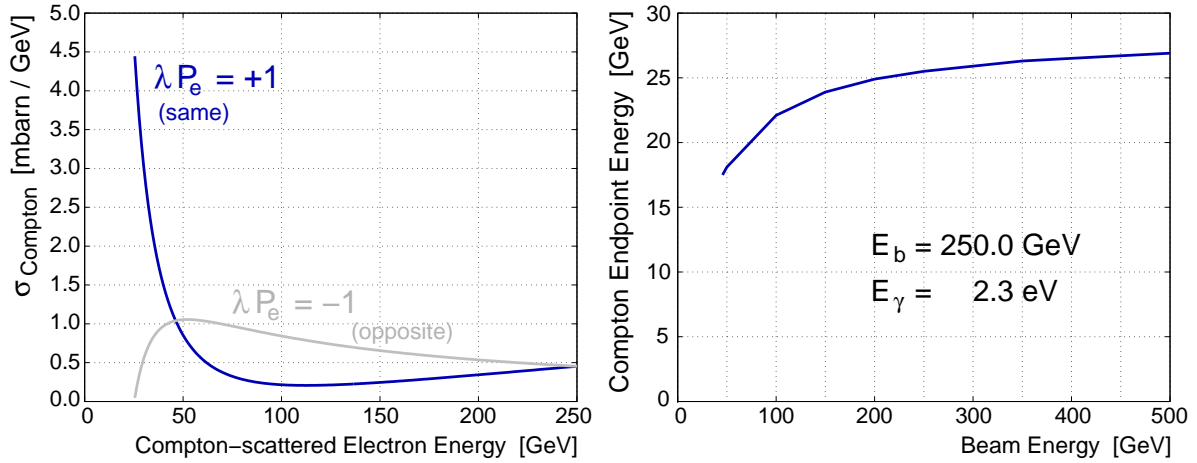
Figure 4.10: *Left: Compton differential cross section versus scattered electron energy for same (black/blue curve) and opposite (gray curve) helicity configuration of laser photon and beam electron. The beam energy is 250 GeV and the laser photon energy is 2.3 eV. Right: Compton edge energy dependence on the beam energy. From [166].*

scattered beam particles, for the same and the opposite helicity configuration of laser photon and beam particles:

$$A(E_e) = \frac{N_L(E_e) - N_R(E_e)}{N_L(E_e) + N_R(E_e)}, \tag{4.14}$$

where $N_L(E_e)$ ($N_R(E_e)$) is the number of scattered beam electrons or positrons, with energy E_e and opposite (same) helicity configuration of laser photon and beam particle. The longitudinal polarization P_Z of the beam is obtained by the formula:

$$A(E_e) = \frac{\Delta S P_Z \Pi(E_e)}{2}, \tag{4.15}$$

where ΔS is the difference between the fully left- and right- polarized laser light helicity (ideally it is $1 - (-1) = 2$) and the analyzing power $\Pi(E_e)$ is the maximum obtainable asymmetry for the energy E_e (obtained when $\Delta S = 2$ and $P_Z = 1$). Magnetic chicanes convert the energy spectrum of the Compton-scattered particles into a spatial distribution, which is then measured by the polarimeter detectors.

Considering the case of a beam energy of 250 GeV and a laser photon energy of 2.3 eV, the Compton cross section versus the scattered electron energy behaves as shown in Fig. 4.10 (left). The graph clearly shows a large asymmetry near the Compton edge energy of ~ 25 GeV. The Compton edge corresponds to a maximum energy of the scattered photon and a minimum energy of the scattered electron and is obtained when the beam particle is back-scattered in the center-of-mass frame. As shown in Fig. 4.10 (right), the Compton edge energy hardly depends on the beam energy.

The motivations for choosing Compton polarimetry are summarized in [166]:

- Compton scattering is perfectly described by QED and the theoretical uncertainties on the radiative corrections are less than 0.1% [218];

- detector backgrounds are easy to measure and correct for using "laser off" pulses;

- the use of magnetic spectrometers allows the isolation of the Compton-scattered beam particles from the background;

- polarimetry data can be taken parasitic to physics data;

- Compton polarimetry allows high statistical precision on a short time scale, since the scattering rate is high (sub-1% precision in one minute is feasible);

- the uncertainty on the polarization of the laser is very low (0.1%);

- the laser helicity can be selected on a pulse-by-pulse basis.

The polarimeters are situated within dedicated magnetic chicanes of about 70 m length. Both chicanes, for the upstream and the downstream polarimeters, are designed to spread the spectrum of the Compton-scattered beam particles horizontally over about 20 cm for all beam energies.

4.2.2 Upstream Polarimeter

As already mentioned, the upstream Compton polarimeter is located at the beginning of the BDS, roughly 1800 m before the IP. In this position it benefits from clean beam conditions and low backgrounds. Fig. 4.11 depicts the planned configuration of the magnetic chicane. The first two dipoles displace the beam horizontally. Between the second and the third magnet the Compton interaction point is situated, where the polarized laser is shot onto the particle bunches of the beam. In order to determine the beam polarization the laser helicity is flipped between $+1$ and -1. From the asymmetry in the energy spectrum of the Compton-scattered particles the polarization of the beam is derived (cf. Eq. 4.14). The pulse structure of the laser is the same as the one of the beam, to ensure measurements of each bunch. This allows the monitoring of time-dependent effects on the polarization with high precision. Behind the Compton interaction point two magnets bend the displaced beam back to its nominal trajectory towards the IP, while the Compton-scattered beam particles are deflected out of the beam line. The same two magnets (at the end of the chicane) also convert the energy spectrum of the scattered beam particles into a spatial distribution, which is measured in a Cherenkov detector.

The Compton interaction point moves laterally with the beam energy, as shown schematically in Fig. 4.11, for beam energies of 250 GeV and 45.6 GeV. Therefore, the laser is mounted on a movable platform adjusted according to the beam energy. The maximum dispersion of 12 cm is obtained at the Z-pole, while for a beam energy of 250 GeV it reduces to 2 cm.

The beam direction at the Compton interaction point must be the same as at the IP, both in the vertical and horizontal direction, within a tolerance of $\sim 50\,\mu$rad.
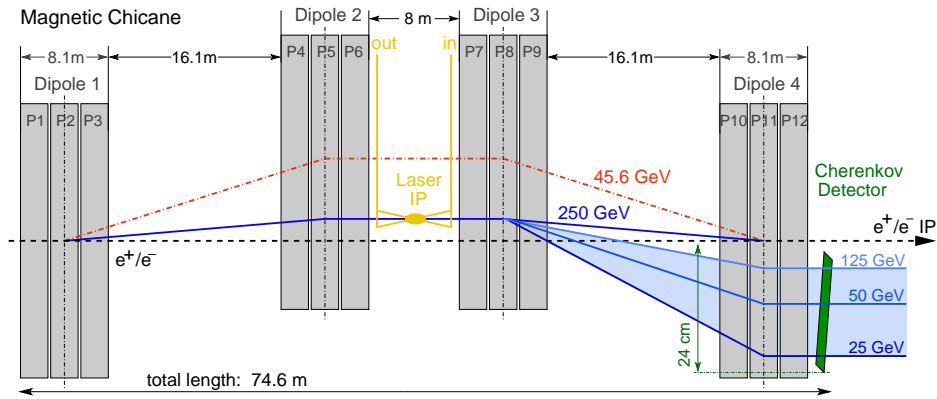
Figure 4.11: *Schematic drawing of the upstream polarimeter chicane. From [166].*
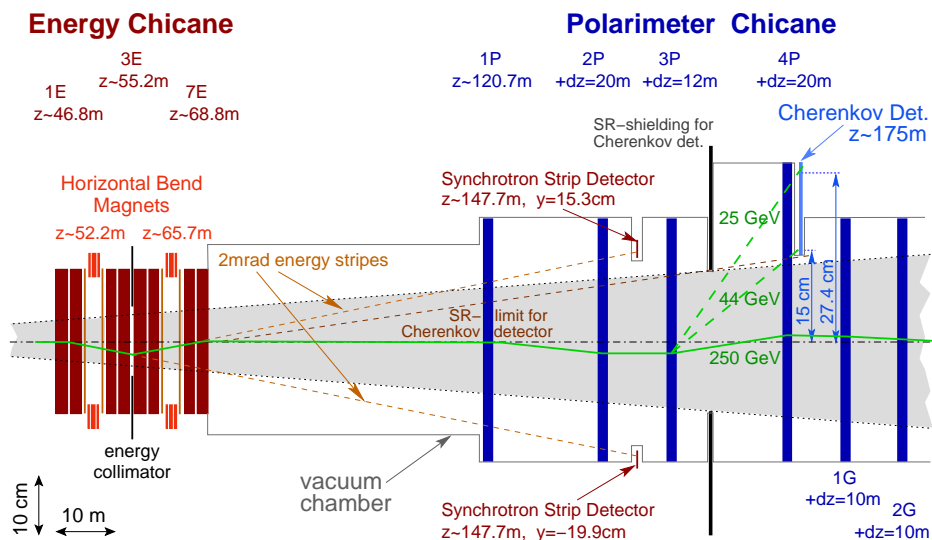

Figure 4.12: *Schematic drawing of a part of the extraction line with the downstream energy spectrometer and the downstream polarimeter. From [166].*

4.2.3 Downstream Polarimeter

An illustration of the downstream chicane is shown in Fig. 4.12. The gray cone around the beam pipe indicates the area which is disfavored for the polarimeter detector, due to the synchrotron radiation fan from the IP. In order to avoid this area, the downstream dipole magnets are larger and have much higher fields than those of the upstream chicane. Magnets 3P and 4P are operated at higher fields, compared to magnets 1P and 2P, in order to bend the scattered electrons further from the main beam axis.

Due to the larger background, the laser for the downstream polarimeter requires high pulse energies. Three 5 Hz laser systems are used to generate Compton collisions for three out of 2800 bunches in a train. The polarimeter is operated both with and without collisions, to test depolarization effects.

4.2.4 Polarimeter Detectors

Cherenkov detectors for the polarimeters are under study. In Fig. 4.13 (right) one possible design option is shown, where the Cherenkov detector consists of an array of about
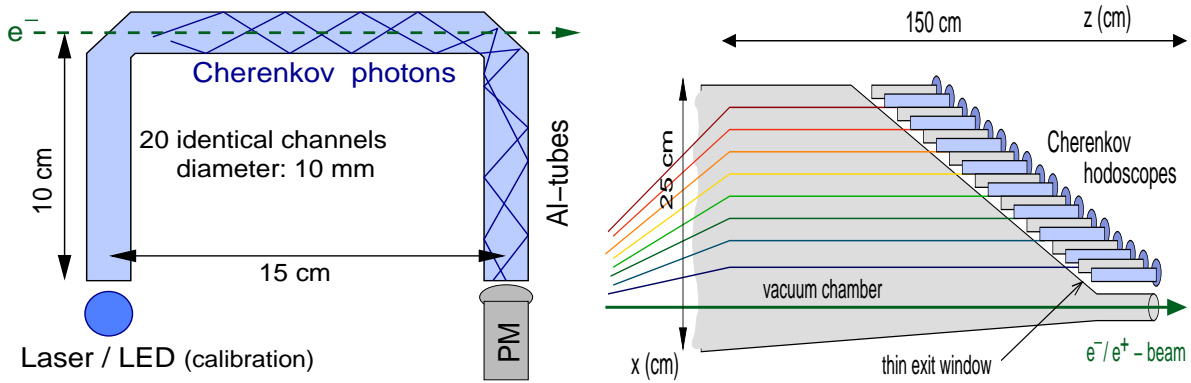
Figure 4.13: *Schematic drawing of a single gas tube (left) and the complete hodoscope array covering the tapered exit window (right) as foreseen for the Cherenkov detectors of both polarimeters. From [166].*

20 gas-filled aluminum tubes. The Compton-scattered particles radiate Cherenkov light while traversing the base of the U-shaped tubes. The light is detected by a photodetector mounted on top of one leg of the tube (indicated with PM in the figure). A longitudinal cross section of one channel is shown in Fig. 4.13 (left). The tubes are filled with perfluorobutane (C_4F_{10}), which was chosen due to its high Cherenkov threshold of 10 MeV for relativistic electrons to avoid radiation from lower-energetic particles. The free leg of the tubes is occupied by a calibration light source (e.g. LED light). The particular U-shaped design allows to place the photodetectors and the foreseen calibration system out of the beam plane reducing the risk of beam induced background radiation.

The upstream polarimeter allows to monitor the polarization on a short time-scale and to obtain a good statistical precision. It offers the possibility to resolve intra-train polarization variations and time-dependent effects. The downstream polarimeter needs a longer time to reach the same statistical precision as the upstream polarimeter, since the downstream laser has a much lower repetition rate.

While the statistical precision of the Compton polarimeters is not an issue, large systematic uncertainties are expected to come from the analyzing power calibration and the detector linearity. Both effects lead to uncertainties in the range of 0.1% to 0.2% [219]. Including these systematic uncertainties it is expected that a final precision of $\Delta P/P = 0.25\%$ can be achieved.

4.3 The Luminosity-Weighted Polarization

In order to deduce the polarization at the IP, depolarization effects between the polarimeter locations and the IP have to be known with high precision.

The main depolarization effects are expected to occur at the IP, due to beam-beam interactions during the bunch crossing. A summary of the topic can be found in [220].

The main sources of depolarization effects during beam-beam interactions are the spin precession and the spin-flip, which increases at higher energies. At the ILC the spin precession is the dominant effect. It is described by the Thomas-Bargman-Michel-

Telegdi (T-BMT) equation [221]:

$$\frac{d\vec{S}}{dt} = -\frac{e}{m\gamma}[(\gamma a + 1)\vec{B}_T + (a+1)\vec{B}_L - \gamma(a + \frac{1}{\gamma+1})\beta\vec{e}_v \times \frac{\vec{E}}{c}] \times \vec{S}, \qquad (4.16)$$

where a is the anomalous magnetic moment of the electron given by the higher-order corrections to the $ee\gamma$ vertex, $\vec{E}$ and $\vec{B}$ are the electric and magnetic fields, e and m are the electron charge and mass and $\vec{S}$ is the spin vector.

Additional depolarization at the IP might happen due to coherent and incoherent pair production. The coherent process consists of the interaction of the beamstrahlung photons with the collective electromagnetic field of the opposite beam, while the incoherent pairs arise from the interaction of both real or virtual photons from each beam with individual particles of the other beam. For center of mass energies up to $1\,\text{TeV}$ the coherent production process is negligible compared to the incoherent one [222].

The beam-beam effects have been implemented both in Guinea Pig++ and CAIN, showing good agreement [223]. The ILC is predicted to display a depolarization of about 0.2% during each bunch crossing. Theoretical work is still ongoing in order to improve the description of beam-beam effects, taking into account higher order effects and reducing theoretical assumptions [224].

Depolarization might also happen in the BDS, due to ground motion-induced misalignments of its lattice elements [225]. For random misalignments of BDS elements with a variance of $5\,\mu\text{m}$ from the true alignment, the mean helicity of the beam decreases by around 0.1%, while the helicity distribution width increases.

The combined effects of both BDS and IP depolarization require the usage of a downstream polarimeter in addition to the upstream measurement, in order to provide independent information on the polarization state after the physics collisions.

An important cross check to the measurements of the polarimeters and to the theoretical calculations of the depolarization can be obtained measuring the polarization directly from the collision data. There are several processes at the ILC whose polarization structure is well known and that might be used in order to measure the luminosity-weighted polarization at the IP, providing the polarimeters with an absolute scale calibration. In order to be competitive with the precision of 0.25% of the polarimeters, an uncertainty on the scale calibration of at least $\sim 0.2\%$ is desired. This topic is described in Chap. 5.

The measurement of the polarization from e^+e^- data is not meant as a replacement of the polarimeters. First of all it requires a high integrated luminosity, in order to reach good statistical precision and any monitoring of the polarization on short time scales requires both polarimeters. Moreover, all methods based on e^+e^- data make some assumptions that need to be checked using the polarimeters (Chap. 5). For the small errors envisaged for measurements at the ILC the complementarity between the polarimeters, the measurement of the luminosity-weighted polarization from e^+e^- data and the simulation studies of depolarization effects, as well as cross checks between different methods are mandatory.

5 Measurement of Triple Gauge Couplings and Polarization

This chapter presents a combined measurement of longitudinal beam polarization and TGCs, that occur in the vertices $WW\gamma$ and WWZ. The motivation for a precise measurement of the TGCs was given in Chap. 2, while the importance of a precise knowledge of the luminosity-weighted beam polarization was explained in Chap. 4. In the following it will be shown how semileptonic decays of the W-pairs can be exploited, in order to combine the two measurements in a simultaneous fit. Two techniques to measure the polarization alone are also compared. In order to obtain reliable estimates of the achievable precision, the study is completed with a realistic evaluation of the main sources of systematics expected at the ILC.

The analysis relies on Monte Carlo events fully simulated using the ILD detector model (Sec. 3.4.2) and includes the complete SM background. A center of mass energy of $500\,\text{GeV}$ and an 80% longitudinally-polarized electron beam are assumed and two options are considered for the longitudinal polarization of the positron beam: a high polarization of 60% and a low polarization of 30%. The final results are reported for an integrated luminosity of $500\,\text{fb}^{-1}$, but propagations of the uncertainties at different luminosities are also shown.

5.1 W-pair Production and Polarization

The results obtained at LEP show that the W-pair production is an excellent channel for the measurement of the TGCs (Sec. 2.9). The total cross section for this process is strongly sensitive to the polarization, as shown in Fig. 5.1. Hence, it is also a perfect candidate for the measurement of the luminosity-weighted polarization. In addition, the large cross section has statistical benefits.

In Fig. 5.2 the leading tree-level Feynman diagrams for the W^+W^- production are shown. In the two s-channel diagrams (center and right) the incoming e^+ and e^- annihilate to give the vector boson mediator. As explained in Chap. 4, in the SM only the recombination into a vector particle with $J = 1$ is possible, i.e. the beams have to carry opposite helicities. This constraint is no longer valid for the t-channel diagram (left). In this case the incoming leptons are directly coupled to the produced W-bosons. Since W-bosons can only couple to left-handed electrons and right-handed positrons, this channel is suppressed for the polarization configuration with right-handed electrons and left-handed positrons and also in the case of same helicity beams. The peak of the total cross section in Fig. 5.1, corresponding to left-handed electrons and right-handed positrons, is due to the t-channel enhancement for such polarizations.

The t- and the s-channel not only have a different dependence on the polarization, but also generate a different topology of the W-pair, since the t-channel production is more boosted in the forward region.
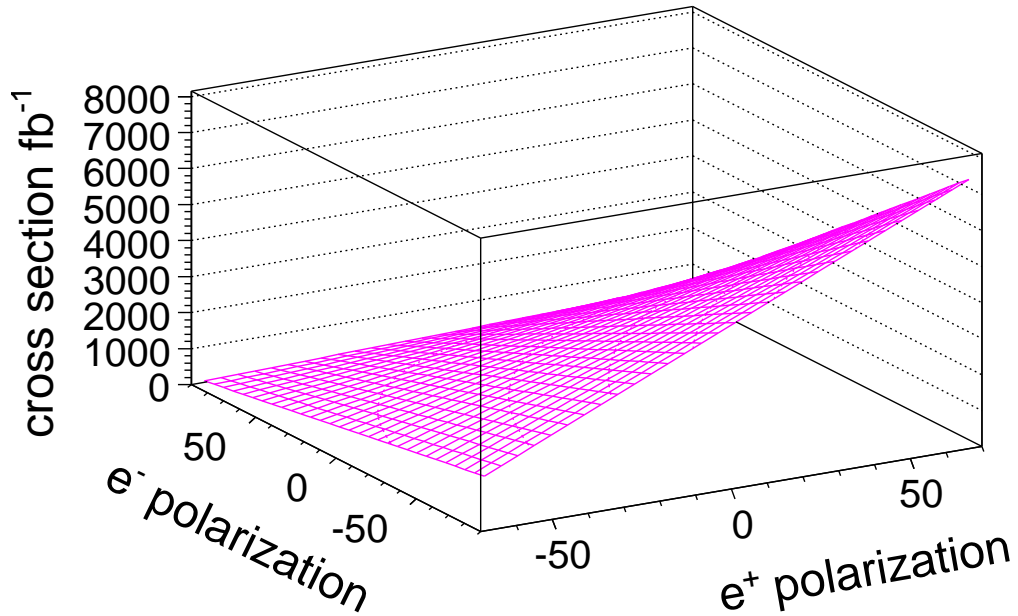
Figure 5.1: *Total cross section of the selected semi-semileptonic decay channels of the W-pairs (Sec. 5.2.2) as a function of the electron and positron beam polarizations, at $\sqrt{s} = 500\,GeV$.*
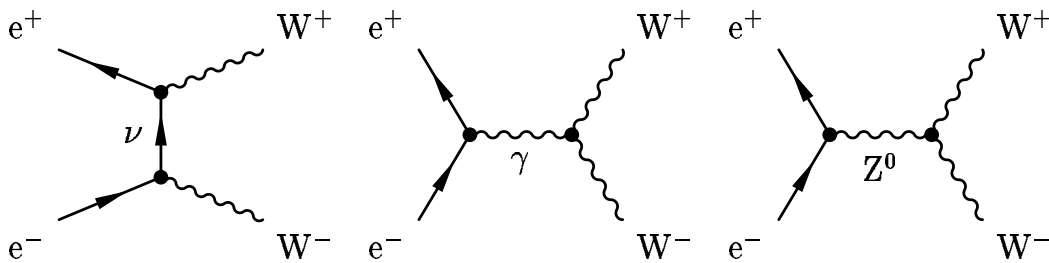

Figure 5.2: *Leading tree-level Feynman diagrams for the W^+W^- production. On the left the t-channel with ν exchange, in the center and on the right the two s-channels with γ or Z^0 exchange.*

5.2 Selection of W-pair Events

This section illustrates how Monte Carlo samples for different polarizations are created and describes in detail the selection applied in order to separate the signal from the background.

5.2.1 Polarization Configurations

The Monte Carlo events are generated for 100%-polarized beams. Events from different files, corresponding to different polarization configurations, need to be properly mixed in order to obtain realistic cases of partial polarizations P_{e^+} and P_{e^-}. The number of events generated with a polarization of $P(e^+, e^-) = (\pm 100\%, \pm 100\%)$ to be used is given by:

$$N_{\pm\pm}^{events} = \sigma_{\pm\pm} \cdot \mathcal{L} \cdot w_{\pm\pm}(P_{e^+}, P_{e^-}), \tag{5.1}$$

where $\sigma_{\pm\pm}$ is the cross section of the considered process, $\mathcal{L}$ is the desired luminosity and the necessary weight $w_{\pm\pm}(P_{e^+}, P_{e^-})$ is derived directly from the properties of the polarization:

$$P = P_R - P_L$$
$$P_R + P_L = 100. \tag{5.2}$$

Here, P is the beam polarization and P_R (P_L) is the percentage of right-handed (left-handed) events. For example, a +60% positron polarization is obtained mixing 80% events with right-handed positron beam with 20% events with left-handed positron beam. Analogously, -80% electron polarization equals 10% right-handed and 90% left-handed electron beam. Combining the two requests, to get +60% positron and -80% electron polarization, one needs:

$$weight_{++}(+60, -80) = 80\% \cdot 10\% = 0.08,$$
$$weight_{+-}(+60, -80) = 80\% \cdot 90\% = 0.72,$$
$$weight_{-+}(+60, -80) = 20\% \cdot 10\% = 0.02,$$
$$weight_{--}(+60, -80) = 20\% \cdot 90\% = 0.18. \tag{5.3}$$

This example can be generalized, obtaining the weight $w_{\pm\pm}(P_{e^+}, P_{e^-})$ for any other desired polarization set. It should be noticed that not all the four $\sigma_{\pm\pm}$ are necessarily non-null. For example, for all processes occurring exclusively via s-channel only events with $P(e^+, e^-) = (+100\%, -100\%)$ and $P(e^+, e^-) = (-100\%, +100\%)$ are available.

5.2.2 Selection

Due to the favorable reconstruction of the angular distributions only semileptonic decays (q$\bar{\text{q}}l\nu$) of the W-pair have been selected, where one W-boson decays either into an electron or a muon, and its associated neutrino, while the other decays into a quark-antiquark pair. The angular distribution of the W-pair is expressed by the $\cos\theta_W$ variable, where θ_W is the angle of the W^- with respect to the e^- beam axis. The charge of the lepton tags the charges of the two W-bosons. Since the W-pair is emitted back-to-back, one can always reconstruct the θ_W angle together with the W-boson invariant mass from the hadronically decaying W-boson, using the four-momenta of the two jets produced in the decay. The same information could be obtained, in principle, also from the leptonically decaying W-boson, using the reconstructed lepton four-momentum and the missing four-momentum due to the neutrino, but a lower precision would be achieved in this case (cf. Fig. 5.7).

The semileptonic decay in which the leptonically-decaying W-boson decays into a tau and the associated neutrino has been excluded, since this signal has a larger background and the determination of the charge of the lepton is less reliable, resulting from the possibility of the candidate tau being formed from tracks from the fragmentation of the quarks. Additionally, multiple neutrinos might be present in the final state due to the decay of the tau. This channel is labeled in the following as *tau-signal* and is considered as background.

The other two excluded decay channels of the W-pair are the fully leptonic decay ($l\nu l\nu$), in which each W-boson decays into a lepton and its associated neutrino, and the fully hadronic decay (q$\bar{\text{q}}$q$\bar{\text{q}}$), in which each W-boson decays into two quarks. The fully hadronic decay has not been selected, since the charge of the W-boson cannot be reconstructed with sufficient precision from the jets of the hadronic decay. Moreover, a combinatoric background is introduced, due to the different possible ways of combining the four jets of the decays into two W-bosons. The fully leptonic decay is excluded as well, due to the lower cross section and selection efficiency. The reconstruction of this channel is also disturbed by the presence of multiple neutrinos in the final state. The different features, which characterize the selection of the different decay channels of the W-pair, are fully described in the LEP literature, see e.g. [226].

The selection has been optimized for a Monte Carlo sample of $20\,\text{fb}^{-1}$ and the results obtained have been propagated to higher luminosities. The entire SM background has been taken into account. The complete four- and six-fermion, q$\bar{\text{q}}$, $\gamma\gamma$ and Z-Strahlung background is included, where the $\gamma\gamma$ processes are given by the interaction between two radiated or Beamstrahlung photons, while the Z-Strahlung events are produced by the scattering of a photon on a beam electron or positron. In the following these two backgrounds are grouped together under the label $\gamma\gamma$.

Not all processes were simulated with sufficient statistics. During the massive ILD Monte Carlo production smaller luminosities were simulated for those processes with a very high cross section and of relatively low importance for most of the physics analysis, most notably the $\gamma\gamma$-background. Therefore, the events for these processes need to be given a weight greater than 1 to compensate the low number of events available. However, the $\gamma\gamma$ is a minor and non-dangerous background for the selected final state and the need of a higher weight does not represent a significant statistical limitation.

Process	Events	%	Weight
Signal	107233	0.071	1.00
Tau-Signal	52926	0.035	1.00
q$\bar{\text{q}}$	390727	0.258	1.00
4 Fermions	431247	0.285	1.00
6 Fermions	20808	0.014	1.00
$\gamma\gamma$	1.50439e+08	99.338	179.98

Table 5.1: *Number of initial signal and background events before the selection. The numbers refer to a positron polarization of +30% and an electron polarization of -80%, at a luminosity of 20 fb^{-1}. The average weight applied to compensate for those processes, for which 20 fb^{-1} of statistics were not available, is also reported.*

Tab. 5.1 shows the initial amount of background and signal events, before any selection. The numbers refer to a positron polarization of +30% and an electron polarization of -80% for an integrated luminosity of 20 fb^{-1}. The same configuration was also chosen for all the figures and tables appearing in this section.

As a preselection of semileptonic W-pair decays, the following criteria, illustrated in Fig. 5.3, are applied:

- track multiplicity $\geq$ 10;

- center of mass energy $\sqrt{s} > 100$ GeV;

- total transverse momentum $P_T > 5$ GeV;

- total energy $E_{SUM} < 500$ GeV;

The first two requirements mainly constrain the $\gamma\gamma$ and the q$\bar{\text{q}}$ SM background, the third and fourth account for the expected missing momentum, due to the neutrino.

The DURHAM jet finder algorithm [192] is applied, forcing the event into three jets: one jet is associated to the lepton and two jets are generated by the quarks produced in the hadronic decay of the W-boson. The jet with the lowest number of particles is identified with the lepton. Clearly, it is not a jet in the physical sense of a compact cascade of particles, but as a distinct object identified using the jet finder algorithm. The lepton could have been isolated, in principle, also employing a specific lepton-finder software, but such an algorithm was not available in the ILCSoft framework at the time this analysis was developed. However, since the lepton tends to occupy a different spacial region, with respect to the jets from the hadronic decay, the jet finder identifies it easily as a separate object. This procedure results in the correct assignment and the proper charge reconstruction of the lepton in about 92% of the cases. An additional criterion is applied to the y_+ and y_- variables of the jet finder, where the logarithm of the y_+ (y_-) variable is accepted in the range [-12,-3] ([-9,-1.5]). The y variables and the accepted ranges are shown in Fig. 5.4.

The jet associated with the lepton is required to have at least one track with energy > 10 GeV and to be isolated from the other two jets. The separation is expressed by means of the following angular selection:
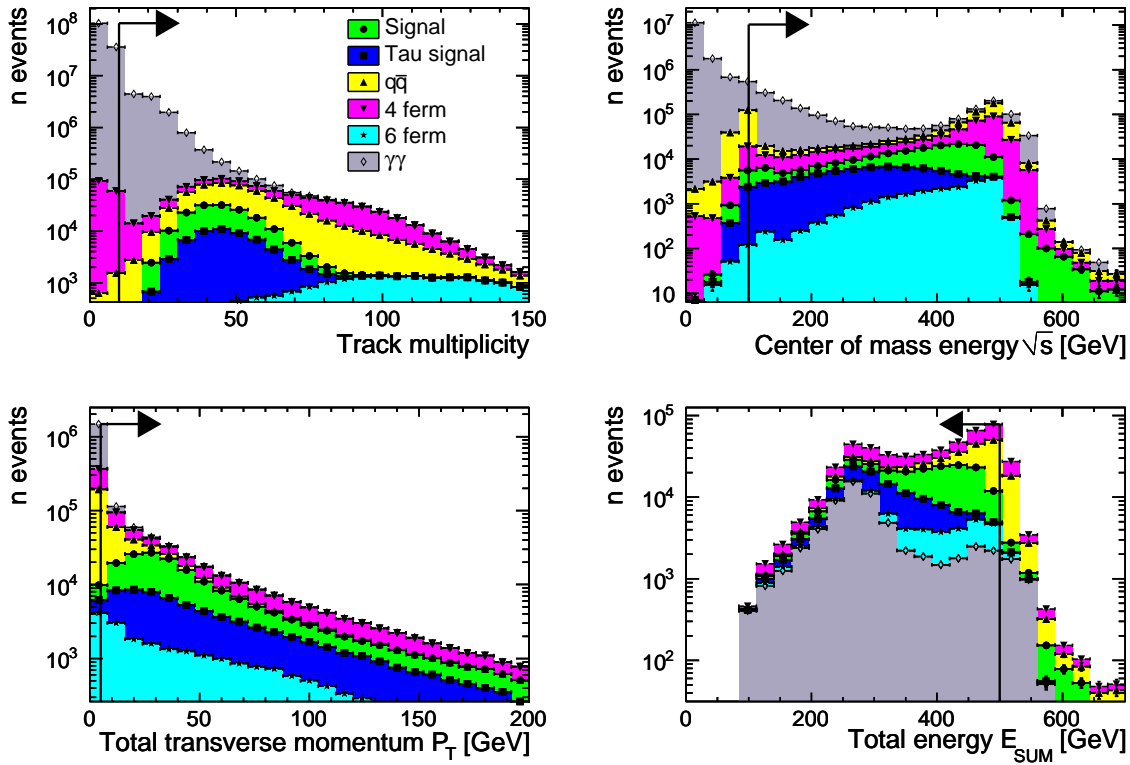
Figure 5.3: *Variables used in the preselection of W-pairs. The actual cut values are indicated by the lines and the accepted regions by the arrows. Top left: track multiplicity. Top right: center of mass energy $\sqrt{s}$. Bottom left: total transverse momentum P_T. Bottom right: total energy E_{SUM}.*
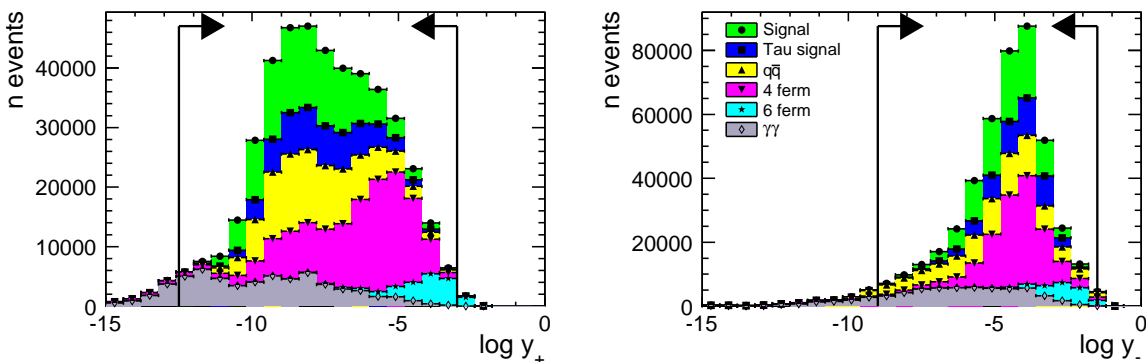

Figure 5.4: *Logarithm of the y_+ (left) and y_- (right) variables of the jet finder algorithm. The actual cut values are indicated by the lines and the accepted regions by the arrows.*
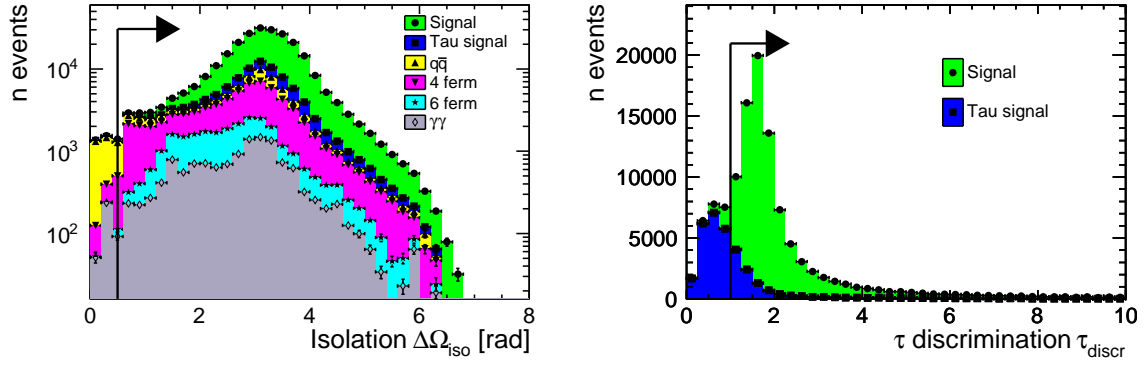
Figure 5.5: *Left: isolation of the jet associated to the lepton from the other two jets, produced in the hadronic decay of the W-boson. The isolation is expressed by means of the $\Delta\Omega_{iso}$ variable defined in Eq. 5.4. Right: discriminating variable τ_{discr} used to suppress the contribution of those W-pair semileptonic events, in which one W-boson decays into a tau and the associated neutrino. The definition of the variable is given in Eq. 5.5. The semileptonic W-boson decays into electrons and muons (signal) are shown in green, while those involving taus (tau-signal) are shown in blue. The discrimination is performed requiring $\tau_{discr} > 1$.*

$$(\phi_{\text{lep}} - \phi_{\text{had}}) < \pi \rightarrow \Delta\Omega_{iso} = \sqrt{(\theta_{\text{lep}} - \theta_{\text{had}})^2 + (\phi_{\text{lep}} - \phi_{\text{had}})^2} > 0.5,$$

$$(\phi_{\text{lep}} - \phi_{\text{had}}) \geq \pi \rightarrow \Delta\Omega_{iso} = \sqrt{(\theta_{\text{lep}} - \theta_{\text{had}})^2 + (2\pi - \mid \phi_{\text{lep}} - \phi_{\text{had}} \mid)^2} > 0.5. \quad (5.4)$$

where θ_{lep} and ϕ_{lep} are the polar and the azimuthal angles of the jet associated with the lepton, while θ_{had} and ϕ_{had} are the polar and the azimuthal angles of one of the two jets produced in the hadronic decay of the W-boson, respectively (the same request is repeated for both jets). The isolation variable $\Delta\Omega_{iso}$ is shown in Fig. 5.5 (left).

The suppression of the tau-signal is performed using the following discriminating variable:

$$\tau_{\text{discr}} = \left(\frac{2E_{\text{lep}}}{\sqrt{s}}\right)^2 + \left(\frac{m_W^{\text{lep}}}{m_W^{\text{true}}}\right)^2 < 1, \quad (5.5)$$

where E_{lep} is the reconstructed lepton energy, m_W^{lep} is the W-boson mass as reconstructed from the leptonic decay and m_W^{true} is the nominal mass of the W-boson. Candidates for which $\tau_{\text{discr}} < 1$ are considered tau-signal events and rejected. Figure 5.5 (right) shows the discriminating variable.

In order to better reconstruct the missing momentum and consequently the W-boson leptonic decay, a simple calculation is done to correct for ISR photons lost along the beam pipe without being measured by the forward calorimeters. The four-momentum conservation leads to the following equations containing the missing momentum of the neutrino, the missing momentum of the lost ISR photons and the total measured momentum:

$$P_x + P_{\nu,x} = 0,$$
$$P_y + P_{\nu,y} = 0,$$
$$P_z + P_{\nu,z} + P_\gamma = 0,$$
$$E_\nu = \sqrt{P_{\nu,x}^2 + P_{\nu,y}^2 + P_{\nu,z}^2},$$
$$E_\gamma^2 = P_\gamma^2,$$
$$E + E_\nu + E_\gamma = 500, \tag{5.6}$$

where P_x, P_y, P_z are the components of the total measured momentum, E is the total measured energy, P_ν and E_ν are the neutrino missing momentum and energy, P_γ and E_γ are the photon momentum and energy. The indices x and y indicate the transverse coordinates (perpendicular to the beam axis), while z denotes the direction along the beam axis. The photon is assumed to have negligible transverse momentum components (x, y), since it is assumed to be lost in the beam pipe.

These equations give two possible solutions for the photon energy:

$$E_\gamma = \frac{(500 - E)^2 - P_x^2 - P_y^2 - P_z^2}{1000 - 2E - 2P_z},$$
$$E_\gamma = \frac{(500 - E)^2 - P_x^2 - P_y^2 - P_z^2}{1000 - 2E + 2P_z}, \tag{5.7}$$

and, therefore, two different momenta for the neutrino. For each set of solutions the W-boson invariant mass is calculated from the invariant mass of the lepton and the reconstructed missing energy of the neutrino. The solution giving a W-boson invariant mass closer to its nominal value is chosen. The benefit of the ISR correction on the reconstruction of m_W^{lep} is shown in Fig. 5.6 (right).

As a consequence of the ISR correction, the invariant mass of the jet associated with the lepton and the missing momentum might be artificially shifted closer to the nominal mass of the W-boson for some backgrounds. This might cause a selection requirement on the measured m_W^{lep} to be less effective in terms of background rejection. In order to minimize this side effect, m_W^{lep} is accepted only in the range $[20,250]$ GeV before applying the ISR correction, as shown in Fig. 5.6.

After the ISR correction, both m_W^{had} (the invariant mass of the products of the W-boson hadronic decay) and m_W^{lep} are required to be in the range $[40,120]$ GeV. Both W-boson invariant masses, m_W^{had} and m_W^{lep}, together with their resolutions are shown in Fig. 5.7.

Finally, the angular requirement $\cos\theta_W > -0.95$ is applied, as shown in Fig. 5.8 (left). The resolution obtained in the reconstruction of $\cos\theta_W$ is shown in Fig. 5.8 (right).

The details of the selection are summarized in Tab. 5.2. The full Monte Carlo sample is sorted in the six groups defined above: signal, tau-signal, q$\bar{\text{q}}$, four- and six-fermions and $\gamma\gamma$. The final efficiency of the selection is about 67%. The selected events include 10% tau-signal events and only 6% of other backgrounds.
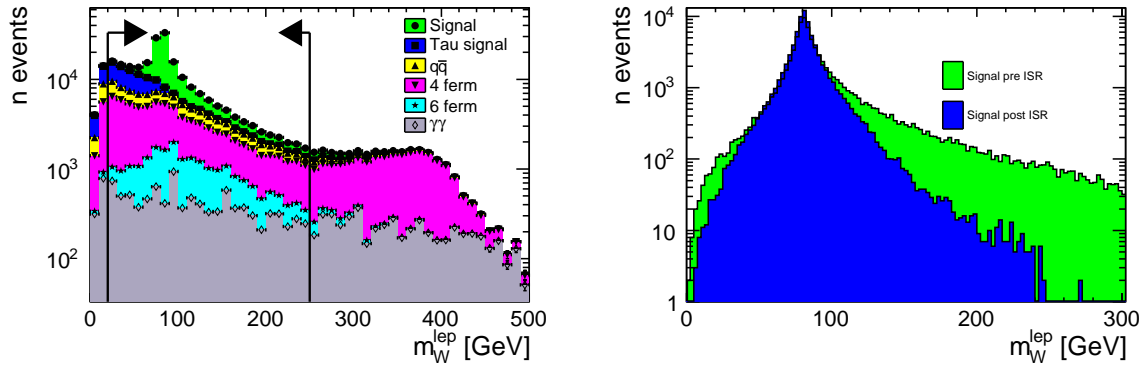
Figure 5.6: *Left: the selection criteria on the invariant mass of the leptonically-decaying W-boson (m_W^{lep}) is applied before the ISR correction. The invariant mass m_W^{lep} is accepted in the range [20,250] GeV. Right: measured m_W^{lep} distribution before (green) and after (blue) the ISR correction.*
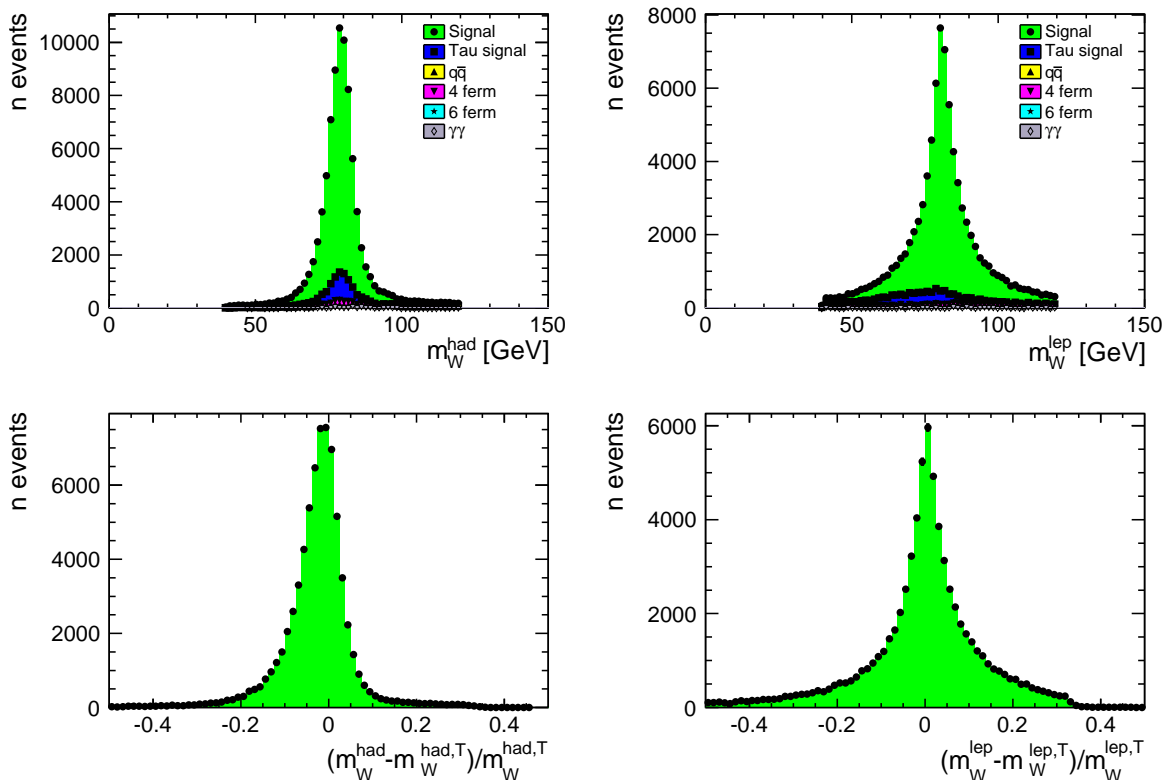

Figure 5.7: *Mass of the W-boson as reconstructed from the hadronic decay m_W^{had} (top left) and from the leptonic decay m_W^{lep} (top right). The two bottom distributions show the respective resolutions with $m_W^{\text{had,T}}$ and $m_W^{\text{lep,T}}$ indicating the true invariant masses from Monte Carlo simulations.*

Cut	Signal	Tau-Signal	$q\bar{q}$	4 Fermions	6 Fermions	$\gamma\gamma$
Initial events	107233	52926	390727	431247	20808	1.50439e+08
n tracks > 10	107229	52925	389290	290297	20663	1.503306e+07
$\sqrt{s} > 100\,$GeV	105050	51384	255396	275494	20532	1.14302e+06
$P_T > 5\,$GeV	103681	50539	109917	139264	18185	64510.6
$E_{SUM} < 500\,$GeV	102259	50502	87326	126275	17604	61484.6
y cuts	101882	50394	84292	122163	15714	43260.6
lepton	84443	39166	31720	76241	13415	1623.9
$20 < m_W^{\mathrm{lep}} < 250$	82149	31951	26361	52364	12955	9712.53
tau selection	79423	11226	16236	30726	9943	7061.11
charge lepton	78830	10123	8720	21934	6636	6775.07
isolation	78730	10050	6016	21569	6625	6472.16
$40 < m_W^{\mathrm{lep}} < 120$	75204	8936	4308	14100	4351	3890.29
$40 < m_W^{\mathrm{had}} < 120$	71776	8422	972	2915	267	2862.12
$\cos\theta_W > -0.95$	71611	8287	875	2548	256	1188.53
Final events	71611	8287	875	2548	256	1188.53
Efficiency	$(66.78 \pm 0.14)\%$	$(15.66 \pm 0.16)\%$	$(0.2240 \pm 0.0076)\%$	$(0.591 \pm 0.011)\%$	$(1.230 \pm 0.076)\%$	$(7.90 \pm 0.23)\cdot10^{-4}\%$

Table 5.2: *Detailed cut flow of the selection. The full Monte Carlo sample is sorted in six groups: signal, tau-signal, $q\bar{q}$, four- and six-fermion SM background and $\gamma\gamma$. The event numbers refer to a positron polarization of +30% and an electron polarization of -80% for an integrated luminosity of 20 fb^{-1}.*
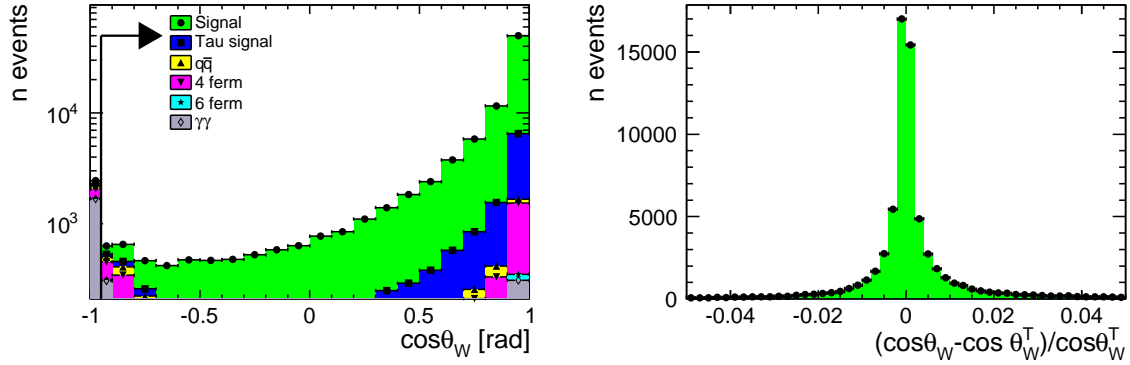
Figure 5.8: *Left: the angular distribution $\cos\theta_W$, with the applied requirement $\cos\theta_W > \text{-0.95}$. Right: resolution of $\cos\theta_W$, with $\cos\theta_W^{\mathrm{T}}$ indicating the true value from Monte Carlo simulations.*

5.3 Measurement of the Polarization

In this section two techniques to measure the beam polarization are considered, while the additional measurement of the TGCs is introduced in the next section. The systematic uncertainty that anomalous values of the TGCs would introduce on the measurement of the polarization is calculated in Sec. 5.4.2.

5.3.1 The Modified Blondel Scheme

The first method considered is a modified Blondel scheme [227]. The original Blondel scheme was intended for processes of electron positron annihilation into two fermions and proposed to collect some data also with unpolarized beams. Contrary to this, a similar method is here applied to the W-pair production, which has also a t-channel component and, in addition, the altered method does not require data collection with unpolarized beams. Hence, it is called *modified* Blondel scheme.

Theory

This technique requires to spend some luminosity on all the four possible combinations of the polarization of the beams: $++$, $+-$, $-+$ and $--$, where the first and the second sign are respectively the sign of the polarization of the positron and of the electron beam. Moreover, the absolute polarization values of the left- and right-handed degrees of beam polarization are required to be equal. Polarization measurements with dedicated polarimeters are needed to measure possible deviations. The beam polarization is then obtained by measuring the total cross section for each helicity configuration [228]:

$$\mid P_{e^\pm} \mid = \sqrt{\frac{(\sigma_{-+} + \sigma_{+-} - \sigma_{--} - \sigma_{++})(\pm\sigma_{-+} \mp \sigma_{+-} + \sigma_{--} - \sigma_{++})}{(\sigma_{-+} + \sigma_{+-} + \sigma_{--} + \sigma_{++})(\pm\sigma_{-+} \mp \sigma_{+-} - \sigma_{--} + \sigma_{++})}}, \quad (5.8)$$

where σ_{+-} is the total cross section measured for right-handed positron beam and left-handed electron beam (σ_{--}, σ_{+-} and σ_{-+} are defined analogously) and P_{e^+} (P_{e^-}) is the resulting positron (electron) beam polarization.

Application

The total cross section is given by:

$$\sigma = \frac{N_{sig}}{\mathcal{L} \cdot \varepsilon_{sig}}, \tag{5.9}$$

where N_{sig} is the number of selected signal events, $\mathcal{L}$ is the luminosity and ε_{sig} is the signal selection efficiency. The selection efficiency is defined, as usual, as the percentage of signal events satisfying the selection criteria.

The number of selected signal events, N_{sig}, is obtained from the number of selected events N_{tot}, rescaled in order to account for a residual background contamination. First, the purity $P_{sig+\tau}$ is defined, which expresses the fraction of signal and tau-signal events in the total amount of selected events:

$$P_{sig+\tau} = \frac{N_{sig+\tau}}{N_{tot}}. \tag{5.10}$$

The number of signal and tau-signal events $N_{sig+\tau}$ is, consequently, calculated as:

$$N_{sig+\tau} = N_{tot} \cdot P_{sig+\tau}. \tag{5.11}$$

Finally, N_{sig} is obtained from $N_{sig+\tau}$:

$$N_{sig} = \frac{N_{sig+\tau}}{1 + \frac{BR_{\tau} \cdot \varepsilon_{\tau}}{BR_{sig} \cdot \varepsilon_{sig}}}, \tag{5.12}$$

where BR_{τ} (BR_{sig}) is the known branching ratio of a W-boson decaying into a tau lepton and its associated neutrino (towards a muon or an electron and associated neutrino). The efficiency ε_{τ} is the percentage of tau-signal events satisfying the selection criteria. In the error propagation the experimental uncertainties on the branching ratios are assumed to be negligible with respect to those on the efficiencies.

The four cross sections σ_{+-}, σ_{--}, σ_{+-} and σ_{-+} have been measured using Monte Carlo samples for an integrated luminosity of $20\,\text{fb}^{-1}$. Equation 5.8 has then been applied and the statistical uncertainty on the measured polarizations has been calculated. The error has been propagated towards higher luminosities, as shown in Fig. 5.9 for both polarization options. The distribution on the left (right) shows the results obtained with 80% electron and 30% (60%) positron polarization. The total luminosity is assumed to be shared equally between the four polarization sets. For an integrated luminosity of $500\,\text{fb}^{-1}$ and a high polarization of the positron beam the precision obtained on the electron and positron polarizations is $\sim 0.1\%$ and $\sim 0.22\%$, respectively. In case of a 30%-polarized positron beam, precisions of the order of 0.5% on the positron polarization and 0.2% on the electron polarization are obtained, respectively. Considering the goal of a precision of the order of 0.2% on the polarization, the low positron polarization option appears strongly unfavoured.
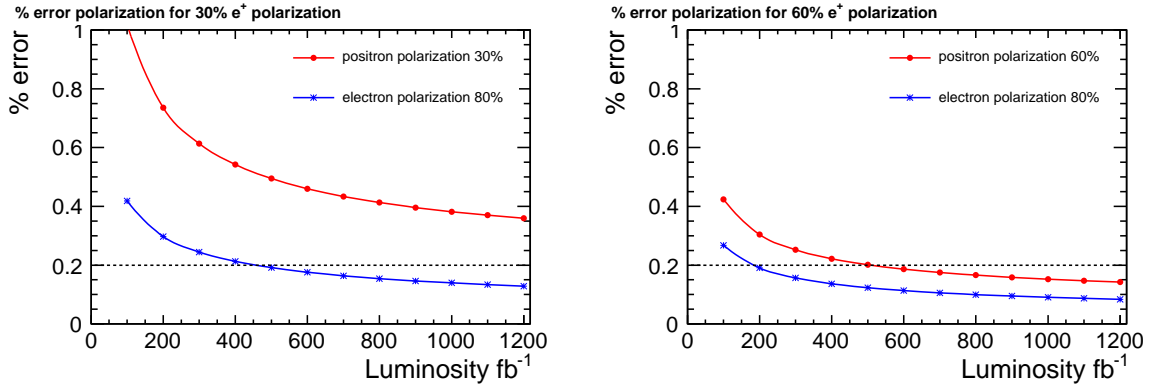
Figure 5.9: *Statistical precision on the polarization obtained with the modified Blondel scheme. Left: results for the low polarization case, with 80% electron beam and 30% positron beam polarization. Right: results for the 60% positron polarization option. The red (blue) curves show the percentage error on the positron (electron) polarization as a function of the total luminosity, which is assumed to be shared equally between the four polarization sets. The horizontal line indicates the optimum precision of 0.2%.*

5.3.2 The Angular Fit

The Blondel scheme requires high luminosities in order to obtain small uncertainties on the polarization. This motivates the quest of alternative techniques. In this section another method is described, denominated *angular fit*, which relies on the $\cos\theta_W$ observable (defined in Sec. 5.2.2). In this way, also the additional information relative to the W-pair production angle is exploited in the polarization measurement, while the Blondel technique uses exclusively the total cross section information. The total cross section still enters the measurement via the normalization of the $\cos\theta_W$ distributions.

The angular fit method is based on the creation of Monte Carlo templates of the $\cos\theta_W$ distribution for several sets of the beam polarization. The $\cos\theta_W$ distributions of the data are fitted to the templates in order to measure the polarization. The creation of the templates and the structure of the fit are described in the following.

Templates of $\cos\theta_W$

The Monte Carlo files are mixed (Sec. 5.2.1) in order to create 99 samples with different polarizations, scanning the polarization of the electron (positron) in the interval $[-90\%, +90\%]$ ($[-70\%, +70\%]$). The selection (Sec. 5.2.2) is applied to each sample, obtaining 99 $\cos\theta_W$ distributions, one for each polarization set. Each distribution is divided into 20 bins, which cover the full range of variability of $\cos\theta_W$ $[-0.95,+1]$. For each bin the three-dimensional distribution of the bin content vs. the polarization of electron and positron is created. These distributions are filled with 99 points, corresponding to the 99 polarization sets considered. The results for two of the 20 $\cos\theta_W$ bins are illustrated in Fig. 5.10 (left). The distributions reflect clearly the total cross section dependency on the polarization of the beams (cf. Fig. 5.1). They have been created using Monte Carlo samples corresponding to an integrated luminosity of $20\,\mathrm{fb}^{-1}$ for each polarization set.
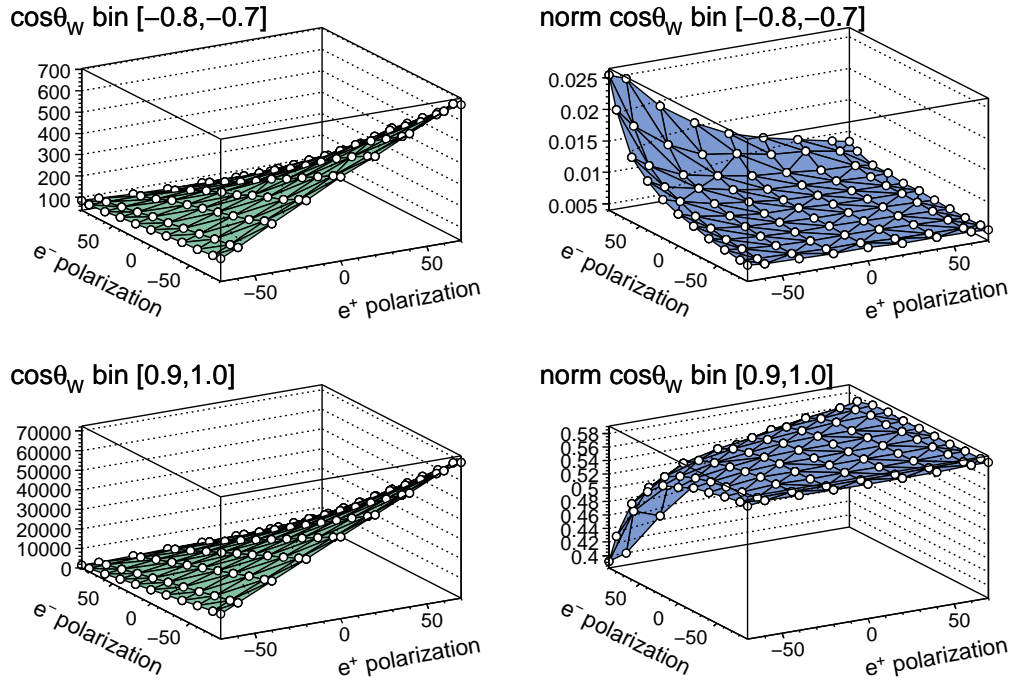
Figure 5.10: *Content of the bins of the $\cos\theta_W$ distribution as a function of the positron and electron beam polarization. The distributions on the right are created using normalized $\cos\theta_W$ distributions. The upper (lower) distributions refer to the bin covering the $\cos\theta_W$ range [−0.8,−0.7] ([0.9,1.0]), a region where the s-channel (t-channel) production prevails.*

The same procedure has been repeated using normalized $\cos\theta_W$ distributions. The normalization cancels the contribution from the total cross section, leaving only the information relative to the angle of production of the W-pair, which is the additional observable introduced with respect to the Blondel scheme. The results are shown in Fig. 5.10 (right).

Different topologies and a different dependency on the polarization are expected, depending on the production diagram of the W-pair (Sec. 5.1). This is confirmed by comparing the two diagrams generated from normalized $\cos\theta_W$ distributions. The upper (lower) distribution in Fig. 5.10 (right) refers to the bin covering the $\cos\theta_W$ range [−0.8,−0.7] ([0.9,1.0]), a region where the s-channel (t-channel) production prevails. The expected t-channel suppression for left-handed positrons and right-handed electrons is clearly visible in the lower distribution, while the upper distribution shows the clear relative enhancement of the s-channel contribution for this polarization combination.

For the purpose of measuring the polarization the distributions for non-normalized $\cos\theta_W$ distributions are used, since they contain the additional information of the total cross section. In order to find a continuous function of the beam polarization, they are fitted with 2D quadratic functions. An illustrative example of a fitted surface is shown in Fig. 5.11 (left). The 20 2D-functions obtained for the 20 $\cos\theta_W$ bins are called *templates* in the following.

It should be noted that the background events surviving the selection have not been subtracted, when creating the distributions in Fig. 5.10, since the smoothness of the
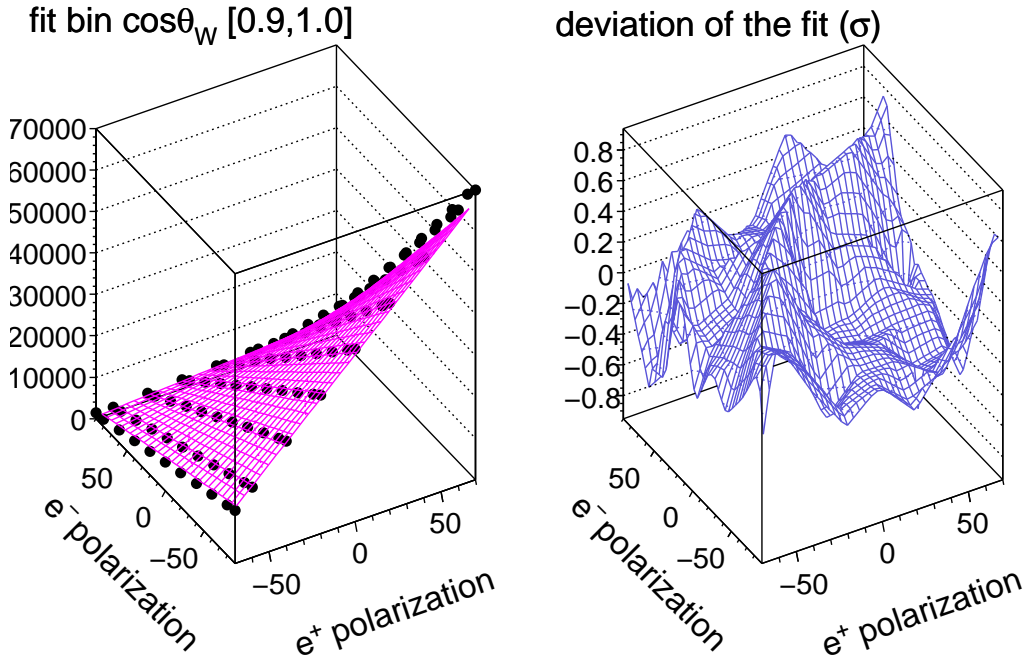
Figure 5.11: *Left: content of the bin of the $\cos\theta_W$ distribution, covering the range [0.9,1.0], as a function of the polarization of the positron and electron beam. The two-dimensional function fitting the distribution is also drawn. Right: deviations of the fitting surface from the discrete points, expressed in number of sigmas.*

distribution is not spoiled by the presence of the residual background. This benefits the error propagation in the polarization measurement (details of the fit procedure are given in the following). The smoothness of the distributions is confirmed by the distribution on the right-hand side in Fig. 5.11, which shows the deviations of one of the template functions (namely for the $\cos\theta_W$ bin [0.9,1.0]) from the discrete points it fits. The residuals are always below one sigma. Statistically, deviations up to three sigma would be expected. The fact that the deviations are so remarkably small is due to statistical independence reasons. The discrete points of the distributions come from the same Monte Carlo sample. For obvious CPU time convenience a new Monte Carlo sample was not simulated for each of the 99 polarization configurations considered. The same Monte Carlo files for 100% polarized beams have been mixed repeatedly to create the 99 different polarization sets. This does not introduce a bias, since there is no error associated to the Monte Carlo templates in the polarization extraction fit. The statistical error of the Monte Carlo templates can be easily reduced with respect to the error on the data in a real experiment, producing Monte Carlo samples for higher luminosities. What is relevant, is the statistical independence of the Monte Carlo sample taking the role of data. This is assured by random smearings, as explained in the following.

Performance of the Angular Fit

For a direct comparison with the modified Blondel scheme, the angular fit was first applied to the same data set and making the same assumption, that while reversing
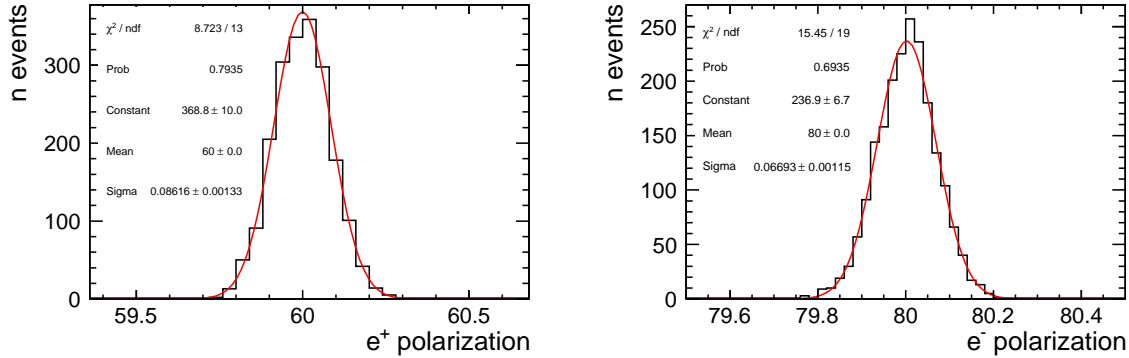
Figure 5.12: *Distributions of the fitted parameters when applying the angular fit with two free parameters, the absolute values of the electron and the positron beam polarizations. The left (right) distribution shows the distribution of the fitted positron (electron) polarization for the option of 60% positron and 80% electron polarization and for an integrated luminosity of 500 fb^{-1}. The fit statistical errors on the measured polarizations are given by the widths of the fitted Gaussians.*

the sign of the polarization the absolute value remains the same. The data set consists again of four samples for the $++$, $+-$, $-+$ and $--$ helicity combinations. The total integrated luminosity is shared equally between the four samples. At the end of this section the performance of the fit is also investigated for different conditions.

The $\cos\theta_W$ distributions for the data are obtained directly from the templates. The content of each bin of the distributions is derived from the template specific for that bin, evaluating the function for the desired polarization of the beams. In order to assure statistical independence a Poissonian random smearing is applied to the value obtained. As already mentioned, the original templates have been created for an integrated luminosity of $20\,\mathrm{fb}^{-1}$, but the results are propagated to higher luminosities changing the normalization of the template functions. The data distributions are fitted to the templates using MINUIT [229] and a χ^2 minimization. The χ^2 function is defined as:

$$\chi^2 = \sum_{j=1}^{4} \sum_{i=1}^{20} \frac{(N_{i,j}^{DATA} - f_i(\pm P_{e^+}, \pm P_{e^-}))^2}{N_{i,j}^{DATA}}, \qquad (5.13)$$

where $N_{i,j}^{DATA}$ is the content of the i-th bin of the $\cos\theta_W$ distribution for the j-th data sample of the four data samples for the different helicity sets. The Monte Carlo template f_i for the same bin of $\cos\theta_W$ and the polarizations P_{e^+} and P_{e^-} depend on the sample j.

The fit has first been performed with two free parameters, the absolute value of the polarizations of the beams. For each considered luminosity the fit is repeated several times, changing randomly the Poissonian smearing of the data distributions for each iteration. The resulting fitted parameters are Gaussian distributed around the expected value, as shown in Fig. 5.12. The fit statistical errors are obtained from the widths of the Gaussian fitted to the parameter distributions.

The error determination has been checked like this in order not to trust blindly the MINUIT output. Moreover, with this technique it is possible to check not only the
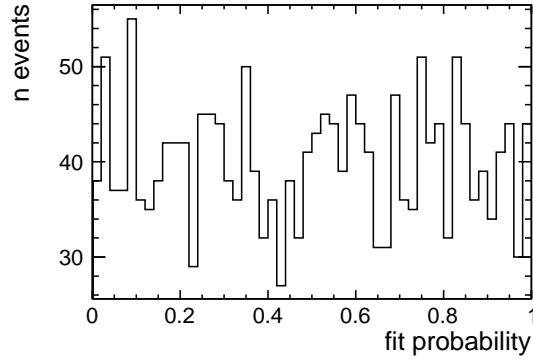
Figure 5.13: *Distribution of the fit probability for the angular fit with two free parameters for the option of 60% positron and 80% electron polarization and an integrated luminosity of 500 fb^{-1}.*
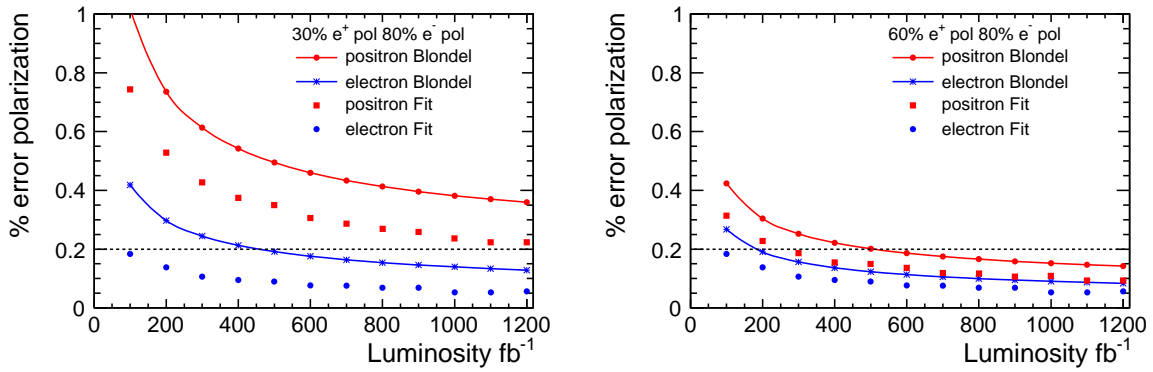

Figure 5.14: *Comparison of the results obtained with the modified Blondel scheme (continuous curves) and with the angular fit method (dots). The distribution on the left (right) shows the results obtained for the low (high) polarization option, with 80% electron and 30% (60%) positron polarization. The red (blue) curves show the percentage error on the positron (electron) polarization as a function of the total luminosity, which is shared equally between the four polarization sets.*

correct distributions of the fitted parameters, but also the behavior of the fit probability and the correlations between the parameters.

The fit probability is shown in Fig. 5.13 (e.g. for 60% positron and 80% electron polarization and for an integrated luminosity of 500 fb^{-1}). It is flat as expected for a correct fit. The correlation between the two fit parameters is negligible for both positron polarization options (see Tab. 5.3).

The precision achieved with the angular fit method is summarized in Fig. 5.14, where it is compared with the Blondel method. For the 60% positron polarization option and a total luminosity of 250 fb^{-1} (Fig. 5.14, right) the desired relative precision of 0.2% is obtained for both polarizations. In case of low positron polarization an integrated luminosity of 1200 fb^{-1} is needed to achieve the same uncertainty. In this case, with an integrated luminosity of 500 fb^{-1} precisions of $\sim 0.1\%$ on the electron polarization and of $\sim 0.35\%$ on the positron polarization are obtained.

The angular fit appears to be more powerful than the modified Blondel scheme, yielding
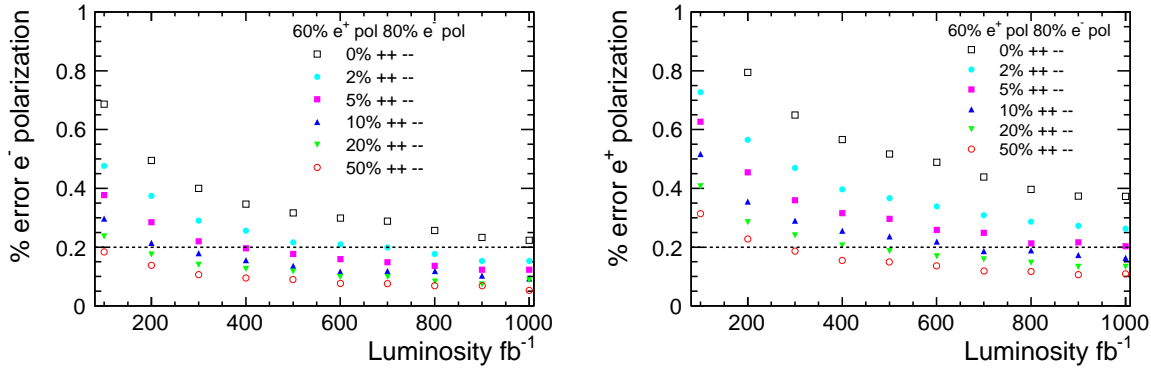
Figure 5.15: *Results obtained with the angular fit method, in the 60% polarization option. The distribution on the left (right) shows the percentage error on the electron (positron) beam polarization as a function of the total luminosity. The different curves are obtained spending different percentages of the total luminosity with the same helicity for both beams, according to the legend.*

e^+ pol	% ++ −−	$\Delta P_{e^+}/P_{e^+}\%$	$\Delta P_{e^-}/P_{e^-}\%$	corr%
30	50	0.34	0.08	6.6
60	50	0.14	0.08	3.4
60	20	0.18	0.11	33.4
60	10	0.23	0.14	58.4

Table 5.3: *Summary of the results obtained with the angular fit method for a total integrated luminosity of $500\,\text{fb}^{-1}$. The percentage of the total luminosity spent on the same-sign helicity configurations of the beams is shown in the second column. The results are shown for an electron polarization of 80%, while both positron polarization options are considered: $P_{e^+} = 30\%$ and $P_{e^+} = 60\%$.*

the same precisions at much lower luminosities.

For the 60% positron polarization option the performance of the fit has also been studied reducing the luminosity spent on the ++ and −− polarization sets. Such configurations of the helicities are of low interest for most of the physics studies, since they suppress the *s*-channel production. The results obtained are shown in Fig. 5.15. When spending only 20% (10%) of the total luminosity on the same-sign polarization sets, precisions of $\sim 0.1\%$ on the electron polarization and of $\sim 0.2\%$ on the positron polarization are obtained at $400\,\text{fb}^{-1}$ ($600\,\text{fb}^{-1}$). In case the luminosity is equally-shared between the four data samples, the same results are obtained at $250\,\text{fb}^{-1}$.

The correlation between the fitted polarizations increases when reducing the amount of luminosity spent on the same-sign helicity sets. However, even reducing the percentage of luminosity spent on the same-sign configurations to only 10%, the correlation between the fitted parameters is still acceptable.

The results obtained with the angular fit method for an integrated luminosity of $500\,\text{fb}^{-1}$ are summarized in Tab. 5.3.

	R_1	R_2	R_3	R_4	R_5	R_6	R_7	R_8	R_9
Δg_1^Z	+0.001	0	0	-0.001	0	0	+0.001	0	+0.001
$\Delta\kappa_\gamma$	0	+0.001	0	0	-0.001	0	+0.001	+0.001	0
$\Delta\lambda_\gamma$	0	0	+0.001	0	0	-0.001	0	+0.001	+0.001

Table 5.4: *Δg_1^Z, $\Delta\kappa_\gamma$ and $\Delta\lambda_\gamma$ values used to calculate the coefficients in Eq. 5.14.*

5.4 Triple Gauge Couplings and Polarization

In this section the simulation of the TGCs using Whizard is illustrated and the additional angular observables introduced to gain sensitivity to the TGCs are described. The systematic impact that anomalous values of the TGCs might have on the performance of the partial measurement of the only polarization is calculated. Finally, an extension of the angular fit method is discussed, which allows a simultaneous measurement of the TGCs in addition to the beam polarizations.

Only three independent couplings are considered, g_1^Z, κ_γ and λ_γ, as in the LEP analysis (Sec. 2.9). Thanks to the foreseen high luminosity of the ILC, these couplings can be measured simultaneously, while in the LEP analysis they are measured in single fits, where one parameter is allowed to vary and the other two are fixed.

5.4.1 Simulation of the Triple Gauge Couplings

In order to perform a fit, it is necessary to associate a weight to the Monte Carlo events. This weight is expressed as a continuous function of the TGCs:

$$
\begin{aligned}
R(\Delta g_1^Z, \Delta\kappa_\gamma, \Delta\lambda_\gamma) \;=\; & 1 + A\Delta g_1^Z + B\Delta\kappa_\gamma + C\Delta\lambda_\gamma + D\Delta g_1^{Z\,2} + E\Delta\kappa_\gamma{}^2 + F\Delta\lambda_\gamma{}^2 \\
& + G\Delta g_1^Z\Delta\kappa_\gamma + H\Delta g_1^Z\Delta\lambda_\gamma + I\Delta\lambda_\gamma\Delta\kappa_\gamma,
\end{aligned}
\tag{5.14}
$$

where the function $R(\Delta g_1^Z, \Delta\kappa_\gamma, \Delta\lambda_\gamma)$ describes the quadratic dependence of the differential cross sections on the three TGCs [60], and the Δ in front of the TGC names indicates that they are expressed as deviations from the SM value. The nine coefficients in Eq. 5.14 are obtained calculating the value assumed by $R(\Delta g_1^Z, \Delta\kappa_\gamma, \Delta\lambda_\gamma)$ for the nine sets of TGCs shown in Tab. 5.4.

The calculation of the weight for these specific values of the couplings is performed using the same WHIZARD configuration used in the event generation. WHIZARD allows to rescan a given event sample, recalculating the matrix element values event-by-event with some modification applied. As a result, each event is assigned a weight, which takes into account the changes due to the different TGC values without modifying the event kinematics. This procedure is perfectly suitable for small tunings of some parameters, such as requiring an anomalous value of the TGCs. With this technique nine weights R_i, $i = 1, 2, ..., 9$ are obtained, for the nine sets of TGCs in Tab. 5.4:

Parameter	68% C.L.	Nominal Value
g_Z^1	$0.984^{+0.022}_{-0.019}$	1
κ_γ	$0.973^{+0.044}_{-0.045}$	1
λ_γ	$-0.028^{+0.020}_{-0.021}$	0

Table 5.5: *The 68% C.L. values for the three TGCs obtained from a combination of ALEPH, L3 and OPAL results. In each case the parameter listed is varied while the other two are fixed to their SM values. Both statistical and systematic errors are included. From [124].*

$$R_1 = 1 + A \mid \Delta g_1^Z \mid + D \mid \Delta g_1^Z \mid^2,$$
$$R_2 = 1 + B \mid \Delta \kappa_\gamma \mid + E \mid \Delta \kappa_\gamma \mid^2,$$
$$R_3 = 1 + C \mid \Delta \lambda_\gamma \mid + F \mid \Delta \lambda_\gamma \mid^2,$$
$$R_4 = 1 - A \mid \Delta g_1^Z \mid + D \mid \Delta g_1^Z \mid^2,$$
$$R_5 = 1 - B \mid \Delta \kappa_\gamma \mid + E \mid \Delta \kappa_\gamma \mid^2,$$
$$R_6 = 1 - C \mid \Delta \lambda_\gamma \mid + F \mid \Delta \lambda_\gamma \mid^2,$$
$$R_7 = 1 + A \mid \Delta g_1^Z \mid + B \mid \Delta \kappa_\gamma \mid + D \mid \Delta g_1^Z \mid^2 + E \mid \Delta \kappa_\gamma \mid^2 + G \mid \Delta g_1^Z \mid\mid \Delta \kappa_\gamma \mid,$$
$$R_8 = 1 + B \mid \Delta \kappa_\gamma \mid + C \mid \Delta \lambda_\gamma \mid + E \mid \Delta \kappa_\gamma \mid^2 + F \mid \Delta \lambda_\gamma \mid^2 + I \mid \Delta \kappa_\gamma \mid\mid \Delta \lambda_\gamma \mid,$$
$$R_9 = 1 + A \mid \Delta g_1^Z \mid + C \mid \Delta \lambda_\gamma \mid + D \mid \Delta g_1^Z \mid^2 + F \mid \Delta \lambda_\gamma \mid^2 + H \mid \Delta g_1^Z \mid\mid \Delta \lambda_\gamma \mid, \quad (5.15)$$

where $|\Delta g_1^Z|=|\Delta \kappa_\gamma|=|\Delta \lambda_\gamma|=0.001$. The value 0.001 is chosen, since it is the approximate order of magnitude of the expected precision. Inverting these equations one derives the nine coefficients A, B, C, D, E, F, G, H, I to be inserted into Eq. 5.14. The procedure is repeated for each signal and tau-signal event, obtaining an individual expression of $R(\Delta g_1^Z, \Delta \kappa_\gamma, \Delta \lambda_\gamma)$ for each event. The impact of the TGCs on the small residual background contamination of the event samples has been neglected.

5.4.2 Triple Gauge Couplings Impact

As motivated in Chap. 2, a precise measurement of the TGCs is extremely important in itself. However, in this section it is shown that anomalous values of the TGCs might affect the measurement of the polarization from the W-pair channel in a non-negligible way, further motivating the study of a simultaneous fit.

Tab. 5.5 summarizes the final 68% C.L. TGCs values obtained at LEP combining the results from ALEPH, L3 and OPAL, already discussed in Chap. 2.

The limits set by the LEP experiments are weak relative to the excellent performance required for the polarization measurement at the ILC and might have a non-negligible systematic impact. This can easily be seen by changing the values of the TGCs in the Monte Carlo "data" sample and repeating the polarization measurement. Using the reweighting technique one coupling at a time was varied from its SM tree-level value used for the standard event generation to either the upper, or the lower 1-σ limit set by the LEP experiments. For example g_Z^1 has been changed from 1 to 1.202(= $0.984 + 0.022$) and to 0.965(= $0.984 - 0.019$). The Blondel scheme and the angular fit

60% positron polarization							
	coupling	g_Z^1		κ_γ		λ_γ	
	Δ	0.006	-0.035	0.017	-0.072	-0.008	-0.049
Fit	$\Delta pol_{e+}\%$	-0.12	0.46	0.15	-1.18	-0.01	0.25
	$\Delta pol_{e-}\%$	-0.15	0.55	0.24	-1.59	0.00	0.23
Blondel	$\Delta pol_{e+}\%$	-0.04	0.17	0.02	-0.39	-0.01	0.24
	$\Delta pol_{e-}\%$	-0.04	0.18	0.04	-0.61	0.00	0.16
30% positron polarization							
	coupling	g_Z^1		κ_γ		λ_γ	
	Δ	0.006	-0.035	0.017	-0.072	-0.008	-0.049
Fit	$\Delta pol_{e+}\%$	-0.15	0.60	0.17	-1.34	-0.03	0.14
	$\Delta pol_{e-}\%$	-0.20	0.69	0.33	-2.17	0.00	0.26
Blondel	$\Delta pol_{e+}\%$	-0.04	0.23	0.01	-0.25	-0.03	-0.14
	$\Delta pol_{e-}\%$	-0.04	0.18	0.05	-0.61	0.00	0.14

Table 5.6: *Systematic uncertainty on the polarization measurement introduced by anomalous values of the TGCs. The upper (lower) part of the table refers to the 60% (30%) positron polarization option. The TGCs are changed, one at a time, by a difference Δ from the SM tree-level value, leaving the others fixed. The chosen differences Δ are the maximum deviations from the SM, allowed by the LEP 68% C.L. limits. The deviations of the measured positron (electron) polarizations Δpol_{e+} (Δpol_{e-}) from the true values are also indicated.*

method have been applied, using the Monte Carlo samples with anomalous values of the TGCs as "data". The results obtained are summarized in Tab. 5.6.

The systematic uncertainty introduced by propagating the experimental error on the TGCs is too high, when considering that precisions of the order of 0.2% on the polarizations are desired. The angular fit method would allow to control the effect of the TGCs by monitoring the χ^2 (which would be blown up by wrong assumptions on the values of the couplings). The full capabilities of the angular fit method can be exploited by implementing a simultaneous fit of the TGCs and the polarization. In order to gain sensitivity to the couplings new observables are introduced into the fit. They are described in the following.

5.4.3 Decay Angles of the W-pair

In order to maximize the sensitivity to the TGCs, two more observables are introduced characterizing the leptonic decay of the W-boson. A W-pair event is described by five angles, as illustrated in Fig. 5.16.

The angle θ_W, already introduced previously, is the angle between the incoming electron beam and the outgoing W^-. The four angles $\cos\theta^*$ and ϕ^* describe the decays of the two W-bosons in their rest frame. They are defined as the angles of the down-type decay product f_d in the right-handed coordinate system of the W-boson rest frame, where the two decay products are back-to-back. The z-axis of each decay coordinate system coincide with the parent W-boson direction in the overall center-of-mass system, while the y-axes direction is given by $\vec{e}^- \times \vec{W}$, where $\vec{e}^-$ is the direction of the incoming
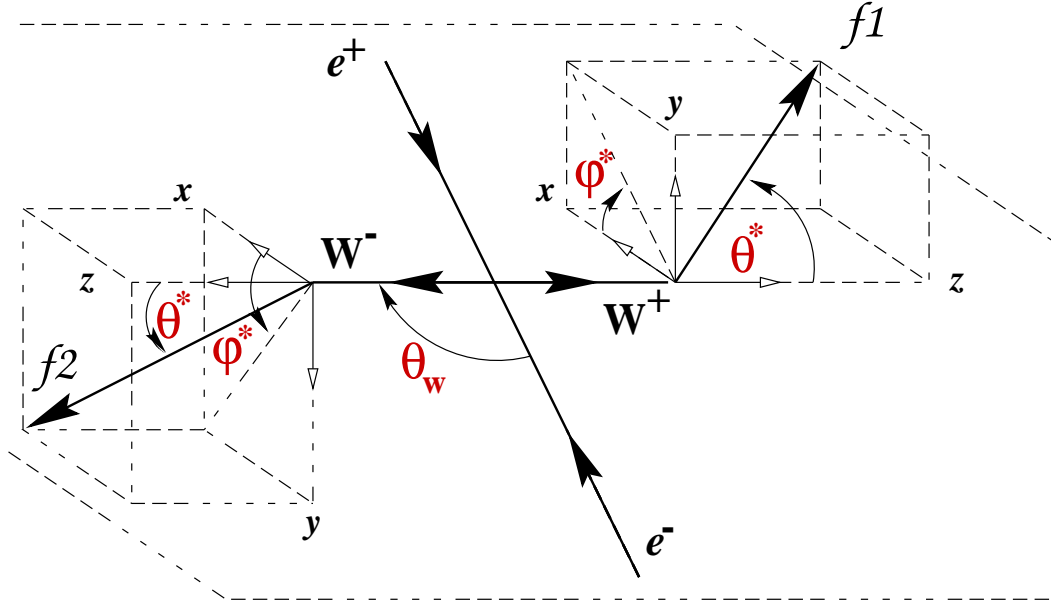
Figure 5.16: *Definition of the angles in an $e^+e^- \rightarrow W^+W^-$ event.*

electron beam and $\vec{W}$ is the flight direction of the parent W-boson. The decay angles can be classified corresponding to the decay type (hadronic or leptonic). The angles describing the hadronic (leptonic) decay are called $\cos\theta_h^*$ ($\cos\theta_l^*$) and ϕ_h^* (ϕ_l^*).

The hadronic decay angles suffer from a two-fold ambiguity, due to the unknown charge of the quarks. The two quarks are back-to-back in the rest frame of the W-boson and the resulting ambiguity is:

$$(\cos\theta_h^*, \phi_h^*) \leftrightarrow (-\cos\theta_h^*, \phi_h^* + \pi), \tag{5.16}$$

which is folded in the following way:

$$\phi_h^* > 0 \rightarrow (\cos\theta_h^*, \phi_h^*)$$
$$\phi_h^* < 0 \rightarrow (-\cos\theta_h^*, \phi_h^* + \pi). \tag{5.17}$$

However, for the present study only the angles describing the leptonic decay are used. Their distributions are shown in Fig. 5.17, with the respective resolutions. Fig. 5.18 compares the $\cos\theta_W$ distribution with no anomalous TGCs with a scenario in which an anomalous value was assigned to the g_1^Z coupling in order to exemplify the impact of the TGCs on the angular observables.

5.4.4 Simultaneous Fit

The distributions used in the combined fit are multi-dimensional distributions of the angular observables. With all four decay angles, in addition to the $\cos\theta_W$ observable, one would need five-dimensional distributions. Filling a five-dimensional distribution leads to poor statistics for the single bins and does not appear to be a convenient choice. It was therefore decided to move to three-dimensional distributions, using only the angles which describe the leptonic decay $\cos\theta_l^*$ and ϕ_l^*, together with $\cos\theta_W$. This
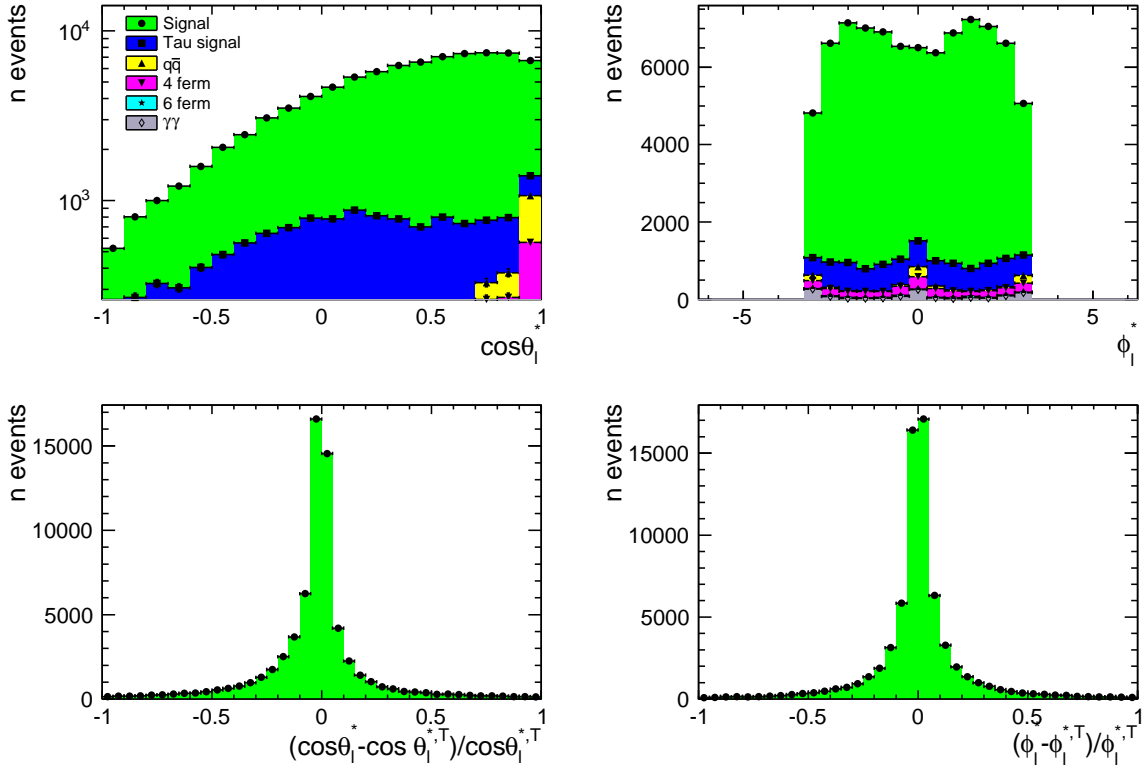
Figure 5.17: *Decay angles (top panels) and their respective resolutions (bottom panels) for the leptonically decaying W-boson. Left: polar angle $\cos\theta_l^*$. Right: azimuthal angle ϕ_l^*. The true Monte Carlo decay angles are denoted $\cos\theta_l^{*,\mathrm{T}}$ and $\phi_l^{*,\mathrm{T}}$, respectively.*
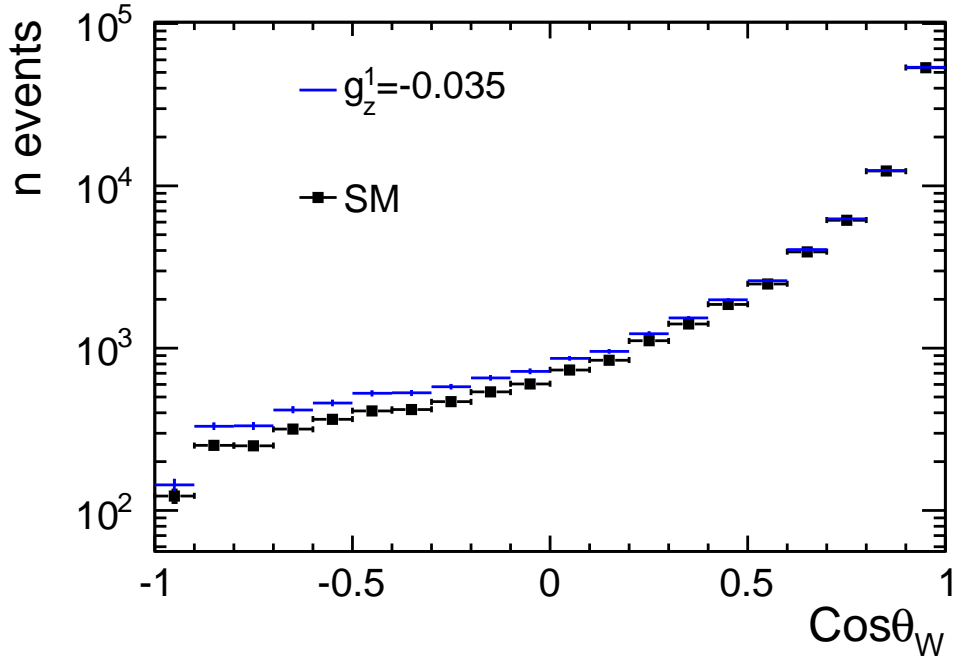
Figure 5.18: *Comparison of two $\cos\theta_W$ distributions: the black squares show the SM distribution, while the blue markers show the distribution obtained for a simulated anomalous value of the g_1^Z coupling, namely $g_1^Z = -0.035$.*

choice is also supported by the fact that these angles are not affected by the two-fold ambiguity, while the remaining, unused angles $\cos\theta_h^*$ and ϕ_h^* are.

A Monte Carlo template of the three-dimensional distribution has been created for $30\,\mathrm{fb}^{-1}$ of luminosity. As for the angular fit of the polarization only, the results have then been propagated to higher luminosities, rescaling the original distributions accordingly.

The "data" are created from the Monte Carlo template, reweighting the events for anomalous values of the TGCs and the desired polarizations. The fit shows slightly different performances for different values of the couplings. Slightly better performances are obtained for values of the couplings far from the SM tree-level expectations. Therefore, the fit was optimized for TGCs coincident with the SM tree-level values, since this option gives the most conservative estimate of the fit uncertainties.

A Poissonian random variation of the content of the 3D-bins of the data distributions is applied, in order to assure statistical independence from the Monte Carlo template sample.

When fitting the template distributions to the data, two weights are applied to each event of the template. One weight is a function of the TGCs (cf. Eq. 5.14) and one of the polarization (Sec. 5.2.1). Since the correlation between the TGCs and the polarization of the incoming beams is negligible, the weights factorize as follows:

$$weight = R(\Delta g_1^Z, \Delta\kappa_\gamma, \Delta\lambda_\gamma) * weight(P_{e^+}, P_{e^-}), \qquad (5.18)$$

where the function R was already introduced in Eq. 5.14 and $P_{e^\pm}$ are the beam polarizations. No R weight has been associated to the background events. The weight that expresses the dependence on the polarization was already discussed in Sec. 5.2.1.

The choice of the binning of the three-dimensional distributions is crucial. The polarization is mainly sensitive to the total cross section information, i.e. to the normalization of the distributions, as clearly shown in Fig. 5.10. A finer binning leads to a higher sensitivity to the shape of the distributions and in general increases the sensitivity to the TGCs, though decreasing the statistics in each bin.

The procedure applied in order to estimate the error of the fit takes into account both the precision and the statistical issues. The fit is repeated several times, each time using a different "data" sample. The different "data" samples were obtained from the same simulated distribution but with a different Poissonian variation, similar to what was done for the angular fit of the polarization only. A too fine binning, leading to poor statistics in most of the bins of the 3D angular distributions, causes the fit to not converge at all or to give non-Gaussian or off-centered distributions of the parameters. An example of a fit suffering from a statistical issue, due to the choice of a too fine binning for the considered luminosity, is shown in Fig. 5.19 (left). The distribution of the measured positron polarization is clearly off-center with respect to the expected value (60) and it is non-Gaussian. The right distribution in the same Figure shows the outcome of a correct fit: the distribution of the fitted parameter is Gaussian and centered around the expected value.

The fit has been repeated both as a log-likelihood minimization and as a χ^2 minimization. The first option is more stable in the low-statistics case, allowing a finer binning. The second technique has been used in order to check the goodness of the
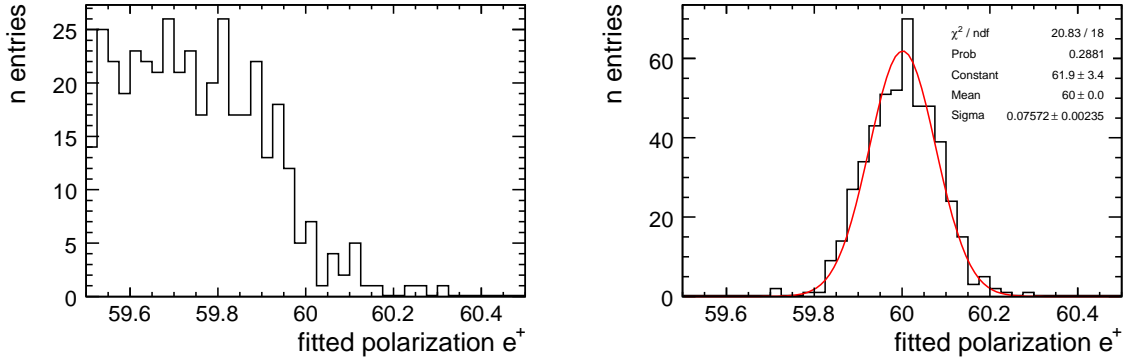
Figure 5.19: *The left distribution shows an example of a fit suffering from too low statistics due to the choice of a too fine binning for the considered luminosity. The distribution of the measured positron polarization is clearly off-center with respect to the expected value (60) and non-Gaussian. On the right the same distribution is shown for a proper choice of the binning.*

fit implementation, via the resulting χ^2 distribution, which has to be consistent with the degrees of freedom of the fit. This is possible since the performance of the fit at sufficiently high luminosities, where the χ^2 minimization is not dramatically affected by statistical issues, is similar for χ^2 and log-likelihood.

The χ^2 function is defined as:

$$\chi^2 = \sum_{++,--,+-,-+} \sum_{bins} \frac{(N_i^{MC}(P_{e^+}, P_{e^-}, TGCs) - N_i^{DATA})^2}{N_i^{DATA}}, \qquad (5.19)$$

where $N_i^{MC}(P_{e^+}, P_{e^-}, TGCs)$ is the content of the i-th bin of the Monte Carlo template, weighted as a function of polarization and TGCs, and N_i^{DATA} is the content of the corresponding bin for the "data" distribution. The sum $\sum_{++,--,+-,-+}$ accounts for the fact that four different "data" samples are used, corresponding to the different helicity sets, as for the previous measurements.

The log-likelihood function is analogously defined as:

$$L = \sum_{++,--,+-,-+} \sum_{bins} (N_i^{DATA} \log N_i^{MC}(P_{e^+}, P_{e^-}, TGCs) - N_i^{MC}(P_{e^+}, P_{e^-}, TGCs)). \qquad (5.20)$$

Where not otherwise specified, the results reported in the following are always meant as results of the log-likelihood fit.

The optimum binning chosen is: 10 bins for the $\cos\theta_W$ distribution and 5 bins for each decay angle distribution. At high luminosities it is possible to move to a finer binning. Starting at a high luminosity of about $500\,\mathrm{fb}^{-1}$, the log-likelihood fit is stable also using a binning of 20, 10 ,10 for the $\cos\theta_W$, $\cos\theta_l^*$ and ϕ_l^* distributions, respectively. The finer binning does not affect significantly the polarization measurement, as already explained, and no improvement can be observed for the measurement of g_1^Z and κ_γ. The sensitivity to λ_γ is the only one affected and is improved by a factor two. In Tab. 5.7 the results of the fit for the two different binnings are compared for a total luminosity of $500\,\mathrm{fb}^{-1}$.

Cross-checks on the fit method have been performed using the χ^2 minimization and a Gaussian smearing of the data instead of the Poissonian one. In fact, the χ^2 is expected to follow a regular behavior only with Gaussian errors. The difference is generally negligible, but due to the presence of low-statistics bins it is appropriate to use the Gaussian smearing to check the regular behavior of the minimization. The χ^2 and the fit probability distributions obtained are shown in the upper panels of Fig. 5.20 for a total luminosity of $500 \, \text{fb}^{-1}$ and a 10-5-5 binning. The χ^2 distribution should follow the behavior expected for 995 degrees of freedom. It was obtained, in fact, using $10 \cdot 5 \cdot 5 = 250$ bins for each of the four data sets, which give 1000 bins in total. Since there are 5 free parameters in the fit, the absolute values of the two beam polarizations and the three couplings, the degrees of freedom are 995.

It is not possible to fit the χ^2 distribution with an analytical expression of the χ^2 function directly. In fact, the Γ functions entering the analytical expression diverge for such a high number of degrees of freedom. In any case the χ^2 function can be well approximated with a two-parameter Gaussian, constraining the width of the Gaussian to the square root of its mean value. Such a fit gives 1021 measured degrees of freedom, a value slightly higher than the expected one. This is mirrored by the fit probability distribution, which peaks at zero, while it is expected to be homogeneously distributed over the whole range [0,1]. The reason for such a behavior is due to the limited statistics used to produce the Monte Carlo sample ($30 \, \text{fb}^{-1}$). Though the number of events is scaled, when propagating the results to higher luminosities, there is still an uncertainty introduced by the low-statistics bins. These bins are affected by fluctuations, when the Monte Carlo 3D template distribution is filled with $30 \, \text{fb}^{-1}$ of events. These fluctuations are directly propagated to higher luminosities, since higher luminosities are obtained reweighting the events and not increasing the number of events. This effect would be canceled by producing a Monte Carlo sample for higher luminosities. A detailed explanation about this topic can be found in [230]. Since a larger Monte Carlo sample was not available, alternatively it was possible to balance the χ^2 by adding an error also for the Monte Carlo in the χ^2 function. Since the error is related to the initial number of events, not to the rescaled number of events, the error on the Monte Carlo enters the χ^2 definition as a simple rescaling. Eq. 5.19 becomes:

$$\chi^2 = \sum_{++,--,+-,-+} \sum_{bins} \frac{(N_i^{MC}(P_{e^+}, P_{e^-}, TGCs) - N_i^{DATA})^2}{N_i^{DATA} \cdot 1.025}, \qquad (5.21)$$

where the value used to rescale the error in the denominator, 1.025, has been obtained empirically. The χ^2 and the fit probability distributions obtained after this change, are shown in the lower panels of Fig. 5.20. The fit of the χ^2 distribution returns the expected number of degrees of freedom and the fit probability distribution is flat. The resulting distributions of the fit parameters are not affected by the χ^2 redefinition. For consistency, the likelihood function was rescaled by the same factor, though the impact on the error of the measured fit parameters for such a tiny factor is negligible.

5.4.5 Results

In Fig. 5.21 the precision on the polarization achieved using the simultaneous fit for the TGCs is compared to the results obtained with the angular fit method of the polarization alone. The total luminosity is shared equally between the four polarization
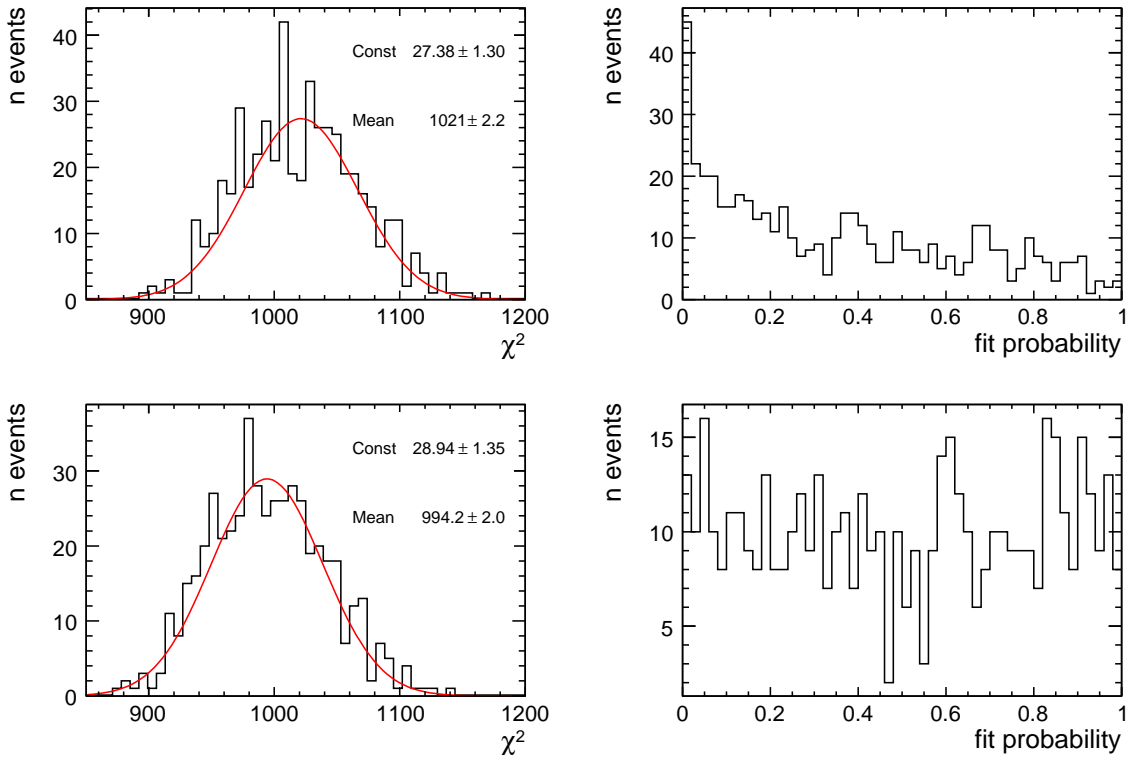
Figure 5.20: *The upper panels show the χ^2 distribution (left) and the fit probability (right) distributions, obtained for an integrated luminosity of $500\,fb^{-1}$ with a simultaneous χ^2 fit of TGCs and polarization. In the lower panels the same distributions are reproduced increasing the error which enters the χ^2 definition in order to account for the limited Monte Carlo statistics (Eq. 5.21).*
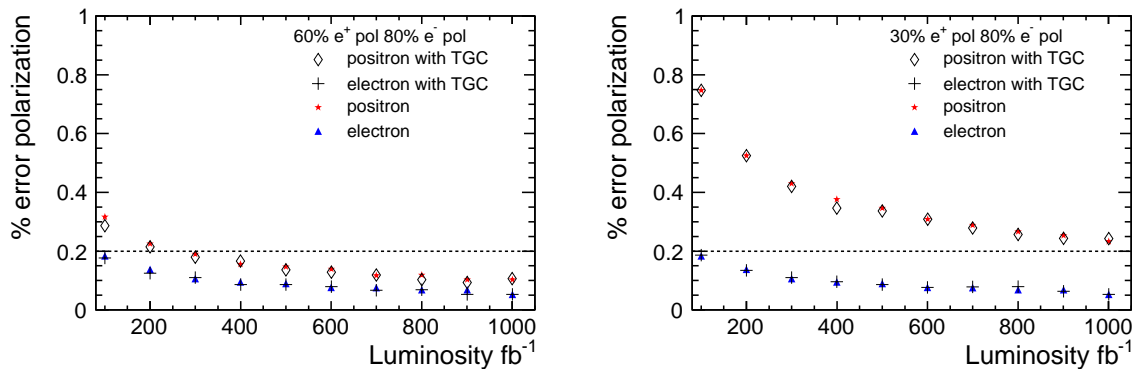
Figure 5.21: *The precision on the polarization achieved by the simultaneous fit with the TGCs is compared to the results obtained with the angular fit method of the polarization alone. The graph on the left (right) refers to a positron polarization of 60% (30%).*

sets $++$, $+-$, $-+$ and $--$. The graphs clearly show that there is no loss in the sensitivity to the polarization, when also fitting simultaneously the TGCs.

Fig. 5.22 shows the precision obtained for the TGCs. The precision is expressed as an absolute uncertainty. The results shown on the left (right) have been obtained with a binning of respectively 10 (20), 5 (10) and 5 (10) bins for the $\cos\theta_W$, $\cos\theta_l^*$ and ϕ_l^* distributions. The fit performed with the finest binning is stable only at high luminosities of more than $500\,\mathrm{fb}^{-1}$.

The results for an integrated luminosity of $500\,\mathrm{fb}^{-1}$ are summarized in Tab. 5.7, comparing the two different binnings, while the correlations between the measured fit parameters are reported in Tab. 5.8. The correlation between the electron and the positron polarizations and between the polarizations and the TGCs are small. The correlations between the couplings are higher, but acceptable. As already anticipated, only the uncertainty on the coupling λ_γ is affected in a non-negligible way by the binning, improving by about a factor 2 when the finest binning is employed.

The precision achievable for an integrated luminosity of $500\,\mathrm{fb}^{-1}$ on the couplings is better than 10^{-3} and could improve the current limits on the couplings by one order of magnitude.

5.5 Systematics

In this section the main sources of systematics that might affect the polarization and the TGCs measurements at the future ILC are investigated. In particular, the assumption made so far that reversing the sign of the polarization does not affect its absolute value is studied in detail.

Efficiency

The measurements implemented make use of non-normalized distributions, therefore a correct evaluation of the selection efficiency is a key factor. At LEP [231] uncertainties on the selection efficiencies of the order of $\sim 0.1\%$ have been obtained, for the
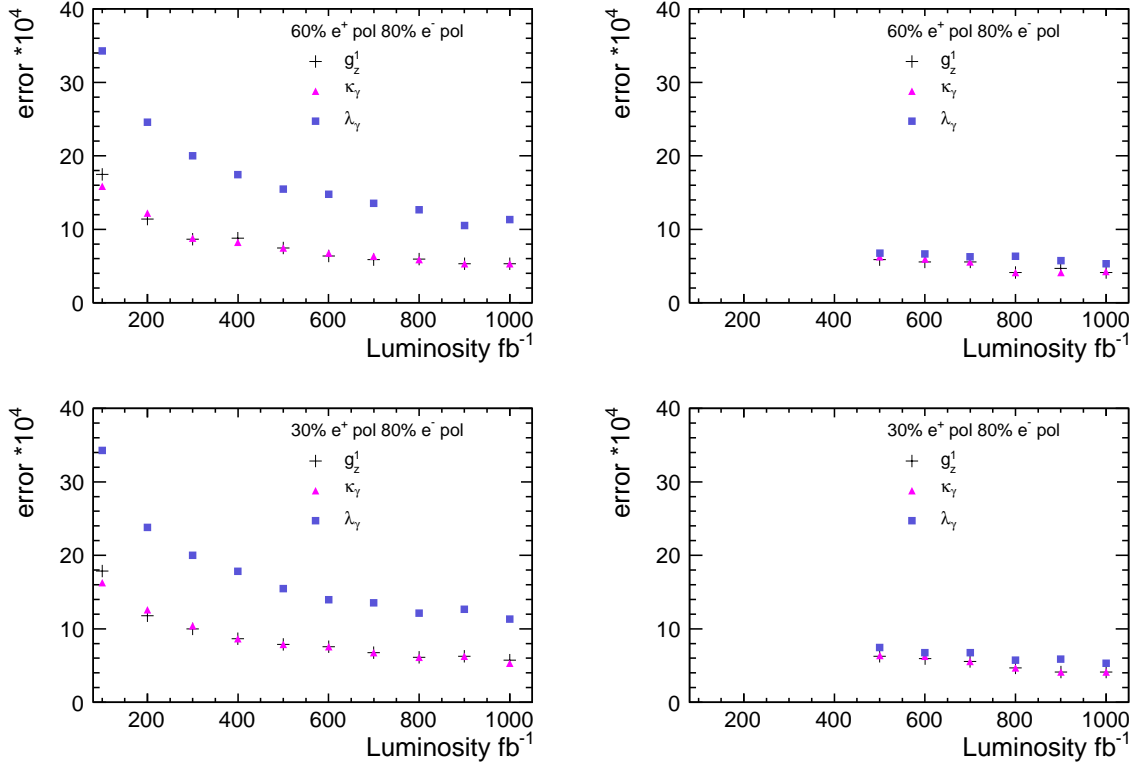
Figure 5.22: *Absolute uncertainty on the TGCs obtained with the simultaneous fit of the TGCs the polarization of the beam. The upper (lower) distributions refer to a positron polarization of 60% (30%). The results shown on the left (right) have been obtained with a binning of respectively 10 (20), 5 (10) and 5 (10) bins for the $\cos\theta_W$, $\cos\theta_l^*$ and ϕ_l^* distributions. The fit performed with the finest binning is stable only at high luminosities of more than $500\,fb^{-1}$.*

Parameter	bin 20-10-10	bin 10-5-5
60% P_{e+}		
ΔP_{e+} %	0.13	0.14
ΔP_{e-} %	0.08	0.09
$\Delta g_1^Z \cdot 10^{-04}$	5.9	7.3
$\Delta\kappa_\gamma \cdot 10^{-04}$	6.2	7.4
$\Delta\lambda_\gamma \cdot 10^{-04}$	6.9	15.3
30% P_{e+}		
ΔP_{e+} %	0.33	0.34
ΔP_{e-} %	0.08	0.08
$\Delta g_1^Z \cdot 10^{-04}$	6.1	7.6
$\Delta\kappa_\gamma \cdot 10^{-04}$	6.4	7.7
$\Delta\lambda_\gamma \cdot 10^{-04}$	7.2	15.5

Table 5.7: *Summary of the results obtained with the simultaneous fit of polarization and TGCS for a total luminosity of $500\,fb^{-1}$ and for two different choices of the binning. A binning of 10-5-5 (20-10-10) is intended as respectively 20 (10), 10 (5) and 10 (5) bins for the $\cos\theta_W$, $\cos\theta_l^*$ and ϕ_l^* distributions.*

Parameters	60% P_{e+}	30% P_{e+}
P_{e-}/P_{e+}	13.3	-2.7
P_{e-}/g_1^Z	-0.8	9.1
P_{e-}/κ_γ	-12.8	-15.3
P_{e-}/λ_γ	4.3	-6.1
P_{e+}/g_1^Z	2.8	0.2
P_{e+}/κ_γ	-7.4	-9.5
P_{e+}/λ_γ	-6.3	-2.5
g_1^Z/κ_γ	70.2	63.4
g_1^Z/λ_γ	47.1	47.7
$\lambda_\gamma/\kappa_\gamma$	47.2	35.4

Table 5.8: *Correlations between the fit parameters obtained with the angular fit of polarization and TGCs. The results for both the options of 60% and 30% positron polarization are reported.*

semileptonic decays of the W-pairs. In order to be conservative, an error of 0.2% on the selection efficiency of signal and tau-signal has been considered (note that the statistical error on the selection efficiencies in Tab. 5.2 refers to just $20\,\mathrm{fb}^{-1}$ of statistics. For the higher considered luminosities, in particular for a total luminosity of $500\,\mathrm{fb}^{-1}$, the statistical error on the selection efficiency is negligible and is expected to be limited by systematic effects). Uncertainties on the selection efficiency of the background of 1% and 5% have been considered. These uncertainty have been propagated as a global rescaling of the background. The case of an error of 0.5% on the selection efficiency of the signal and of the tau-signal has also been considered.

The impact on the measurement of polarization and TGCs is summarized in Tables 5.9 and 5.10, respectively for the low and high positron polarization options. If the selection efficiency of the signal can be controlled with a precision of at least 0.2% the measurements are robust with regard to this source of systematics. Uncertainties of the order of 0.5% would limit the statistical precision on the TGCs at high luminosities, though at the 10^{-3} level, which would still be one order of magnitude better than the limits obtained at LEP. The measurement of the polarization is found to be reasonably robust with regard to this source of systematics. Even with the most conservative assumtpions the propagation of the uncertainty to the measurement of the polarization does not exceed the statistical uncertainty for an integrated luminosity of $500\,\mathrm{fb}^{-1}$.

Integrated Luminosity

A relative accuracy better than 10^{-3} on the integrated luminosity is needed at the ILC in order to achieve the physics goals [163]. An error of the order of 10^{-3} was achieved in preliminary simulation studies using Bhabha events [232]. Some of the uncertainties contributing to this error could still be improved, like the large uncertainty coming from the two-photon background, that can be reduced correcting for it and instead using the uncertainty from higher order simulations as a true source of systematics on the luminosity measurement [232].

The biggest impact on the polarization and TGCs measurement coming from this source of systematic error is obtained in case it influences the four polarization sets $++$, $+-$, $-+$ and $--$ differently, namely increasing the integrated luminosity of some

Parameter	Blondel	Angular no TGCs	Angular with TGCs
0.2% signal 1% background			
ΔP_{e^+}	0.03%	0.01%	0.01%
ΔP_{e^-}	0.02%	0.01%	0.01%
Δg_1^Z	-	-	0.0006
$\Delta \kappa_\gamma$	-	-	0.0007
$\Delta \lambda_\gamma$	-	-	0.00002
0.2% signal 5% background			
ΔP_{e^+}	0.08%	0.05%	0.05%
ΔP_{e^-}	0.07%	0.05%	0.05%
Δg_1^Z	-	-	0.001
$\Delta \kappa_\gamma$	-	-	0.001
$\Delta \lambda_\gamma$	-	-	0.0007
0.5% signal 1% background			
ΔP_{e^+}	0.04%	0.01%	0.01%
ΔP_{e^-}	0.03%	0.01%	0.01%
Δg_1^Z	-	-	0.001
$\Delta \kappa_\gamma$	-	-	0.001
$\Delta \lambda_\gamma$	-	-	0.0004
0.5% signal 5% background			
ΔP_{e^+}	0.08%	0.05%	0.05%
ΔP_{e^-}	0.07%	0.05%	0.06%
Δg_1^Z	-	-	0.002
$\Delta \kappa_\gamma$	-	-	0.002
$\Delta \lambda_\gamma$	-	-	0.0008

Table 5.9: *Summary of the systematics due to the uncertainties on the selection efficiencies, for the low positron polarization option of 30%. The impact on the polarization and TGCs measurement is shown, both for the Blondel technique and for the angular fit method.*

Parameter	Blondel	Angular no TGCs	Angular with TGCs
0.2% signal 1% background			
ΔP_{e^+}	0.02%	0.01%	0.01%
ΔP_{e^-}	0.03%	0.01%	0.01%
Δg_1^Z	-	-	0.0006
$\Delta \kappa_\gamma$	-	-	0.0006
$\Delta \lambda_\gamma$	-	-	0.0002
0.2% signal 5% background			
ΔP_{e^+}	0.08%	0.05%	0.05%
ΔP_{e^-}	0.07%	0.05%	0.05%
Δg_1^Z	-	-	0.001
$\Delta \kappa_\gamma$	-	-	0.002
$\Delta \lambda_\gamma$	-	-	0.0006
0.5% signal 1% background			
ΔP_{e^+}	0.03%	0.01%	0.01%
ΔP_{e^-}	0.03%	0.01%	0.01%
Δg_1^Z	-	-	0.001
$\Delta \kappa_\gamma$	-	-	0.001
$\Delta \lambda_\gamma$	-	-	0.0002
0.5% signal 5% background			
ΔP_{e^+}	0.08%	0.05%	0.05%
ΔP_{e^-}	0.07%	0.05%	0.05%
Δg_1^Z	-	-	0.002
$\Delta \kappa_\gamma$	-	-	0.002
$\Delta \lambda_\gamma$	-	-	0.0008

Table 5.10: *Summary of the systematics from the selection efficiencies, for the high positron polarization option of 60%. The impact on the polarization and TGCs measurement is shown, both for the Blondel technique and for the angular fit method.*

Parameter	Blondel	Angular no TGCs	Angular with TGCs
60% e^+ polarization			
ΔP_{e^+}	0.1%	0.08%	0.07%
ΔP_{e^-}	0.04%	0.02%	0.02%
$\Delta g_1^Z \cdot 10^{-04}$	-	-	0.0002
$\Delta \kappa_\gamma \cdot 10^{-04}$	-	-	0.0002
$\Delta \lambda_\gamma \cdot 10^{-04}$	-	-	0.0002
30% e^+ polarization			
ΔP_{e^+}	0.3%	0.2%	0.2%
ΔP_{e^-}	0.08%	0.03%	0.02%
$\Delta g_1^Z \cdot 10^{-04}$	-	-	0.0002
$\Delta \kappa_\gamma \cdot 10^{-04}$	-	-	0.0002
$\Delta \lambda_\gamma \cdot 10^{-04}$	-	-	0.0001

Table 5.11: *Maximum impact of the luminosity uncertainty on the measurement of polarization and TGCs. An error of 10^{-3} on the integrated luminosity was assumed.*

samples with respect to the nominal value, while reducing it for others. Using fast helicity flipping also for the positron beam, this eventuality can most probably be warded off. The maximum impact of a 10^{-3} error on the integrated luminosity to the polarization and TGCs measurements is shown in Tab. 5.11. It is found that this source of systematics does not limit significantly the statistical precision obtained for an integrated luminosity of $500\,\text{fb}^{-1}$, both for the polarization and the TGCs measurements.

Assumptions on the Polarization

So far it was assumed that the left-handed and the right-handed states of the polarizations have the same magnitude. In order to make realistic estimates of the precisions achievable at the ILC this constraint needs to be checked. This assumption is in principle not necessary in the angular fit method, unlike the Blondel scheme. The fit of the polarizations can be executed using two different parameters for the different signs of the polarizations. However, this leads to a dramatic worsening of the statistical precision. The results obtained for a total luminosity of $500\,\text{fb}^{-1}$ are summarized in Tab. 5.12. The luminosity is assumed to be equally shared between the four polarization sets. The precision obtained is well above the desired 0.2% and the correlation between the fit parameters is very high.

It is possible to repeat the measurement with different assumptions, taking into account the additional information given by the polarimeters. This possibility has been addressed for the most precise technique implemented, the angular fit method, both with and without additional measurement of the TGCs.

At the ILC, the polarization will be measured by the polarimeters with an expected uncertainty of $\sim \Delta P/P = 0.25\%$ [166]. Preliminary spin tracking studies, based on the ILC RDR lattice and beam parameter set, show that the depolarization between the polarimeters and the IP is the same for the two helicity states of the same beam, with negligible residual differences[1]. Therefore, the 4 average luminosity-weighted po-

---
[1]Moritz Beckmann, private communication.

	30% P_{e+}	60% P_{e+}
$\Delta P^+_{e+}/P^+_{e+}\%$	8.04	3.87
$\Delta P^-_{e+}/P^-_{e+}\%$	4.06	0.94
$\Delta P^+_{e-}/P^+_{e-}\%$	0.44	0.34
$\Delta P^-_{e-}/P^-_{e-}\%$	4.04	3.22
corr $P^+_{e+}\ P^+_{e-}\%$	97.8	96.9
corr $P^+_{e+}\ P^-_{e-}\%$	99.7	99.6
corr $P^-_{e+}\ P^+_{e-}\%$	95.8	95.7
corr $P^-_{e+}\ P^-_{e-}\%$	99.2	98.6

Table 5.12: *Summary of the results obtained with the angular fit method, without making the assumption that the absolute value of the polarization remains unchanged, when flipping its sign. The total luminosity of $500\,fb^{-1}$ is equally shared between the four polarization sets.*

larizations at the IP P^+_{e+}, P^-_{e+}, P^+_{e-} and P^-_{e-} can be constrained as follows:

$$
P_+ = \frac{P^+_{e+} + P^-_{e+}}{2},
$$

$$
\varepsilon_+ = \frac{P^+_{e+} - P^-_{e+}}{2},
$$

$$
P_- = \frac{P^+_{e-} + P^-_{e-}}{2},
$$

$$
\varepsilon_- = \frac{P^+_{e-} - P^-_{e-}}{2}, \tag{5.22}
$$

where P^-_{e+} (P^-_{e-}) and P^+_{e+} (P^+_{e-}) are the magnitudes of the positron (electron) polarization in the left-handed and in the right-handed state, respectively, as measured by the polarimeters.

When performing the angular fit, one free parameter for the polarization of each beam is used, par_+ for the positron beam and par_- for the electron beam. In the data samples where the positron is right-handed, the positron polarization is fitted with:

$$
par_+ + \varepsilon_+, \tag{5.23}
$$

while the left-handed state is fitted with:

$$
-par_+ + \varepsilon_+. \tag{5.24}
$$

The same equations hold for the polarization of the electron beam. The performance of the fit is not affected by the value of $\varepsilon_\pm$, what matters is the precision with which it can be determined, which is:

$$
\sigma_{\varepsilon_\pm} \approx \frac{0.0025 P_\pm}{\sqrt{2}}, \tag{5.25}
$$

where $P_\pm$ was defined in Eq. 5.22. In order to take this uncertainty into account, for each iteration of the fit $\varepsilon_\pm$ is smeared randomly using a Gaussian with a width of $\sigma_{\varepsilon_\pm}$.

e^+ pol	$\Delta P_{e^+}/P_{e^+}\%$	$\Delta P_{e^-}/P_{e^-}\%$	corr%
Idealistic			
30	0.34	0.08	6.6
60	0.14	0.08	3.4
Realistic			
30	0.35	0.16	-3.7
60	0.17	0.16	-5.9

Table 5.13: *Summary of the results obtained with the angular fit method for a total luminosity of $500\,fb^{-1}$. The idealistic case is compared with the realistic case, which takes into account the polarimeters measurement, with a 0.25% uncertainty. The numbers refer to an electron polarization of 80%. The results for both the options of 30% and 60% positron polarization are shown.*
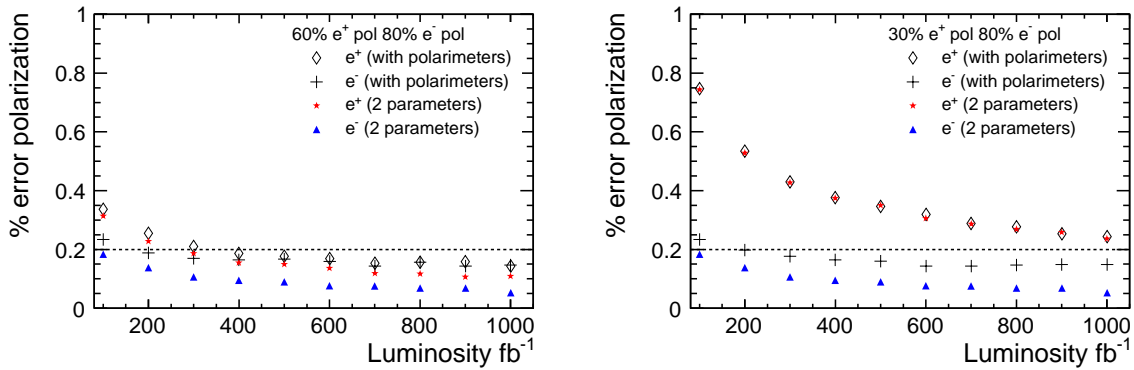
Figure 5.23: *Summary of the results obtained with the angular fit method. The idealistic case is compared with the realistic case, which takes into account the polarimeters measurement, with a 0.25% uncertainty. The distribution on the left (right) refers to a positron polarization of 60% (30%). The simultaneous fit of polarization and TGCs has been performed using the log-likelihood technique and a binning of respectively 10, 5 and 5 bins for the $\cos\theta_W$, $\cos\theta_l^*$ and ϕ_l^* distributions.*

This smearing is performed in addition to the Poissonian smearing of the data samples for each iteration of the fit. For simplicity this version of the fit will be called in the following *realistic*, as opposed to the *idealistic* fit, where $|P_{e^+}^-| = |P_{e^+}^+|$ and $|P_{e^-}^-| = |P_{e^-}^+|$.

The two modalities of the fit are compared in Fig. 5.23 and Tab. 5.13. The dependence of the obtained precisions on the total luminosity is shown in Fig. 5.23. For a total luminosity of $500\,fb^{-1}$ the error is essentially dominated by the systematic uncertainty from the ± polarization differences, when considering the 60% positron polarization option. In the 30% polarization option, improvements at higher luminosites can be obtained for the positron polarization, due to the lower statistical precision. Considering that this is a result realistically achievable at the ILC, it is fully satisfactory. Precisions better than 0.2% can be obtained on the electron polarization and on the positron polarization, if a high positron polarization is considered. In the case of 30% positron polarization, the effect of the uncertainty on the measurement of the positron polarization is negligible, since the polarization has a worse statistical precision.

Parameter	Realistic	Idealistic
60% P_{e+}		
ΔP_{e+} %	0.17	0.14
ΔP_{e-} %	0.16	0.09
$\Delta g_1^Z \cdot 10^{-04}$	7.7	7.3
$\Delta \kappa_\gamma \cdot 10^{-04}$	7.9	7.4
$\Delta \lambda_\gamma \cdot 10^{-04}$	15.2	15.3
30% P_{e+}		
ΔP_{e+} %	0.35	0.34
ΔP_{e-} %	0.16	0.08
$\Delta g_1^Z \cdot 10^{-04}$	7.9	7.6
$\Delta \kappa_\gamma \cdot 10^{-04}$	7.6	7.7
$\Delta \lambda_\gamma \cdot 10^{-04}$	15.6	15.5

Table 5.14: *Summary of the results obtained for the angular fit of polarization and TGCs for a total luminosity of $500\,fb^{-1}$ and with a binning of 10-5-5. The realistic and the idealistic fits are compared.*

Parameters	60% P_{e+}	30% P_{e+}
P_{e-}/P_{e+}	-2.9	-1.7
P_{e-}/g_1^Z	32.2	35.6
P_{e-}/κ_γ	28.6	26.0
P_{e-}/λ_γ	3.3	4.8
P_{e+}/g_1^Z	20.3	7.2
P_{e+}/κ_γ	13.9	3.1
P_{e+}/λ_γ	3.1	-0.1
g_1^Z/κ_γ	72.2	70.1
g_1^Z/λ_γ	38.6	41.0
$\lambda_\gamma/\kappa_\gamma$	37.3	38.5

Table 5.15: *Correlations between the fit parameters obtained with the angular fit of polarization and TGCs, in both the options of 60% and 30% positron polarization. The results shown were obtained with the realistic fit.*

When moving from the idealistic to the realistic assumptions in the simultaneous measurement of TGCs and polarization, no significant impact on the TGCs measurement is found. The results are compared in Tab. 5.14. The sensitivity to the couplings is comparable to the sensitivity obtained with the idealistic assumptions, while the sensitivity to the polarization is comparable to the one obtained with the realistic fit of the polarization only. The correlations between couplings and polarization are summarized in Tab. 5.15 and are acceptable.

5.6 Conclusions

Using the W-pair production it will be possible to measure the average luminosity-weighted beam polarization at the ILC with high sensitivity, providing the polarimeters with an absolute scale calibration.

Applying a modified Blondel scheme, a statistical uncertainty of 0.1% (0.2%) on the e^- (e^+) polarization is obtained for an integrated luminosity of $\mathcal{L} = 500\,\mathrm{fb}^{-1}$, an electron polarization of 80% and for a high positron polarization of 60%. When considering the lower positron polarization option of 30%, the measurement precision reduces to 0.2% (0.5%) for the e^- (e^+) polarization.

Using an angular fit technique, which compares the distribution of the production angle of the W-pair to a Monte Carlo template, the same precision on the polarization is obtained already for lower luminosities. This method requires a total luminosity of only $250\,\mathrm{fb}^{-1}$ for the high positron polarization option, in order to achieve a statistical precision of the order of 0.1% (0.2%) on the polarization of the electron (positron) beam. For the lower positron polarization option a precision of 0.1% (0.34%) on the e^- (e^+) polarization is obtained for an integrated luminosity of $\mathcal{L} = 500\,\mathrm{fb}^{-1}$.

Since the angular fit method require lower luminosities, it also allows a reduction of the luminosity spent with both beams right-handed or left-handed. Such configurations of the helicities are of low interest for most of the physics studies, since they suppress the s-channel diagrams. With the angular fit method, only 20% of the total luminosity need to be spent on these polarization configurations to obtain a statistical precision of the order of 0.1% (0.2%) on the polarization of the e^- (e^+) beam for an integrated luminosity of $400\,\mathrm{fb}^{-1}$.

The angular fit method can be extended to a simultaneous fit of polarization and TGCs without loosing sensitivity on the polarization. Three independent couplings in the vertices $WW\gamma$ and WWZ were fitted together with the polarization, obtaining an absolute statistical precision better than 10^{-3} for an integrated luminosity of $\mathcal{L} = 500\,\mathrm{fb}^{-1}$.

A study of the possible systematic errors that might affect the performance of the measurement has been performed. The major effect comes from differences in the values of the left- and right-handed states of the polarizations, that need to be corrected using the polarimeters. Propagating the expected 0.25% uncertainty of the polarimeters, the impact on the polarization and TGCs measurement has been evaluated. While no significant impact on the TGCs measurement is found, the systematic uncertainty on the polarization is non-negligible and dominates over the statistical precision at high luminosities. However, good precisions are achieved even considering this source of systematics. For a high positron polarization of 60%, an uncertainty of 0.16% (0.17%) for the e^- (e^+) polarization is obtained for an integrated luminosity of $\mathcal{L} = 500\,\mathrm{fb}^{-1}$. Assuming a lower positron polarization of 30%, the achieved precision is 0.16% (0.35%) for the e^- (e^+) polarization.

6 Calorimetry

Calorimeters are detectors dedicated to the measurement of energy, based on the principle of particle shower. The particles interact with the material of the calorimeter losing their energy, which is converted into a cascade of particles. Some of the particles produced give rise to detectable signals, whose total energy can be related to the initial energy of the incoming particle. The multiplication process continues until the energy of the generated particles is too low to produce additional ones. After passing this limit the particles are slowed down by elastic interactions until they are stopped and the shower extinguishes. When the cascade reaches the borders of the calorimeter before being concluded, part of the original energy gets lost without being detected by the calorimeter. This phenomenon is commonly known as leakage.

The showers are classified into two main types: electromagnetic and hadronic. Electromagnetic showers are induced by electrons, positrons and photons. Hadronic showers are initiated by hadronic particles, which undergo strong interactions when traversing matter, and contain localized electromagnetic showers inside the main cascade.

In this chapter the interactions of particles with matter, responsible for the development of showers, are described and the principles of calorimetry are explained. Special attention is paid to sampling calorimeters, as they are very common in high energy physics as well as the chosen calorimeters for the ILD detector (Sec. 3.4.2).

6.1 Interactions of Particles and Matter

The interactions that a particle undergoes when traversing a material depend on the type of particle considered. This section provides an overview of the most relevant processes, that determine the behavior of electromagnetic and hadronic particles inside a calorimeter.

6.1.1 Interactions of Electrons with Matter

The different processes contributing to the energy loss of an electron (positron) traversing matter are shown in the left plot of Fig. 6.1.

For high-energy electrons the main interaction is bremsstrahlung. Bremsstrahlung occurs when a charged particle interacts with the Coulomb field of atomic nuclei, losing its energy by radiating photons. It is more significant in materials with a high atomic number Z and for particles with a light mass m, just like electrons, since its cross section is proportional to $1/m^2$.
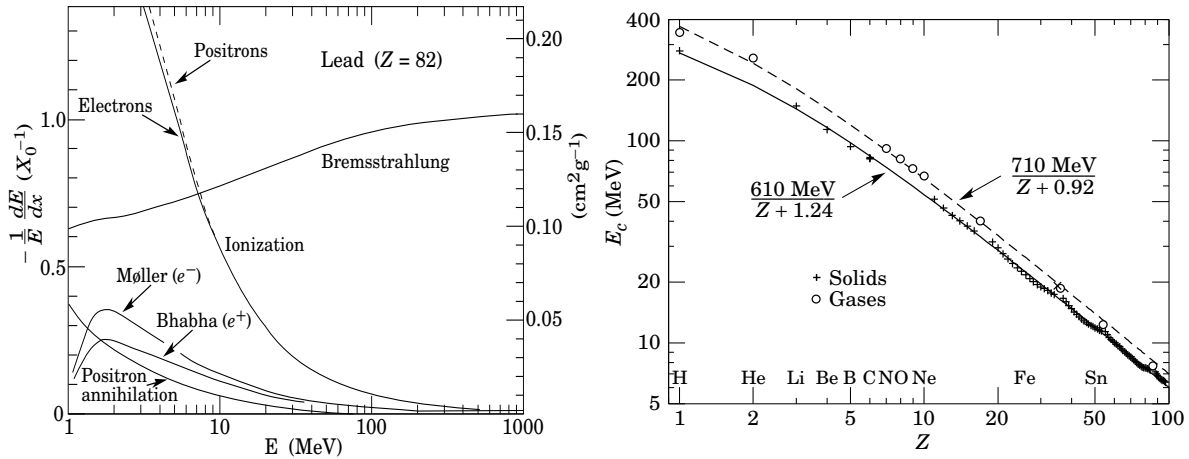
Figure 6.1: *Left: fractional energy loss per radiation length in lead as a function of the electron energy. Electron scattering is considered as ionization when the energy loss per collision is below 0.255 MeV, and as Møller (Bhabha) scattering when it is above. Right: electron critical energy for several chemical elements. The fits shown are for solids and liquids (solid line) and gases (dashed line). From [58].*

The mean energy loss dE by bremsstrahlung of an electron of energy E on a path dx is given by:

$$-\left\langle \frac{dE}{dx} \right\rangle_{brems} = \frac{E}{X_0}, \tag{6.1}$$

where the radiation length X_0 can be approximated as [58]:

$$X_0 = \frac{716.4\,A}{Z(Z+1)\ln(287/\sqrt{Z})}[\text{g cm}^{-2}]. \tag{6.2}$$

A and Z are respectively the atomic mass and the atomic number of the medium. The radiation length is the appropriate scale length for describing high-energy electromagnetic cascades. It is both the mean distance over which a high-energy electron loses all but $1/e$ of its energy by bremsstrahlung, and $7/9$ of the mean free path for pair production by a high-energy photon (described below) [58]. The radiation length can be expressed in cm as well, by dividing it by the density of the material.

The radiation length in a mixture or compound may be approximated by [58]:

$$\frac{1}{X_0} = \sum_i \frac{f_i}{X_i}, \tag{6.3}$$

where f_i and X_i are the fraction by weight and the radiation length for the i-th element.

Another process contributing to the energy loss is ionization, which occurs when the traversing electron loses energy by ionizing the atoms of the medium. While bremsstrahlung losses rise nearly linearly with energy, ionization loss rates decrease logarithmically. When the energy of the electron is below a certain critical energy ε_c, the energy loss by ionization becomes dominant. The critical energy can be defined as the

energy at which the ionization loss per radiation length is equal to the electron energy (the so-called Rossi's definition, which is always assumed in the following). In the right plot of Fig. 6.1 the value of ε_c is shown for different materials. For media in the solid state it can be approximated as [58]:

$$\varepsilon_c = \frac{610\,\text{MeV}}{Z + 1.24}.\tag{6.4}$$

Typical absorber materials used in sampling calorimeters (described below) have critical energies for electrons of the order of 10 MeV.

At low energies the energy loss has minor contributions also from other processes: the Møller scattering ($e^- e^- \rightarrow e^- e^-$), the Bhabha scattering ($e^+ e^- \rightarrow e^+ e^-$) and positron annihilation ($e^+ e^- \rightarrow \gamma\gamma$).

An electron traversing a medium is deflected by many small-angle scatters. Most of this deflection is due to Coulomb scattering from nuclei and hence the effect is called multiple Coulomb scattering. Multiple scattering is responsible for changes in the trajectory of the traversing particle and does not account for energy losses.

6.1.2 Interactions of Muons with Matter

The mean rate of energy loss dE by moderately relativistic charged heavy particles on a path dx in a material with atomic number Z and atomic mass A is given by the Bethe-Bloch formula [58]:

$$-\left\langle \frac{dE}{dx} \right\rangle = K z^2 \frac{Z}{A} \frac{1}{\beta^2} \left[\frac{1}{2} \ln \frac{2 m_e c^2 \beta^2 \gamma^2 T_{max}}{I^2} - \beta^2 - \frac{\delta(\beta\gamma)}{2} \right],\tag{6.5}$$

where $K \approx 0.31\,\text{MeV cm}^2\,\text{mol}^{-1}$ is a constant factor, z is the charge of the incident particle, expressed in units of electron charge, and $m_e = 0.511\,\text{MeV}$ is the electron mass. T_{max} is the maximum kinetic energy which can be imparted to a free electron in a single collision and I is the mean excitation energy of the absorber material. The term $\delta(\beta\gamma)$ is a correction term, accounting for the so-called density effect (explained below).

Eq. 6.5 describes the mean rate of energy loss in the region $0.1 \lesssim \beta\gamma \lesssim 1000$ for intermediate-Z materials with an accuracy of a few %. This is the region where the particle mainly loses energy via ionization. At the lower limit several corrections to the formula have to be taken into account (e.g. [233]) and at the upper limit radiative effects begin to be important. Both limits are Z dependent.

$\langle -dE/dx \rangle$ is expressed in units of $\text{MeVg}^{-1}\text{cm}^2$ and for a given material is essentially a function of β alone, though a minor dependence on the mass of the incoming particle at the highest energies is introduced through T_{max}. The dependence of $\langle -dE/dx \rangle$ on $\beta\gamma$ of the incoming particle, for several absorber materials, is shown in Fig. 6.2.

The energy loss decreases with increasing energy, until it reaches a minimum, which depends weakly on Z and on the mass of the incoming particle. The particles with energy corresponding to the minimum of the ionization are called Minimum Ionizing Particles (*mip*). After the minimum, as the particle energy increases to the relativistic region, its electric field flattens and extends, so that distant-collisions are possible and
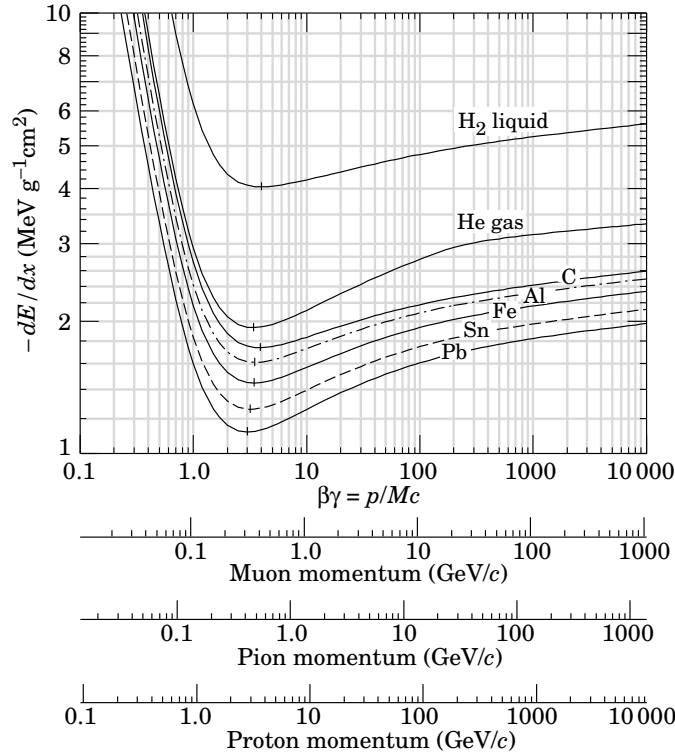
Figure 6.2: *Mean energy loss rate in liquid (bubble chamber) hydrogen, gaseous helium, carbon, aluminum, iron, tin, and lead as a function of $\beta\gamma$. Radiative effects, relevant for muons and pions, are not included. From [58].*

contribute to the energy loss. T_{max} increases as well, and the two effects contribute together to a logarithmic rise of $\langle -dE/dx \rangle$ for high $\beta\gamma$. However, at the same time the medium becomes polarized, limiting the field extension and truncating the rise. This effect is called density effect and is accounted for by the δ term in Eq. 6.5

Fig. 6.3 shows the energy loss of a muon in copper as a function of the muon momentum. Vertical bands indicate boundaries between different approximations. Muons with a momentum in the GeV range behave like *mips*. At high energies radiative processes become more important than ionization. Due to the low rate of energy loss, the depth of the material needed to contain muons is extremely large. Thus, calorimeters are not designed for this purpose. However, muons are useful in calorimetry for calibration purposes.

6.1.3 Interactions of Photons with Matter

Contributions to the photon energy loss in a light element (carbon) and a heavy element (lead) are shown in Fig. 6.4.

At high energies ($E_\gamma \geq 2 \cdot m_e c^2$) the pair production becomes kinematically accessible and is the dominant process. It can occur either in the nuclear field (κ_{nuc} in the figure) or in the field of atomic electrons (κ_e). As already mentioned, the mean free path for pair production by an highly energetic photon is related to the radiation length:

$$\lambda_\gamma \approx \frac{9}{7} X_0. \tag{6.6}$$
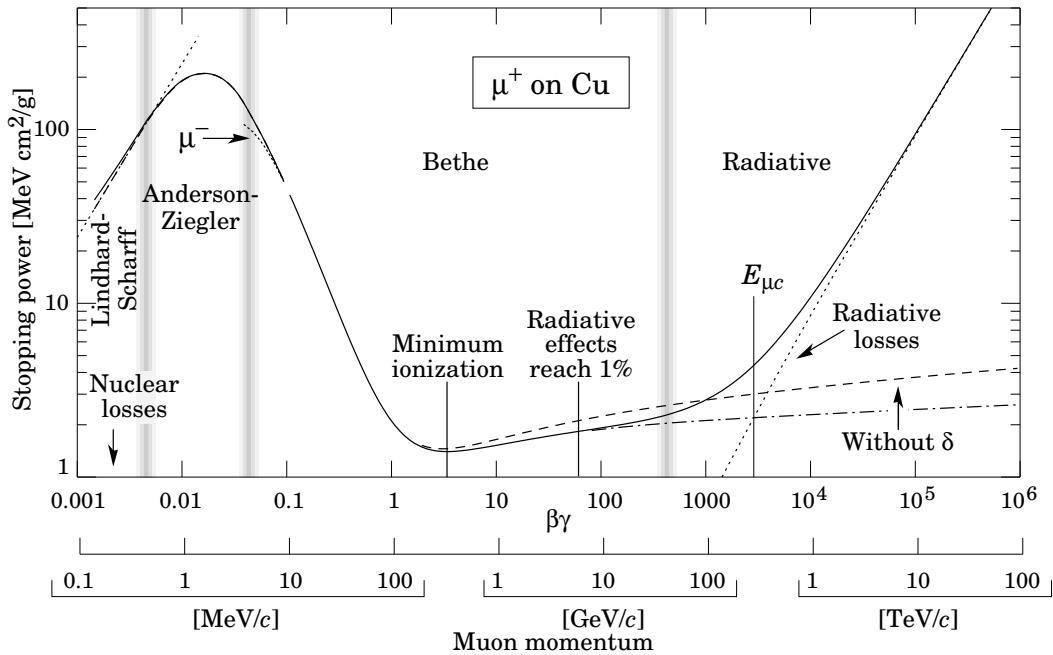
Figure 6.3: *Stopping power (= $\langle -dE/dx \rangle$) for positive muons in copper as a function of $\beta\gamma = p/Mc$ over nine orders of magnitude in momentum (12 orders of magnitude in kinetic energy). Solid curves indicate the total stopping power. From [58].*

Al low energies the dominant process is the photoelectric effect, which consists in the absorption of the photon by an atomic electron with consequent ejection of the electron. In the medium energy range the major contribution comes from the Compton scattering $(\gamma e^- \to \gamma e^-)$.

A minor process occurring at low energies is the Rayleigh scattering off an atom, which occurs when the radiation length of the photon is bigger than the atomic diameter and the atom gets neither ionized nor excited. At higher energies, for heavy media, a minor contribution to the energy loss of the photon comes also from giant dipole resonances, which consist in photonuclear interactions resulting in the break-up of the nucleus [234].

6.1.4 Interactions of Hadrons with Matter

The absorption in matter of hadronic particles, which interact strongly, develops as a cascade process called hadronic shower. While a complete theory does not exist, several models, mostly valid in a limited energy range, concur to describe the development of hadronic showers, either based on theoretical calculations or on phenomenological observations and parameterizations of existing data.

The particle multiplicity in a hadronic cascade increases logarithmically with the energy of the primary particle. The nuclear processes involved in the generation of the shower produce relativistic mesons (mainly π, but also η) and nucleons.

The three charge states of the pion are produced roughly equally. The neutral pions, π^0 decay via electromagnetic interaction into two photons or into a photon plus a positron-electron pair, originating a localized electromagnetic cascade inside the main
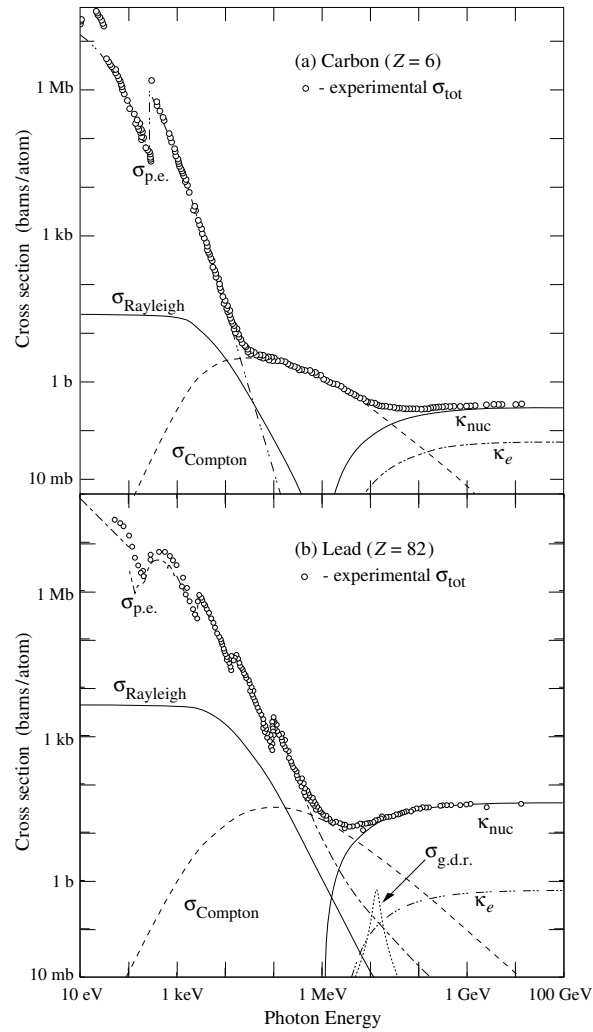
Figure 6.4: *Photon total cross sections as a function of energy in carbon and lead, show-*
ing the contributions of different processes. p.e. indicates the photoelectric
effect, κ_{nuc} the pair production in the nuclear field, κ_e the pair production
in the electron field and g.d.r. stays for photonuclear interactions, most
notably the Giant Dipole Resonance. From [58].

shower. The average number n_0 of produced neutral pions can be approximated by a function of the incoming hadron energy in GeV [235, 236]:

$$n_0 \approx 5\ln(E) - 4.6. \tag{6.7}$$

The average fraction f_{em} of the primary particle energy deposited by electromagnetic cascades of secondary particles is given by [237, 238]:

$$f_{em} \approx 0.12\ln(E). \tag{6.8}$$

Eq. 6.8 is clearly inadequate for very low energies (the logarithm becomes null at $1\,\mathrm{GeV}$ and is negative below) and for energies of a few TeV or higher (the resulting f_{em} diverges to and even exceeds 1).

The purely hadronic component of the shower deposits its energy in the calorimeter via several mechanisms, which have been studied by means of Monte Carlo simulations [239]:

- by ionization (between 40% and 60%, decreasing with increasing A of the absorber material). The primary particle ionizes before the first inelastic interaction occurs, but the largest contribution to the total amount of energy deposited by ionization (about the 70%) comes from secondary spallation protons, produced in nuclear inelastic interactions.

- by the generation of neutrons (between 10% and 15%, decreasing with decreasing A).

- by the production of photons ($\sim 3\%$, from fission).

- by nuclear break-up and recoil of nuclear fragments and target (between 30% and 45%, decreasing with decreasing A).

The dependence with A of the various processes is mainly due to the different average binding energy of the nucleons inside the nuclei and to the ratio Z/A (larger in low-A nuclei), which influences the amount of spallation protons.

In the purely hadronic component of the shower part of the energy disappears without contributing to the calorimeter signal. This is the case of neutrinos, produced mainly in pion decays, and a certain fraction of neutrons, generated during nuclear reactions. The energy spent in breaking up the nuclei is invisible as well.

As long as a hadron does not interact strongly with a nucleus of the absorber material it loses energy mainly by ionization. The probability P_I of having an inelastic hadron-nucleus interaction after a distance x is given by:

$$P_I = 1 - e^{-x/\lambda_I}, \tag{6.9}$$

where λ_I is the nuclear interaction length. The interaction length can be approximated by [236]:

$$\lambda_I = \frac{A}{\left[N\rho\sigma_{nA(inelastic)}\right]} \approx 35\frac{A^{1/3}}{\rho}\mathrm{cm}, \tag{6.10}$$

where ρ is the density (in gcm^{-3}) of the absorber material and N is the Avogadro number. $\sigma_{nA(inelastic)}$ (in cm^{-2}) is the inelastic cross section on the nucleus with mass number A, measured with incoming neutrons [239, 58, 240].

λ_I is taken as unit for hadronic showers. The ratio between λ_I and X_0 can be approximated by [239]:

$$\frac{\lambda_I}{X_0} \approx 0.12\, Z^{4/3}. \tag{6.11}$$

λ_I is in general larger than X_0, which makes hadronic showers longer and less dense than electromagnetic showers.

6.2 Electromagnetic Showers

When the initial energy of an electron (positron) or photon penetrating the calorimeter is high enough ($>> \varepsilon_c$) to initiate a multiplication process, the number of particles (electrons, positrons and photons) increases rapidly with the cascade depth until a maximum is reached, called shower maximum. After the maximum is reached, the multiplicity decreases slowly until the shower extinguishes. To understand this behavior a very simplified approximation can be considered, for an electromagnetic shower initiated by an electron or photon with energy $E >> \varepsilon_c$:

- each electron with energy $> \varepsilon_c$ after a depth of $1\ X_0$ emits a bremsstrahlung photon, loosing half of its energy;

- each photon with energy $> \varepsilon_c$ travels $1\ X_0$ and creates an electron-positron pair, each lepton carrying half the energy of the initial photon;

- when the energy of the produced electrons decreases below ε_c, the radiation process ceases and the residual energy is lost in collisions;

- when the energy of the generated photons decreases below ε_c, they lose their energy via Compton scattering and the photoelectric process;

- no difference between the behavior of electrons and positrons is taken into account.

With this simple model at each interaction step the number of particles roughly doubles, while the energy per particle is on average divided by half. At the depth t, where t is expressed in units of X_0, the number of particles is $N(t) \approx 2^t$ and the average energy per particle is $E(t) \approx \frac{E}{N(t)} = E2^{-t}$. When the average energy is equal to ε_c, the multiplication no longer continues. This occurs at the shower maximum t_{max}, for which $\varepsilon_c \approx E2^{-t_{max}}$, obtaining:

$$t_{max} \approx \ln\frac{E}{\varepsilon_c}. \tag{6.12}$$

After the shower maximum the multiplication ceases and the shower follows a slow exponential decay.
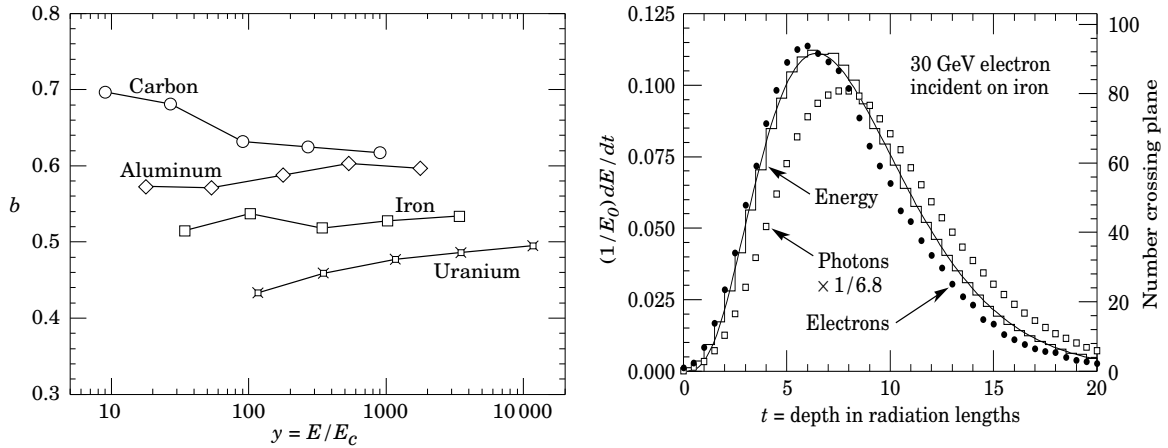
Figure 6.5: *Left: fitted values of the scale factor b (Eq. 6.13) for energy deposition pro-files obtained for a variety of elements for incident electrons with energy in the range [1,100] GeV. Values obtained for incident photons are essentially the same. Right: simulation of a 30 GeV electron-induced cascade in iron. The histogram shows the fractional energy deposition per radiation length, and the curve is a gamma-function fit to the distribution (Eq. 6.13). Circles indicate the number of electrons with total energy greater than 1.5 MeV crossing planes at $X_0/2$ intervals (scale on the right) and the squares the number of photons with $E \geq 1.5$ MeV crossing the same planes (scaled down to have the same area as the electron distribution). From [58].*

Using simulations based on more elaborate assumptions, the following equation to describe approximately the longitudinal development (along the incoming particle direction) of an electromagnetic shower has been found [58, 241]:

$$\frac{dE}{dt} = E_0 b \frac{(bt)^{a-1} e^{-bt}}{\Gamma(a)}, \tag{6.13}$$

where E_0 is the initial energy. $b \approx 0.5$, but in order to determine it accurately the energy of the incident particle and the medium need to be taken into account. Precise values of b, obtained from the simulation of incident electrons in the energy range [1,100] GeV for a variety of absorber materials, are shown in the left plot of Fig. 6.5.

The position of the shower maximum is given by:

$$t_{max} = \frac{a-1}{b} = 1.0 \times (\ln y + C_j), \ j = e, \gamma, \tag{6.14}$$

where $C_e = -0.5$ for electron-induced cascades and $C_\gamma = +0.5$ for photon-induced cascades. y is the energy expressed in units of critical energy. The value of a is derived from the value of b using Eq. 6.14.

The plot on the right in Fig. 6.5 shows an example of the longitudinal profile of a 30 GeV electron traversing iron. The number of electrons and photons as a function of the shower depth is compared with the total energy deposition. The electron multiplicity falls off more quickly than the energy deposition. This happens because, with increasing depth, a larger fraction of the cascade energy is carried by photons. The function of Eq. 6.13 is fitted to the energy deposition, showing a good agreement.

The decay of the shower after the maximum follows an exponential behavior $e^{-t/\lambda_{att}}$, where λ_{att} is called longitudinal attenuation length. The value of λ_{att} is easily derived from b according to Eq. 6.13:

$$\lambda_{att} = \frac{1}{b}. \tag{6.15}$$

The 95% longitudinal containment, $L_{95\%}$, the average calorimeter depth within which 95% of the electromagnetic cascade energy is deposited, can be parametrized as [239]:

$$L_{95\%} \approx 1.01 \left[\ln \left(\frac{E}{\varepsilon_c} \right) - c \right] + 0.08Z + 9.6, \tag{6.16}$$

where $L_{95\%}$ is expressed in units of X_0, E is the incoming energy and $c = 1.0$ or 0.5 for incident electrons or photons, respectively.

The development of electromagnetic showers is characterized also by a transverse spread, i.e. along the direction orthogonal to that of the primary particle. Several physics processes contribute to this lateral development. Secondary electrons generated by photoelectric process and Compton scattered photons are no longer aligned with the incoming photon direction. Also, multiple Coulomb scatterings of those low-energy electrons that cannot radiate, but have enough energy to travel inside the calorimeter, lead to the spread of electron directions out of the axis defined by the primary particle direction.

The unit to describe the transverse development of a cascade is the Molière radius, defined as:

$$R_M = \left(\frac{E_M}{\varepsilon_c} \right) X_0, \tag{6.17}$$

where:

$$E_M = \sqrt{\frac{4\pi}{\alpha}} (m_e c^2) = 21.2 \, \text{MeV}. \tag{6.18}$$

In a compound material containing the weight fraction w_j of the element with critical energy E_{cj} and radiation length X_j, the Molière radius is given by:

$$\frac{1}{R_M} = \frac{1}{E_S} \sum_j \frac{w_j E_{cj}}{X_j}. \tag{6.19}$$

On the average, only the 10% of the total energy is deposited outside a cilinder of radius R_M. The 95% radial containment is reached approximately at $2R_M$.

The transverse development of electromagnetic showers has a double structure, which displays a narrow central and a broad peripheral part. The core of the shower scales as R_M and is mainly due to multiple scattering of electrons. The propagation of photons is responsible for the peripheral part. The spatial distribution of this latter component is
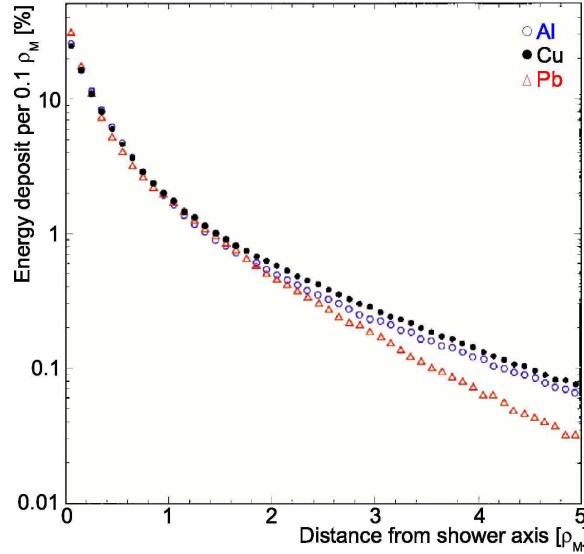
Figure 6.6: *Simulated transversal development of electromagnetic showers, induced by 10 GeV electrons in aluminum, copper and lead. From [243].*

determined by the mean free path of photons, which depends strongly on the absorber material. Grindhammer describes the transversal shape of the showers as [58, 242]:

$$f(r) = \frac{2rR^2}{(r^2 + R^2)^2},$$
(6.20)

where R is a phenomenological function of the shower depth in units of X_0 and $\ln E$. The simulated energy deposition along the transverse direction of electromagnetic showers in various absorbers is shown in Fig. 6.6.

6.3 Hadronic Showers

The hadronic cascade, similarly to the electromagnetic cascade, develops along the longitudinal direction, as long as the produced secondaries have enough energy to continue the multiplication process.

The longitudinal development is described in units of interaction length λ_I, already introduced in Eq. 6.10.

The position of the shower maximum can be approximated by [239]:

$$t_{max} \approx 0.2 \ln[E(\text{GeV})] + 0.7,$$
(6.21)

while the longitudinal attenuation length, describing the exponential decay of the cascade beyond t_{max}, varies with energy like [239]:

$$\lambda_{att} = [E(\text{GeV})]^{0.13},$$
(6.22)

both t_{max} and λ_{att} being expressed in units of λ_I. Using the expressions in Eq. 6.21 and 6.22, the 95% longitudinal containment of hadronic showers is given by [239]:

$$L_{95\%} \approx t_{max} + 2.5\lambda_{att}.$$
(6.23)
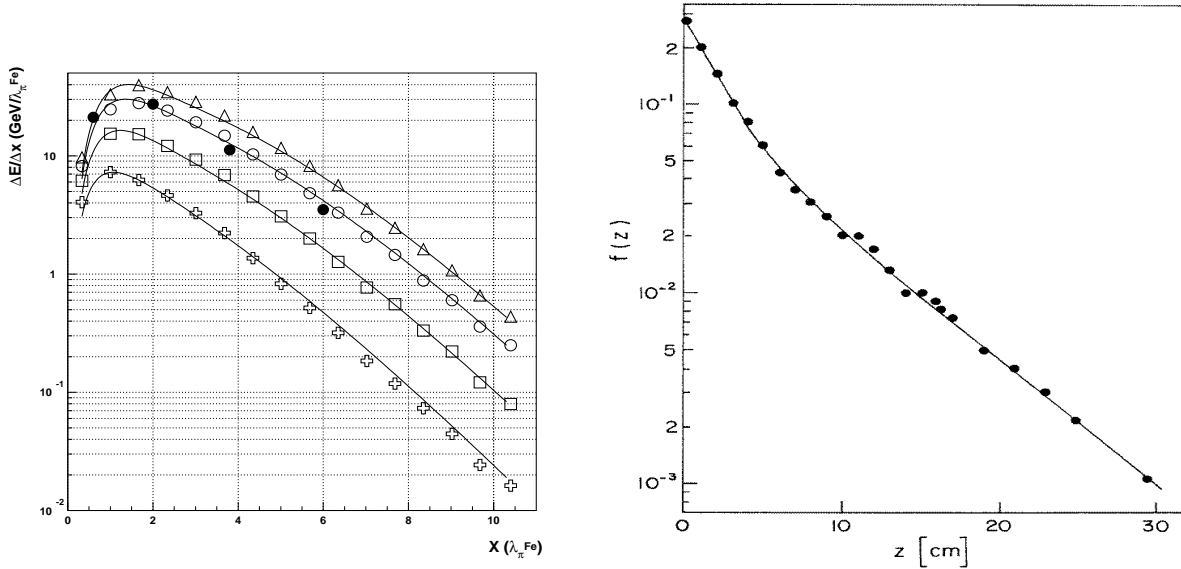
Figure 6.7: *Left: longitudinal profiles of hadronic showers of 20 GeV (crosses), 50 GeV (squares), 100 GeV (open circles) and 140 GeV (triangles) energies as a function of the longitudinal coordinate x in units of λ_I for conventional iron-scintillator calorimeter and of 100 GeV (black circles) for tile iron-scintillator calorimeter. The solid lines are derived from analytical calculation. From [244]. Right: mean differential lateral profile, $f(z)$, as a function of the lateral distance z (cm) for incoming antiprotons of 25 GeV in a scintillator/Fe calorimeter. From [239].*

The longitudinal profile of hadronic showers is similar to the profile of electromagnetic showers. However, the scale is quite different, since the containment of hadronic showers is much more demanding in terms of calorimeter depth. This is reflected in the significant difference between X_0 and λ_I. Some values of the two quantities, for common materials employed in calorimetry, are given in Tab. 6.1.

The analytical representation of the longitudinal hadronic shower development has been studied in [244], using data from iron-scintillator calorimeters. The results, shown in the left plot of Fig. 6.7, demonstrate a good agreement between the theoretical parametrization and the data.

The transverse profile of hadronic showers in exemplified by the right plot of Fig. 6.7. The lateral spread is due to the production of secondaries at large angles (e.g. [245]). As in the case of electromagnetic showers, also the transverse behavior of hadronic showers has two components: a main component along the cascade axis, which decays fast, and a broad peripheral component of mostly low-energy particles, which carry a relevant fraction of the shower energy away from the central core of the cascade. The transverse profile can be described by the sum of two exponentials, accounting for the two components [239]:

$$f(z) = A_1 \exp\left(-\frac{|z - z_0|}{b_1}\right) + A_2 \exp\left(-\frac{|z - z_0|}{b_2}\right), \qquad (6.24)$$

where z is the transverse coordinate in cm and z_0 is the impact point of the cascade. For the example of Fig. 6.7, of 25 GeV antiprotons in an iron-scintillator calorimeter, $A_1 \approx \frac{2}{3}$, $A_2 \approx \frac{1}{3}$, $b_1 = 2.2$ cm and $b_2 = 7.0$ cm.

Material	Symbol	Z	ρ [g/cm^3]	X_0 [cm]	R_M [cm]	ε_c [MeV]	λ_I [cm]
Aluminum	Al	13	2.7	8.90	4.42	42.70	39.70
Iron	Fe	26	7.9	1.76	1.72	21.68	16.77
Copper	Cu	29	9.0	1.44	1.57	19.42	15.32
Tungsten	W	74	19.3	0.35	0.93	7.97	9.95
Lead	Pb	82	11.4	0.56	1.60	7.43	17.59
Uranium	U	92	19.0	0.32	1.01	6.65	11.03
Polystyrene	$[C_6H_5CHCH_2]_n$		1.1	41.3	9.41	93.11	77.07
Silicon	Si	14	2.3	9.37	4.94	40.19	46.52
Liquid Argon	Ar	18	1.4	14.00	9.04	32.84	85.77

Table 6.1: *Relevant quantities to describe showers in common materials employed in high energy physics calorimetry. The first part of the table lists common absorbers, while the second part lists materials used as sensitive detectors. The critical energy reported ε_c is for electrons. Values from [58].*
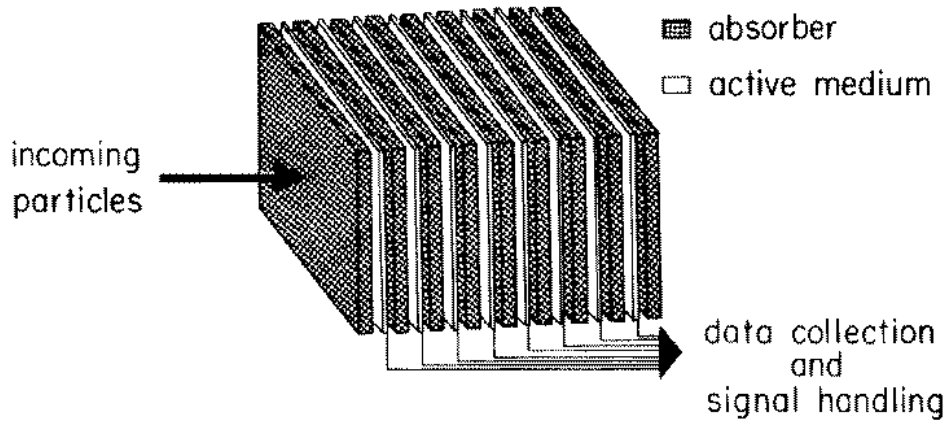
Figure 6.8: *Sampling calorimeter: passive samplers interspaced by active readout detector planes. From [239].*

The 95% radial containment ($R_{95\%}$) for hadronic cascades is:

$$R_{95\%} \approx 1\lambda_I. \tag{6.25}$$

Some relevant quantities to describe electromagnetic and hadronic showers in several materials common in high energy physics calorimeters are summarized in Tab. 6.1.

6.4 Sampling Calorimeters

The common structure of sampling calorimeters is shown in Fig. 6.8: layers of passive samplers are interleaved with active readout planes.

The passive layers are responsible for the shower development. The absorber material is generally dense, with a high atomic number and short interaction and radiation lengths. The readout material has usually a lower density and a lower atomic number. The active layers have a thickness (in terms of radiation length) much smaller than the thickness of the absorber layers. Their task is to measure those components of the

shower that produce in the readout material visible signals. The measurable deposited energy is called visible energy ε_{vis}. Usually, it consists just in a tiny fraction of the energy of the incoming particle E, to which it is proportional:

$$\varepsilon_{vis} \propto E. \tag{6.26}$$

Eq. 6.26 is the basic principle of calorimetry and holds very well for electromagnetic showers, in which almost all the energy of the incoming particle is dissipated in detectable processes. The response of the calorimeter is then expected to have a linear dependence with energy, excluding leakage or intrinsic non-linearities of the readout devices.

The response to hadronic showers in more complex. As explained in Sec. 6.1.4, the development of the cascade includes processes that do not produce visible signals, such as the breaking up of nuclei or the production of neutrons and neutrinos. Moreover, hadronic showers have an electromagnetic component that fluctuates event-to-event, which represents an additional complication. This is due to the fact that many hadron calorimeters respond differently to the pure hadronic and the electromagnetic fractions of hadronic showers.

Details about the response to electromagnetic and hadronic showers in sampling calorimeters are given in the following.

6.4.1 Response to Electromagnetic Showers

The response of the calorimeter depends on the incident particle type and energy. The scale for the calorimetric signal is defined by the response to a *mip*. The *mip* is here meant as an imaginary particle that loses energy only by ionization at the minimum of the dE/dx (Sec. 6.1.2). The energy loss of a *mip* depends mainly on the thickness of the traversed material and only weakly on the material itself. The behavior of a *mip* can be approximated by the response to a low energetic muon in the GeV range or computed, by using the mean dE/dx values of the different materials composing the calorimeter.

The response of the calorimeter to a *mip* is expressed by the sampling fraction, which is the ratio of the detected energy to the total energy E_{tot} deposited in the calorimeter. This definition is extended also to real showering particles. Sometimes the inverse of the sampling fraction, called sampling factor SF, is used instead:

$$SF \equiv \frac{E_{tot}}{\varepsilon_{vis}}. \tag{6.27}$$

The response of the calorimeter to particles originating electromagnetic showers, electrons, positrons and photons, is defined by the e/mip ratio:

$$\frac{e}{mip} \equiv \frac{\varepsilon_{vis}(e)}{\varepsilon_{vis}(mip)}, \tag{6.28}$$

where $\varepsilon_{vis}(e)$ is the average signal deposited in the sensitive part of the calorimeter by an electron (or photon) with initial energy E and $\varepsilon_{vis}(mip)$ is the average signal

generated by a *mip* losing the same energy E when traversing the calorimeter. The *e/mip* ratio provides a way to determine how much the energy-deposition processes for electromagnetic showering particles and *mips* differ from each other. It is energy independent and represents the fundamental characteristic of the structure of sampling calorimeters, essentially related to the difference between the readout and absorber Z values. The *e/mip* ratios are smaller than 1 for $Z_{absorber} > Z_{readout}$, approximately 1 for $Z_{absorber} = Z_{readout}$ and bigger than 1 for $Z_{absorber} < Z_{readout}$. This difference is mainly due to the soft component of the electromagnetic shower, constituted by the low-energy particles produced in the cascade, by which most of the initial energy is deposited in matter. For a fixed amount of matter in g cm^{-2}, the flux of low-energy photons is less attenuated in low-Z than in high-Z media. Less soft photoelectrons are generated and locally absorbed in low-Z materials [239].

Common active materials like scintillator, silicon and liquid argon have lower Z than absorber materials, resulting in a *e/mip* ratio smaller than 1 (referred to as *electromagnetic sampling inefficiency*). For medium-Z passive absorbers, like Fe or Cu, typical *e/mip* values are ≈ 0.85, while for high-Z passive absorbers, like W, Pb or U, *e/mip* ≈ 0.65.

6.4.2 Response to Hadronic Showers

For the same incoming energy, the signal of electrons (or photons), e, is usually larger than the signal of hadrons, due to the invisible component of hadronic showers (Sec. 6.1.4). Indicating with h the signal of an ideal hadron, generating a pure hadronic cascade without electromagnetic sub-showers ($f_{em} = 0$), the difference between the response to electromagnetic and ideal hadronic showers is expressed by the e/h ratio:

$$\frac{e}{h} \equiv \frac{\varepsilon_{vis}(e)}{\varepsilon_{vis}(h)}, \tag{6.29}$$

where $\varepsilon_{vis}(e)$ and $\varepsilon_{vis}(h)$ are the visible energies, at the same incoming particle energy. The ratio e/h is usually larger than 1 and is energy independent, being both $\varepsilon_{vis}(e)$ and $\varepsilon_{vis}(h)$ proportional to the energy of the incoming particle. Thus, the e/h ratio can be considered an intrinsic property of the calorimeter, depending on the type and the thickness of the passive and active layers.

The response to a real hadron is usually indicated with π and is the sum of pure electromagnetic and ideal hadronic signals:

$$\varepsilon_{vis}(\pi) = f_{em}\varepsilon_{vis}(e) + (1 - f_{em})\varepsilon_{vis}(h). \tag{6.30}$$

On the contrary to $\varepsilon_{vis}(e)$ and $\varepsilon_{vis}(h)$, which are proportional to the original energy, f_{em} has a logarithmic energy dependence (cf. Sec. 6.1.4). As a result $\varepsilon_{vis}(\pi)$ is not linearly dependent on the incoming hadron energy. The ratio e/π, summarizing the difference between the response to electromagnetic and real hadronic showers, depends on the energy of the incoming particle, the atomic weight of the absorber, and the Z-values of both active and passive layers. The atomic weight of the absorber mainly matters since it influences the amount of invisible energy, while the Z-dependence is

mostly caused by the electromagnetic shower component. The e/π signal ratio is given by:

$$\frac{e}{\pi} \equiv \frac{\varepsilon_{vis}(e)}{\varepsilon_{vis}(h)} = \frac{\varepsilon_{vis}(e)}{f_{em}\varepsilon_{vis}(e) + (1 - f_{em})\varepsilon_{vis}(h)} = \frac{e/h}{1 - f_{em}(1 - e/h)}. \qquad (6.31)$$

The relation between e/h and e/π is:

$$\frac{e}{h} = \frac{(e/\pi)(1 - f_{em})}{1 - f_{em}(e/\pi)}. \qquad (6.32)$$

Analogously to e/mip it is possible to define as well h/mip and π/mip, using the calorimeter response to mips as a scale of measurement of the response to ideal and real hadrons. For the reasons mentioned above, while h/mip is an intrinsic energy-independent property of the calorimeter, π/mip depends on the hadron incoming energy, owing to the energy-dependent term f_{em}.

In hadron calorimeters the neutrons produced in the cascade usually contribute in a minimal way to the overall visible energy. The main contribution to the signal comes from ionization processes, mostly due to spallation protons. As mentioned in Sec. 6.1.4, these processes deposit between $\approx 40\%$ (high-A nuclei) and $\approx 60\%$ (low-A nuclei) of the incoming energy. If the active media have a linear response to the energy deposited by collisions, the h/mip ratio is expected consequently to be slighlty larger than ≈ 0.4 and ≈ 0.6 for high-A and low-A nuclei, respectively [239].

6.4.3 Compensation

The condition $e/h = e/\pi = 1$ (or, equivalently, $h/mip = \pi/mip = e/mip$) is called the *compensating condition*, satisfied when a calorimeter gives the same response to hadrons and electrons (or photons), for equal incoming energy.

The importance of compensation is due to the mixed nature of hadronic showers, which include an electromagnetic component, f_{em}. Such a component increases in average with energy (cf. Eq. 6.8). In Eq. 6.30 it is shown that the response to pions depends on such an energy-dependent quantity f_{em}. Only in case of compensation the energy dependence of f_{em} cancels that of $(1 - f_{em})$, otherwise the response of the calorimeter to real hadrons is intrinsically non-linear. Moreover, if e/h is different from 1, the large event-to-event fluctuations of f_{em} lead to a deterioration of the resolution for hadrons (Sec. 6.4.4). Since such fluctuations are non-Gaussian, the resulting signal for monoenergetic hadrons is non-Gaussian as well. This is a non-negligible drawback, especially in an environment where high trigger selectivity is required. For example, if one wants to trigger on transverse energy, it will be very difficult to unfold a steeply falling transverse energy distribution and a non-Gaussian response function. Moreover, severe trigger biases are likely to occur: if $e/h < 1$ (> 1) one will predominantly select events that contain small (considerable) amounts of f_{em} [246].

Most of the calorimeters are non-compensating. Typically $e/h \simeq 1.1 - 1.35$ (though also $e/h < 1$ is possible). Methods to achieve the compensating condition, or to minimize the drawbacks of a missing compensation, are illustrated in the following.

Hardware Compensation

The hardware compensation is achieved by enhancing the hadronic signal and/or attenuating the electromagnetic signal.

The increase of the hadronic signal can be obtained by enhancing the detection of the neutrons generated during the cascade. Employing hydrogen-rich materials (for instance plastic scintillators) as active media, fast recoiling and ionizing protons are generated via neutron-proton scattering and are detected in the sensitive layers. The increase of the hadronic signal is limited by the saturation of the scintillator response, which occurs in the presence of dense ionization loss, as described by the Birk's law [247]. Another possible contribution to the enhancement of the hadronic response comes from employing a fissionable absorber material (depleted U^{238}), due to the high yield of neutrons produced in the fission process and nuclear γs produced in the de-excitation of fission fragments. In this case it is necessary to detect a large fraction of the abundantly produced fission neutrons, in order to achieve a sensible benefit. This is achieved either by increasing the signal integration time, or by using hydrogenous active materials.

The attenuation of the electromagnetic response can be achieved by shielding the active layers by thin sheets of passive low-Z materials, in order to suppress the photoelectric signal generated by the soft photons component of the shower.

Finally, the adjustment of the relative thicknesses of absorber and active layers also plays an important role in achieving the compensating condition. The fraction of the neutron's kinetic energy transferred to recoil protons in the active layers varies much more slowly with the relative amounts of passive and active material than does the fraction of the energy deposited by charged particles. Therefore, the relative contribution of neutrons to the calorimeter signal, and hence to e/h, can be varied by changing the sampling fraction [238].

Software Compensation

The software compensation is a completely different approach from the hardware compensation. It is applied to reduce the mentioned disadvantages of an intrinsically non-compensating detector by means of off-line corrections to the measured data. In this approach, which requires a very fine-grained detector, one tries to identify the electromagnetic content on a shower-by-shower basis and a weighting scheme is used to correct for the different calorimeter responses to the pure hadronic and the electromagnetic components of hadronic showers. One experiment successfully using such a technique was the Pb/LAr H1 calorimeter [248]. Using the CALICE prototype (described in Chap. 7), thanks to the high granularity, it was also possible to apply weighting algorithms to improve the hadronic response. The significant improvement on the energy resolution that was obtained for hadrons at several energies is shown in fig 6.9.

The Dual Readout

Traditionally, hadron calorimeters detect signals related to the total energy deposited in the active medium of the calorimeter. In the innovative Dual-Readout calorimetry realized by the DREAM collaboration [250] the signal due to the electromagnetic
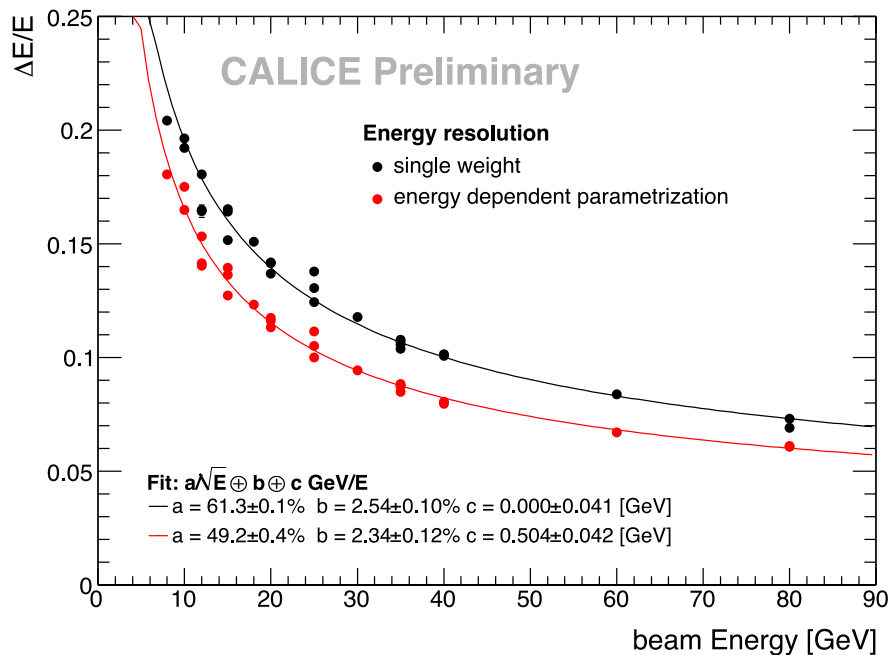
Figure 6.9: *Energy resolution for hadrons with (red) and without (black) software compensation. Weights are determined from and applied to pion data collected using the full CALICE setup (Chap. 7). From [249].*

components of hadronic showers is measured separately. Since electromagnetic particles are still relativistic at low energies, their energy deposition is well characterized by Cherenkov light, whereas heavy particles generate Cherenkov light only at higher energies. Therefore, the electromagnetic component and the total visible energy of the shower can be measured by detecting the Cherenkov light and the scintillation light separately. This is possible using both scintillating fibers and quartz fibers, which are sensitive to the Cherenkov light. The two signals are then properly combined after weighting. Also investigated is the possibility to separately detect the Cherenkov and the scintillation light using scintillating crystals, exploiting the different features of the two signals [251].

6.4.4 Energy Resolution

The measurement of the energy of particles in calorimeters is a statistical process. The fraction of energy deposited in the active media, where the detection takes actually place, underlies statistical fluctuations on an event-by-event basis.

The statistical fluctuations in ε_{vis} are determined, among other factors, by the fluctuations in the number n of particles contributing to the visible signal. Since the multiplicity of the cascade increases with increasing energy of the incoming particle, the energy resolution will relate to n as:

$$\left(\frac{\sigma_E}{E}\right)_{\text{samp}} = \frac{\sigma \varepsilon_{vis}}{\varepsilon_{vis}} \propto \frac{1}{\sqrt{n}} \propto \frac{1}{\sqrt{E}}, \tag{6.33}$$

where σ_E is the width of the measured energy distribution for the detection of monoenergetic particles with energy E. The relevant feature that emerges from this equation

is that the statistical component of the resolution improves with increasing energy. Moreover, due to the pure statistical nature of the fluctuations, this component of the energy resolution has a Gaussian behavior. However, in many detectors other factors contribute in a non-negligible way to the energy resolution. These factors may concern statistical processes with a Gaussian probability distribution, or they may be of a different nature. In the latter case, their contribution to the energy resolution will cause deviations from the $1/\sqrt{E}$ scaling law.

An energy-independent degradation of the energy resolution is given by calibration uncertainties, non-uniformities and non-linearities of detectors and read-out electronics:

$$\left(\frac{\sigma_E}{E}\right)_{\text{const}} \propto c. \tag{6.34}$$

An important role is also played, in particular at low energies, by instrumental effects, e.g. noise. Just like the signal coming from physics events, the noise is translated into a corresponding amount of measured energy. Though the average contribution of noise can be evaluated and subtracted, it underlies fluctuations, which are independent of the cascade development and, therefore, contribute to the resolution as:

$$\left(\frac{\sigma_E}{E}\right)_{\text{noise}} \propto \frac{b}{E}. \tag{6.35}$$

In the specific case of sampling calorimeters, the statistical fluctuations in the energy measurement depend on the sampling fraction and on the sampling frequency, i.e. the number of readout active layers in a given detector volume [246]. The dependency of the energy resolution on the sampling frequency f is given by [246, 252]:

$$\left(\frac{\sigma_E}{E}\right)_{\text{samp}} \propto \frac{1}{\sqrt{f}}, \tag{6.36}$$

In calorimeters with dense active material (plastic-scintillator, LAr), the energy resolution gets worse, when increasing the thickness t_{abs} of the absorber layers, like [246]:

$$\left(\frac{\sigma_E}{E}\right)_{\text{samp}} \propto \sqrt{\frac{t_{abs}}{E}}. \tag{6.37}$$

Increasing the thickness t_{act} of the active planes benefits the resolution, with a scaling low which depends on the material used. For Fe/LAr, one finds approximately [246]:

$$\left(\frac{\sigma_E}{E}\right)_{\text{samp}} \propto t_{act}^{-\frac{1}{4}}. \tag{6.38}$$

The performance of a calorimeter depends also on the type of particle considered. The resolution for electromagnetic particles is better than the resolution for hadrons. First of all, there is a pure statistical reason. In hadronic showers less particles with a larger average energy are responsible for the signal (due in particular to the contribution of protons), with respect to electromagnetic showers (lower n in Eq. 6.33). Additionally, two more sources of fluctuations have to be considered: the fluctuations of the electromagnetic fraction (which are non-Gaussian) and the invisible energy.

The impact of the fluctuations of the electromagnetic fraction vanishes only for compensating calorimeters, otherwise it contributes with a constant term to the resolution.

Detector	Accelerator	EM techn.	HAD techn.	EM $(\sigma_E/E)_{samp}$ GeV$^{-1/2}$	HAD $(\sigma_E/E)_{samp}$ GeV$^{-1/2}$
ZEUS	HERA (ep)	U/scint.	U/scint.	18%	35%
H1	HERA (ep)	Pb/LAr	Fe/LAr	11%	50%
DØ	Tevatron ($p\bar{p}$)	U/LAr	U/LAr	15.7%	41%
CDF	Tevatron ($p\bar{p}$)	Pb/scint.	Fe/scint.	13.5%	80%
ATLAS	LHC (pp)	Pb/LAr	Barrel: Fe/scint. Endcap: Cu/LAr Forward: W/Cu/LAr	10-12%	50%
CMS	LHC (pp)	PbWO$_4$	Barrel: brass/scint. Endcap: brass/scint. Forward: Fe/quartz	2.8-3.6%	85%
ALEPH	LEP (e^+e^-)	Pb/PWC	Fe/lim. streamer	18%	84%
OPAL	LEP (e^+e^-)	Pb glass	Fe/lim. streamer	6.3%	120%
SLD	SLC (e^+e^-)	Pb/LAr	Pb/LAr Fe/lim. streamer	15%	≈60%

Table 6.2: *Sampling (or stochastic) terms of the energy resolution for important high-energy physics detectors. Abbreviations: EM, electromagnetic; HAD, hadron; techn., technology; LAr, Liquid Argon; PWC, Proportional Wire Chamber; lim., limited. Values from [254].*

The fluctuations of the invisible energy constitute the so-called *intrinsic resolution* of the calorimeter, which represents the ultimate limit for the energy resolution achievable with hadron calorimeters. An efficient neutron-detection, given for example by employing hydrogen-rich materials (for instance plastic scintillators) as active material, helps to improve the intrinsic resolution, since it reduces the invisible energy (Sec. 6.4.3). The DREAM Collaboration (Sec. 6.4.3) plans a triple-readout calorimeter in which the neutron signal is measured for each event using the time response of the scintillation signal [253].

The resolution for hadronic showers can be summarized as [246]:

$$\left(\frac{\sigma_E}{E}\right)_{\text{had}} \propto \sqrt{\frac{c_{int}^2 + c_{samp}^2}{E}} + \phi(e/\pi), \qquad (6.39)$$

where $\phi(e/\pi)$ is the constant term present in case of non-compensation.

Due mainly to cost issues, the dimensions of the calorimeters are limited and effects of non-containment of the showers might also contribute to deteriorate the energy resolution. These effects are usually indicated as leakage and are discussed below in Sec. 6.4.6.

The sampling (also known as stochastic) terms of the energy resolution for important high-energy physics electromagnetic and hadron calorimeters are given in Tab. 6.2.

6.4.5 Position Measurement

The active layers of sampling calorimeters are usually segmented in the transverse direction in single units, called cells, which are read-out individually. If the dimensions of the cells are equal or smaller than the Molière radius, from the lateral spread of the cascade over several cells it is possible to derive the impact point of the incident particle:

$$\bar{x} = \frac{\sum_i x_i E_i}{\sum_i Ei},$$
(6.40)

where x_i is the x coordinate of the cell i, where an energy E_i was deposited. x is one of the two coordinates identifying the plane orthogonal to the incoming particle direction. The same equation is valid also along the other coordinate. The precision obtained in this way on the impact point improves with decreasing cell sizes. It improves also with increasing energy, like:

$$\sigma_{\bar{x}} \propto \frac{1}{\sqrt{E}},$$
(6.41)

where $\sigma_{\bar{x}}$ is the resolution on $\bar{x}$.

6.4.6 Impact of Leakage

As already mentioned in Sec. 6.4.4, the leakage has an impact on the energy resolution. Usually one indicates with leakage the non-containment of showers in the lateral or longitudinal direction. However, the loss of part of the showers might be also due to cracks and dead areas/cells. Some clustering algorithms might contribute to the leakage, as well. For instance, isolated energy deposits in the peripheral part of the shower might be identified as noise and not added to the cluster reconstructed energy.

The effects of the lateral and longitudinal shower leakage have been investigated experimentally by the CHARM collaboration [255, 239], both for electromagnetic and hadronic showers, using a fine-grained marble calorimeter. The results are shown in Fig. 6.10.

For energy losses up to about 15-20% the calorimeter energy resolution is related linearly to the average fraction, in per cent, of the lateral and longitudinal leakage. The impact of the longitudinal leakage is visibly more dramatic, due to the different fluctuations that determine the amount of leakage in the longitudinal and transverse direction. The longitudinal leakage is dominated by the fluctuations in the shower starting point, which are due to the statistical behaviour of one single particle, the initial one. The fluctuations in the lateral development of the shower are the effect of the statistical behaviour of hundreds of particles generated during the cascade, which is in average more stable.
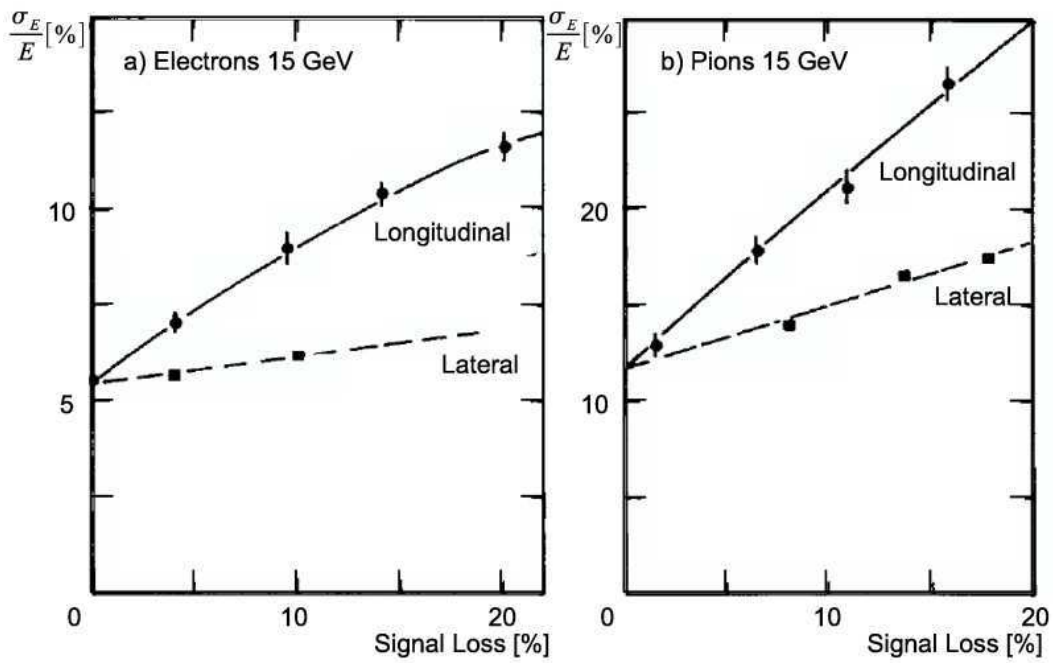
Figure 6.10: *Energy resolution measured as a function of the fraction of lateral and longitudinal deposited energy losses, for electromagnetic showers (left) and hadronic showers (right). From [243, 236].*

7 The CALICE Prototypes

The CALICE (CAlorimeter for the LInear Collider Experiment) collaboration has constructed prototypes of highly granular calorimeters, with the main aim to test the feasibility of the particle flow paradigm (Sec. 3.4.1). The high precision in the reconstruction of the shower development, allowed by the fine granularity, gives new challenges to the shower models used for the Monte Carlo simulations and provide valuable inputs to their validation (Sec. 8.2). Moreover, it provides precision observables, that can be exploited in several physics studies.

In Chap. 8 hadronic data collected using the CALICE prototypes are analyzed, focusing in particular on the leakage (Sec. 6.4.6). During the test beam operations, when the analyzed data were acquired, the full CALICE setup consisted of a silicon-tungsten electromagnetic sampling calorimeter (SiW-ECAL) [256], a scintillator-steel hadron sampling calorimeter with analog readout (AHCAL) [257] and a scintillator-steel tail catcher and muon tracker (TCMT) [258]. In the following a description of the three prototypes is given, focusing in particular on the AHCAL, since it plays a central role in the performed study. The other detectors mainly support the event selection (Sec. 8.1.2).

7.1 The CALICE Prototypes

In this section the main characteristics of the three prototypes, SiW-ECAL, AHCAL and TCMT, are described. An outline of the full test beam installation is also given, as it was at CERN in 2007, when the data used in this work were collected.

7.1.1 The SiW-ECAL

The SiW-ECAL detector is the sum of three stacks, each composed of 10 modules of alternating tungsten and silicon layers. Each stack has tungsten layers with different thicknesses: $1.4\,\text{mm}$ (0.4 radiation lengths X_0) per layer in the first stack, $2.8\,\text{mm}$ or $0.8\,X_0$ in the second and $4.2\,\text{mm}$ or $1.2\,X_0$ in the third one. The active silicon layers are segmented into diode pads of $1 \times 1\,\text{cm}^2$.

The overall thickness of the prototype is about $20\,\text{cm}$, corresponding to about $24.6\,X_0$ or 0.9 nuclear interaction lengths λ_I. The SiW-ECAL has only a small lateral area of $\sim 20 \times 20\,\text{cm}^2$, which makes lateral leakage likely for hadronic showers.

7.1.2 The AHCAL

The AHCAL is a sampling structure of 38 modules, each consisting of a $\sim 2\,\text{cm}$ thick absorber steel plate and a sensitive layer instrumented with $0.5\,\text{cm}$ thick scintillator tiles.
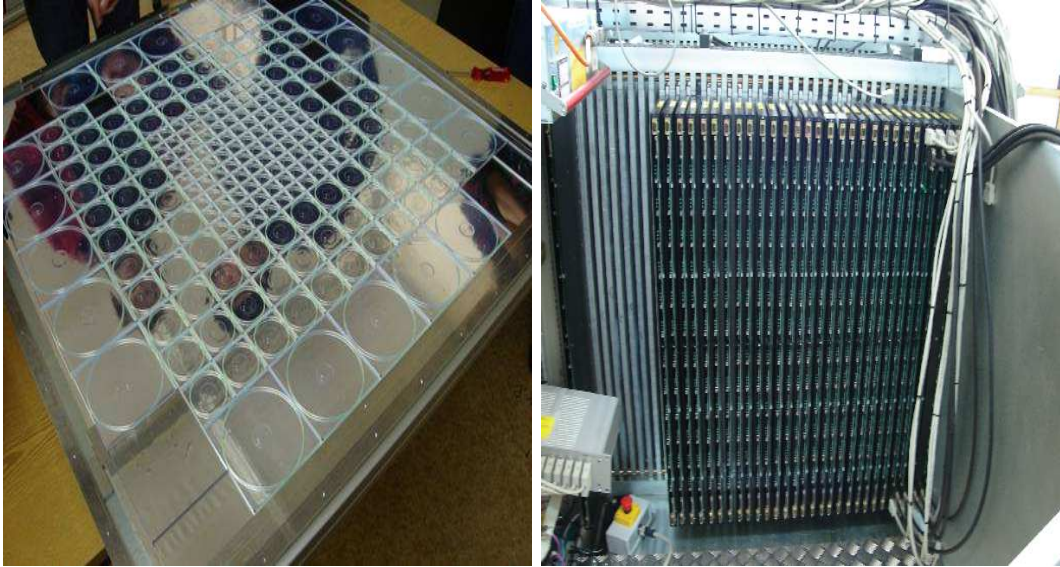
Figure 7.1: *Left: segmentation of a sensitive layer of the AHCAL. The size of the scintillator tiles increases towards the outer region. Right: steel stack support structure of the AHCAL, with active layers installed. From [259].*

Each sensitive layer is an array of 216 scintillators of different sizes. The $30 \times 30\,\mathrm{cm}^2$ core has a granularity of $3 \times 3\,\mathrm{cm}^2$, while the outer region is equipped with tiles of increasing sizes ($6 \times 6\,\mathrm{cm}^2$ and $12 \times 12\,\mathrm{cm}^2$). The segmentation of the sensitive layers is shown in Fig. 7.1. For the last eight layers the highly granular core is replaced by $6 \times 6\,\mathrm{cm}^2$ tiles for cost reasons. Each tile is read out individually by a Silicon Photo-Multiplier (SiPM) (Sec. 7.2.3), coupled to the scintillator via a WaveLength Shifting (WLS) fiber (Sec. 7.2.2).

The total depth of the prototype is 1.2 m, giving 5.3 nuclear interaction lengths λ_I or equivalently 4.3 pion interaction lengths. The lateral section has a size of approximately $1\,\mathrm{m}^2$.

More details on the AHCAL are given in the following.

7.1.3 The TCMT and the ILC-Like Configuration

A TCMT is positioned after the AHCAL, in order to increase the total depth of the calorimetric system and to absorb the tails of the showers leaking out from the AHCAL. The TCMT has a lateral section of $109 \times 109\,\mathrm{cm}^2$ and is 142 cm long (corresponding to $5.8\,\lambda_\mathrm{I}$). It consists of two sections, a *fine* one and a *coarse* one. Each section has 8 sensitive layers, alternated with steel absorbers. The absorber plates are 2 cm thick in the fine section and 10 cm thick in the coarse. The sensitive layers are 0.5 cm thick and are segmented into 5 cm wide and 1 m long scintillator strips, with alternated horizontal and vertical orientation in adjacent layers. The scintillation light is collected by WLS fibers and detected by SiPMs, as for the AHCAL prototype.

In this work, the TCMT mainly serves the event selection, in particular the rejection of muons, but it also allows one to create more closely the conditions of the calorimetric system planned for the ILD detector (Sec. 3.4.2), in terms of longitudinal depth.

The hadron calorimeter for the ILD has a depth of about $6\,\lambda_\mathrm{I}$ and is separated from the tail catcher by a coil of $1.9\,\lambda_\mathrm{I}$ [163]. This design can be approximately reproduced
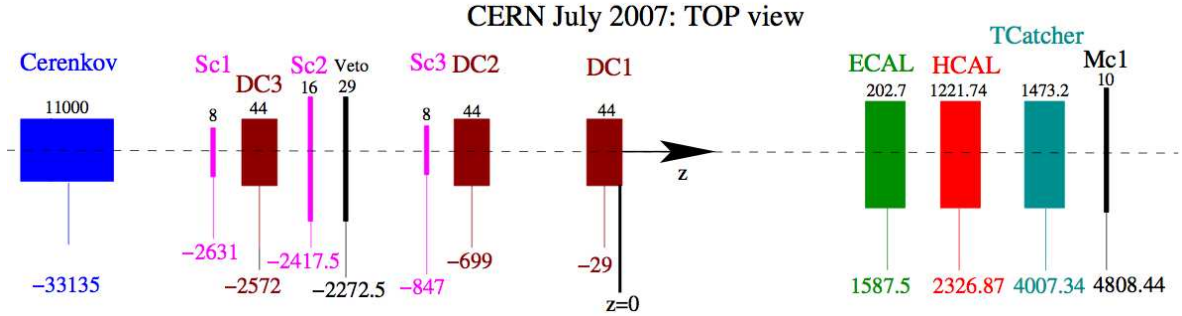
Figure 7.2: *Schematic layout of the CALICE beam tests at CERN in 2007. The figure is not to scale, real dimensions are indicated in mm. From [260].*

by adding to the AHCAL measurements the information collected using the first 8 layers of the TCMT and dropping the energy collected in the first 3 layers of the coarse section of the TCMT, to simulate the presence of a non-instrumented coil. Such a configuration is called in the following *ILC-Like*. According to the nominal thicknesses of the TCMT absorber layers, this corresponds approximately to a $6.3\,\lambda_I$ long hadron calorimeter and a $1.8\,\lambda_I$ long coil. The available amount of layers is not enough to reproduce the depth of the ILD instrumented yoke. One is left with 5 TCMT coarse layers after the simulated coil. The ILD yoke has 10 layers with similar composition, plus 2 (end cap) or 3 (barrel) thicker additional layers, with 560 mm thick iron plates as absorber. However, since the leakage from the TCMT is very small in the energy range considered in this work (Chap. 8), up to 100 GeV, this does not limit significantly the ILC-Like configuration, with respect to the ILD design.

7.1.4 The Test Beam

In 2007 tests using particle beams were conducted, in order to evaluate the performance of the CALICE prototypes. The detectors were installed at the CERN Super Proton Synchrotron and exposed to muon, positron and pion beams provided by the H6 beam line. During these tests the SiW-ECAL and the AHCAL were mounted on a movable stage, providing the possibility to translate and rotate the calorimeters with respect to the beam. However, for the work described in this thesis, only those data were used, which were collected with the beam incident in the center of the calorimeters, along the calorimeters axis.

Three sets of wire chambers were operated during the data taking upstream the detectors, in order to check the beam coordinates. Three upstream scintillator counters and one downstream muon veto counter were used for triggering purposes. A Cherenkov counter was also operated in threshold mode to improve the particle identification. For electron runs the pressure of the Cherenkov detector was adjusted in order to veto the pions, while in the π^+ runs it was so as to separate the protons.

The layout of the test beam configuration is shown in Fig. 7.2.
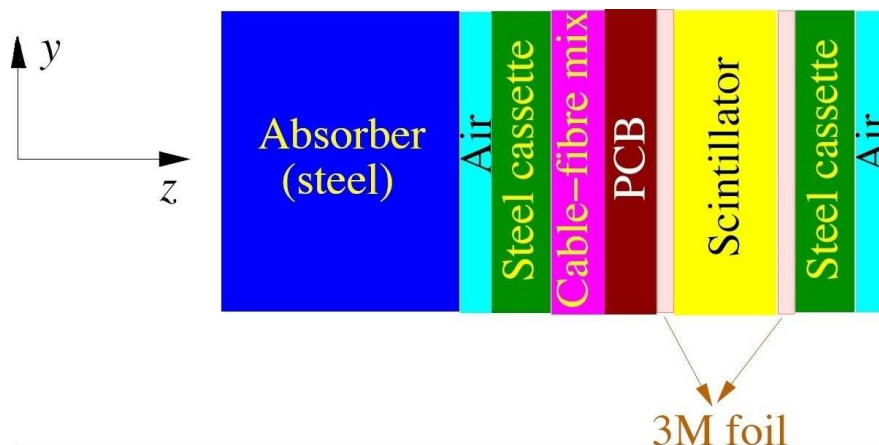
Figure 7.3: *Schematic cross section of an AHCAL module (not to scale). From [257].*

material	$\#\lambda_\pi$	$\#\lambda_I$	$\#X_0$	t [cm]	t_{layer} [cm]
Steel plate	3.237	3.941	37.555	66.19	1.74
Cassette plates	0.743	0.905	8.624	15.2	2×0.2
Scintillator tile	0.177	0.247	0.460	19.0	0.5
FR4	0.053	0.072	0.217	3.8	0.1
3M foil	0.008	0.011	0.021	0.9	0.023
Air gaps				9.5	2×0.125
Cable mix	0.061	0.081	0.286	5.7	0.15
AHCAL	4.28	5.26	47.16	120.26	3.163

Table 7.1: *Number of pion interaction lengths (λ_π), nuclear interaction lengths (λ_I), radiation lengths (X_0) and thickness in the 38 layers of the AHCAL. The last column shows the average thickness of an individual layer. The exact thickness per layer varies from 3.093 cm to 3.183 cm due to variable sizes of the steel plates. From [257].*

7.2 The Analog Hadron Calorimeter

This section describes the layout of the AHCAL prototype and its readout electronics in more detail. A particular focus lies on the novel SiPM technology employed to read out the signal from the scintillator tiles. Testing the performance and the reliability of such devices on large scales is the main technical goal of the detector, which comprises 7608 channels, all individually read out by a SiPM. The challenge of cell equalization and calibration of such a large number of cells is discussed in Sec. 7.3. Where not otherwise specified, the information about the AHCAL hardware has been obtained from [257].

7.2.1 Layout of an AHCAL Module

The schematic view of an AHCAL module is shown in Fig. 7.3, while Tab. 7.1 summarizes the dimensions of the individual components.

The sensitive layers with the mosaic of scintillator tiles are housed inside rigid cassettes. A cassette is a 1 cm wide and 8 mm thick aluminum frame, with the front and the rear

sides covered by 2 mm thick steel sheets. A plastic plate made of FR4 is also housed inside the cassette, in order to support the cables for the readout and the bias voltage and the optical fibers from the calibration system (Sec. 7.3.2). The cables and the fibers reach the sensitive layer through circular holes in the FR4 plate, two of which are positioned properly right by each tile. The pins of the SiPMs are soldered to a Printed Circuit Board (PCB) foil of 0.3 mm thickness, to protect the SiPMs from mechanical stress. The PCB sheet is in turn glued to the FR4 plate. Two 115 μm thick foils of 3M reflector are glued to the side of the steel sheet and to the side of the FR4 foil looking onto the sensitive layer, in order to maximize the light collection efficiency.

The absorber layers consist of 1 m × 1 m wide steel plates, with an average thickness of 17.4 mm. Standard S235 steel has been chosen, since the magnetic properties are irrelevant, as no measurement inside a magnetic field has been performed during the test beams that would require stainless steel. The gaps between two consecutive layers have a width of 1.4 cm, which allows a smooth insertion and/or exchange of the cassettes with the sensitive layers. A tolerance to account for the aplanarity of the steel plates has also been accounted for in the gaps. With the additional 2 mm thick steel sheets in each cassette the average absorber thickness for each module is 21.4 mm.

7.2.2 The Scintillator Tiles

The scintillator material employed in the active layers is p-terphenyle plus POPOP dissolved in polystyrene (BASF130). The AHCAL uses altogether 3000 tiles of scintillator large 3×3 cm^2, 3848 tiles large 6×6 cm^2 tiles and 760 tiles large 12×12 cm^2. The thickness of the tiles is 5 mm. A special chemical treatment of the edges of each tile assures a white surface that serves as a diffuse reflector. This feature allows the tiles to be placed directly next to each other, without the need of intermediate reflector foils.

A charged particle traversing the tiles deposits its energy exciting the scintillator molecules, which subsequently emit UV-light during de-excitation. The scintillator is transparent to the signal it generates. Kuraray Y11 WLS fibers are employed to guide the signal from the scintillator to the photo detectors, improving the uniformity in response to particles traversing the tile at different positions. At the same time, the fibers shift the wavelength from the UV to the green, since the SiPMs have a better detection efficiency in such a wavelength range. The absorption spectrum of the fibers meets the wavelength range of the scintillator signal, peaking at about 420 nm. The emission spectrum on the other side fulfills the requirements of the photo sensors, with a peak at about 500 nm. To improve the light collection efficiency, the fibers are cladded with a material of higher refraction index than the surrounding scintillator.

Each tile has a 1 mm diameter WLS fiber inserted into a 2 mm deep groove. The fiber is coupled to the SiPM via an air gap that can vary between 50 μm and 100 μm. The other fiber end is pressed against a 3M reflector foil, to increase the light yield. The grooves have a quarter-circle shape in the 3×3 cm^2 tiles and a full-circle shape for the other tiles, as shown in Fig. 7.4. The full circle is not achievable for the small tiles, since the bending radius becomes too small. The circular shape for the grooves has been chosen, since it yields a better light collection with respect to a simple diagonal readout [261].
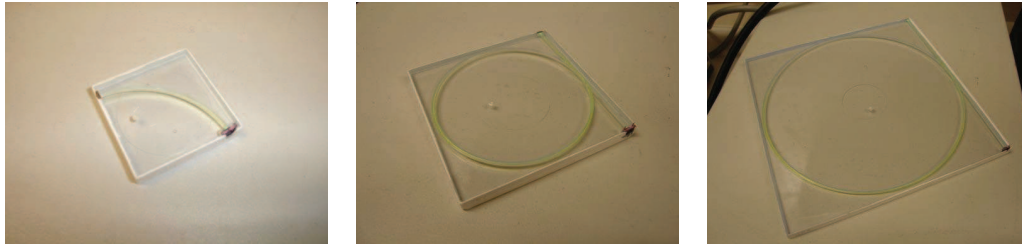
Figure 7.4: *Readout of* $3\,\mathrm{cm} \times 3\,\mathrm{cm}$ *(left),* $6\,\mathrm{cm} \times 6\,\mathrm{cm}$ *(middle), and* $12\,\mathrm{cm} \times 12\,\mathrm{cm}$ *tiles (right) with WLS fibers and SiPMs. From [257].*
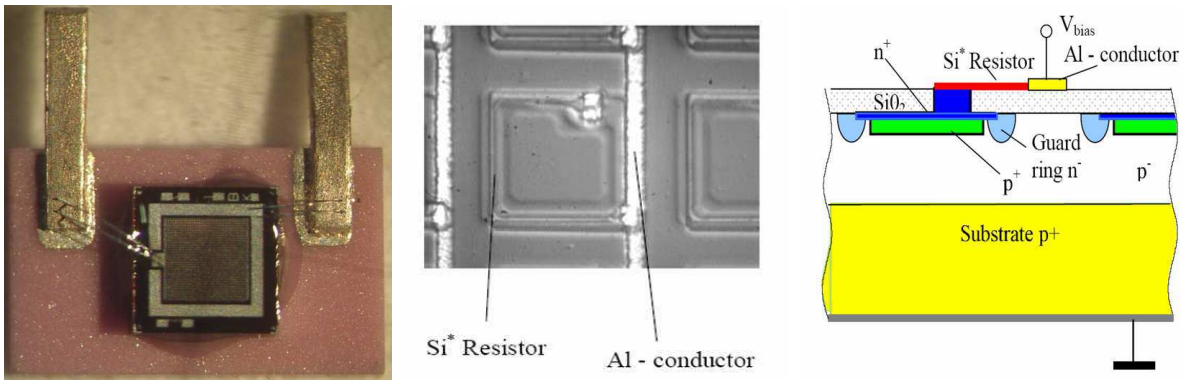
Figure 7.5: *Left: SiPM mounted onto a ceramic plate. Center: zoom on the SiPM, showing the single pixels. The location of the aluminum bias line and of the resistor are pointed out. Right: schematic view of the section of a SiPM pixel. From [264].*

7.2.3 The Silicon Photomultipliers

SiPMs are multi-pixel silicon photodiodes operated in Geiger mode, dedicated to the detection and amplification of light signals [262, 263]. The MEPhI-PULSAR SiPMs employed in the AHCAL (Fig. 7.5, left) have a photosensitive surface of $1.1\,\mathrm{mm}^2$, which is divided into 1156 pixels. Each pixel represents an individual photodiode and is electrically decoupled from the others by means of polysilicon resistive strips, as shown in Fig. 7.5 (middle). In the same picture also the guard ring is visible, that assures a good uniformity of the electric field within the pixel, and the aluminum strips, that connect the pixels in order to collect all the individual signals in the readout of the full SiPM.

The structure of a single pixel is sketched in Fig. 7.5 (right). Each pixel corresponds to an individual p-n junction, to which an external reversed bias voltage V_{bias} is applied. Incident photons create electron-hole pairs, which drift towards the pixel electrodes, producing a current signal. SiPMs are operated in Geiger mode, applying a reversed bias voltage of $\sim 50\,\mathrm{V}$, which lies a few volts above the breakdown voltage. This means that the amount of electron-hole pairs produced grows faster than they can be collected at the electrodes, producing an exponential rise of the signal. In order to

prevent the material from overheating, causing a thermal damage, pixels are equipped with quenching resistors of a few MΩ, that break off the Geiger discharge. The resulting gain is of the order of $\sim 10^6$ and is not sensitive to the magnitude of the original signal. Therefore, the single pixel signals provide a digital information. The quasi-analog signal is obtained by summing the information from all the pixels. The number of fired pixels is proportional to the amount of incident light, as long as the light amplitude does not exceed a certain limit, when saturation occurs.

SiPMs are ideal photodetectors for a calorimeter designed specifically for particle flow. As explained in Sec. 3.4.1, such a calorimeter needs to be placed inside the magnetic coil. Tests in magnetic fields up to 4 T confirm that the SiPMs are unaffected by magnetic fields [265]. Moreover, the small size of the detectors allows a compact design, which is particularly relevant due to the fine granularity and the high number of channels to be read out.

In the following the relevant properties of SiPMs are briefly discussed. More details can be found e.g. in [262, 263].

Saturation

The saturation depends mainly on the number of pixels and on their dead time. If the recovery time of a pixel is short enough, it can fire several times during one measurement, reducing the saturation effects. The recovery time can be shortened by reducing the quenching resistance of the pixels. However, this is not a convenient choice, as the SiPM saturation would then depend on the signal shape. Longer signals would in average cause more multiple pixel firings and would lead to less saturation with respect to shorter signals with the same intensity. Thus, it was chosen to use relatively high quenching resistances, giving a recovery time between 25 ns and 1 μs. The treatment of the saturation during the calibration is described in more details in Sec. 7.3.

Optical Crosstalk

During the avalanche process photons are produced, that can cross the pixel boundaries and induce a signal in the neighboring pixels. The size of the effect, which is known as inter-pixel or optical crosstalk, depends on the gain and on the geometrical layout of the pixels. In order to assure stable operations, only detectors with an inter-pixel crosstalk less than 35% have been selected. Lower values of crosstalk are in principle achievable by adding optical barriers between the pixels. However, this additional boundaries reduce the active area of the SiPM and its geometrical efficiency, therefore a compromise needs to be made.

Dark Currents

Thermal noise in the SiPM can initiate an avalanche and generate a signal, that cannot be distinguished from a light-induced one. The average value of the noise can in principle be measured and subtracted, but its statistical fluctuations cannot be compensated. The noise increases with temperature and with the reversed bias voltage. Also the crosstalk can affect the noise, as it increases the probability for coherent firing of several pixels, with consequent increase of the average amplitude of the noise signals.

During the ITEP tests (Sec. 7.3.1), only SiPMs with noise rates at the chosen bias voltage of less than 3 kHz at half a MIP threshold (corresponding here to approximately 7.5 fired pixels) have been selected.

Efficiency

The photon detection efficiency $\varepsilon_{\mathrm{PDE}}$, the probability to detect an incident photon, is an important parameter to characterize a SiPM. It is given by [266]

$$\varepsilon_{\mathrm{PDE}} = \varepsilon_{\mathrm{QE}} \cdot \varepsilon_{\mathrm{geo}} \cdot \varepsilon_{\mathrm{Geiger}}. \tag{7.1}$$

$\varepsilon_{\mathrm{QE}}$ is the quantum efficiency, which is the probability to generate an electron-hole pair from an incident photon. $\varepsilon_{\mathrm{Geiger}}$ is the probability to start a Geiger-avalanche after an electron-hole pair has been generated. Finally, $\varepsilon_{\mathrm{geo}}$ takes into account geometrical limitations, indicating the percentage of the SiPM surface which is actually sensitive to light. The overall $\varepsilon_{\mathrm{PDE}}$ is of the order of 12% for the MEPhi/PULSAR SiPMs.

7.2.4 The Readout System

The AHCAL prototype readout system was not subject to constraints of scalability to a full detector for the ILC, which is being separately investigated by the CALICE collaboration. An engineering prototype is being developed, that will contain about 2500 detector channels per layer and will take into account all the design aspects demanded by the intended operation at the ILC [267].

The AHCAL readout concept was mainly driven by the readout architecture of the ECAL prototype [256]. Since the number of channels of the two prototypes is similar, adopting a compatible design provides a considerable simplification. In the combined test beam setup, where the ECAL and the AHCAL are operated at the same time, the same data acquisition system may then be used.

The schematic view of the chosen readout system is shown in Fig. 7.6. The very front-end (VFE) electronics, which is dedicated to the collection of the signals from the SiPMs, is based on Application-Specific Integrated Circuit (ASIC) chips [268]. A single ASIC can amplify and shape the signals of eighteen SiPMs. The signals from twelve ASICs, that are located on common base boards, are fed into one of the eight input ports of a CALICE Readout Card (CRC) and digitized by 16-bit ADCs (Analog-to-Digital Convertors) [269]. Five cards are needed to read out the full AHCAL prototype.

The CRC boards are inserted into one nine-unit Versa Module Eurocard (VME) crate. The VME sends the signal from the whole AHCAL prototype to the Data AcQuisition system (DAQ) through the VME-PCI (Peripheral Component Interconnect).

The readout system was operated in two different modes, called calibration and physics mode. For calibration purposes single photons need to be resolved in the SiPM spectrum (Sec. 7.3). Therefore, a short shaping time (40 ns) and a high amplification are needed. On the contrary, during physics runs high signals (some hundreds MIPs) are sometimes produced, and the amplification needs to be reduced by approximately a factor 10. Furthermore, a longer shaping time of about 180 ns is used, in order to provide sufficient latency for the particle beam trigger decision.

In the following the main steps of the readout chain are described in more detail.
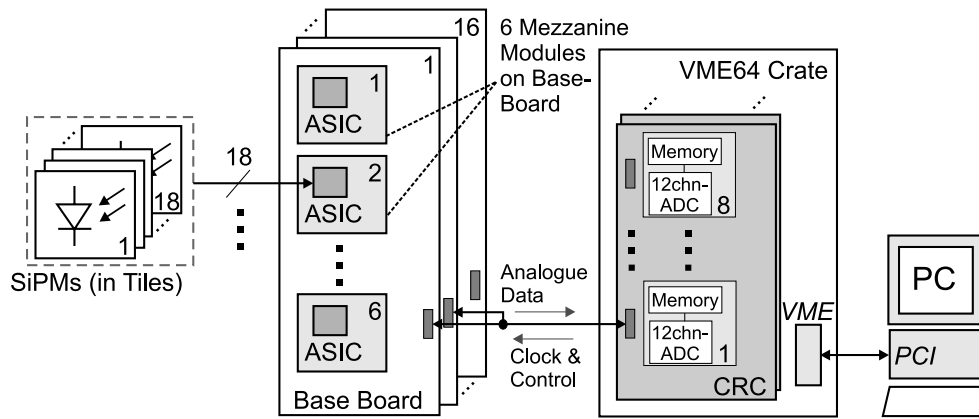
Figure 7.6: *Schematic view of the readout and data acquisition system. From [257].*
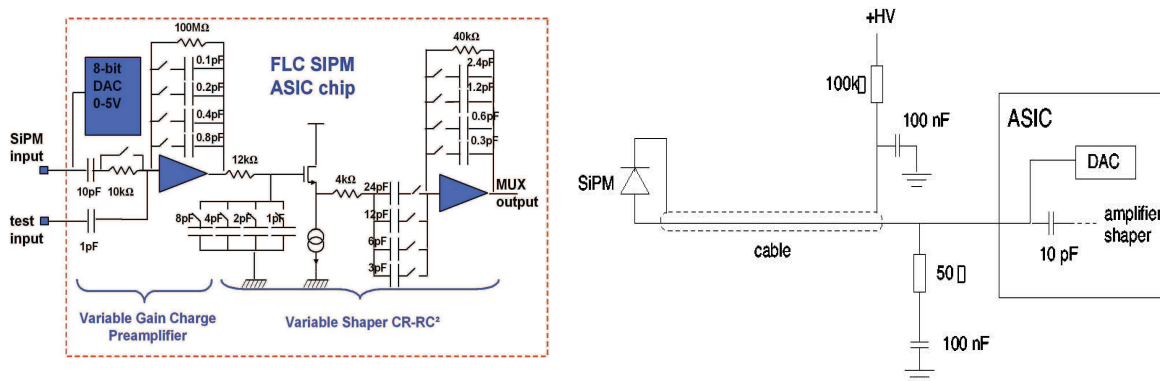
Figure 7.7: *Left: schematic diagram of the ASIC chip. Right: coupling diagram of the SiPM to the ASIC chip. From [257].*

Very Front-End Electronics

The ASIC chips used, called ILC-SiPM ASICs, house 18 channels each. The schematic view of a single channel is depicted in Fig. 7.7 (left).

The integrated components allow the choice of a preamplification gain factor between 1 and 100 mV/pC and a shaping time between 40 and 180 ns, in order to adapt the ASICs to the needs of both operation modes. After the shaping, the signal is held at its maximum amplitude with a sample-and-hold method, that freezes the analog information at a constant level for a specified minimal period of time needed for the digital conversion. The 18 signals from the different channels are multiplexed by an 18-channel multiplexer to provide a single analog input to the ADCs. The total power consumption of an ASIC is about 200 mW for a 5 V supply voltage.

The SiPMs are connected to the ASICs as shown in Fig. 7.7 (right), using a high voltage decoupling and a cable matching. An eight-bit DAC (Digital-to-Analog Convertor) is also employed, placed directly at the preamplifier input to adjust the reversed bias voltage of the SiPMs individually.

The linearity of the preamplifier and the shaper in the physics mode are better than 3% for input charges up to 190 pC. The calibration mode covers a range up to 10 pC with a linearity better than 1%.

The ASICs are located on AHCAL analog boards (HABs), that are mounted onto AHCAL base boards (HBABs), carrying each up to six HABs. This modular design

Figure 7.8: *CALICE Readout Card. From [269].*

was chosen, as it allows the replacement of the individual boards in case of malfunction. The boards contain the control and configuration electronics, that is set remotely by the DAQ, and provide the correct bias voltage for the SiPMs.

Off-Detector Readout Electronics

The sample-and-hold analog signal from the ASICs is transmitted by the boards to the CRCs (Fig. 7.8), that have a fully digital signal processing. The CRCs contain eight front-end (FE) sections that are fanned into a single back-end (BE) section, providing the interface to the VME crate. The FE sections contain each twelve 16-bit ADCs to digitize the multiplexed signals from the ASICS. The dynamic range of the ADC is around 100 MIPs. It is slightly higher than the dynamic range of the SiPMs, of about 70 MIPs, in order to avoid introducing non-linearity effects at high ADC bins.

The digitized signals are collected by the BE and stored into an 8 MByte memory. The typical size of an event is ~ 4 kByte per CRC, therefore about 2000 events can be stored before readout is required. The BE handles also the trigger control, which is set via software and allows significant complexity. A trigger busy signal is set to prevent further triggers until the digitization of the VFE analog data is completed. The rising edge of the trigger signal serves as synchronization of the entire system.

The data are saved as C++ objects, together with the hardware configuration and the beam properties. The DAQ system tests the integrity of the raw data and converts them into LCIO format (see. 3.5.2). During the conversion a database is filled with all the relevant information of the detector configuration, such as temperature recordings, voltage settings and other machine-related parameters.

In a second step the data are reconstructed, obtaining calibrated calorimeter hits as output. During the reconstruction also zero suppression is applied and the size of the events is reduced by approximately a factor two.

The DAQ includes the information from the other detectors of the test beam, such as the tracks from the tracking chambers or the hits from the Cherenkov trigger, in the event output.

The CALICE data processing is explained in detail in [270].

7.3 Calibration Procedure

As typical for semiconductor devices, SiPMs are very sensitive to temperature and bias voltage, that affect most of the SiPM parameters (Sec. 7.3.1). Moreover, they suffer from saturation effects, as discussed above. One of the main technical aims of the AHCAL prototype is to show that these effects can be handled for a large number of channels, i.e. establishing a robust calibration procedure. How this goal could be achieved is summarized in the following. More details can be found in [271, 257] and references therein.

7.3.1 ITEP Tests

Before being installed on the AHCAL, the SiPMs have been tested at ITEP (Institute for Theoretical and Experimental Physics, in Moscow) using an automated setup. The SiPMs have been illuminated with LED light, before mounting them on the tiles, so as to ensure a homogeneous irradiation of all the pixels. The relevant properties of the SiPMs, like gain, noise and the relative efficiency with respect to a reference photomultiplier, have been measured as a function of the reversed bias voltage. The working point was chosen such that the signal from a MIP, provided by the LED light, yielded a response of 15 pixels. This gives a MIP signal well separated from the noise signal (also called *pedestal*) and, at the same time, allows a sufficiently large dynamic range.

Using low intensities of the LED light, the SiPM spectrum was then measured at the chosen voltage. A typical SiPM spectrum is shown in Fig. 7.9 (left). The first peak is the pedestal, while the successive peaks correspond to an increasing number of pixels fired. The width of the peaks is dominated by electronic noise. The excellent resolution, that allows a clearly disentanglement of the different peaks, is extremely important for physics applications, since it provides a tool to self-calibrate each channel of the prototype.

The SiPM gain is given by the distance between two consecutive peaks in the spectrum, derived using a multi-Gaussian fit. Fits with a bad chi-square or those spectra with too low statistics in the first two peaks are excluded. The uncertainty on the gain for the successful fits is dominated by the fit uncertainty and is about 2%.

The response of the SiPMs was also measured at ITEP for 20 different light intensities over the full dynamic range, from zero up to saturation, as shown in Fig. 7.9 (right). The response curves show the number of pixels fired versus the intensity of the incoming light. The individual curves for different SiPMs are generally within about 15% of one another. The saturation trend at high light intensities is clearly visible.

Finally, the relative variation of the SiPM parameters for a 0.1 V change of the voltage was measured and found to be of the order of 2-3% for the gain, the efficiency and the noise frequency. The SiPM response and the inter-pixel cross talk showed larger effects of the order of 5%. An increase (decrease) of 0.1 V is equivalent to a decrease (increase) of 2°C in temperature, since temperature changes reflect in variations of the breakdown voltage of the SiPMs.
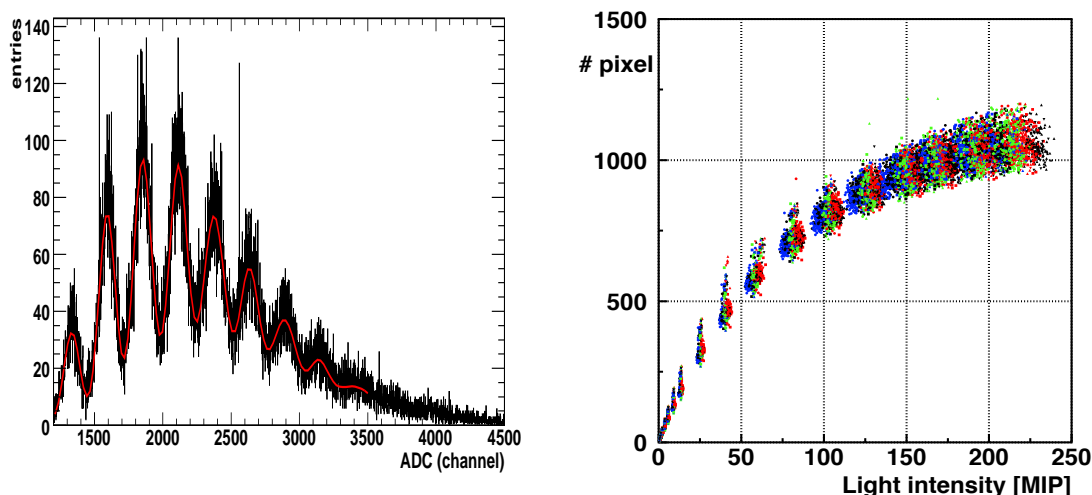
Figure 7.9: *Left: typical spectrum of the SiPM response expressed in ADC channels, for low-intensity light. From [271]. Right: response curves of several bare SiPMs, measured before mounting them on the scintillator tiles. The response is expressed as number of pixels fired versus the input light intensity. From [257].*

After mounting the SiPMs on the tiles, the MIP response was measured again using triggered electrons from a ^{90}Sr source. The trigger signal was obtained from a scintillator positioned below the tile. The ^{90}Sr spectrum collected with the trigger is compatible with the MIP spectrum obtained at ITEP. The mean value of the MIP response varies from tile to tile because of the different light collection efficiencies. Amongst the available tiles, the 7608 tiles with light yields closest to 15 pixels have been selected. A lower yield reduces the separation of the MIP from the noise, while a higher light yield reduces the dynamic range.

The reversed bias voltage needs to be adjusted for the in-situ measurements, once the tiles are mounted on the AHCAL, to take into account the voltage drop over the several meters of cable between the AHCAL and the power supply and the different temperatures. The optimization for the 2007 data taking lead to an average light yield of 13 pixels/MIP and an average noise level per cell of $1.3 - 2 \times 10^{-3}$, which is about a factor ten higher than the design goal of 10^{-4}. The noise could not be reduced by decreasing the voltage, since this would have reduced also the light yield, which is already inferior to the design value of 15 pixels/MIP.

7.3.2 The Calibration and Monitoring System

As shown by the ITEP measurements, the SiPMs are very sensitive to changes in temperature and operation voltage. Therefore it is necessary to monitor them during the test beam activity. The monitoring is performed thanks to Calibration and Monitoring Boards (CMBs) [272], which are connected to one side of each AHCAL module cassette. Each CMB contains 12 UV LEDs and 12 PIN photodiodes. The light from the LEDs is distributed using clear optical fibers to each AHCAL tile and to the PIN diodes, which have the purpose to monitor the LED light itself. A preamplifier is used

for the readout of the PIN photodiodes, since they have a gain of one, while the readout of the SiPMs proceeds as for the beam signal.

The LED light amplitudes are tunable from low intensities, yielding single pixel spectra, to high intensities, reaching the saturation level of the SiPMs. The response of the SiPMs is measured both in physics and calibration mode in order to determine the gain and saturation level of the SiPMs and the electronics intercalibration between the two operation modes. Typical pulse widths of the order of 10 ns are used for the LED light, since longer pulses would increase the probability to have multiple pixel firings. The pulses are nearly rectangular, with fast rise and fall times of the order of 1 ns.

Each CMB operated also seven temperature sensors, two of which are located on the readout board and five are distributed at the center of the cassette. The sensors are read out via a 12 bit ADC. They have an accuracy better than 0.6 °C. A slow control system reads out regularly the temperature information, which is stored together with a time stamp in a database.

7.3.3 Calibration

The calibration chain proceeds through the following steps:

- equalization of inter-cell response;

- calibration of the SiPM signal and correction for the non-linear response;

- calibration from the MIP to the GeV scale.

In the following, the first two calibration steps are described. For the presented work, the conversion to the GeV scale is obtained through a χ^2 optimization, which is discussed in Chap. 8.

SiPM Gain and Intercalibration Factors

The equalization of the responses of the 7608 AHCAL cells is performed using the reference signal from 120 GeV muons [273]. Muons represent the best approximation of the behavior of a MIP. The ADC value for a considered cell i is converted to a number of MIPs by taking the Most Probable Value (MPV) of the response to a muon beam, which gives the cell equalization factor C_i^{MIP}. The MPV is derived by fitting the convolution of a Landau and a Gaussian to the signal, which is well separated from the noise pedestal, as shown in Fig. 7.10. One can then write:

$$E_i[\mathrm{MIP}] = \frac{A_i[\mathrm{ADC}]}{C_i^{\mathrm{MIP}}}, \tag{7.2}$$

where $A_i[\mathrm{ADC}]$ is the amplitude of the signal expressed in ADC counts and $E_i[\mathrm{MIP}]$ is the signal in units of MIPs. This procedure does not only determine the absolute energy scale of the detector, but also provides the threshold to suppress signals attributed to noise only. The threshold is chosen to be 0.5 MIP.
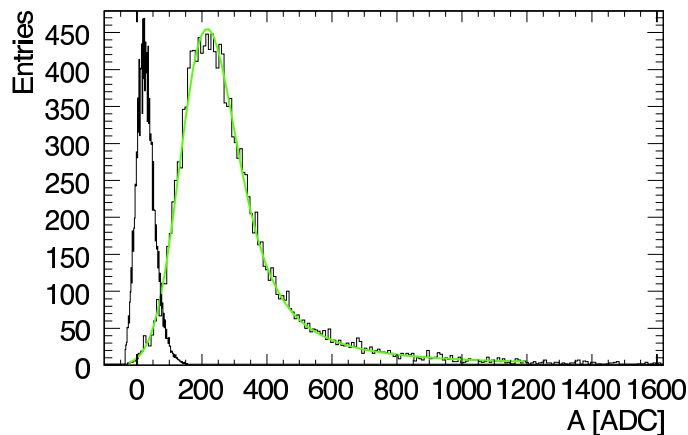
Figure 7.10: *Single cell response to muons with corresponding fit (green line) and noise spectrum of the same cell. From [243].*

Since the response of the SiPM and, in particular, its saturation depend on the number of pixels fired, $A_i[\text{pix}]$, it is necessary to derive such a number from the ADC scale, to which it is related by the factor $C_i^{\text{pix}}[\text{ADC}]$:

$$A_i\,[\text{pix}] = \frac{A_i\,[\text{ADC}]}{C_i^{\text{pix}}[\text{ADC}]}. \tag{7.3}$$

The factor $C_i^{\text{pix}}[\text{ADC}]$ is related to the gain of the SiPM. However, one has to consider that the gain, G_i^{fit}, is measured in calibration mode, since it is necessary to distinguish the single pixel peaks in the SiPM spectrum (Sec. 7.3.1, cf. Fig. 7.9). In contrast, the muon calibration as well as the data taking are performed in physics mode. Therefore, an intercalibration factor, I_i, between the two modes has to be taken into account, when determining $C_i^{\text{pix}}[\text{ADC}]$:

$$C_i^{\text{pix}} = \frac{G_i^{\text{fit}}[\text{ADC(CM)}]}{I_i}, \tag{7.4}$$

where CM indicates that the gain is measured in Calibration Mode.

The factors I_i are obtained by the ratio between the responses of the SiPMs in the two operation modes. The intensity of the signals is chosen such that the SiPM response is linear, avoiding the saturation region. The intercalibration factors obtained range between 4 and 13. The variations are mainly due to the differences between the SiPM signal forms (i.e. quenching resistors): longer signals (larger resistors) give bigger intercalibration factors.

SiPM gain measurements were repeated approximately every eight hours during the test beam operation. 2% of SiPMs are considered inactive, due to initial bad soldering, and cannot be calibrated, together with the 0.11% of channels that are connected to a broken LED. For the remaining channels the calibration efficiency is very high. For the cells that cannot be calibrated the average calibration of the module to which they belong is taken.

Since the SiPM properties depend on the temperature and the voltage, a given set of calibration constants is only valid for measurements at the same operation conditions.

While the gain is measured periodically during the data taking, the MIP constants are determined in dedicated muon runs, that are taken just once before or after the data runs. Therefore, the calibration constants need to be extrapolated to the temperature of the detector during the beam data taking [274].

SiPM Response

The response of a SiPM can be approximated by the function

$$N_{\text{pix}} = N_{\text{tot}} \cdot (1 - e^{-N_{\text{pe}}/N_{\text{tot}}}), \tag{7.5}$$

with N_{tot} the maximum number of fired pixels, in the specific case set to 1156. This ideal response function correlates the observed number of pixels fired, N_{pix}, to the effective number of generated photoelectrons. In principle, it can be parametrized from the individual measurements performed during the ITEP tests (Sec. 7.3.1). However, during the laboratory tests the SiPMs were not mounted on the tiles, therefore they have been homogeneously illuminated with light. In the final configuration, the light is guided to the SiPM by the WLS fibers and a geometrical mismatch between the two has to be taken into account. The laboratory curves need to be rescaled, with a factor that is obtained from dedicated measurements in-situ with the calibration and monitoring system. The response of the SiPMs is scanned with high intensities of the LED light and fitted with an exponential function, which is compared to the corresponding ITEP response curve. The ratio of the maximum number of pixels, N_{tot}, measured in-situ with SiPM mounted on a tile to that measured at ITEP with bare SiPM in the laboratory tests, is found to be on average 80.5% with an RMS of 9%.

The uncertainty of the determination of the rescaling factor for a single channel is lower than 3%, if the LED light range properly covers the SiPM saturation region, and if this region is measured well below the ADC saturation. Unfortunately, these conditions could be achieved only for about 73% of the channels. Furthermore, the measured SiPM response curves, from which the correction of non-linear detector response is calculated, are affected by the SiPM gain uncertainty of 2%. For these reasons, the average rescaling factor is used for all channels. Further studies will investigate the possibility of using a channel-by-channel factor instead.

From the rescaled response curves of the SiPMs the correction $f_{\text{sat}}(A_i\,[\text{pix}])$, to be applied to correct for the saturation, is obtained. $A_i\,[\text{pix}]$, the amplitude of the signal in unit of number of pixels fired, is obtained from the amplitude of the signal in ADC counts, using eq. 7.3. The calibrated energy, E_i, is finally given in units of MIP according to

$$E_i\,[\text{MIP}] = \frac{A_i\,[\text{ADC}]}{C_i^{\text{MIP}}} \cdot f_{\text{sat}}(A_i\,[\text{pix}]). \tag{7.6}$$

7.4 Calibration Validation

Although the AHCAL is designed to measure hadrons, during the test beam operations it has been exposed also to positrons. While performing such measurements the SiW-ECAL was moved out of the beam line, since the electromagnetic showers

are compact and the SiW-ECAL would have absorbed most of them. The study of the electromagnetic response serves to prove the understanding of the detector and to validate the calibration procedure. In fact, the electromagnetic showers have a regular development and can be described by the Monte Carlo simulations more precisely than the hadronic showers, for which several models exist with sensible differences from one another (Sec. 8.2.1). Moreover, the non-compensating nature of the calorimeter (Sec. 6.4.3) further complicates the behavior of hadronic showers.

The study of the electromagnetic response of the AHCAL is described in detail in [271]. Positron runs of energies between 10 and 50 GeV are used, applying a careful selection to suppress contaminations in the beam, mainly from muons, and to reduce the noise contribution. The selected events are compared to realistic Monte Carlo simulations, which take into account all known detector effects (Sec. 8.2.1), and the systematic uncertainties associated to the different steps of the calibration procedure are estimated. The uncertainties on the MIP scale give an energy-independent systematic error of 2%. Saturation corrections and gain determination give energy-dependent uncertainties, up to 2.6% and 1.4% at 50 GeV, respectively.

The response linearity is also studied. The resulting Monte Carlo linearity is better than 0.5% over the full energy range. For the data the deviation from linearity is less than 1% for energies up to 30 GeV, while at high energies it increases up to 3%. This remaining non-linearity hints at a yet non-perfect treatment of the saturation corrections (Sec. 7.3.3). This issue affects the data only, since in the Monte Carlo the same SiPM response curves are used both to simulate the saturation and to evaluate the correction for it. The linearity of the AHCAL for pions is discussed in Chap. 8 (cf. Fig. 8.18).

The electromagnetic analysis provides confidence that the detector performance and simulation are sufficiently understood, in order to carry on studies based on hadronic data.

8 Study of a Correction to the Shower Leakage

The study presented in this chapter makes use of the data collected at CERN in 2007 using the CALICE prototypes (Sec. 7.1).

Pion events have been selected and analyzed, focusing on the effects of the leakage on the energy response of the calorimeter. The full experimental setup corresponds to a total depth of approximately 12 nuclear interaction lengths (λ_I) and the leakage in the energy range considered (up to $100\,\text{GeV}$) is only a small effect. The impact on the average response for pions starting to shower in the AHCAL is less than 0.4%. However, in a future detector for a collider experiment, a coil is expected to be placed between the hadron calorimeter and the tail catcher. The presence of the coil will cause part of the hadronic showers to be lost, since the coil will not be instrumented.

In order to study the full potential of a highly granular hadron calorimeter, the energy resolution has been studied removing completely the TCMT information, which corresponds to reducing the total depth of the calorimetric system by about 5.8 λ_I. In such a configuration, the amount of leakage is significant and the energy resolution decreases accordingly. Exploiting the high granularity of the AHCAL and the possibility to reconstruct the shower development with high precision, a correction for the leakage has been developed, which does not rely on the TCMT information.

Some of the results obtained are compared to the performance obtained with the ILC-like configuration (Sec. 7.1.3), which reproduces more closely the conditions of the ILD detector.

8.1 Data Analysis

For the purpose of this analysis the SiW-ECAL is essentially used only as a tracker, to select the pions that start showering in the AHCAL, behaving in the SiW-ECAL as Minimum Ionizing Particles (MIPs) (Sec. 6.1.2). This choice simplifies the study and the selection, reducing the sources of systematics. Further complications would arise in particular from the lateral leakage from the SiW-ECAL. The use of the full sample of showers, including those starting in the SiW-ECAL, is forseen as an upgrade of the study.

In this section the details of the event selection are reviewed, the quality of the selected sample is checked and the distributions of the relevant observables are presented.

8.1.1 The Primary Track Finder Algorithm

The first hard interaction of the showers is found using the Primary Track Finder (PTF) processor, developed by Marina Chadeeva [275] (version 4.00). The PTF algorithm

tracks the primary particle entering the SiW-ECAL up to the point where the first hard interaction occurs and the cascade begins. The shower starting point is identified using the following relations:

$$A_i + A_{i+1} > A_{min}[\text{MIP}],$$
$$N_i + N_{i+1} > N_{min}, \tag{8.1}$$

where N_i is the number of hits in the i-th layer and A_i is defined as:

$$A_i = \frac{\sum_{k=0}^{i} E_k}{i+1}, \ i < 10$$
$$A_i = \frac{\sum_{k=i-9}^{i} E_k}{10}, \ i \geq 10 \tag{8.2}$$

with E_i being the energy in unit of MIPs deposited in the i-th layer. The index i runs from 0 to 67, accounting for the 68 layers of SiW-ECAL + AHCAL. The processor does not search for showers starting in the TCMT. The thresholds A_{min} and N_{min} depend on the beam energy E_{beam} in GeV:

$$A_{min} = 6.0 + 0.1 E_{beam},$$
$$N_{min} = int(3.77 + 1.44 \log E_{beam} + 0.5). \tag{8.3}$$

Once the conditions in Eq. 8.1 are satisfied for the layer i, the shower first hard interaction is assumed to take place in the layer i when:

$$i < 65 \text{ and } E_{i+2} < E_i \text{ and } E_{i+3} < E_i \text{ and } E_{i+3} + E_{i+2} < E_{i+1} + E_i, \tag{8.4}$$

otherwise the layer $i-1$ is taken as the layer where the shower starts.

The systematic uncertainty of the PTF algorithm are studied in [260]. The positions where the first hard interaction occurs according to the Monte Carlo truth and to the PTF algorithm are compared. The performance of the PTF algorithm is found to depend on the beam energy and the physics list used (Sec. 8.2.1). The first interaction layer found by the PTF algorithm agrees with the MC truth within one (two) layers for 74% (84%) of events. Averaged over all energies and all physics lists, there is a systematic shift of -0.2 layers and a correlation of 85.8% between the two quantities. The study in [260] makes use of a private version of the PTF algorithm, which has a slightly different tuning with respect to the version 4.00, which is used here. However, the estimated uncertainties should hold at least approximately. In any case, a study on the systematics of the PTF algorithm is not included in the here presented analysis.

8.1.2 Selecting a Pure Pion Sample

In order to reduce the noise contribution, hits of less than 0.5 MIPs are rejected in all the calorimeters. Beam events are selected using the beam trigger and the muon contamination in the beam is reduced using a selection included in the PTF algorithm.

coeff.	$E_{beam} > 20$ GeV	$E_{beam} \leq 20$ GeV
a	0.25	0.067
b [GeV]	0.25	0.73
c	-0.91	-2
d [GeV]	8.4	9
e	13	10.4
f [GeV]	-12.5	-9.6

Table 8.1: *Coefficients for the requirements*

The PTF algorithm rejects muon-like events using the 2-dimensional distribution of the energy deposited in SiW-ECAL+AHCAL versus the energy deposited in the TCMT (Fig. 8.1 and 8.2 bottom-left). The events in the bottom-left corner of the distribution have low energy depositions both in SiW-ECAL+AHCAL and in the TCMT and are thus rejected as muons. The requirement is only applied if at least 16 cells of the SiW-ECAL, or 18 cells of the AHCAL contain energy depositions. Events are rejected when:

$$E_{TCMT}[\text{GeV}] > a \cdot E_{SiW-ECAL+AHCAL}[\text{GeV}] + b \text{ and}$$
$$E_{TCMT}[\text{GeV}] < c \cdot E_{SiW-ECAL+AHCAL}[\text{GeV}] + d \text{ and}$$
$$E_{TCMT}[\text{GeV}] < e \cdot E_{SiW-ECAL+AHCAL}[\text{GeV}] + f. \tag{8.5}$$

The coefficients in Eq. 8.5 have different values depending on the beam energy, as summarized in Tab. 8.1.

The visible energy (in MIPs) collected in the different calorimeter sections is converted to the total deposited energy (in GeV) using default weights. A detailed explanation about such conversion factors and the optimization performed on them is given in 8.1.3.

The selection is refined using the following criteria:

- empty events that are caused by fake triggers are rejected by requiring:

$$N_{SiW-ECAL} \neq 0 \quad \text{or} \quad N_{AHCAL} \neq 0, \tag{8.6}$$

  where $N_{SiW-ECAL}$ (N_{AHCAL}) is the number of SiW-ECAL (AHCAL) cells with energy depositions.

- multi-particle events are rejected using the selection:

$$E_{SiW-ECAL} + E_{AHCAL} + E_{TCMT} > 1.5 \cdot E_{beam}. \tag{8.7}$$

- electron events are rejected by requiring certain minimum and maximum numbers of cells with energy depositions in the different calorimeteres:

$$N_{SiW-ECAL} > 50 \quad \text{or} \quad N_{AHCAL} + N_{TMCT} < 30. \tag{8.8}$$

- only events with a shower starting point in the AHCAL layers 2-36 are kept.

Run	E_{beam} (GeV)	Initial	Trash	Multi	Muons	Start	Electrons	Eff. (%)
330334	8	105774 (*)	105743	105577	97513	23587	23335	22.1
330332	10	178504	178464	178287	166621	42672	42280	23.7
330330	12	261601	261522	261410	244006	72758	72191	27.6
330328	15	179131	179088	179031	167644	58399	57656	32.2
330327	18	178369	178323	178268	167480	59739	59066	33.1
330326	20	180279	180236	180180	169742	60566	59936	33.2
330325	25	177620	177583	177535	167452	59436	58784	33.1
330650	25	224151	224098	224075	210723	74569	73664	32.9
330960	35	182907	182817	182774	151289	51424	50838	27.8
330557	35	217820	217773	217734	180544	61290	60392	27.7
330961	45	174589	174492	174473	164919	57889	57223	32.8
330550	45	222620	222587	222537	210210	73653	72518	32.6
331568	60	237980	237856	237776	229186	81511	80397	33.8
330962	80	179777	179722	179677	172752	60164	59060	32.9
330392	80	229843	229812	229704	222172	77972	76127	33.1
330393	100	231974	231951	231899	224540	79227	77098	33.2

* Additional events in the run have been excluded due to pedestal shift.

Table 8.2: *Summary table with the selection efficiency at different energies. The number of events in the runs, before and after the selection cuts used in order to obtain a pure pion sample, is given, as well as the number of events left after each step of the selection.*

The effect of the cuts is shown in Fig. 8.1 and 8.2, respectively for a low- and a high-energy run. For the selected events the energy deposited in the SiW-ECAL is small, compatible with the passage of a non-showering pion, as can be seen from a comparison of the energy distributions in the two upper panels of Fig. 8.1 and 8.2. A large fraction of the pion energy is contained in the AHCAL. For the low-energy run (Fig. 8.1) the energy deposited in the AHCAL follows the expected Gaussian distribution, while a low-energy tail is present in the AHCAL energy distribution of the high-energy run (Fig. 8.2), due to leakage into the TCMT. The 2-dimensional distributions in the bottom panels of Fig. 8.1 and 8.2 show the correlation between the energy deposited in the TCMT and the sum of the energy deposited in the SiW-ECAL and the AHCAL. The events in the lower-left corner of the left-hand side distributions are rejected, since they are attributed mainly to muons, as explained above (cf. Eq. 8.5).

The selection efficiency for different energies is summarized in Tab. 8.2. The efficiencies are simply given as a percentage of the initial events in the run, which survive the selection criteria. Since the initial events contained in the run are not purely pion events, the efficiencies are not to be interpreted as pion selection efficiencies.

8.1.3 Sampling Weights Optimization

The so-called sampling weights are necessary in order to convert the visible energy measured with the different calorimeters, to the deposited energy of the traversing particle. Six sampling weights have initially been introduced for the six different regions
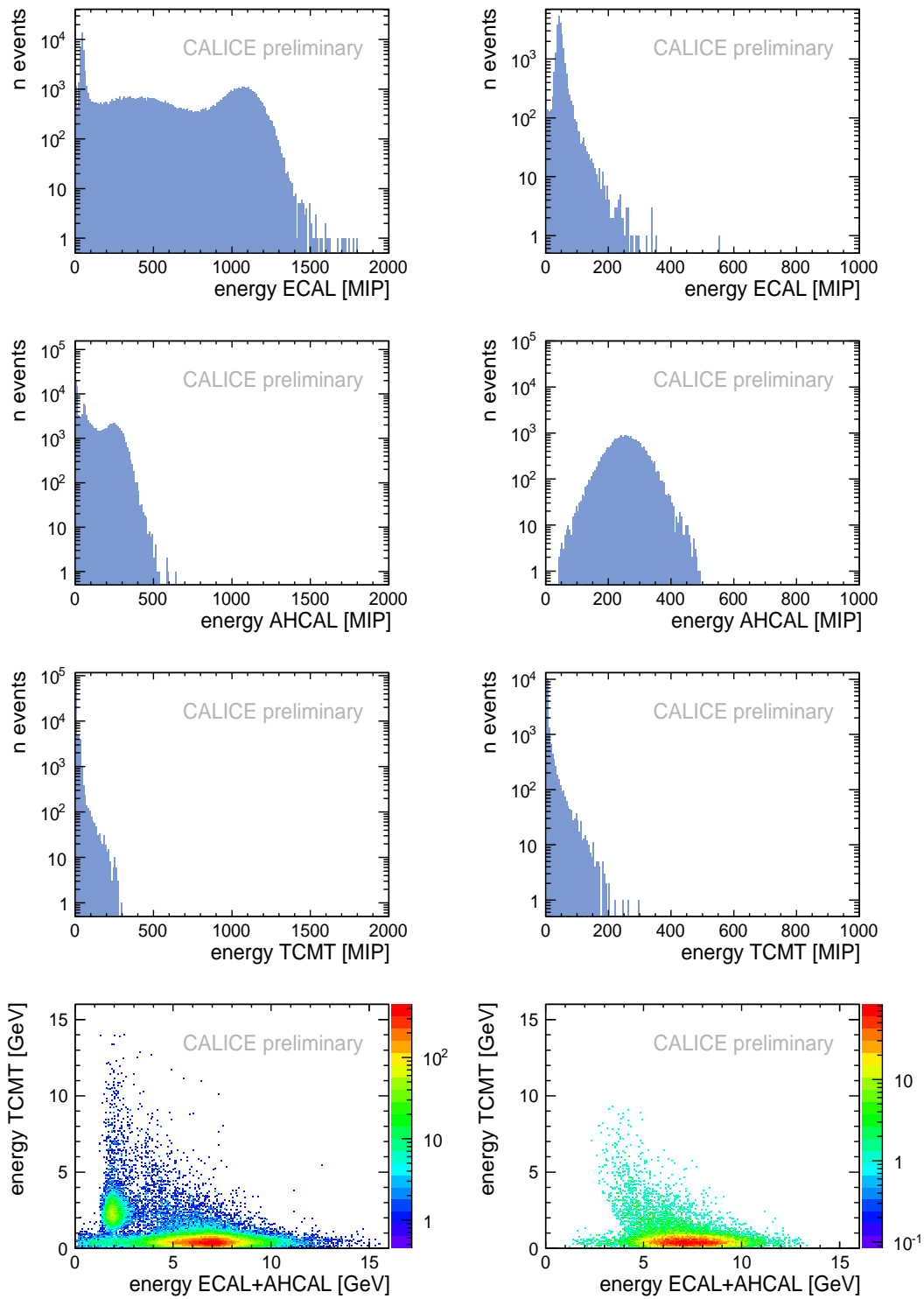
Figure 8.1: *Comparison of distributions before (left column) and after (right column) the pion selection at 8 GeV. From top to bottom are shown: the total energy measured in the SiW-ECAL, in the AHCAL and in the TCMT. The bottom plot shows the 2-dimensional distribution of the energy deposited in SiW-ECAL+AHCAL versus the energy deposited in the TCMT. This last distribution is used by the PTF algorithm in order to reject muons.*
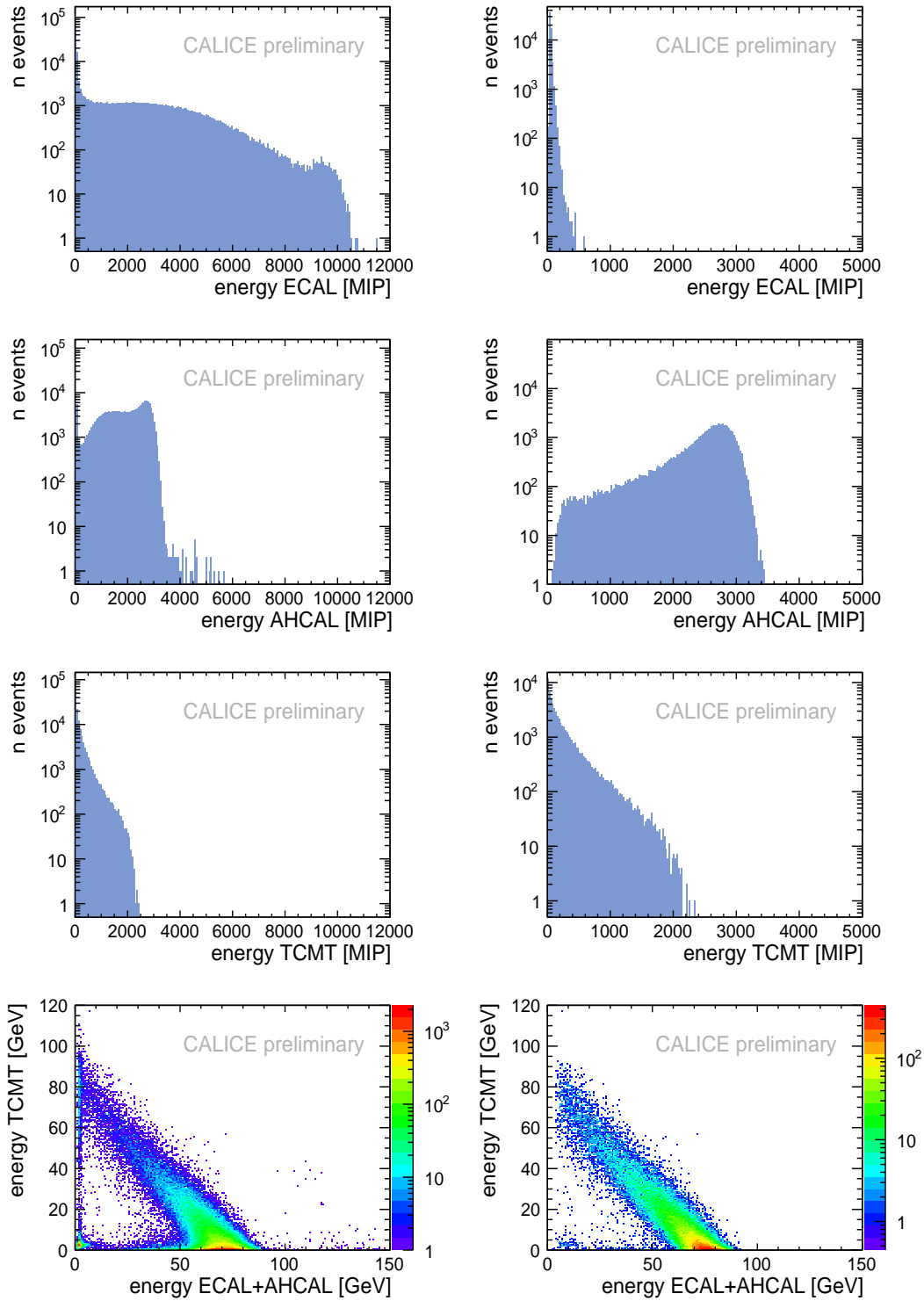
Figure 8.2: *Comparison of distributions before (left column) and after (right column) the pion selection at 80 GeV. From top to bottom are shown: the total energy measured in the SiW-ECAL, in the AHCAL and in the TCMT. The bottom plot shows the 2-dimensional distribution of the energy deposited in SiW-ECAL+AHCAL versus the energy deposited in the TCMT. This last distribution is used by the PTF algorithm in order to reject muons.*

of the calorimeters: three for the three sections of the SiW-ECAL (w_1, w_2, w_3), with different absorber thicknesses, one for the AHCAL (w_4) and two for the two sections with different structure of the TCMT (w_5, w_6). These factors can in principle be calculated from the known composition of the calorimeters, but a more precise evaluation is obtained using a χ^2 optimization as described in the following.

After the calibration procedure (Sec. 7.3) the calibrated energy is given in units of MIP. The MIP-to-GeV conversion is calculated during the χ^2 minimization of the sampling weights, such that the obtained factors account for both the sampling structure of the calorimeters and the conversion to the GeV scale. The calculated conversion factors are applied directly to the visible energy given in MIPs. The total energy in GeV for the j-th event is then:

$$
\begin{aligned}
E_j = E_{SiW-ECAL1,j} \cdot w_1 + E_{SiW-ECAL2,j} \cdot w_2 + E_{SiW-ECAL3,j} \cdot w_3 \\
+ E_{AHCAL,j} \cdot w_4 \\
+ E_{TCMT1,j} \cdot w_5 + E_{TCMT2,j} \cdot w_6,
\end{aligned} \tag{8.9}
$$

where $E_{SiW-ECAL1,j}$ is the energy in MIPs measured in the first section of the SiW-ECAL and $E_{SiW-ECAL2,j}$, $E_{SiW-ECAL3,j}$, $E_{AHCAL,j}$, $E_{TCMT1,j}$ and $E_{TCMT2,j}$ are defined analogously.

The χ^2 function to be minimized is given by:

$$
\chi^2 = \sum_{j=1}^{N} (E_{beam} - E_j)^2, \tag{8.10}
$$

where N is the number of selected pion events in the considered run of energy E_{beam} (in GeV), and the energy E_j (in GeV) of the j-th event is given by the expression in Eq. 8.9.

Due to the selection of events with only one track in the SiW-ECAL, the energy deposited in the SiW-ECAL is not sensitive to the sampling structure of the calorimeter and the optimization of the three weights for the SiW-ECAL is not reliable. Therefore, the weights w_1, w_2 and w_3 are fixed to the values calculated in [276] using Monte Carlo simulations.

The minimization is repeated for 9 runs with energies in the range from $25\,\mathrm{GeV}$ to $80\,\mathrm{GeV}$. It is not performed for low-energy runs, since the energy deposition in the TCMT is limited and the sensitivity to the weights w_5 and w_6 is not accurate. The final weights are obtained from the arithmetic mean of the results for different runs and the errors from the respective RMS.

A summary of the obtained weights and errors is shown in Tab. 8.3 and their dependence on the beam energy is shown in Fig. 8.3. The three free weights for AHCAL and TCMT are compatible with the expectations from the sampling composition of the detectors, in particular the proportions between the absorber thicknesses: the weight for the AHCAL and the one for the first part of the TCMT are expected to be very similar, while the weight for the second part of the TCMT is expected to be about 5 times larger. The weight for the AHCAL has an accuracy better than 1%, while the weights for the TCMT have an accuracy of 3.5% to 5%.

Detector section	Sampling Weight GeV/MIP	% error
SiW-ECAL1	0.0030	fixed
SiW-ECAL2	0.0060	fixed
SiW-ECAL3	0.0089	fixed
AHCAL	0.0276	0.94
TCMT1	0.0293	3.5
TCMT2	0.1219	5.0

Table 8.3: *Sampling weights used to convert the visible energy (in MIPs) collected in the different sections of the calorimeters to the total deposited energy (in GeV). The weights have been obtained from a minimization procedure, fixing the weights for the SiW-ECAL to the values calculated in [276].*
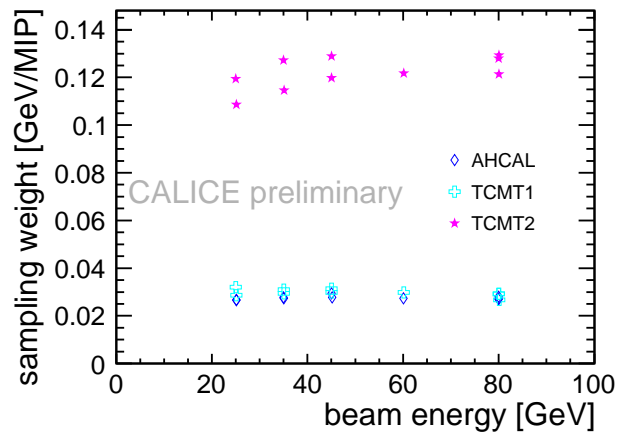
Figure 8.3: *Sampling weights as a function of the beam energy of the run from which they were derived.*
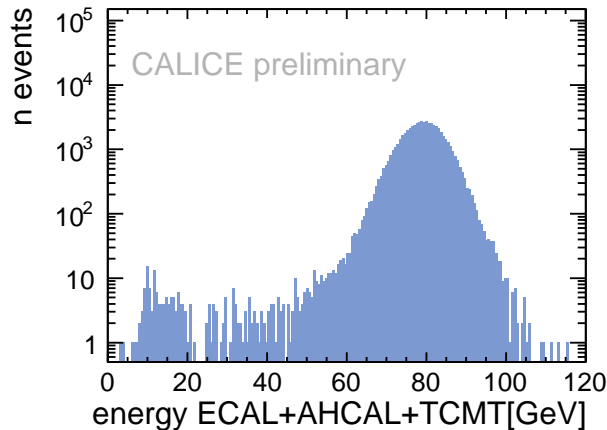
Figure 8.4: *Total energy distribution for an 80 GeV run.*

8.1.4 Control Distributions for the Data

In this section some control distributions are shown, in order to confirm the accuracy of the pion selection and of the sampling weights optimization. All shown distributions were generated for events from the 80 GeV run 330962.

The distribution of the total energy measured using the full calorimeter is shown in Fig. 8.4. The peak is very clean and centered around the expected beam energy, confirming the quality of the event selection and of the sampling weights optimization. The low-energy tail is due to the leakage from the full calorimeter, which is a minor effect. The smaller peak of events at very low energies is due to a small residual contamination from muons, surviving the selection.

Figure 8.5 (left) shows the average longitudinal development of the showers, given by the average energy deposited versus layer. The bin width is proportional to the layer interaction length. The smooth transitions of the profile shape between the AHCAL and the TCMT and between the first and the second part of the TCMT confirm that the sampling weights obtained with the optimization procedure are correct. The average energy deposition in the SiW-ECAL is compatible with the passage of non-showering pions. The small spikes on a layer by layer basis are due to noise contribution, calibration uncertainties and dead channels.

Thanks to the high granularity of the calorimeter and the possibility to determine the first hard interaction of the showers, it is possible to reconstruct the development of the showers relative to their starting point, instead of considering the development relative to the calorimeter front face. These two ways to reconstruct the longitudinal profile are compared in Fig. 8.5 (right), considering only the energy deposited in the AHCAL. The layer-by-layer effects are clearly washed out and the profile development appears to be smooth.

The average measured energy and its deviation from the expected beam energy is shown in Fig. 8.6 for runs at different energies. Three configurations are considered: the full calorimeter, the configuration with only the SiW-ECAL and the AHCAL and the ILC-like configuration described in Sec. 7.1.3. The difference between the beam energy and the energy measured using SiW-ECAL+AHCAL only increases with the beam energy, since the leakage increases and more energy is lost. Obviously, the leakage
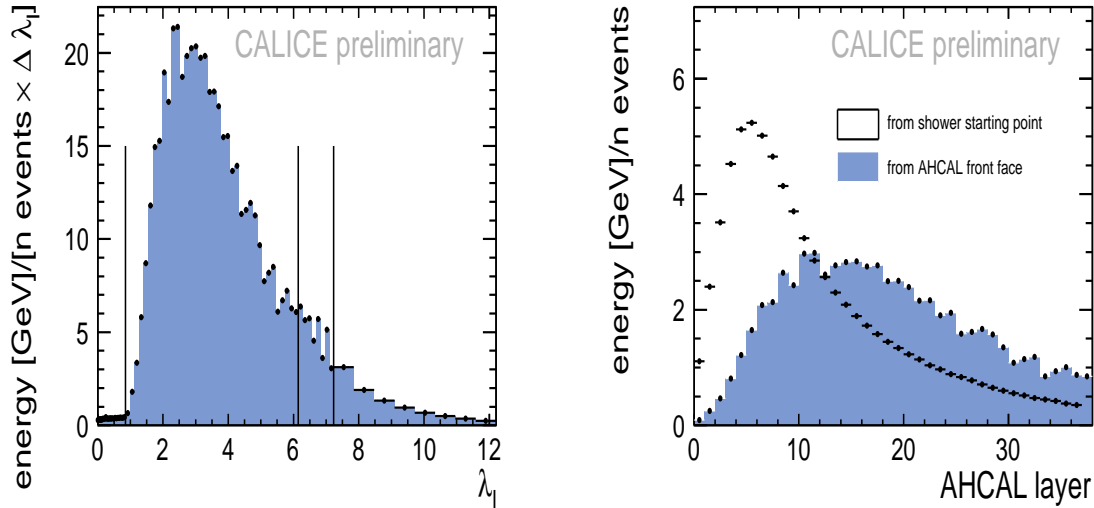
Figure 8.5: *Left: average energy deposition of the showers versus the depth of the calorimeter system for an 80 GeV run. Right: longitudinal profile in the AHCAL only, drawn with respect to the first hard interaction of the showers or w.r.t. the calorimeter front face. Showers starting in the first layer of the AHCAL have been rejected, therefore the longitudinal profile relative to the shower starting point does not reach the very last bin.*

increases also when the full length of the calorimeter is reduced, considering only the SiW-ECAL+AHCAL information, or excluding part of the TCMT in the ILC-like configuration, to simulate the presence of a coil. When using the full information, including the energy measured by the TCMT, the response of the calorimeter is linear within a 2% accuracy. Since no software compensation has been applied (Sec. 6.4.3) such a precision is satisfactory. Differences in the energy response for runs at the same beam energy are due to calibration uncertainties.

8.2 Comparison of Data and Monte Carlo

The high precision in the reconstruction of the hadronic showers, allowed by the fine granularity of the AHCAL, poses new challenges to the shower models used in the Monte Carlo simulations. Although this is not the main purpose of the present study, some comparisons of data and Monte Carlo are shown in this section, since they are of interest on their own. Moreover, the understanding of the differences between data and Monte Carlo is relevant also for the specific purpose of building a correction for the leakage, since the corrections that will be applied to the data can also be derived from the Monte Carlo simulations (Sec. 8.4.2).

8.2.1 Monte Carlo Simulations

Simulation

The Monte Carlo simulations for the CALICE prototypes are carried out in the framework of GEANT4 [184] (version 9.3.p01). The geometries of the detectors are simulated
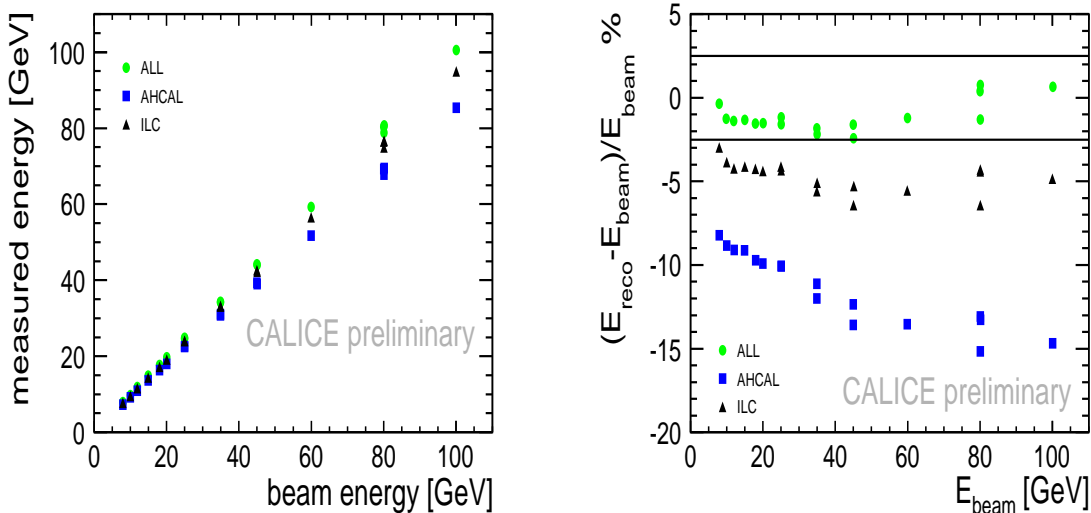
Figure 8.6: *Measured energy (left) and deviation of the measured energy from the expected beam energy (right) are shown for three different cases: using the information of all the calorimeters (ALL, green circles), excluding the TCMT information (AHCAL, blue squares) and excluding part of the TCMT information to simulate the presence of a coil (ILC, black triangles). Runs in the range from 8 GeV to 100 GeV have been considered.*

within GEANT4 using Mokka [183, 277] (see Sec. 3.5.2). The detectors upstream of the calorimeters (the Cherenkov counter, the scintillators for the trigger and the tracking chambers) are simulated as well. The origin of the simulated pions is located upstream of the full system, such that also the interactions with the Cherenkov counter, the scintillator-triggers, the tracking chambers and the air volumes in between are taken into account. Sensitive and passive materials, gaps and support structures are also taken into account in detail. A thorough description of the AHCAL simulation can be found in [278]. The simulated AHCAL active layers have a uniform granularity of $1 \times 1 \, \text{cm}^2$ cell size. The realistic geometry of the AHCAL is obtained during the digitization procedure, as described below.

Digitization

In order to compare the measured data with the Monte Carlo simulations, the simulated events are adapted to realistic conditions through a process called digitization. The digitization allows the same treatment for data and Monte Carlo through all the following analysis steps, such as calibration and reconstruction. This procedure takes into account several factors:

- the detector granularity. The signal amplitude of the $1 \times 1 \, \text{cm}^2$ virtual cells is summed up to obtain the real geometry with 3×3, 6×6 and $9 \times 9 \, \text{cm}^2$ cells, which is described in Sec. 7.1.2.

- the light leakage between neighboring tiles (cross-talk). From the comparison of the energy reconstructed in simulation and data, the value of 2.5% for the light cross-talk on each tile edge is found to be adequate.

- non-linearity effects of the SiPMs, based on their specific saturation curves (Sec. 7.3).

- statistical smearing of the detector response at the pixel scale.

- the noise contribution. The noise is overlaid to the simulation, using real noise from the data, measured during pedestal events.

Physics Lists

The interactions of hadrons with matter cannot be described exactly and several models, working with different approximations, exist. Several "physics lists" are available in GEANT4, which combine different models for different energy ranges, with a random choice of which model is used for overlapping energy regions. A complete description of the models is given in [264]. The main features of the physics lists used in this analysis are summarized here:

- **FTF_BIC**. Uses the Binary Cascade (BIC) model at low energies, with a transition to the Fritiof model (FTF) between 4 GeV and 5 GeV. The BIC model is again used also in the Fritiof energy region for the rescattering of the secondaries. Both models are theory driven. While the BIC is based on nucleon-nucleon scattering via resonance formation and decay, the FTF is based on string formation via the scattering of projectiles on nucleons.

- **FTFP_BERT**. This physics list uses the theory-based Bertini cascade and the Pre-compound models for low energies, making a transition to the FTFP model, based on a GEANT4 implementation of the FTF model, at energies between 4 GeV and 5 GeV. The GEANT4 implementations of the Bertini and Pre-compund models incorporate the Bertini intra-nuclear cascade, a pre-equilibrium model, a nucleus explosion model, a fission model, and an evaporation model.

- **QGSP_BERT**. This physics list makes use of the QGS (Quark-Gluon-String) model together with the Pre-compound model at energies greater than 12 GeV. The Bertini cascade is used at energies lower than 9.9 GeV and the LEP parametrization between 9.5 GeV and 25 GeV. The QGS model is a theory driven model, used to simulate the interaction with nuclei of protons, neutrons, pions and kaons. The Pre-compound model is needed by QGS in order to de-excite and fragment the nuclei after the interactions. The LEP (Low Energy Parametrization) model is based upon parametrization of existing data.

8.2.2 Comparison Plots

The longitudinal profiles reconstructed relative to the calorimeter front face (cf. Fig. 8.5) for data and Monte Carlo are compared in Fig. 8.7. Three energies have been chosen: 8 GeV (left), 18 GeV (center) and 80 GeV (right). They are interesting since the physics lists usually make use of different models in these three energy regions. The Monte Carlo longitudinal profile is compared with the data for the three physics lists separately. The distributions in the bottom panels show the ratio of Monte Carlo to data for all the physics lists together. At 8 GeV and 18 GeV the description of the data longitudinal profile by the Monte Carlo in the AHCAL is correct at the 10-15% level,

for all the physics lists, and the position of the shower maximum is well reproduced. At 80 GeV the energy deposited in the shower maximum region is overestimated by up to 30%. Additionally, there is an evident layer-to-layer effect in the ratio of Monte Carlo to data in the shower maximum region. This might hint at saturation effects in the data, that are not reproduced by the Monte Carlo. As already mentioned, the same SiPM response curves are used both to simulate saturation effects in the Monte Carlo and to correct for them. As a consequence, the saturation corrections might work more effectively for the Monte Carlo than for the data. Improvements of the saturation correction and of the simulation of the saturation effects in the Monte Carlo are under study.

The situation for the simulation of the TCMT response is different. There is a shift in the Monte Carlo simulations, for all the physics list, when passing from the AHCAL to the TCMT region in the longitudinal profile, which is well visible from the ratio plots. This shift is most likely due to issues with the simulation of the TCMT rather than to features of the physics lists. The simulation of the TCMT, as well as its calibration procedure, are known to be not as advanced as for the AHCAL. However, this does not compromise the present study since the central part of the analysis is performed using the SiW-ECAL+AHCAL information only.

Figure 8.8 illustrates the comparison between data and Monte Carlo for two observables that will be used in building the correction for the leakage. The first observable is the shower starting point (distributions in the first and second row), i.e. the AHCAL layer where the PTF algorithm identifies the first hard interaction. The second observable is the end-fraction (distributions in the third and fourth row). The end-fraction is defined as the fraction of energy deposited in the last four layers of the AHCAL divided by the total shower energy measured by SiW-ECAL+AHCAL (details in Sec. 8.3.2). It is a continuous variable and the shape of the distributions is influenced by the choice of the binning. For the purpose of comparing data and Monte Carlo the binning [0, 0.01, 0.025, 0.05, 0.1, 0.2, 0.4, 1] was used. Since the number of events decreases with increasing end-fraction, variable bin sizes have been chosen, in order to keep the statistics meaningful in all the bins.

The same energies as were chosen for the distributions of the longitudinal profile are also used for the comparison of data and Monte Carlo for the shower starting point and the end-fraction: 8 GeV (left), 18 GeV (center) and 80 GeV (right). The distribution of the shower starting point is reproduced at the 10-20% level by the Monte Carlo in the first part of the AHCAL. In the Monte Carlo to data ratios (second row) some scattering is visible in case of late showers, starting towards the end of the AHCAL, but the statistics is low in this region, in particular for the 8 GeV run (left column).

The Monte Carlo to data ratios for the end-fraction observable are shown in the bottom panels of the figure. For the low energy runs, at 8 GeV and 18 GeV (left and center column, respectively), the accuracy of the Monte Carlo is at the 10-20% level. For the high energy run, at 80 GeV (right column), the Monte Carlo simulation overestimates the events with low end-fraction. This means that the showers are more compact in the Monte Carlo and tend to deposit a lower fraction of energy in the end of the AHCAL, when compared to the data.

In Fig. 8.9 and 8.10 the comparison of data and Monte Carlo is shown respectively for the mean value and the RMS90 of the total energy distributions, using either the full calorimeter (right-hand side) or SiW-ECAL+AHCAL only (left-hand side). At 8 GeV
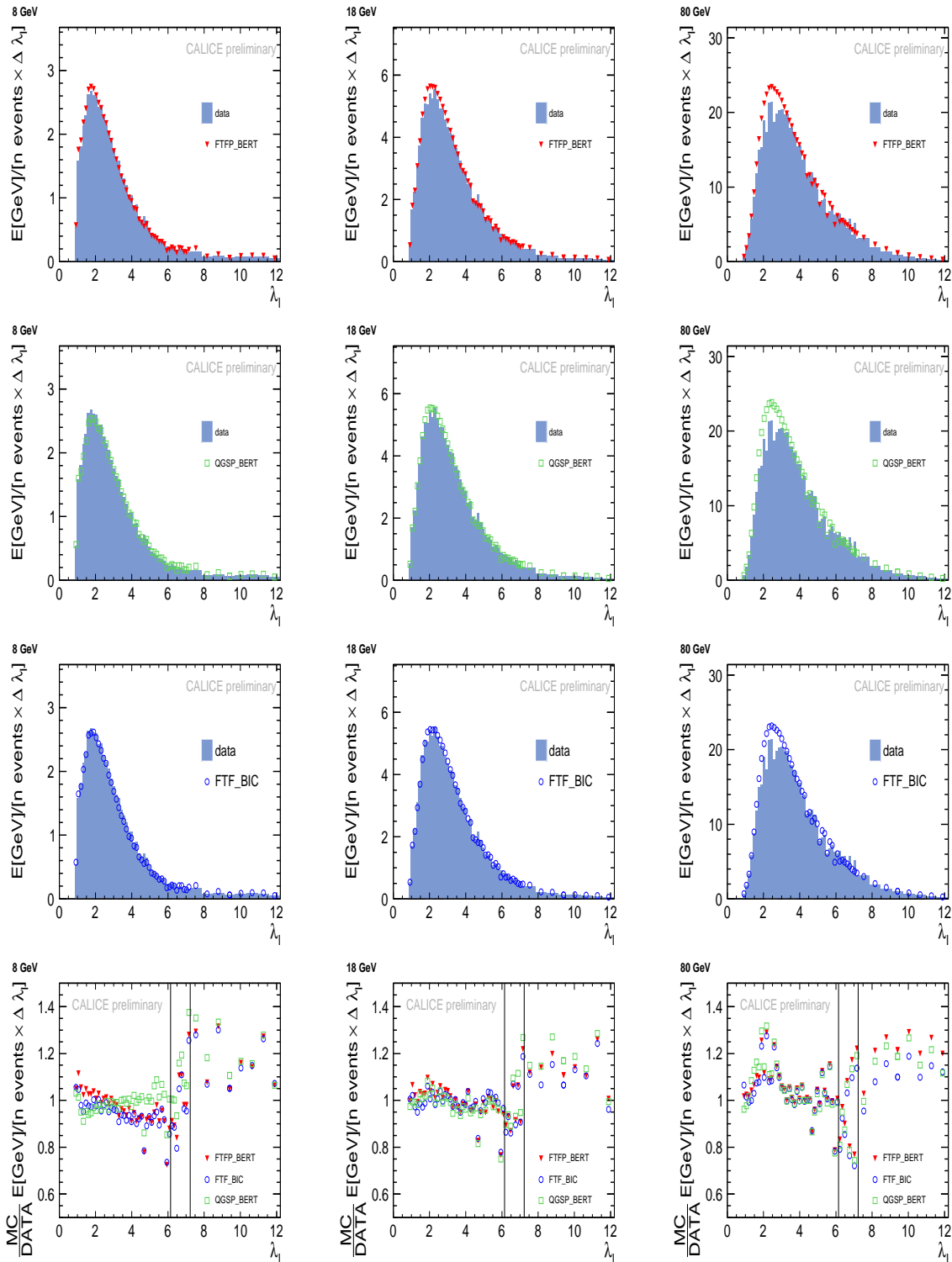
Figure 8.7: *Comparison of the average longitudinal profile of showers in data and Monte Carlo, for three physics lists, at 8 GeV (left), 18 GeV (center) and 80 GeV (right). The profiles are reconstructed relative to the AHCAL front face. The vertical bars in the ratio plots (bottom) divide the different regions of the calorimetric system: AHCAL, TCMT (first 8 layers), TCMT (last 8 layers).*
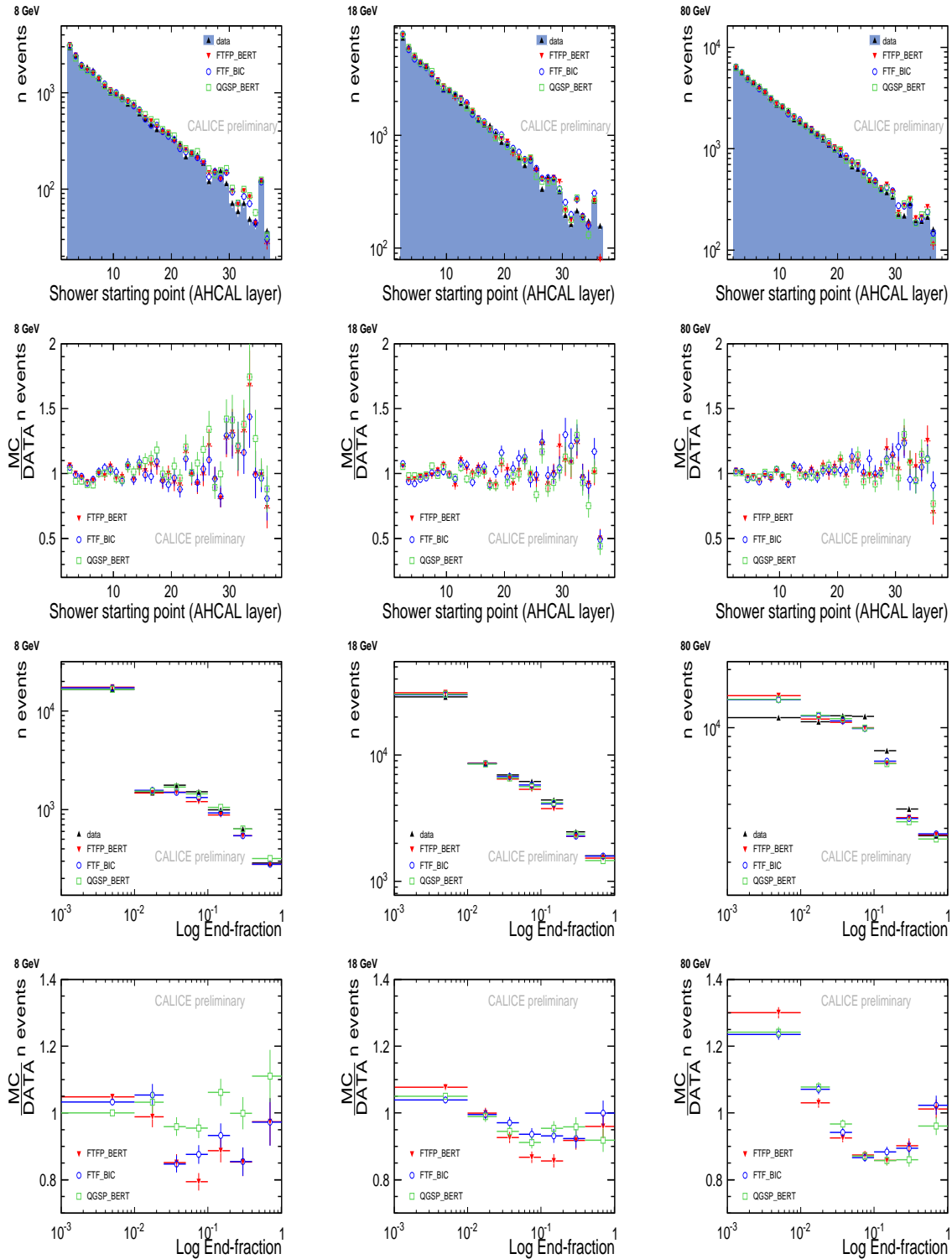
Figure 8.8: *Comparison of the shower starting point and the end-fraction observables in data and Monte Carlo, for three physics lists, at 8 GeV (left), 18 GeV (center) and 80 GeV (right). From top to bottom are shown: shower starting point, Monte Carlo to data ratio of the shower starting point, end-fraction and Monte Carlo to data ratio of the end-fraction.*
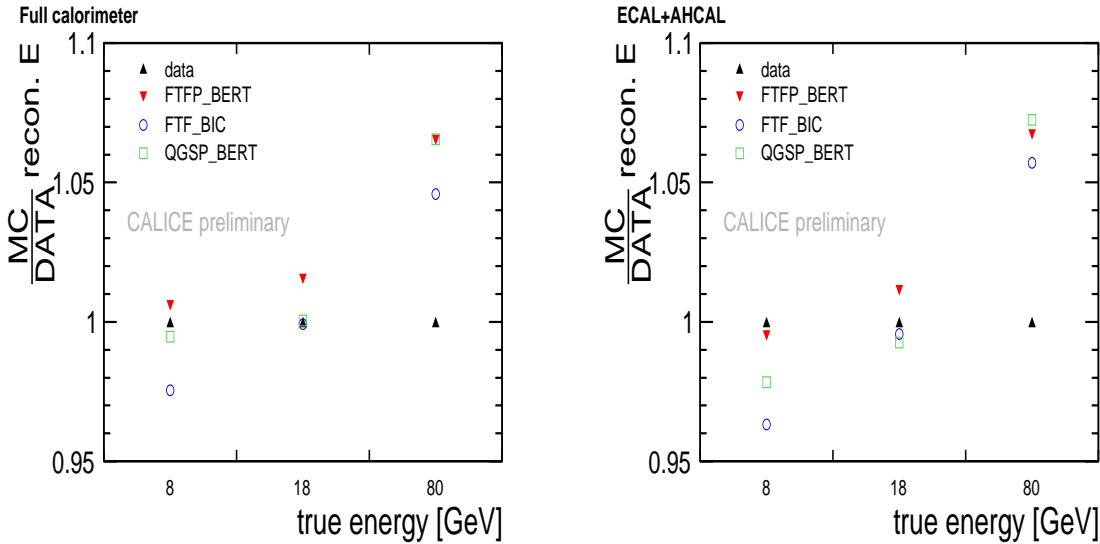
Figure 8.9: *The mean value of the reconstructed energy distribution for data and Monte Carlo are compared for the beam energies 8 GeV, 18 GeV and 80 GeV. The graphs on the left show the total energy reconstructed using the full calorimeter, while the graphs on the right were made excluding the TCMT information.*
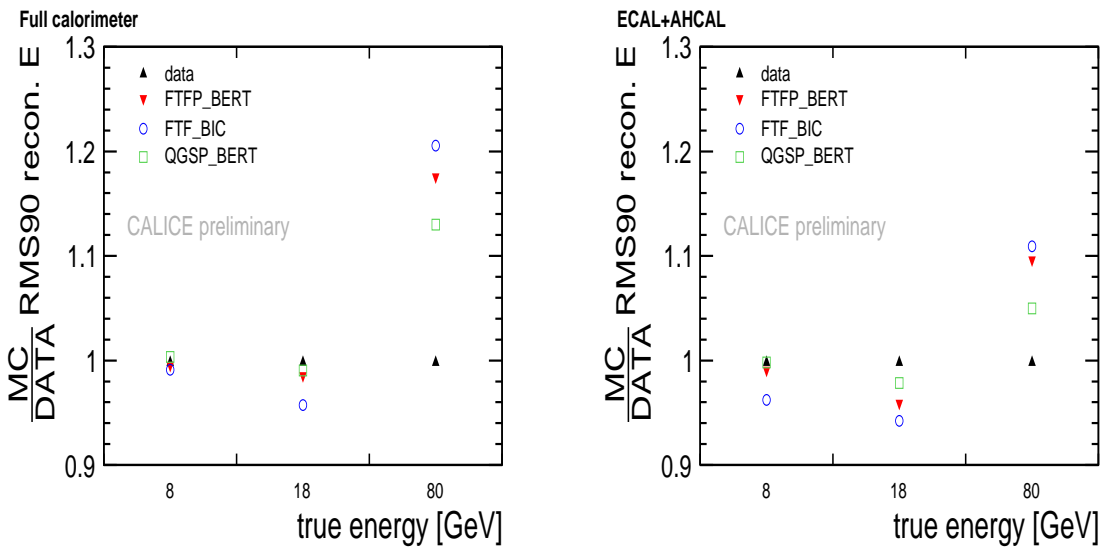
Figure 8.10: *The spread of the reconstructed energy distributions for data and Monte Carlo are compared for the beam energies 8 GeV, 18 GeV and 80 GeV. The graphs on the left show the RMS90 when using the full calorimeter, while the graphs on the right were made excluding the TCMT information.*

and 18 GeV the energy scale of the data is well reproduced within the calibration uncertainties. At 80 GeV the Monte Carlo simulations overestimate the total reconstructed energy with respect to the data by about 5%. All the physics lists considered show an energy-dependent behavior, such that the Monte Carlo to data ratios increase with energy. This behavior is partly explained again as a non-perfect implementation of saturation effects in the simulation, such that the saturation in data appears more pronounced.

Figure 8.10 shows the RMS90 of the measured energy distributions for both the full calorimeter (left) and when excluding the TCMT information (right). The physics lists show a similar behavior. The resolution is reproduced at the 5% level for low energies (8 GeV and 18 GeV), while the Monte Carlo simulations overestimate the RMS90 of the data for a high beam energy of 80 GeV. The effect is significantely reduced from 13-20% to 5-11% when excluding the TCMT and considering only the energy reconstructed by SiW-ECAL+AHCAL. This might hint at problems in the TCMT calibration, which were already mentioned.

8.3 Observables sensitive to the Leakage

Some showers do not conclude their development before reaching the end of the AH-CAL, depositing a non-negligible amount of energy in the TCMT. In order to show the potential of a highly granular calorimeter a technique has been implemented, to correct for the leakage from the AHCAL without relying on any information collected by the TCMT.

The fine granularity of the AHCAL allows the reconstruction of the shower development with good accuracy, revealing the shape and the starting point of the cascade. Some information about the showers can be correlated to the leakage. For instance, those showers that start in the last part of the AHCAL, as well as those with a high percentage of the visible energy deposited in the last layers of the AHCAL, are good candidates for having a non-negligible leakage into the TCMT.

The correlation between the variables carrying information about the shower development and the leakage is spoiled by event-to-event fluctuations typical for hadronic showers. This limits intrinsically the potential of any correction for the leakage, in terms of energy resolution improvement.

Some corrections for the leakage from the AHCAL have already been studied in the past (e.g. [264]), but they have been developed relying on the beam energy information. In this section two corrections for the leakage are studied using the same beam energy constraint, in order to show the potential of two observables correlated to the leakage. In the following section these two observables will be used together to implement a correction not relying on the knowledge of the beam energy.

The punchthrough pions, those pions that start showering in the TCMT, have not been considered in this analysis. When studying the benefits of a TCMT, one should also mention that the TCMT would allow to reconstruct their energy, at least partially, while without a TCMT they are lost. However, they represent only a small amount of the full statistics (less than 1%), due to the exponential behavior of the shower starting point (Fig. 8.8).

It can be noticed that the PTF algorithm makes use of the beam energy information, a fact that might seem to contradict the purpose of this study to implement an energy-independent correction. The idea is that in a real experiment the starting point of the showers will be found using some more elaborate and general algorithms (as e.g. the Pandora [174] algorithm developed for the ILC detectors), without using the "forbidden" information that the PFT algorithm requires. For the purpose of this study, it is possible to use this rather test beam specific software, while building a correction which does not itself rely on the beam energy information, even though one of the
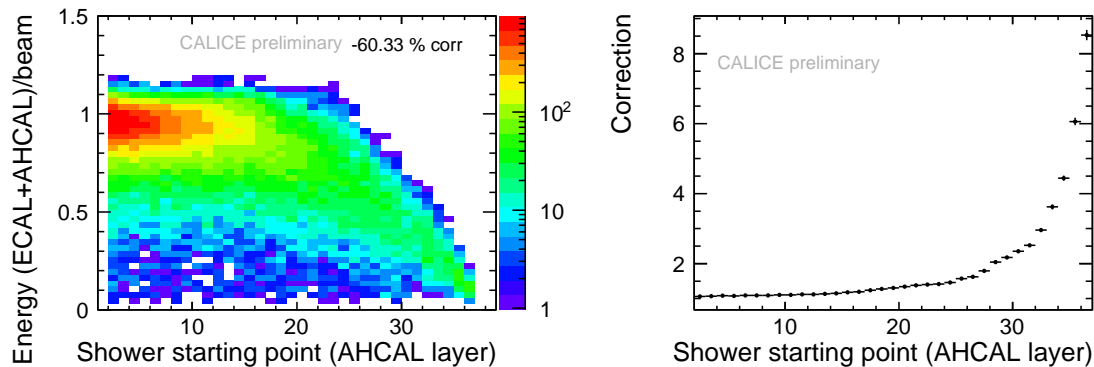
Figure 8.11: *Left: shower starting point versus the ratio between the measured energy in SiW-ECAL+AHCAL and the beam energy. Right: correction factors that have to be applied to the measured energy in SiW-ECAL+AHCAL in order to recover from the leakage, depending on the layer where the shower starts. The chosen example distributions correspond to an 80 GeV run.*

used observables (namely the shower starting point) is found using the beam energy information. The validation of the capabilities of more general algorithms (such as Pandora) in identifying the first hard interaction of the showers is definitely a separate task. However, existing studies show that finding the first hard interaction in the AHCAL in a more general way should not be an issue. A more general algorithm was studied in [264], while in [260] a private version of the PTF algorithm was tuned using the measured energy information instead of the beam energy, without any performance losses.

8.3.1 The Shower First Hard Interaction

In the following, since the information of the TCMT is excluded, measured energy will indicate the energy measured by SiW-ECAL+AHCAL, where not otherwise specified.

The left distribution in Fig. 8.11 shows the correlation between the shower starting point and the ratio between the measured energy and the beam energy. A correlation between the two quantities is clearly visible. When the shower starts at the beginning of the AHCAL, the measured energy is close to the expected beam energy for most of the events. This means that the energy lost, leaking from the AHCAL, is usually negligible. On the contrary, for showers starting late in the AHCAL the fraction of the beam energy which is measured becomes smaller and the effect of the leakage is non-negligible anymore. As already mentioned, due to event-to-event fluctuations typical for hadronic showers, the correlation between the leakage and the shower starting point is spoiled, resulting in a broad distribution.

The distribution on the right in Fig. 8.11 shows the average correction to be applied to the measured energy in order to recover from the leakage, depending on the layer where the first hard interaction occured. For each layer, the correction to the leakage is calculated for every event, that has its first hard interaction in that layer:
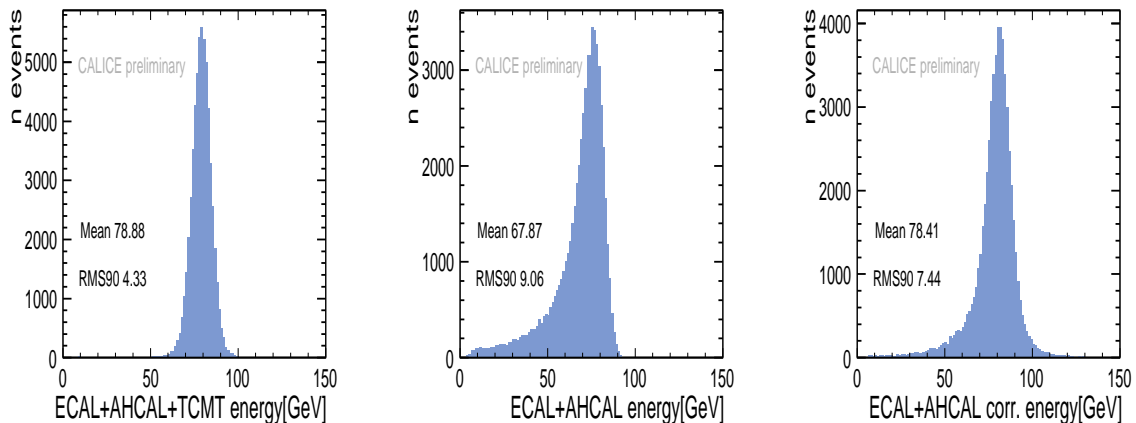
$$c_j = \frac{E_{beam}}{E_{SiW-ECAL+AHCAL,j}},$$

(8.11)
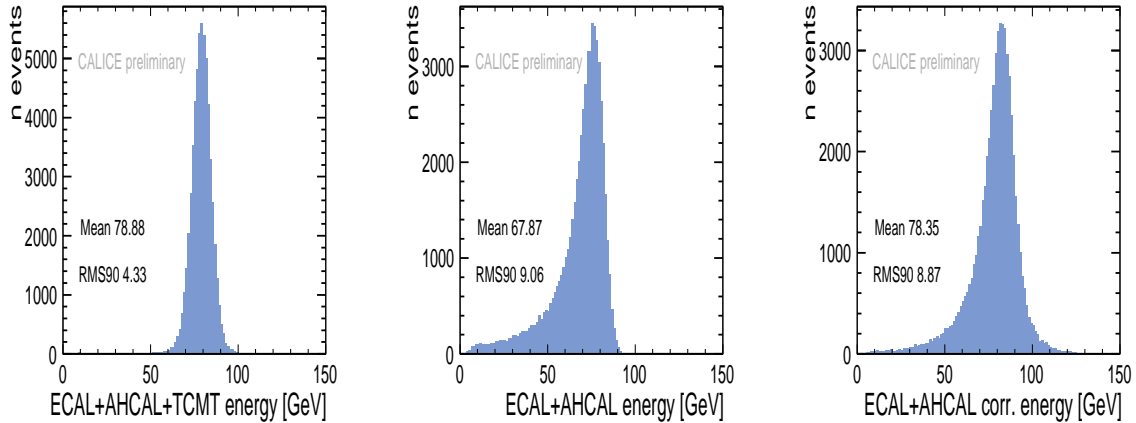
Figure 8.12: *Left: total energy measured using the full calorimeter. Center: energy measured by SiW-ECAL+AHCAL only. Right: energy measured by SiW-ECAL+AHCAL only, with correction based on the shower starting point. The chosen example distributions correspond to an 80 GeV run.*

where c_j is the correction factor for the event j, to be applied to the energy measured in SiW-ECAL+AHCAL $E_{SiW-ECAL+AHCAL,j}$ in order to recover from the leakage. The correction factors shown on the right of Fig. 8.11 are obtained by averaging over the corrections for events having their first hard interaction in the same layer.

The application of the correction is shown in Fig. 8.12 for an 80 GeV run. The correction factors have been derived from a different 80 GeV run in order to assure statistical independence. The distribution on the left shows the total energy measured using the full calorimeter, while the center distribution shows the energy measured when excluding the TCMT information. The degradation, both in terms of mean and RMS90 in the center distribution, when excluding the TCMT, is clearly visible. The distribution on the right shows the energy measured in SiW-ECAL+AHCAL, after the correction based on the shower starting point. The mean of the distribution is well recovered, thanks to the beam energy constraint used in calculating the correction factors. The RMS90 is reduced, with respect to the center distribution, but is still much larger than the RMS90 obtained using the full calorimeter. As already mentioned this is mainly due to event-to-event fluctuations, which limit the power of the correction. For example, considering the events with their first hard interaction occurring in the first layers, the average correction to be applied to the measured energy is close to one, since most of the events with an early shower start have no leakage. However, as shown in the left distribution of Fig. 8.11, few events have a non-negligible leakage, even if their first hard interaction occurs at the beginning of the AHCAL. These events are also corrected with factor close to one, which means that almost no correction is applied to the measured energy and the leakage is not recovered. These events remain in the low-energy tail of the energy distribution, and a dramatic RMS90 improvement cannot be obtained. Analogously, some events are over-corrected, contributing to the high-energy tail of the corrected energy distribution.

The uncertainty introduced by the PTF algorithm also contributes to limit the power of the correction. As shown in the right distribution of Fig. 8.11, the correction factors can change significantly even for consecutive layers, in particular for the last layers of the AHCAL.
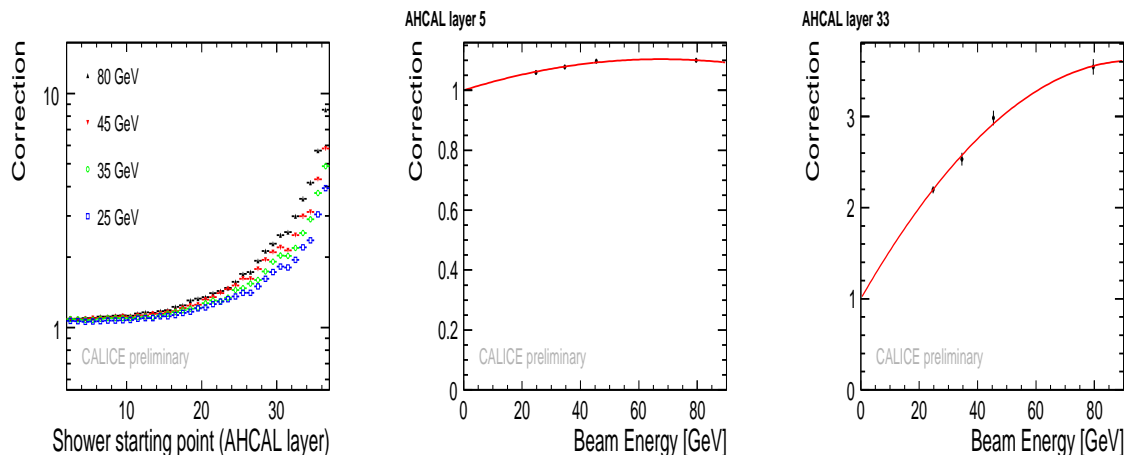
Figure 8.13: *Left: correction factors for the leakage, based on the shower starting point. The corrections for different energies are shown in different colors. Center (right): energy dependence of the correction factors for events having their first hard interaction in the 5th (33rd) layer of the AHCAL. The red lines are drawn to guide the eye.*

The correction factors, as given by Eq. 8.11, are tuned using the beam energy information. The correction factors strongly depend on the beam energy, as shown in left distribution of Fig. 8.13. The dependence on the beam energy is stronger when the shower starts late in the AHCAL. This is visible from the central and right distributions in Fig. 8.13, which show the energy dependence of the correction factors respectively for the layer 5 and 33 of the AHCAL. The dependency is visibly steeper for a late shower starting point (right). A way to overcome this energy dependence of the correction is discussed in Sec. 8.4.

8.3.2 The End-Fraction

The end-fraction is defined as the fraction of energy deposited in the last four layers of the AHCAL devided by the total shower energy measured by SiW-ECAL+AHCAL. The left distribution in Fig. 8.14 shows the end-fraction versus the ratio between the measured energy and the beam energy, for an 80 GeV run. The two quantities are correlated. A small fraction of energy deposited at the end of the AHCAL indicates that the shower is in general almost concluded before reaching the end of the calorimeter. In fact, the ratio between the measured energy and the beam energy is mainly close to one, for those events that have a small end-fraction. On the contrary, a high end-fraction indicates a shower still in development, that could leak into the TCMT with a high probability. As a consequence, the ratio between the measured and the beam energy decreases when the end-fraction increases, due to increasing leakage.

The correlation between the leakage and the end-fraction can be exploited to develop a correction for the leakage, as was done for the shower starting point observable.

The end-fraction is a continuous variable and can be arbitrarily binned. The chosen binning is [0, 0.01, 0.025, 0.05, 0.1, 0.15, 0.2, 0.25, 0.3, 0.35, 0.4, 0.45, 0.5, 0.55, 0.6, 0.65, 0.7, 0.75, 0.8, 0.85, 0.9, 0.95, 1]. The average correction to be applied to the events falling in the same end-fraction bin was calculated as in the previous example and is shown in the right distribution of Fig. 8.14, for an 80 GeV run.
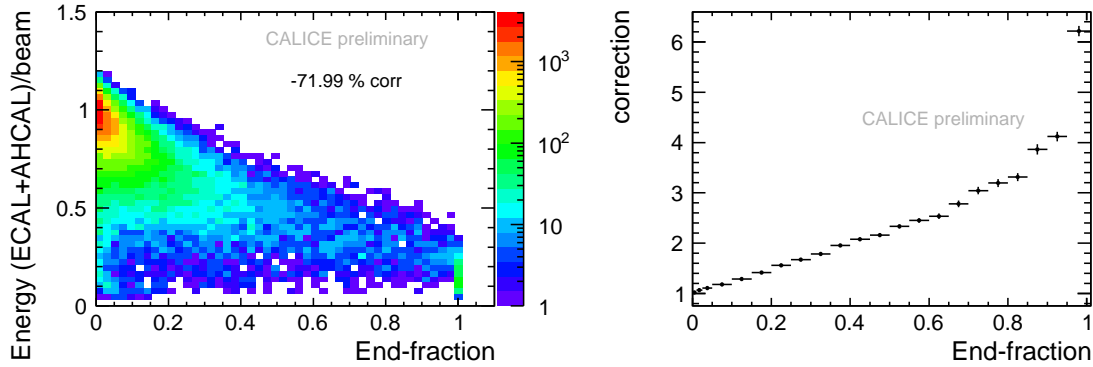
Figure 8.14: *Left: end-fraction versus the ratio between the energy measured in SiW-ECAL+AHCAL and the beam energy. The cluster of events for an end-fraction of approximately one is due to the fact that events with a shower starting point in layers 35 or 36 have an end-fraction exactly equal to one according to the end-fraction definition. Right: correction factors versus the end-fraction. The chosen example distributions correspond to an 80 GeV run.*

Figure 8.15: *Left: total energy measured using the full calorimeter. Center: energy measured by SiW-ECAL+AHCAL only. Right: energy measured by SiW-ECAL+AHCAL only, after applying the correction based on the end-fraction. The chosen example distributions correspond to an 80 GeV run.*

The application of the correction is shown in Fig. 8.15. The results are similar to those obtained for the correction based on the shower starting point and the same considerations are valid. The mean of the measured energy distribution is well recovered and the RMS90 is reduced, though not reaching the precision given by the additional TCMT information.

The correction factors are in this case also strongly energy dependent, as shown in the left distribution of Fig. 8.16. The energy dependence is stronger for higher end-fractions. This is visible from the center and the right distribution in the same figure. The two distributions show the energy dependence of the correction factors to be applied to events having a low or a high end-fraction, respectively. For a high end-fraction, the slope of the distribution is visibly steeper.
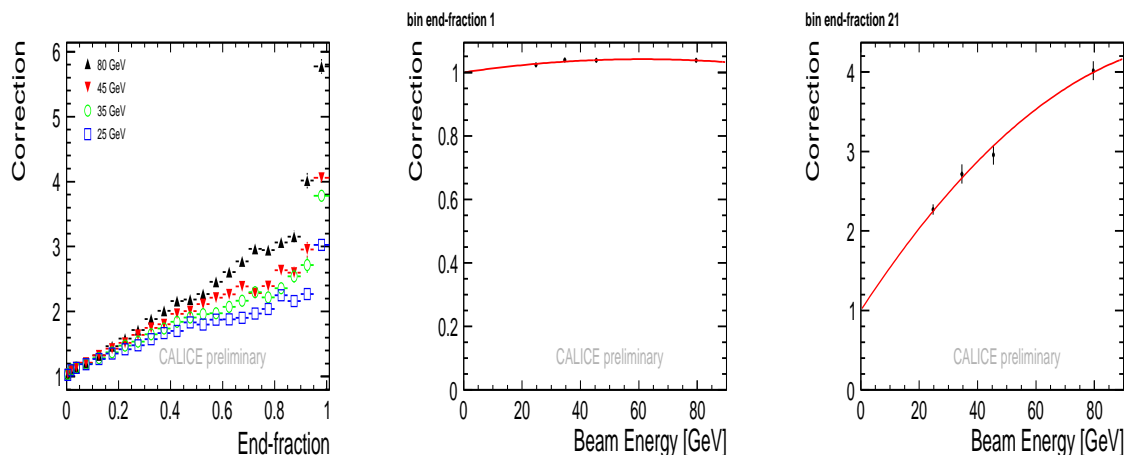
Figure 8.16: *Left: correction factors for the leakage based on the end-fraction. The corrections for different energies are shown in different colors. Center (right): energy dependence of the correction factors for events having a low (high) end-fraction (i.e. an end-fraction falling in the first (21st) bin). The red lines are drawn to guide the eye.*

8.4 A Correction for the Leakage

The two observables studied in the previous section, the shower starting point and the end-fraction, have been used together in order to implement a realistic correction for the leakage. In this case realistic means that the correction should not be tuned using the beam energy information. In order to replace the beam energy information a third variable is used, namely the measured energy in SiW-ECAL+AHCAL. The three-dimensional distribution of these three variables is shown in Fig. 8.17 (top, left). Events of runs with different energies tend to occupy different regions of the 3D-space, though with overlaps. The 2D-projections (Fig. 8.17, top-right and bottom panels) of the 3D-distribution contain, of course, the same information. However, in particular the 2D-projection of the shower starting point versus the end-fraction (top-right) shows that the measured energy information is necessary in order to separate different beam energies, i.e. different runs. Events of runs with different beam energies tend to overlap in this distribution, which excludes the information of the measured energy.

The separation of the different beam energies in the chosen 3D-space can be used in order to build a realistic correction for the leakage. The energy of the events can be corrected depending on the measured energy, the end-fraction and the shower starting point, without requiring a priori knowledge of the beam energy. For instance, an event with an early shower starting point and a negligible end-fraction is, in general, an event without significant leakage and the measured energy is, on average, very close to the beam energy. An event with a shower starting point further into the calorimeter and a high end-fraction is expected to be an event with leakage that needs to be corrected. The correction will depend on the measured energy of the event and will not be tuned using the beam energy information.

The correction was first implemented in a Monte Carlo study. Two possible applications to the data have then been considered, obtaining the correction to the data either from a Monte Carlo template or from independent data runs.
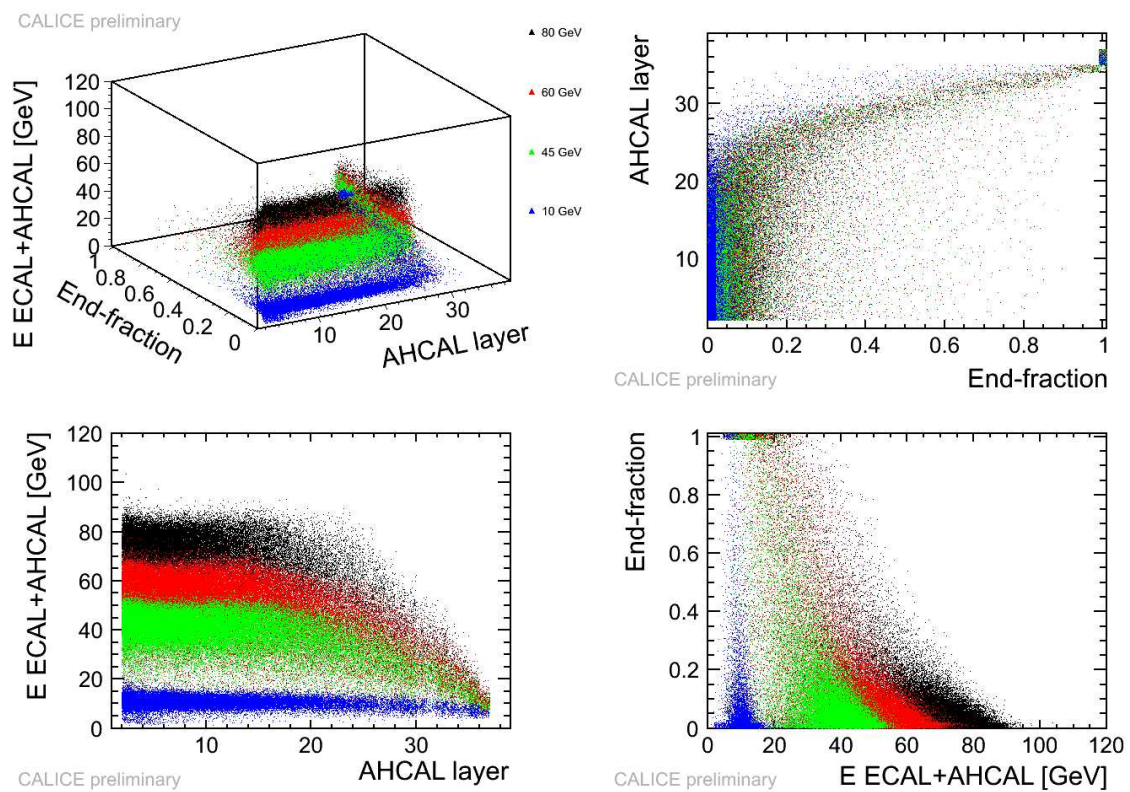
Figure 8.17: *Top-left: 3D-distribution of the measured energy, the end-fraction and the shower starting point. Different runs with different beam energies are shown in different colors. The other three distributions are the 2D-projections of the 3D-distribution. Top-right: end-fraction versus shower starting point. Bottom-left: shower starting point versus measured energy. Bottom-right: measured energy versus end-fraction.*
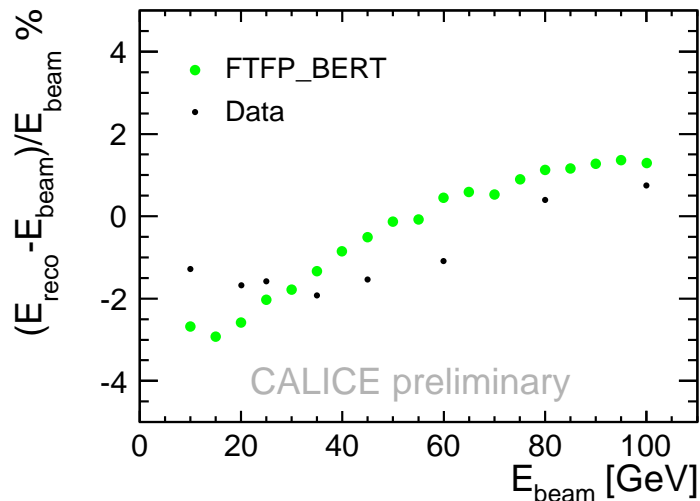
Figure 8.18: *Deviations of the Monte Carlo reconstructed energy from the beam energy as a function of the beam energy. The reconstructed energy refers to the energy reconstructed using the full calorimeter, such that leakage effects are negligible. The corresponding distribution for the data is also shown for direct comparison. Different sampling weights have been used for data and Monte Carlo in order to obtain a similar energy scale.*

8.4.1 Monte Carlo Study

Monte Carlo simulations in the energy range from $7.5\,\text{GeV}$ to $100\,\text{GeV}$ have been generated using the physics list FTFP_BERT (Sec. 8.2.1). The correction is built from and applied to statistically independent runs. In order to show its regular behavior over the whole energy range, the correction is applied also to runs at beam energies that are not used for calculating the correction factors.

The sampling weights have been optimized specifically for these Monte Carlo simulations in the same way as it was done for the data (Sec. 8.1.3). As seen in Sec. 8.2.2, the Monte Carlo does not perfectly reproduce the energy scale of the data, when comparing data and Monte Carlo by using the same sampling weights (which include the MIP to GeV conversion). For the pure Monte Carlo study this comparison is not relevant anymore and different sampling weights can be applied to the Monte Carlo simulations, in order to recover its energy scale. After the sampling weights optimization, the Monte Carlo reconstructed energy using the full prototype, including the TCMT (i.e. without leakage effects), should peak at the beam energy for which the events were generated. The deviations from the expected beam energy for runs in the considered energy range are shown in Fig. 8.18. The linearity of the response is accurate at the 2% level, which is acceptable and comparable to the linearity of the response of the data, though the slope of the Monte Carlo response appears to be slightly steeper. Since the AHCAL is a non-compensating calorimeter, the response is expected to increase with energy, due to the increasing amount of the electromagnetic fraction (Sec. 6.1.4). In the data this effect is compensated by saturation effects, which act in the opposite way, limiting the rise of the response with increasing energy. The saturation is not yet perfectly reproduced in the Monte Carlo, hence a steeper distribution is obtained.

The two variables, the end-fraction and the shower starting point, are binned respec-
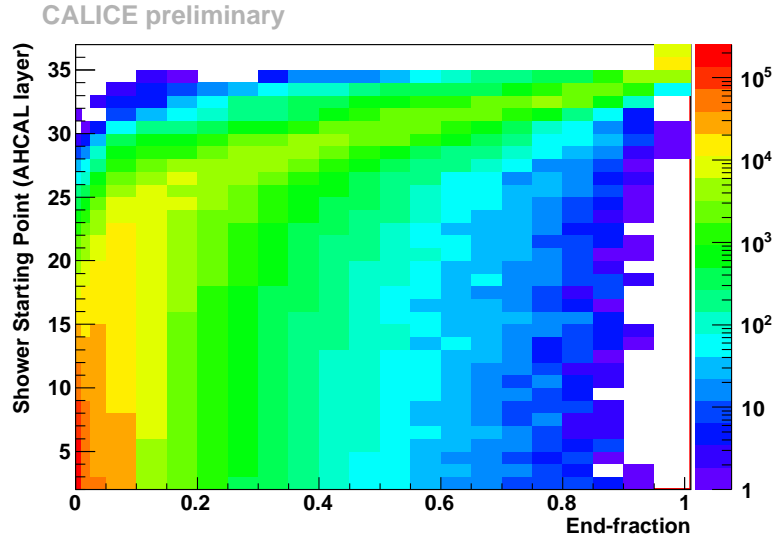
Figure 8.19: *2D-distribution of the shower starting point versus the end-fraction of the events from the Monte Carlo runs used to build the correction for the leakage. The distribution clarifies the chosen binning for the two observables and the global amount of events in the different bins. The distribution contains the events for all energies used to create the Monte Carlo templates.*

tively in 22 and 35 bins. The end-fraction chosen binning is [0, 0.01, 0.025, 0.05, 0.1, 0.15, 0.2, 0.25, 0.3, 0.35, 0.4, 0.45, 0.5, 0.55, 0.6, 0.65, 0.7, 0.75, 0.8, 0.85, 0.9, 0.95, 1] while the binning chosen for the shower starting point is [2, 3, 4, 5, 6, 7, 8, 9, 10, 11, 12, 13, 14, 15, 16, 17, 18, 19, 20, 21, 22, 23, 24, 25, 26, 27, 28, 29, 30, 31, 32, 33, 34, 35, 36, 37]. The total amount of events falling in the different bins of the 2-dimensional distribution of the end-fraction versus the shower starting point is shown in Fig. 8.19.

For the events from different runs falling in same 2D-bin another distribution is created of the average measured energy in SiW-ECAL+AHCAL versus the beam energy for which the events were generated. The average is calculated from all the events of the same run (same energy) falling in the same bin. The mean value of the measured energy is drawn versus the beam energy of the run, for all the runs which have events falling in the considered bin. Two examples of such distributions are shown in Fig. 8.20. The error bars show the statistical errors, determined by the number of events per bin. The left-hand side distribution originates from a bin corresponding to an early shower starting point and a low end-fraction, i.e. with low expected leakage. In fact, the average measured energy is very close to the beam energy. The right-hand side distribution stems from a bin corresponding to a more advanced shower starting point and a higher end-fraction, i.e. where a significant leakage contribution is expected. In fact, the measured energy decreases more and more with increasing beam energy since the leakage increases as well.

The distributions are fitted with a second order polynomial. In those cases, in which the coefficient of the second order term of the fitted polynomial is very small (< 0.0001), the distribution is fitted with a first order polynomial, instead. Each 2D-bin of the end-fraction/shower starting point plane has been associated to a function, that will be called in the following *template function*. The template functions for the two illustrative bins considered are also shown in Fig. 8.20.
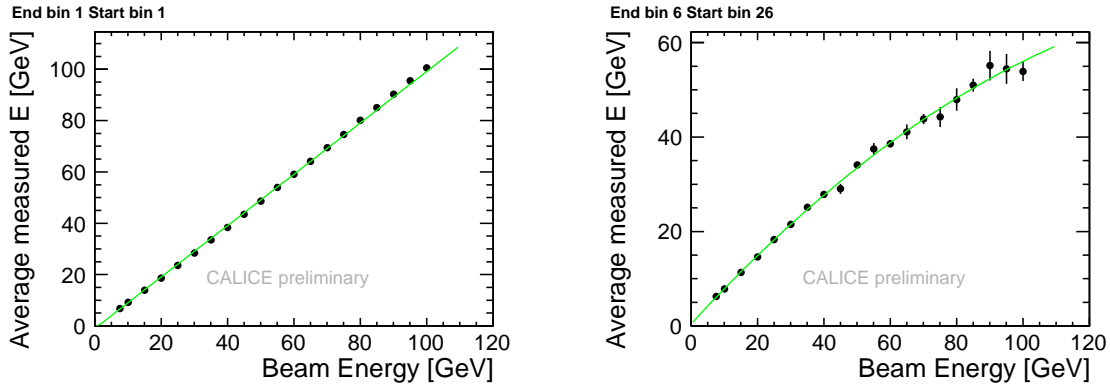
Figure 8.20: *Distributions of the average measured energy versus the beam energy, for the events falling in two different bins of the end-fraction versus the shower starting point distribution. The distribution on the left (right) contains events falling in the end-fraction bin 1 (7) and shower starting point layer bin 1 (27). The Monte Carlo samples for different energies have not exactly the same statistics, therefore the error bars show some fluctuations.*
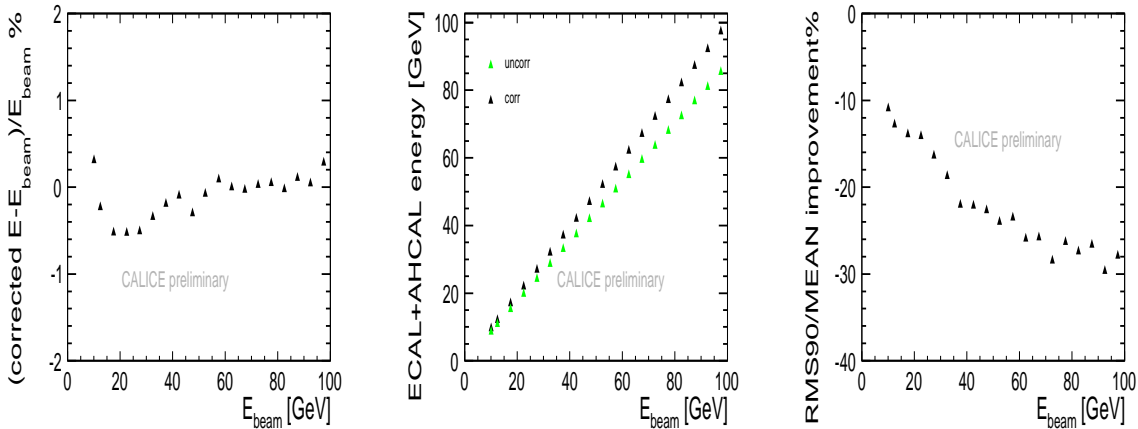
Figure 8.21: *Final results of the leakage correction for Monte Carlo. Left: the relative deviation of the mean value of the corrected energy distributions from the beam energy versus the beam energy. Center: mean value of the measured energy distributions before and after the correction. Right: relative improvement of RMS90/Mean versus the beam energy.*

The template functions are the central part of the correction. For each event the three quantities end-fraction, shower starting point and measured energy in SiW-ECAL+AHCAL are considered. The proper template function is chosen depending on the end-fraction and the shower starting point. Using its inverse the measured energy of the event is associated to a specific beam energy, which is taken as the correct value of the measured energy.

The performance of the correction is summarized in Fig. 8.21. The correction is capable of identifying the energy of the run with a precision better than 0.5%. The RMS90/Mean improves by up to 30% at high energies, while decreasing towards lower energies together with the impact of the leakage.

In Fig. 8.22 the effect of the correction on a simulation for a beam energy of 82.5 GeV
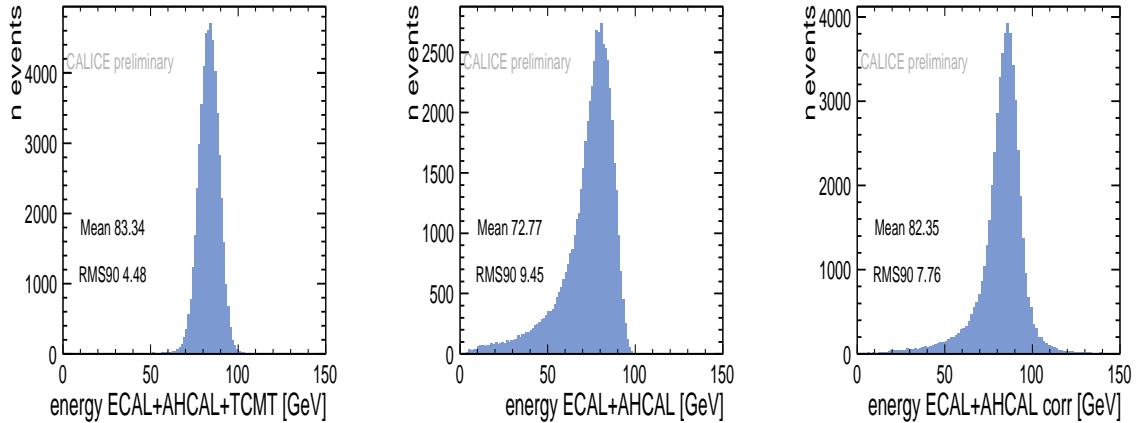
Figure 8.22: *Left: total energy measured using the full calorimeter. Center: energy measured by SiW-ECAL+AHCAL only. Right: energy measured by SiW-ECAL+AHCAL, after applying the correction for the leakage. Example distributions of a Monte Carlo simulation for a beam energy of 82.5 GeV.*

is shown. The mean value of the energy measured by SiW-ECAL+AHCAL is well recovered despite the leakage, and goes from 72.77 GeV to 82.35 GeV, which is very close to the nominal 82.5 GeV. At the same time the RMS90 is reduced from 9.45 to 7.76 GeV. While the mean value of the measured energy can be perfectly recovered without using the TCMT information, thanks to the correction, the RMS90 improves but does not reach the precision achieved with the additional TCMT information, in which case the RMS90 is only 4.48 GeV.

8.4.2 Application to Data

When applying the correction to data, the template functions can be obtained either using an independent set of data or Monte Carlo simulations.

In the first option data from runs with energies of 8 GeV, 12 GeV, 15 GeV, 25 GeV, 35 GeV, 45 GeV, 80 GeV and 100 GeV have been used. The correction has then been applied to events from independent runs with energies of 10 GeV, 20 GeV, 25 GeV, 35 GeV, 45 GeV, 60 GeV and 80 GeV. The events from the three runs with energies of 10 GeV, 20 GeV and 60 GeV allow the performance of the correction to be tested also at energies not used to build the templates.

The results are shown in Fig. 8.23. The mean energy measured by SiW-ECAL+AHCAL is shifted to the expected beam energy, correcting for the average leakage, with an accuracy better than 1%, which is comparable to the precision given by the additional information of the TCMT (cf. Fig. 8.6). The RMS90/Mean improvement is up to 25% at 80 GeV while decreasing towards lower energies together with the impact of the leakage.

In Fig. 8.24 the effect of the correction on a 80 GeV run is shown. The mean value of the energy measured by SiW-ECAL+AHCAL is well recovered from the impact of the leakage, and goes from 69.29 GeV to 80.48 GeV, which is very close to the nominal 80 GeV. At the same time the RMS90 is reduced from 9.12 to 8.10 GeV. While the mean value of the measured energy can be perfectly recovered without using the TCMT
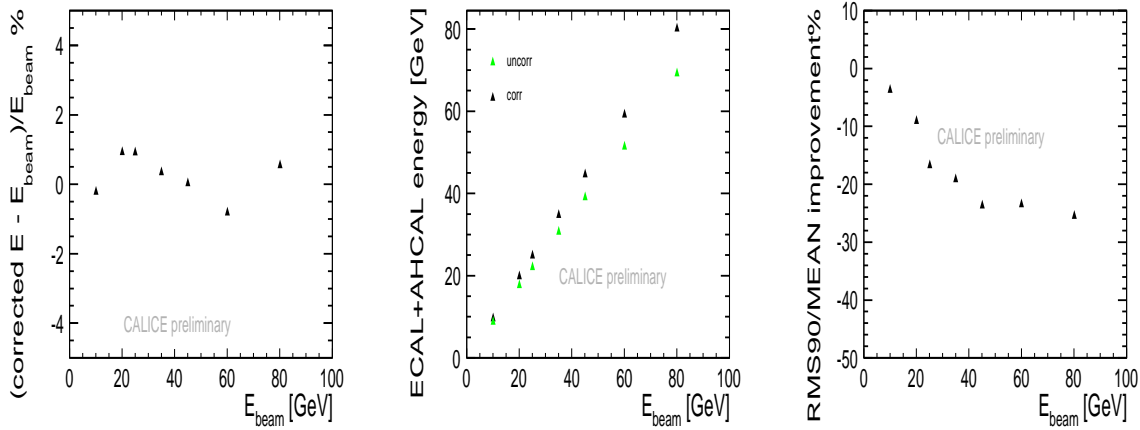
Figure 8.23: *Final results of the leakage correction applied to data runs. Left: the relative deviation of the mean value of the corrected energy distributions from the beam energy versus the beam energy. Center: mean value of the measured energy distributions before and after the correction. Right: relative improvement of RMS90/Mean versus the beam energy. The templates for the correction have been obtained from independent data runs.*
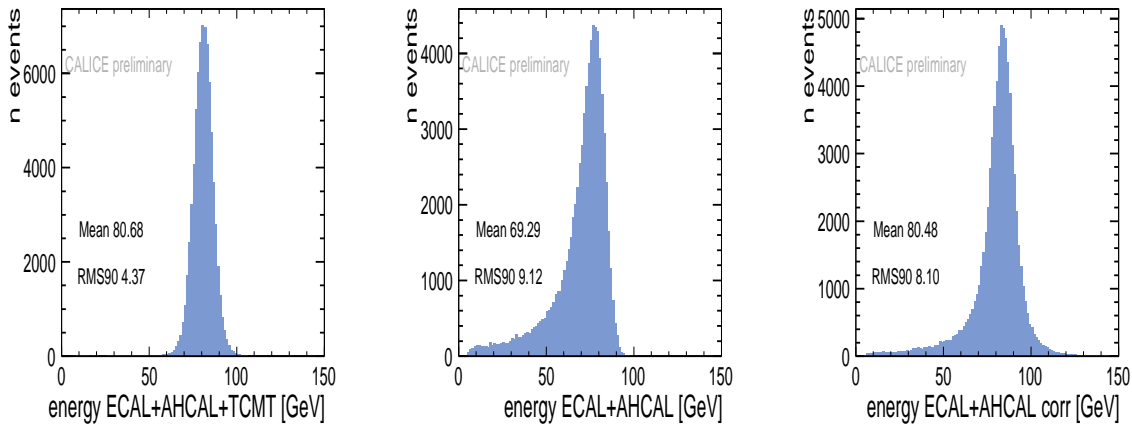
Figure 8.24: *Left: total energy measured using the full calorimeter. Center: energy measured by SiW-ECAL+AHCAL only. Right: energy measured by SiW-ECAL+AHCAL, after applying the correction for the leakage. Example distributions for a beam energy of 80 GeV. The templates for the correction have been obtained from independent data runs.*

information, thanks to the correction, again the RMS90 improves but does not reach the precision given by the additional TCMT information. Using the TCMT the RMS90 is only 4.37 GeV.

The same Monte Carlo templates used for the Monte Carlo study performed in the previous section have also been used to correct the same data runs. The sampling weights used for the Monte Carlo are different from the sampling weights used for the data, as already mentioned, to recover the different energy scale. Otherwise, it would not be possible to apply the correction using a Monte Carlo template, since the energy scale is essential. The results obtained are shown in Fig. 8.25. The performance is comparable to the results obtained building the correction from the data, but the
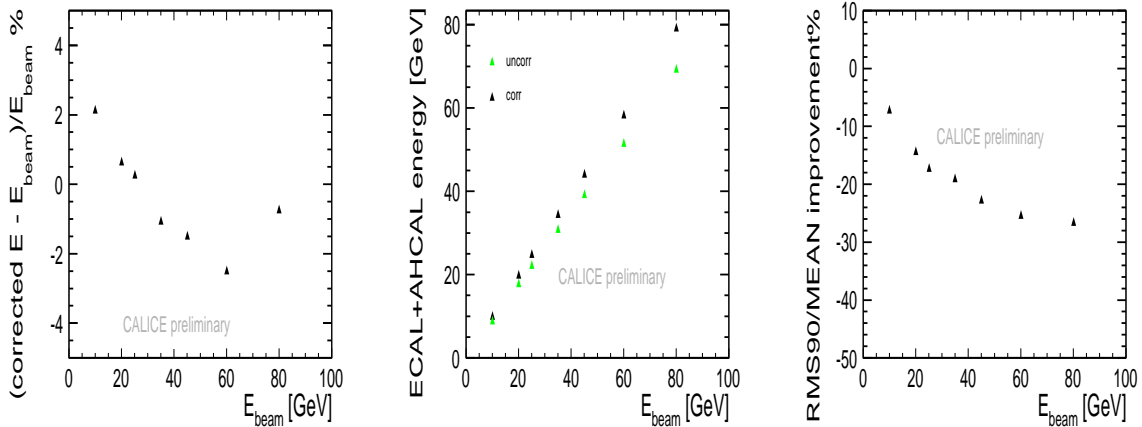
Figure 8.25: *Final results of the leakage correction applied to the data. Left: the relative deviation of the mean value of the corrected energy distributions from the beam energy, as a function of the beam energy. Center: mean value of the measured energy distributions before and after the correction. Right: relative improvement of RMS90/Mean as a function of the beam energy. The templates for the correction have been obtained from the Monte Carlo.*
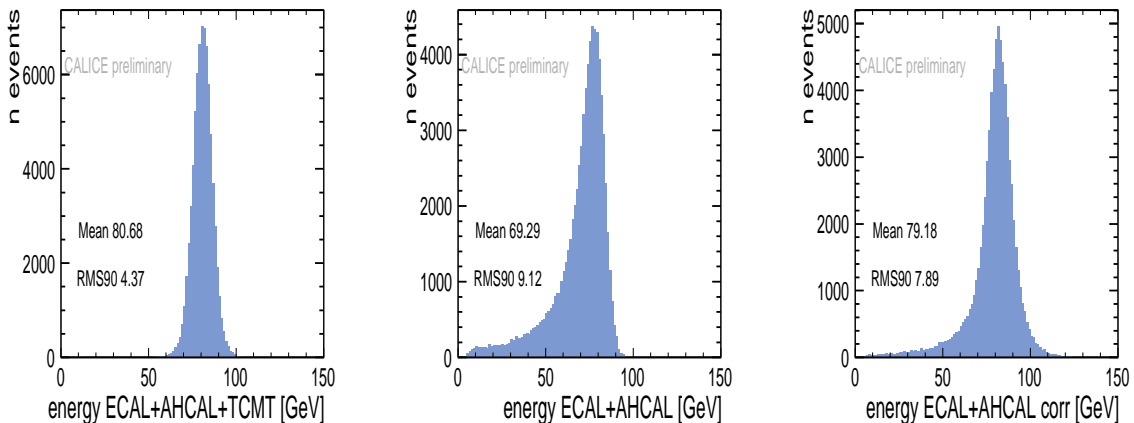
Figure 8.26: *Left: total energy measured using the full calorimeter. Center: energy measured by SiW-ECAL+AHCAL only. Right: energy measured by SiW-ECAL+AHCAL, with correction for the leakage. The plots show examples distributions for an 80 GeV data run. The templates for the correction have been obtained from the Monte Carlo.*

linearity of the response is slightly worse, of about 2% versus the 1% obtained using data templates, and a slope is visible in the response linearity (left plot). This effects are simply due to the original differences between data and Monte Carlo in the energy response, seen in Fig. 8.18.

In Fig. 8.26 the performance of the correction on a 80 GeV run is shown, which gives similar results to those obtained in Fig. 8.24, using data templates.

8.5 Conclusions

8.5.1 Correction Performance

Pion data collected using the CALICE prototypes during the 2007 test beam campaign at CERN were analyzed. Pion showers having their first hard interaction in the AHCAL were selected. A correction to the leakage from the AHCAL was implemented, which does not rely on the information registered by the TCMT. The correction exploits the fine granularity of the AHCAL and the possibility to reconstruct the development of the showers with good accuracy. Two observables were employed, which are correlated to the leakage: the shower starting point and the end-fraction, the fraction of energy measured in the last four layers of the AHCAL. Using these two quantities together with the information of the energy reconstructed in SiW-ECAL+AHCAL, it was possible to develop a correction to the leakage that does not require the knowledge of the beam energy information.

The correction was applied to selected pion data and it was tuned either using independent data runs or Monte Carlo files. The results obtained are better in case the correction is built using data, due to discrepancies between data and simulations. The correction reduces significantly the impact of the leakage. The mean of the energy distributions after the correction is centered around the expected beam energy with a 1% or 2% accuracy, depending on whether the corrections are built using data or Monte Carlo runs. Such a precision is approximately the same given by the additional use of the TCMT. The resolution is improved up to 25% at high energies, with an effect decreasing at lower energies, together with the impact of the leakage.

The resolution improvement obtained with the correction is remarkable, but cannot be compared to the accuracy given by the additional information of the full TCMT, that the correction cannot replace.

8.5.2 Possible Improvements

Further improvements to the implemented correction might come from exploiting additional observables, with some kind of correlation to the leakage. One proposed observable, complementing the information of the shower starting point, is the shower maximum. As shown in the right plot of Fig. 8.27, the correlation between the shower maximum and the shower starting point is good, but not perfect. There are events where the shower has an early minor activity, triggering the PTF algorithm, but the major development is delayed. Using only the shower starting point information leads on average to an underestimation of the leakage. The shower maximum would help to recover from this effect. Comparing the left plot of Fig. 8.27 with the left plot of Fig. 8.11 one sees that the correlation between the shower maximum and the leakage is worse than the correlation between the shower starting point and the leakage, mainly due to the fact that some late showers have their real maximum in the TCMT. Simply replacing the shower starting point observable with the shower maximum observable in the implemented correction would not be a solution. One should rather use the two observables together. Since the real shower maximum is sometimes "lost" in the TCMT, another option that could be investigated is a redefinition of the shower starting point. The PTF could be improved in order to search for the real shower starting point, distinguishing it from early minor activities.
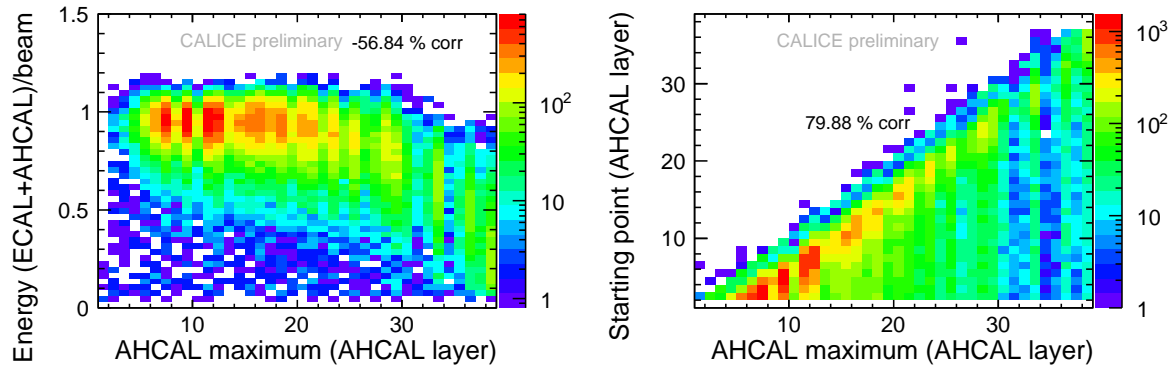
Figure 8.27: *Left: correlation between the shower maximum and the SiW-ECAL+AHCAL response. Right: correlation between the shower starting point and the shower maximum.*

In order to add further observables it would probably be better to move from the chosen binned technique chosen to other techniques, such as a neural network, which would help in avoiding statistical problems in single bins when using multi-dimensional distributions.

An additional improvement might be obtained applying the correction in addition to a software compensation technique. The software compensation would improve the initial linearity of the response with energy and reduce part of the event-to-event fluctuations of the showers, at least those fluctuations connected to the electromagnetic fraction.

9 Summary and Outlook

9.1 Measurement of Triple Gauge Couplings and Polarization

The average luminosity-weighted beam polarization at the ILC can be measured with high sensitivity using the W-pair production process. This polarization measurement will provide the polarimeters with an absolute scale calibration.

Measuring the polarization using a modified Blondel leads to a statistical uncertainty of 0.1% (0.2%) on the electron (positron) polarization for an integrated luminosity of $\mathcal{L} = 500\,\mathrm{fb}^{-1}$, an electron polarization of $P_{e^-} = 80\%$ and for a high positron polarization of $P_{e^+} = 60\%$. When considering the lower positron polarization option (with only $P_{e^+} = 30\%$), the precision of the measurement degrades to 0.2% (0.5%) for the electron (positron) polarization.

An angular fit technique, comparing the distribution of the production angle of the W-pair to a Monte Carlo template, already achieves similar precisions on both beam polarizations for only half the integrated luminosity, $\mathcal{L} = 250\,\mathrm{fb}^{-1}$. In case of the high positron polarization option, a statistical precision of the order of 0.1% (0.2%) on the polarization of the electron (positron) beam is achieved, while in the low positron polarization option and for a total luminosity of $\mathcal{L} = 500\,\mathrm{fb}^{-1}$ a precision of 0.1% (0.34%) is obtained on the electron (positron) polarization.

Since the angular fit method requires less luminosity in general, this technique allows a reduction of the luminosity spent on configurations with both beams right-handed, or left-handed. Such same-sign helicity configurations are of low interest for most of the physics studies, since they suppress the s-channel diagrams. With the angular fit method, it is possible to spend only 20% of the total luminosity on these polarization configurations and still obtain a statistical precision of the order of 0.1% (0.2%) on the polarization of the electron (positron) beam for a total luminosity of $\mathcal{L} = 400\,\mathrm{fb}^{-1}$.

The angular fit method can be extended to a simultaneous fit of polarization and TGCs without loosing sensitivity on the polarization. Three independent couplings of the vertices $WW\gamma$ and WWZ were fitted simultaneously with the polarization, achieving an absolute statistical precision better than 10^{-3} for a total luminosity of $\mathcal{L} = 500\,\mathrm{fb}^{-1}$.

Possible systematic errors that might affect the performance of the measurement have been studied in detail. The major effect stems from differences in the values of the left- and right-handed states of the polarizations, that need to be corrected using the measured values of the polarimeters. Propagating the expected 0.25% uncertainty of the polarimeter measurements, the impact on the polarization and TGCs measurement has been evaluated. While no significant impact on the TGCs measurement is found, the systematic uncertainty on the polarization is non-negligible and dominates over

the statistical precision at high luminosities. However, even considering this source of systematics, the achieved precisions are still good. For an integrated luminosity of $\mathcal{L} = 500\,\text{fb}^{-1}$, an uncertainty of 0.16% (0.17%) is obtained for the electron (positron) polarization for a high positron polarization of $P_{e+} = 60\%$, while for a lower positron polarization of $P_{e+} = 30\%$ the achieved precision on the electron (positron) polarization is found to be 0.16% (0.35%).

9.2 Leakage Studies

Pion data collected using the CALICE prototypes during the 2007 test beam campaign at CERN were analyzed. Pion showers having their first hard interaction in the AHCAL were selected. A correction to the leakage from the AHCAL was implemented, which does not rely on the information registered by the TCMT. The correction exploits the fine granularity of the AHCAL and the possibility to reconstruct the development of the showers with good accuracy. Two observables were employed, which are correlated to the leakage: the shower starting point and the end-fraction, the fraction of energy measured in the last four layers of the AHCAL. Using these two quantities together with the information of the energy reconstructed in SiW-ECAL+AHCAL, it was possible to develop a correction to the leakage that does not require the knowledge of the beam energy information.

The correction was applied to selected pion data and it was tuned either using independent data runs or Monte Carlo files. The results obtained are better in case the correction is built using data, due to discrepancies between data and simulations. The correction reduces significantly the impact of the leakage. The mean of the energy distributions after the correction is centered around the expected beam energy with a 1% or 2% accuracy, depending on whether the corrections are built using data or Monte Carlo runs. The resolution is improved up to 25% at high energies, with an effect decreasing at lower energies, together with the impact of the leakage.

List of Tables

List of Figures

Bibliography

[1] S. L. Glashow, "Partial Symmetries of Weak Interactions," *Nucl. Phys.*, vol. 22, pp. 579–588, 1961.

[2] A. Salam and J. C. Ward, "Gauge theory of elementary interactions," *Phys. Rev.*, vol. 136, pp. B763–B768, 1964.

[3] S. Weinberg, "A Model of Leptons," *Phys. Rev. Lett.*, vol. 19, pp. 1264–1266, 1967.

[4] G. 't Hooft, "Renormalization of Massless Yang-Mills Fields," *Nucl. Phys.*, vol. B33, pp. 173–199, 1971.

[5] G. 't Hooft, "Renormalizable lagrangians for massive Yang-Mills Fields," *Nucl. Phys.*, vol. B35, pp. 167–188, 1971.

[6] F. J. Hasert *et al.*, "Search for elastic muon neutrino electron scattering," *Phys. Lett.*, vol. B46, pp. 121–124, 1973.

[7] F. J. Hasert *et al.*, "Observation of neutrino-like interactions without muon or electron in the Gargamelle neutrino experiment," *Phys. Lett.*, vol. B46, pp. 138–140, 1973.

[8] A. C. Benvenuti *et al.*, "Observation of Muonless Neutrino Induced Inelastic Interactions," *Phys. Rev. Lett.*, vol. 32, pp. 800–803, 1974.

[9] H. Fritzsch, M. Gell-Mann, and H. Leutwyler, "Advantages of the Color Octet Gluon Picture," *Phys. Lett.*, vol. B47, pp. 365–368, 1973.

[10] M. Banner *et al.*, "Observation of single isolated electrons of high transverse momentum in events with missing transverse energy at the CERN $\bar{p}p$ collider," *Phys. Lett.*, vol. B122, pp. 476–485, 1983.

[11] G. Arnison *et al.*, "Experimental observation of lepton pairs of invariant mass around $95\,\text{GeV}/c^2$ at the CERN SPS collider," *Phys. Lett.*, vol. B126, pp. 398–410, 1983.

[12] P. Bagnaia *et al.*, "Evidence for $Z^0 \rightarrow e^+ e^-$ at the CERN $\bar{p}p$ collider," *Phys. Lett.*, vol. B129, pp. 130–140, 1983.

[13] A. Martin, "History of spin and statistics," 2002.

[14] J. Baggot, "Beyond Measure," 2004. Oxford: Univ. Pr.

[15] M. H. Anderson, J. R. Ensher, M. R. Matthews, C. E. Wieman, and E. A. Cornell, "Observation of Bose-Einstein condensation in a dilute atomic vapor," *Science*, vol. 269, pp. 198–201, 1995.

[16] M. Bustamante, L. Cieri, and J. Ellis, "Beyond the Standard Model for Montaneros," 2009.

[17] Q. R. Ahmad *et al.*, "Measurement of the charged current interactions produced by B-8 solar neutrinos at the Sudbury Neutrino Observatory," *Phys. Rev. Lett.*, vol. 87, p. 071301, 2001.

[18] P. Vogel, "Towards absolute neutrino masses," *Nucl. Phys. Proc. Suppl.*, vol. 168, pp. 23–28, 2007.

[19] J. D. Jackson and L. B. Okun, "Historical roots of gauge invariance," *Rev. Mod. Phys.*, vol. 73, pp. 663–680, 2001.

[20] N. Straumann, "Gauge principle and QED," *Acta Phys. Polon.*, vol. B37, pp. 575–594, 2006.

[21] H. Weyl, "Gravitation and electricity," *Sitzungsber. Preuss. Akad. Wiss. Berlin (Math. Phys.)*, vol. 1918, p. 465, 1918.

[22] F. London, "Quantum Mechanical Interpretation of the new Weyl's Theory. (in German)," *Z. Phys.*, vol. 42, pp. 375–389, 1927.

[23] H. Weyl, "Electron and gravitation," *Z. Phys.*, vol. 56, pp. 330–352, 1929.

[24] V. Fock, "On the invariant form of the wave equations and the equations of motion for a charged point mass," *Z. Phys.*, vol. 39, pp. 226–232, 1926.

[25] O. Klein, "Quantum theory and five-dimensional theory of relativity," *Z. Phys.*, vol. 37, pp. 895–906, 1926.

[26] A. Salam and J. C. Ward, "On a Gauge Theory of Elementary Interactions," *Nuovo Cim.*, vol. 19, pp. 165–170, 1961.

[27] S. F. Novaes, "Standard model: An Introduction," 1999.

[28] S. Pokorski, "Gauge Field Theories," Cambridge, Uk: Univ. Pr. (1987) 394 P. (Cambridge Monographs On Mathematical Physics).

[29] W. Heisenberg, "On the structure of atomic nuclei," *Z. Phys.*, vol. 77, pp. 1–11, 1932.

[30] C.-N. Yang and R. L. Mills, "Conservation of isotopic spin and isotopic gauge invariance," *Phys. Rev.*, vol. 96, pp. 191–195, 1954.

[31] G. Breit, E. U. Condon, and R. D. Present, "Theory of Scattering of Protons by Protons," *Phys. Rev.*, vol. 50, pp. 825–845, 1936.

[32] J. Schwinger, "On the Charge Independence of Nuclear Forces," *Phys. Rev.*, vol. 78, pp. 135–139, 1950.

[33] T. Lauritsen, "Energy levels of light nuclei," *Ann. Rev. Nucl. Part. Sci.*, vol. 1, pp. 67–96, 1952.

[34] R. Utiyama, "Invariant theoretical interpretation of interaction," *Phys. Rev.*, vol. 101, pp. 1597–1607, 1956.

[35] J. Chadwick, "The intensity distribution in the magnetic spectrum of β particles from radium (B + C)," *Verh. Phys. Gesell.*, vol. 16, pp. 383–391, 1914.

[36] W. Pauli, "Open Letter To radioactive Persons," 1930.

[37] J. Chadwick, "Possible Existence of a Neutron," *Nature*, vol. 129, p. 312, 1932.

[38] W. Pauli, "Septième Conseil de Physique, Solvay, 1933," *Gauthier-Villars, Paris*, p. 324, 1934.

[39] E. Fermi, "An attempt of a theory of beta radiation. 1," *Z. Phys.*, vol. 88, pp. 161–177, 1934.

[40] E. Fermi, "Trends to a Theory of beta Radiation. (In Italian)," *Nuovo Cim.*, vol. 11, pp. 1–19, 1934.

[41] G. Gamow and E. Teller, "Selection rules for the β-disintegration," *Phys. Rev.*, vol. 49, pp. 895–899, 1936.

[42] B. Pontecorvo, "Nuclear capture of mesons and the meson decay," *Phys. Rev.*, vol. 72, p. 246, 1947.

[43] J. Tiomno and J. A. Wheeler, "Energy spectrum of electrons from meson decay," *Rev. Mod. Phys.*, vol. 21, pp. 144–152, 1949.

[44] T. D. Lee, M. Rosenbluth, and C.-N. Yang, "Interaction of Mesons with Nucleons and light Particles," *Phys. Rev.*, vol. 75, p. 905, 1949.

[45] G. S. Alvarez, L. W. *Nuovo Cim.*, vol. 2, p. 344, 1955.

[46] R. W. Birge *et al.*, "Bevatron K Mesons," *Phys. Rev.*, vol. 99, pp. 329–330, 1955.

[47] T. D. Lee and C.-N. Yang, "Question of Parity Conservation in Weak Interactions," *Phys. Rev.*, vol. 104, pp. 254–258, 1956.

[48] C. S. Wu, E. Ambler, R. W. Hayward, D. D. Hoppes, and R. P. Hudson, "Experimental Test of Parity Conservation in Beta Decay," *Phys. Rev.*, vol. 105, pp. 1413–1414, 1957.

[49] T. D. Lee and C.-N. Yang, "Parity Nonconservation and a Two Component Theory of the Neutrino," *Phys. Rev.*, vol. 105, pp. 1671–1675, 1957.

[50] M. Goldhaber, L. Grodzins, and A. W. Sunyar, "Helicity of Neutrinos," *Phys. Rev.*, vol. 109, pp. 1015–1017, 1958.

[51] J. S. Schwinger, "A Theory of the Fundamental Interactions," *Annals Phys.*, vol. 2, pp. 407–434, 1957.

[52] T. D. Lee and C.-N. Yang, "Possible Nonlocal Effects in μ Decay," *Phys. Rev.*, vol. 108, pp. 1611–1614, 1957.

[53] T. D. Lee and C. S. Wu, "Weak Interactions," *Ann. Rev. Nucl. Part. Sci.*, vol. 15, pp. 381–476, 1965.

[54] B. W. Lee, C. Quigg, and H. B. Thacker, "The Strength of Weak Interactions at Very High-Energies and the Higgs Boson Mass," *Phys. Rev. Lett.*, vol. 38, pp. 883–885, 1977.

[55] M. Spira and P. M. Zerwas, "Electroweak symmetry breaking and Higgs physics," *Lect. Notes Phys.*, vol. 512, pp. 161–225, 1998.

[56] N. Cabibbo, "Unitary Symmetry and Leptonic Decays," *Phys. Rev. Lett.*, vol. 10, pp. 531–533, 1963.

[57] M. Kobayashi and T. Maskawa, "CP Violation in the Renormalizable Theory of Weak Interaction," *Prog. Theor. Phys.*, vol. 49, pp. 652–657, 1973.

[58] K. Nakamura *et al.*, "Review of particle physics," *J. Phys.*, vol. G37, p. 075021, 2010.

[59] C. Bouchiat, J. Iliopoulos, and P. Meyer, "An Anomaly Free Version of Weinberg's Model," *Phys. Lett.*, vol. B38, pp. 519–523, 1972.

[60] J. Sekaric, "Studies of gauge boson production with a $\gamma\gamma$ collider at TESLA," 2005.

[61] G. Abbiendi *et al.*, "W^+W^- production and triple gauge boson couplings at LEP energies up to 183-GeV," *Eur. Phys. J.*, vol. C8, pp. 191–215, 1999.

[62] P. Spagnolo, "Boson gauge couplings at LEP," 2005.

[63] G. S. Guralnik, C. R. Hagen, and T. W. B. Kibble, "Global Conservation Laws and Massless Particles," *Phys. Rev. Lett.*, vol. 13, pp. 585–587, 1964.

[64] F. Englert and R. Brout, "Broken Symmetry and the Mass of Gauge Vector Mesons," *Phys. Rev. Lett.*, vol. 13, pp. 321–322, 1964.

[65] P. W. Higgs, "Broken symmetries, massless particles and gauge fields," *Phys. Lett.*, vol. 12, pp. 132–133, 1964.

[66] J. Goldstone, "Field Theories with Superconductor Solutions," *Nuovo Cim.*, vol. 19, pp. 154–164, 1961.

[67] B. W. Lee, C. Quigg, and H. B. Thacker, "Weak Interactions at Very High-Energies: The Role of the Higgs Boson Mass," *Phys. Rev.*, vol. D16, p. 1519, 1977.

[68] M. B. Einhorn and D. R. T. Jones, "The effective potential, the renormalisation group and vacuum stability," *JHEP*, vol. 04, p. 051, 2007.

[69] J. A. Casas, J. R. Espinosa, and M. Quiros, "Standard Model stability bounds for new physics within LHC reach," *Phys. Lett.*, vol. B382, pp. 374–382, 1996.

[70] C. Quigg, "Unanswered Questions in the Electroweak Theory," *Ann. Rev. Nucl. Part. Sci.*, vol. 59, pp. 505–555, 2009.

[71] T. Hambye and K. Riesselmann, "Matching conditions and Higgs mass upper bounds revisited," *Phys. Rev.*, vol. D55, pp. 7255–7262, 1997.

[72] R. Barate *et al.*, "Search for the standard model Higgs boson at LEP," *Phys. Lett.*, vol. B565, pp. 61–75, 2003.

[73] N. Krumnack, "Combined SM Higgs Limits at the Tevatron," 2009.

[74] N. Jarosik *et al.*, "Seven-Year Wilkinson Microwave Anisotropy Probe (WMAP) Observations: Sky Maps, Systematic Errors, and Basic Results," *Astrophys. J. Suppl.*, vol. 192, p. 14, 2011.

[75] A. Harvey, "Dark energy and the cosmological constant: A brief introduction," *Eur. J. Phys.*, vol. 30, pp. 877–889, 2009.

[76] K. C. Freeman, "On the disks of spiral and SO Galaxies," *Astrophys. J.*, vol. 160, p. 811, 1970.

[77] G. Bertone, D. Hooper, and J. Silk, "Particle dark matter: Evidence, candidates and constraints," *Phys. Rept.*, vol. 405, pp. 279–390, 2005.

[78] M. Markevitch *et al.*, "Direct constraints on the dark matter self-interaction cross-section from the merging galaxy cluster 1E0657-56," *Astrophys. J.*, vol. 606, pp. 819–824, 2004.

[79] B. Ratra, M. S. Vogeley, and M. S. Vogeley, "Resource Letter BE-1: The Beginning and Evolution of the Universe," *Publ. Astron. Soc. Pac.*, vol. 120, pp. 235–265, 2008.

[80] J. M. Cline, "Baryogenesis," 2006.

[81] A. D. Sakharov, "Violation of CP Invariance, C Asymmetry, and Baryon Asymmetry of the Universe," *Pisma Zh. Eksp. Teor. Fiz.*, vol. 5, pp. 32–35, 1967.

[82] G. 't Hooft, "Symmetry breaking through Bell-Jackiw anomalies," *Phys. Rev. Lett.*, vol. 37, pp. 8–11, 1976.

[83] G. R. Farrar and M. E. Shaposhnikov, "Baryon asymmetry of the universe in the standard electroweak theory," *Phys. Rev.*, vol. D50, p. 774, 1994.

[84] M. B. Gavela, P. Hernandez, J. Orloff, and O. Pene, "Standard Model CP-violation and Baryon asymmetry," *Mod. Phys. Lett.*, vol. A9, pp. 795–810, 1994.

[85] P. A. M. Dirac, "Quantised singularities in the electromagnetic field," *Proc. Roy. Soc. Lond.*, vol. A133, pp. 60–72, 1931.

[86] P. A. M. Dirac, "The theory of magnetic poles," *Phys. Rev.*, vol. 74, pp. 817–830, 1948.

[87] P. A. M. Dirac, "The Monopole Concept," *Int. J. Theor. Phys.*, vol. 17, pp. 235–247, 1978.

[88] G. 't Hooft, "Magnetic monopoles in unified gauge theories," *Nucl. Phys.*, vol. B79, pp. 276–284, 1974.

[89] A. M. Polyakov, "Particle spectrum in quantum field theory," *JETP Lett.*, vol. 20, pp. 194–195, 1974.

[90] C. P. Dokos and T. N. Tomaras, "Monopoles and Dyons in the SU(5) Model," *Phys. Rev.*, vol. D21, p. 2940, 1980.

[91] P. J. E. Peebles and B. Ratra, "The cosmological constant and dark energy," *Rev. Mod. Phys.*, vol. 75, pp. 559–606, 2003.

[92] A. G. Riess *et al.*, "Observational Evidence from Supernovae for an Accelerating Universe and a Cosmological Constant," *Astron. J.*, vol. 116, pp. 1009–1038, 1998.

[93] S. Perlmutter *et al.*, "Measurements of Omega and Lambda from 42 High-Redshift Supernovae," *Astrophys. J.*, vol. 517, pp. 565–586, 1999.

[94] E. Komatsu *et al.*, "Seven-Year Wilkinson Microwave Anisotropy Probe (WMAP) Observations: Cosmological Interpretation," *Astrophys. J. Suppl.*, vol. 192, p. 18, 2011.

[95] E. V. Shuryak, "The QCD vacuum, hadrons and the superdense matter," *World Sci. Lect. Notes Phys.*, vol. 71, pp. 1–618, 2004.

[96] Y. A. Golfand and E. P. Likhtman, "Extension of the Algebra of Poincare Group Generators and Violation of p Invariance," *JETP Lett.*, vol. 13, pp. 323–326, 1971.

[97] J. Wess and B. Zumino, "A Lagrangian Model Invariant Under Supergauge Transformations," *Phys. Lett.*, vol. B49, p. 52, 1974.

[98] D. V. Volkov and V. P. Akulov, "Is the Neutrino a Goldstone Particle?," *Phys. Lett.*, vol. B46, pp. 109–110, 1973.

[99] Y. Shirman, "TASI 2008 Lectures: Introduction to Supersymmetry and Supersymmetry Breaking," 2009.

[100] J. Terning, "Non-perturbative supersymmetry," 2003.

[101] M. A. Luty, "2004 TASI lectures on supersymmetry breaking," 2005.

[102] J. Wess and J. Bagger, "Supersymmetry and supergravity," Princeton, USA: Univ. Pr. (1992) 259 p.

[103] E. Witten, "Dynamical Breaking of Supersymmetry," *Nucl. Phys.*, vol. B188, p. 513, 1981.

[104] U. Amaldi, W. de Boer, and H. Furstenau, "Comparison of grand unified theories with electroweak and strong coupling constants measured at LEP," *Phys. Lett.*, vol. B260, pp. 447–455, 1991.

[105] M. S. Carena, J. M. Moreno, M. Quiros, M. Seco, and C. E. M. Wagner, "Supersymmetric CP-violating currents and electroweak baryogenesis," *Nucl. Phys.*, vol. B599, pp. 158–184, 2001.

[106] G. Jungman, M. Kamionkowski, and K. Griest, "Supersymmetric dark matter," *Phys. Rept.*, vol. 267, pp. 195–373, 1996.

[107] H. Georgi and S. L. Glashow, "Unity of All Elementary Particle Forces," *Phys. Rev. Lett.*, vol. 32, pp. 438–441, 1974.

[108] H. Georgi, H. R. Quinn, and S. Weinberg, "Hierarchy of Interactions in Unified Gauge Theories," *Phys. Rev. Lett.*, vol. 33, pp. 451–454, 1974.

[109] M. S. Chanowitz, J. R. Ellis, and M. K. Gaillard, "The Price of Natural Flavor Conservation in Neutral Weak Interactions," *Nucl. Phys.*, vol. B128, p. 506, 1977.

[110] A. J. Buras, J. R. Ellis, M. K. Gaillard, and D. V. Nanopoulos, "Aspects of the Grand Unification of Strong, Weak and Electromagnetic Interactions," *Nucl. Phys.*, vol. B135, pp. 66–92, 1978.

[111] D. V. Nanopoulos and D. A. Ross, "m_b/m_τ in Supersymmetric GUTS: Superflavor Meter," *Phys. Lett.*, vol. B118, p. 99, 1982.

[112] G. Senjanovic, "Proton decay and grand unification," *AIP Conf. Proc.*, vol. 1200, pp. 131–141, 2010.

[113] L. Randall and R. Sundrum, "A large mass hierarchy from a small extra dimension," *Phys. Rev. Lett.*, vol. 83, pp. 3370–3373, 1999.

[114] L. Randall and R. Sundrum, "An alternative to compactification," *Phys. Rev. Lett.*, vol. 83, pp. 4690–4693, 1999.

[115] S. Weinberg, "Implications of Dynamical Symmetry Breaking: An Addendum," *Phys. Rev.*, vol. D19, pp. 1277–1280, 1979.

[116] L. Susskind, "Dynamics of Spontaneous Symmetry Breaking in the Weinberg-Salam Theory," *Phys. Rev.*, vol. D20, pp. 2619–2625, 1979.

[117] K. D. Lane, "An Introduction to technicolor," 1993.

[118] C. T. Hill and E. H. Simmons, "Strong dynamics and electroweak symmetry breaking," *Phys. Rept.*, vol. 381, pp. 235–402, 2003.

[119] J. R. Ellis, G. L. Fogli, and E. Lisi, "Technicolor and precision electroweak data revisited," *Phys. Lett.*, vol. B343, pp. 282–290, 1995.

[120] M. T. Frandsen, "Minimal Walking Technicolor," 2007.

[121] W. Buchmuller and D. Wyler, "Effective Lagrangian Analysis of New Interactions and Flavor Conservation," *Nucl. Phys.*, vol. B268, p. 621, 1986.

[122] G. Gounaris *et al.*, "Triple gauge boson couplings," 1996.

[123] H. Aronson, "Spin-1 electrodynamics with an electric quadrupole moment," *Phys. Rev.*, vol. 186, pp. 1434–1441, 1969.

[124] T. L. C. ALEPH, DELPHI, L3, OPAL, and the LEP TGC Working Group, "A combination of results on charged triple gauge boson couplings measured by the LEP experiments," LEPEWWG/TGC/2005-01.

[125] P. Achard *et al.*, "Production of single W bosons at LEP and measurement of $WW\gamma$ gauge coupling parameters," *Phys. Lett.*, vol. B547, pp. 151–163, 2002.

[126] S. Schael *et al.*, "Single vector boson production in e^+e^- collisions at centre-of-mass energies from $183\,\text{GeV}$ to $209\,\text{GeV}$," *Phys. Lett.*, vol. B605, pp. 49–62, 2005.

[127] A. Heister *et al.*, "Single photon and multiphoton production in e^+e^- collisions at $\sqrt{s}$ up to $209\,\text{GeV}$," *Eur. Phys. J.*, vol. C28, pp. 1–13, 2003.

[128] P. Achard *et al.*, "Single photon and multiphoton events with missing energy in e^+e^- collisions at LEP," *Phys. Lett.*, vol. B587, pp. 16–32, 2004.

[129] K. J. F. Gaemers and G. J. Gounaris, "Polarization Amplitudes for $e^+e^- \to W^+W^-$ and $e^+e^- \to ZZ$," *Zeit. Phys.*, vol. C1, p. 259, 1979.

[130] S. Schael *et al.*, "Improved measurement of the triple gauge-boson couplings γWW and ZWW in e^+e^- collisions," *Phys. Lett.*, vol. B614, pp. 7–26, 2005.

[131] V. M. Abazov *et al.*, "Measurement of the $WZ \to \ell\nu\ell\ell$ cross section and limits on anomalous triple gauge couplings in $p\bar{p}$ collisions at $\sqrt{s} = 1.96$ TeV," *Phys. Lett.*, vol. B695, pp. 67–73, 2011.

[132] T. Aaltonen *et al.*, "Limits on Anomalous Triple Gauge Couplings in $p\bar{p}$ Collisions at $\sqrt{s} = 1.96\,\text{TeV}$," *Phys. Rev.*, vol. D76, p. 111103, 2007.

[133] G. Aad *et al.*, "Expected Performance of the ATLAS Experiment - Detector, Trigger and Physics," 2009.

[134] J. D. Jackson, *Classical Electrodynamics*. John Wiley & Sons, 1998.

[135] R. Assmann, M. Lamont, and S. Myers, "A brief history of the LEP collider," *Nucl. Phys. Proc. Suppl.*, vol. 109B, pp. 17–31, 2002.

[136] J. Brau, (ed.) *et al.*, "International Linear Collider reference design report. 1: Executive summary. 2: Physics at the ILC. 3: Accelerator. 4: Detectors," ILC-REPORT-2007-001.

[137] N. W. ILC GDE, Editors M. Ross and A. Yamamoto, "SB2009 Proposal Document," 2009.

[138] H. Olsen and L. C. Maximon, "Photon and Electron Polarization in High-Energy Bremsstrahlung and Pair Production with Screening," *Phys. Rev.*, vol. 114, pp. 887–904, 1959.

[139] G. Alexander *et al.*, "Observation of Polarized Positrons from an Undulator-Based Source," *Phys. Rev. Lett.*, vol. 100, p. 210801, 2008.

[140] B. Aurand *et al.*, "Beam Polarization at the ILC: the Physics Impact and the Accelerator Solutions," 2009.

[141] Y. K. Batygin, "Spin rotation and energy compression in the ILC linac-to-ring positron beamline," *Nucl. Instrum. Meth.*, vol. A570, pp. 365–373, 2007.

[142] S. Riemann, A. Schalicke, and A. Ushakov, "Frequency of Positron Helicity Reversal," 2009.

[143] B. Aurand *et al.*, "Executive Summary of the Workshop on Polarization and Beam Energy Measurements at the ILC," 2008.

[144] K. Moffeit, M. Woods, P. Schuler, K. Mönig, and P. Bambade, "Spin rotation schemes at the ILC for two interaction regions and positron polarization with both helicities," SLAC-TN-05-045.

[145] K. Moffeit, M. Woods, and D. Walz, "Spin Rotation al lower energy than the damping ring," ILC-NOTE-2008-040.

[146] F. Furuta *et al.*, "Experimental comparison at KEK of high gradient performance of different single cell superconducting cavity designs," Prepared for European Particle Accelerator Conference (EPAC 06), Edinburgh, Scotland, 26-30 Jun 2006.

[147] H. Padamsee, J. Knobloch, and T. Hays, "RF superconductivity for accelerators," ISBN-9783527408429.

[148] K. Yokoya and P. Chen, "Beam-beam phenomena in linear colliders," *Lect. Notes Phys.*, vol. 400, pp. 415–445, 1992.

[149] D. Schulte, "*PhD Thesis:* Study of Electromagnetic and Hadronic Background in the Interaction Region of the Tesla Collider," 1997. DESY-TESLA-97-08.

[150] C. Hensel, "Beam-induced background at a TESLA detector," 2000. LC-DET-2000-001.

[151] A. Vogel, "Beam-induced backgrounds in detectors at the ILC," DESY-THESIS-2008-036.

[152] M. Berggren, "ILC Beam-Parameters and New Physics," 2010.

[153] V. Balakin, "Travelling Focus Regime for Linear Collider VLEPP," *Proc. 7/th ICFA Workshop on Beam Dynamics, Los Angeles*, May 13-16, 1991.

[154] W. Liu and W. Gai, "Update on the ILC Positron Source Study at ANL," 1st International Particle Accelerator Conference: IPAC'10, 23-28 May 2010, Kyoto, Japan.

[155] J. A. Aguilar-Saavedra *et al.*, "Supersymmetry parameter analysis: SPA convention and project," *Eur. Phys. J.*, vol. C46, pp. 43–60, 2006.

[156] P. Garcia-Abia and W. Lohmann, "Measurement of the Higgs Cross Section and Mass with Linear Colliders," *Eur. Phys. J. direct*, vol. C2, p. 2, 2000.

[157] S. Heinemeyer and G. Weiglein, "Top, GigaZ, MegaW," 2010.

[158] S. Heinemeyer, S. Kraml, W. Porod, and G. Weiglein, "Physics impact of a precise determination of the top quark mass at an e^+e^- linear collider," *JHEP*, vol. 09, p. 075, 2003.

[159] and others, "Combination of CDF and D0 Results on the Mass of the Top Quark," 2010.

[160] I. Borjanovic *et al.*, "Investigation of top mass measurements with the ATLAS detector at LHC," *Eur. Phys. J.*, vol. C39S2, pp. 63–90, 2005.

[161] M. Beneke *et al.*, "Top quark physics," 2000.

[162] G. L. Bayatian *et al.*, "CMS technical design report, volume II: Physics performance," *J. Phys.*, vol. G34, pp. 995–1579, 2007.

[163] T. Abe *et al.*, "The International Large Detector: Letter of Intent," 2010.

[164] A. Djouadi, "The Anatomy of electro-weak symmetry breaking. I: The Higgs boson in the standard model," *Phys. Rept.*, vol. 457, pp. 1–216, 2008.

[165] K. Abe *et al.*, "Design and performance of the SLD vertex detector, a 307 Mpixel tracking system," *Nucl. Instrum. Meth.*, vol. A400, pp. 287–343, 1997.

[166] S. Boogert *et al.*, "Polarimeters and Energy Spectrometers for the ILC Beam Delivery System," *JINST*, vol. 4, p. P10015, 2009.

[167] A. Hinze and K. Mönig, "Measuring the beam energy with radiative return events," 2005.

[168] D. Buskulic *et al.*, "Performance of the ALEPH detector at LEP," *Nucl. Instrum. Meth.*, vol. A360, pp. 481–506, 1995.

[169] E. Boos *et al.*, "Strongly interacting vector bosons at TeV e^+e^- linear colliders," *Phys. Rev.*, vol. D57, p. 1553, 1998.

[170] M. S. Chanowitz, "The no-Higgs signal: Strong W W scattering at the LHC," *Czech. J. Phys.*, vol. 55, pp. B45–B58, 2005.

[171] T. Suehara and J. List, "Chargino and Neutralino Separation with the ILD Experiment," 2009.

[172] H. Aihara *et al.*, "SiD Letter of Intent," SLAC-R-944.

[173] I. G. Knowles and G. D. Lafferty, "Hadronization in Z^0 decay," *J. Phys.*, vol. G23, pp. 731–789, 1997.

[174] M. A. Thomson, "Particle Flow Calorimetry and the PandoraPFA Algorithm," *Nucl. Instrum. Meth.*, vol. A611, pp. 25–40, 2009.

[175] C. Adloff *et al.*, "Response of the CALICE Si-W Electromagnetic Calorimeter Physics Prototype to Electrons," *J. Phys. Conf. Ser.*, vol. 160, p. 012065, 2009.

[176] T. Behnke, "The LDC detector concept," *Pramana*, vol. 69, pp. 697–702, 2007.

[177] C. Kasselman and I. Foster, "The Grid: Blueprint for a New Computing Infrastructure," *Morgan Kaufmann Publishers*, 1998.

[178] "GNU Project software page." http://www.gnu.org/software/bash/.

[179] "MySQL Home Page." http://www.mysql.com/.

[180] I. Bird, (ed.) *et al.*, "LHC computing Grid. Technical design report," CERN-LHCC-2005-024.

[181] R. Poeschl, "Software Tools for ILC Detector Studies," In the Proceedings of 2007 International Linear Collider Workshop (LCWS07 and ILC07), Hamburg, Germany, 30 May - 3 Jun 2007.

[182] F. Gaede *et al.*, "LCIO persistency and data model for LC simulation and reconstruction,"

[183] P. Mora de Freitas and H. Videau, "Detector Simulation with Mokka and Geant4: Present and Future," Tech. Rep. LC-TOOL-2003-010, LC Note, mar 2003.

[184] G. Simone, "GEANT4: Simulation for the next generation of HEP experiments," Prepared for International Conference on Computing in High-energy Physics (CHEP 95), Rio de Janeiro, Brazil, 18-22 Sep 1995.

[185] D. Wright, "Linear Collider Physics List Description." http://www.slac.stanford.edu/comp/physics/geant4/slac_physics_lists/ilc/physlistdoc.html.

[186] "Standard Model Data Samples." http://confluence.slac.stanford.edu/display/ilc/Standard+Model+Data+Samples.

[187] W. Kilian, T. Ohl, and J. Reuter, "WHIZARD: Simulating Multi-Particle Processes at LHC and ILC," 2007.

[188] M. Moretti, T. Ohl, and J. Reuter, "O'Mega: An optimizing matrix element generator," 2001.

[189] T. Ohl, "O'Mega: An optimizing matrix element generator," *AIP Conf. Proc.*, vol. 583, pp. 173–175, 2001.

[190] D. Schulte *et al.*, "GUINEA PIG++ : An Upgraded Version of the Linear Collider Beam Beam Interaction Simulation Code GUINEA PIG," Particle Accelerator Conference PAC07 25-29 Jun 2007, Albuquerque, New Mexico.

[191] F. Gaede, "Marlin and LCCD: Software tools for the ILC," *Nucl. Instrum. Meth.*, vol. A559, pp. 177–180, 2006.

[192] Y. L. Dokshitzer, G. D. Leder, S. Moretti, and B. R. Webber, "Better jet clustering algorithms," *JHEP*, vol. 08, p. 001, 1997.

[193] G. A. Moortgat-Pick *et al.*, "The role of polarized positrons and electrons in revealing fundamental interactions at the linear collider," *Phys. Rept.*, vol. 460, pp. 131–243, 2008.

[194] K. Hikasa, "Transverse polarization effects in e^+e^- collisions: the role of chiral symmetry," *Phys. Rev.*, vol. D33, p. 3203, 1986.

[195] G. Moortgat-Pick, "Impact of polarized e⁻ and e⁺ beams at a future Linear Collider and a Z-factory. Part I: Fundamentals in polarization and electroweak precision physics," DESY-10-242.

[196] J. H. Kuhn, "Polarized beams and the top threshold," LC-TH-2001-004.

[197] J. A. Aguilar-Saavedra and T. Riemann, "Probing top flavor changing neutral couplings at TESLA," 2001.

[198] W. Kilian, M. Kramer, and P. M. Zerwas, "Higgs-strahlung and WW fusion in e^+e^- collisions," *Phys. Lett.*, vol. B373, pp. 135–140, 1996.

[199] G. A. Moortgat-Pick and H. M. Steiner, "Physics opportunities with polarized e^- and e^+ beams at TESLA," *Eur. Phys. J. direct*, vol. C3, p. 6, 2001.

[200] K. Hagiwara, S. Ishihara, J. Kamoshita, and B. A. Kniehl, "Prospects of measuring general Higgs couplings at e^+e^- linear colliders," *Eur. Phys. J.*, vol. C14, pp. 457–468, 2000.

[201] R. Yonamine, K. Ikematsu, S. Uozumi, and K. Fujii, "A study of top-quark Yukawa coupling measurement in $e^+e^- \to t\bar{t}H$ at $\sqrt{s} = 500\,\mathrm{GeV}$," 2010.

[202] M. W. Grunewald, "Combined Electroweak Analysis," *J. Phys. Conf. Ser.*, vol. 110, p. 042008, 2008.

[203] W. de Boer, "The constrained MSSM revisited," 1996.

[204] G. Moortgat-Pick, "Physics aspects of polarized e^+ at the linear collider," 2006.

[205] M. Consonni, "Prospects for SUSY discovery and measurements with the ATLAS detector at the LHC," Prepared for 18th International Conference on Particles and Nuclei (PANIC 08), Eilat, Israel, 9-14 Nov 2008.

[206] I. J. R. Aitchison, "Supersymmetry and the MSSM: An Elementary introduction," 2005.

[207] J. R. Ellis, S. Heinemeyer, K. A. Olive, and G. Weiglein, "Indications of the CMSSM mass scale from precision electroweak data," 2006.

[208] G. A. Moortgat-Pick, "Motivation for polarised e^- and e^+ beams," 2004.

[209] A. Freitas, A. von Manteuffel, and P. M. Zerwas, "Slepton production at e^+e^- and e^-e^- linear colliders," *Eur. Phys. J.*, vol. C34, pp. 487–512, 2004.

[210] H. K. Dreiner and S. Lola, "Resonant single superparticle productions via supersymmetric R parity violation," Prepared for Physics with e^+e^- Linear Colliders (The European Working Groups 4 Feb - 1 Sep 1995: Session 3), Hamburg, Germany, 30 Aug - 1 Sep 1995.

[211] M. Heyssler, R. Ruckl, and H. Spiesberger, "Leptoquark and R-parity violating SUSY processes," 1999.

[212] A. Leike, "The Phenomenology of extra neutral gauge bosons," *Phys. Rept.*, vol. 317, pp. 143–250, 1999.

[213] T. G. Rizzo, "Distinguishing indirect signatures of new physics at the NLC: Z' versus R-parity violation," *Phys. Rev.*, vol. D59, p. 113004, 1999.

[214] A. Bartl *et al.*, "CP-odd observables in neutralino production with transverse e^+ and e^- beam polarization," *JHEP*, vol. 01, p. 170, 2006.

[215] T. G. Rizzo, "Transverse polarization signatures of extra dimensions at linear colliders," *JHEP*, vol. 02, p. 008, 2003.

[216] T. G. Rizzo, "More transverse polarization signatures of extra dimensions at linear colliders," *JHEP*, vol. 08, p. 051, 2003.

[217] M. Diehl, O. Nachtmann, and F. Nagel, "Probing triple gauge couplings with transverse beam polarisation in $e^+e^- \rightarrow W^+W^-$," *Eur. Phys. J.*, vol. C32, pp. 17–27, 2003.

[218] M. L. Swartz, "A complete order-α^3 calculation of the cross section for polarized Compton scattering," *Phys. Rev.*, vol. D58, p. 014010, 1998.

[219] J. List and D. Käfer, "Improvements to the ILC Upstream Polarimeter," 2009.

[220] G. A. Moortgat-Pick *et al.*, "Depolarization and Beam-beam Effects at the Linear Collider," EPAC'08, 11th European Particle Accelerator Conference, 23- 27 June 2008, Genoa, Italy.

[221] G. Moortgat-Pick *et al.*, "Challenge of polarized beams at future colliders," *J. Phys. Conf. Ser.*, vol. 110, p. 112004, 2008.

[222] C. Rimbault, P. Bambade, K. Mönig, and D. Schulte, "Incoherent pair generation in a beam-beam interaction simulation," *Phys. Rev. ST Accel. Beams*, vol. 9, p. 034402, 2006.

[223] C. Rimbault, G. Le Meur, F. Blampuy, P. Bambade, and D. Schulte, "Implementation of depolarization due to beam-beam effects in the beam-beam interaction simulation tool GUINEA- PIG++," *J. Phys. Conf. Ser.*, vol. 198, p. 012006, 2009.

[224] I. R. Bailey, (ed.) *et al.*, "Advanced QED methods for future accelerators. Proceedings, Joint IPPP Durham/Cockcroft Institute/ICFA Workshop, Warrington, UK, March 3-4, 2009," Prepared for Advanced QED Methods for Future Accelerators, Warrington, United Kingdom, 3-4 Mar 2009.

[225] C. Bartels, A. Hartin, C. Helebrant, D. Käfer, and J. List, "Precision Polarimetry at the ILC: Concepts, Simulations and experiments," *Nucl. Instrum. Meth.*, vol. A623, pp. 570–572, 2010.

[226] G. Abbiendi *et al.*, "Measurement of the $e^+e^- \rightarrow W^+W^-$ cross section and W decay branching fractions at LEP," *Eur. Phys. J.*, vol. C52, pp. 767–785, 2007.

[227] A. Blondel, "A Scheme to measure the polarization asymmetry at the Z pole in LEP," *Phys. Lett.*, vol. B202, p. 145, 1988.

[228] K. Mönig, "The use of positron polarization for precision measurements," LC-PHSM-2000-059.

[229] F. James and M. Roos, "Minuit: A System for Function Minimization and Analysis of the Parameter Errors and Correlations," *Comput. Phys. Commun.*, vol. 10, pp. 343–367, 1975.

[230] R. J. Barlow and C. Beeston, "Fitting using finite Monte Carlo samples," *Comput. Phys. Commun.*, vol. 77, pp. 219–228, 1993.

[231] A. Heister *et al.*, "Measurement of W pair production in e$^+$ e$^-$ collisions at centre-of-mass energies from 183 GeV to 209 GeV," *Eur. Phys. J.*, vol. C38, pp. 147–160, 2004.

[232] I. Bozovic-Jelisavcic *et al.*, "Luminosity Measurement at ILC," 2010.

[233] "Stopping powers and ranges for protons and alpha particles," Bethesda, USA: ICRU (1993) 286 p. (ICRU report: 49).

[234] B. L. Berman and S. C. Fultz, "Measurements of the giant dipole resonance with monoenergetic photons," *Rev. Mod. Phys.*, vol. 47, pp. 713–761, 1975.

[235] A. Baroncelli, "Study of total-absorption counters for very-high-energy particles," *Nucl. Instrum. Meth.*, vol. 118, pp. 445–451, 1974.

[236] U. Amaldi, "Fluctuations in Calorimetry Measurements," *Phys. Scripta*, vol. 23, p. 409, 1981.

[237] C. W. Fabjan and T. Ludlam, "Calorimetry in High-Energy Physics," *Ann. Rev. Nucl. Part. Sci.*, vol. 32, pp. 335–389, 1982.

[238] R. Wigmans, "On the Energy Resolution of Uranium and Other Hadron Calorimeters," *Nucl. Instrum. Meth.*, vol. A259, pp. 389–429, 1987.

[239] C. Leroy and P. Rancoita, "Physics of cascading shower generation and propagation in matter: Principles of high-energy, ultrahigh-energy and compensating calorimetry," *Rept. Prog. Phys.*, vol. 63, pp. 505–606, 2000.

[240] T. J. Roberts, H. R. Gustafson, L. W. Jones, M. J. Longo, and M. R. Whalley, "Neutron nucleus Inelastic Cross-Sections from 160 GeV/c to 375 GeV/c," *Nucl. Phys.*, vol. B159, pp. 56–66, 1979.

[241] E. Longo and I. Sestili, "Monte Carlo Calculation of Photon Initiated Electromagnetic Showers in Lead Glass," *Nucl. Instrum. Meth.*, vol. 128, p. 283, 1975.

[242] G. Grindhammer, M. Rudowicz, and S. Peters, "The Fast Simulation of Electromagnetic and Hadronic Showers," *Nucl. Instrum. Meth.*, vol. A290, p. 469, 1990.

[243] N. Wattimena, "Calorimetry at the International Linear Collider: From simulation to reality," DESY-THESIS-2010-006.

[244] Y. A. Kulchitsky and V. B. Vinogradov, "Analytical representation of the longitudinal hadronic shower development," *Nucl. Instrum. Meth.*, vol. A413, pp. 484–486, 1998.

[245] Y. Muraki *et al.*, "Radial and Longitudinal Behaviour of Nuclear Electromagnetic Cascade Showers Induced by 300 GeV Protons in Lead and Iron Absorbers," *Nucl. Instr. Meth.*, vol. A236, p. 47, 1985.

[246] R. Wigmans, "Advances in hadron calorimetry," *Ann. Rev. Nucl. Part. Sci.*, vol. 41, pp. 133–185, 1991.

[247] J. B. Birks, "The Theory and practice of scintillation counting," International series of Monographs on Electronics and Instrumentation, v. 27 Macmillan, New York.

[248] I. Abt *et al.*, "The Tracking, calorimeter and muon detectors of the H1 experiment at HERA ," *Nucl. Instrum. Meth.*, vol. A386, pp. 348–396, 1997.

[249] F. Simon, "Particle Showers in a Highly Granular Hadron Calorimeter," 2010.

[250] N. Akchurin *et al.*, "Hadron and jet detection with a dual-readout calorimeter," *Nucl. Instrum. Meth.*, vol. A537, pp. 537–561, 2005.

[251] S. Franchino, "New crystals for the DREAM project," *Nucl. Instrum. Meth.*, vol. A623, pp. 240–242, 2010.

[252] D. Acosta *et al.*, "Results of Prototype Studies for a Spaghetti Calorimeter," *Nucl. Instrum. Meth.*, vol. A294, pp. 193–210, 1990.

[253] J. Hauptman, "Estimate of neutrons event-by-event in DREAM," *J. Phys. Conf. Ser.*, vol. 160, p. 012072, 2009.

[254] J. E. Brau *et al.*, "Advances in Calorimetry," *Annu. Rev. Nucl. Part. Sci.*, vol. 60, pp. 615–644, 2010.

[255] A. N. Diddens *et al.*, "A Detector for Neutral Current Interactions of High-Energy Neutrinos," *Nucl. Instr. Meth.*, vol. 178, p. 27, 1980.

[256] J. Repond *et al.*, "Design and Electronics Commissioning of the Physics Prototype of a Si-W Electromagnetic Calorimeter for the International Linear Collider," *JINST*, vol. 3, p. P08001, 2008.

[257] C. Adloff *et al.*, "Construction and Commissioning of the CALICE Analog Hadron Calorimeter Prototype," *JINST*, vol. 5, p. P05004, 2010.

[258] R. Abrams *et al.*, "LC scintillator-based muon detector tail-catcher R&D," Presented at 2007 International Linear Collider Workshop (LCWS07 and ILC07), Hamburg, Germany, 30 May - 3 Jun 2007.

[259] E. Garutti, B. Lutz, J. Samson, and O. Wendt, "Preliminary results from hadron shower data with the CALICE tile AHCAL prototype," CALICE Note, CAN-011.

[260] A. Kaplan, "Pion Showers in the CALICE AHCAL Prototype," CALICE Note, CAN-026.

[261] V. Korbel, "A hadronic tile calorimeter for the TESLA detector," *Nucl. Instrum. Meth.*, vol. A518, pp. 49–53, 2004.

[262] G. Bondarenko *et al.*, "Limited Geiger-mode microcell silicon photodiode: New results," *Nucl. Instrum. Meth.*, vol. A442, pp. 187–192, 2000.

[263] P. Buzhan *et al.*, "Silicon photomultiplier and its possible applications," *Nucl. Instrum. Meth.*, vol. A504, pp. 48–52, 2003.

[264] B. Lutz, "Hadron showers in a highly granular calorimeter," DESY-THESIS-2010-048.

[265] E. Garutti, M. Groll, A. Karakash, and S. Reiche, "Magnetic field dependence studies for silicon photomultiplier," 2004. LC-DET-2004-025.

[266] A. Tadday *et al.*, "Characterisation studies of silicon photomultipliers for a calorimeter for the ILC," *PoS*, vol. PD09, p. 021, 2010.

[267] M. Terwort, "Realization and Test of the Engineering Prototype of the CAL-ICE Tile Hadron Calorimeter," 2010. Prepared for the IEEE Nuclear Science Symposium, Knoxville, TN, USA, 30 Oct - 6 Nov 2010.

[268] S. Manen *et al.*, "Dedicated front-end electronics for the next generation of linear collider electromagnetic calorimeter," 2005.

[269] P. D. Dauncey, "CALICE electromagnetic calorimeter readout status," 2004.

[270] R. Poeschl, "Calice Data Processing," 2007. EUDET-MEMO-2007-57.

[271] C. Adloff *et al.*, "Electromagnetic response of a highly granular hadronic calorimeter," 2010.

[272] N. Wattimena, "Commissioning of an LED calibration and monitoring system for the prototype of a hadronic calorimeter," DESY-THESIS-2006-039.

[273] N. D'Ascenzo, "Study of the neutralino sector and analysis of the muon response of a highly granular hadron calorimeter at the International Linear Collider," DESY-THESIS-2009-004.

[274] N. Feege, "Silicon photomultipliers: Properties and application in a highly granular calorimeter," DESY-THESIS-2008-050.

[275] M. Chadeeva, "Primary track finder processor." Talk, slides available at `http://www-flc.desy.de/hcal/meetings/internal/minutes2009/090225-MC_trackFinder.pdf`, 2009.

[276] K. Seidel, "Si-W ECAL treatment for HCAL only analysis and development of event selection processors." Talk, slides available at `http://ilcagenda.linearcollider.org/getFile.py/access?contribId=11&sessionId=1&resId=0&materialId=slides&confId=4932`, 2011.

[277] "Mokka web site." `http://mokka.in2p3.fr`.

[278] A. Lucaci-Timoce, "Description of the Analog HCAL Prototype in Mokka," tech. rep., Technical Note, 2009.

Acknowledgments